



---

Contribution to the Experimental Channel Evaluation of  
Optical Camera Communication for Wireless Sensor  
Networks

---

Vicente Matus Icaza

Doctoral thesis  
to achieve the academic degree of

Doctor of Philosophy  
(*Ph.D.*)

in the doctorate program  
EmITIC - *Empresa, Internet y Tecnologías de las Comunicaciones*

IDeTIC - *Instituto para el Desarrollo Tecnológico e Innovación en Comunicaciones*  
Universidad de Las Palmas de Gran Canaria  
Date: November 2021

## Supervisors

Prof. Dr. Rafael Pérez Jiménez  
IDeTIC, Universidad de Las Palmas de Gran Canaria

Dr. Jose Rabadán Borges  
IDeTIC, Universidad de Las Palmas de Gran Canaria

## Examiners

Prof. Dr. Zabih Ghassemlooy  
Northumbria University

Prof. Dr. Luis Nero Alves  
Universidade de Aveiro

**D. JOSÉ A. RABADÁN BORGES**  
**COORDINADOR DEL PROGRAMA DE DOCTORADO**  
**EMPRESA, INTERNET Y TECNOLOGÍAS DE LAS COMUNICACIONES**  
**DE LA UNIVERSIDAD DE LAS PALMAS DE GRAN CANARIA**

**INFORMA,**

De que la Comisión Académica del Programa de Doctorado, en su sesión de fecha ..... tomó el acuerdo de dar el consentimiento para su tramitación, a la tesis doctoral titulada "*Contribution to the Experimental Channel Evaluation of Optical Camera Communication for Wireless Sensor Networks*" presentada por el/la doctorando/a D Vicente Matus Icaza y dirigida por los Doctores Rafael Pérez Jiménez y José Rabadán Borges.

Y para que así conste, y a efectos de lo previsto en el Artº 11 del Reglamento de Estudios de Doctorado (BOULPGC 04/03/2019) de la Universidad de Las Palmas de Gran Canaria, firmo la presente en Las Palmas de Gran Canaria, a... de.....de dos mil veintiuno

**UNIVERSIDAD DE LAS PALMAS DE GRAN CANARIA  
ESCUELA DE DOCTORADO**

Programa de doctorado: Empresa, Internet y Tecnologías de las Comunicaciones.

Título de la Tesis: Contribution to the Experimental Channel Evaluation of Optical Camera Communication for Wireless Sensor Networks.

Tesis Doctoral presentada por D. Vicente Matus Icaza.

Dirigida por el Dr. Rafael Pérez Jiménez.

Codirigida por el Dr. José Rabadán Borges.

Las Palmas de Gran Canaria, a ..... de ..... de 2021

El/la Director/a,

El/la Codirector/a

El/la Doctorando/a,

# Dedication

---

*A aquellas personas que me motivaron a seguir el camino de la ciencia,  
en especial la Prof. Olga Hernández de la Fuente,  
4<sup>to</sup>J, Liceo Abate Molina de Talca, 2006-2009.*



# Acknowledgments

---

## Funding

This work has received funding from European Union's Horizon 2020 Marie Skłodowska-Curie Actions, under Grant Agreement no. 764461 (Project VisIoN).

It also received funding by the Spanish Research Administration (MINECO project: OSCAR, ref.: TEC 2017-84065-C3-1-R)

## Collaborators

The author thanks the technical contributions and active support from the team members at the Institute (IDeTIC) in Las Palmas de Gran Canaria, Spain, the Czech Technical University (CTU) in Prague, Czechia, and Northumbria University (NU), in Newcastle upon Tyne, United Kingdom, listed as follows:

- **Main supervisor:** Prof. Rafael Perez-Jimenez (IDeTIC).
- **Second supervisor:** Dr. Jose Rabadan (IDeTIC).
- **Academic staff:**
  - Dr. Victor Guerra (IDeTIC).
  - Dr. Julio Rufo (IDeTIC).
  - Prof. Stanislav Zvanovec (CTU).
  - Prof. Zabih Ghassemlooy (NU).
- **Technical support:**
  - Cristo Jurado Verdu (IDeTIC).
  - Dr. Patricia Chávez Burbano (IDeTIC).
  - Dr. Jan Bohata (CTU).
  - Dr. Shivani Teli (CTU).
  - Dr. Elizabeth Eso (NU).





The importance of reliable communication infrastructure has become relevant for all of the services offered in our contemporary society: automation, messaging, streaming, data access, security, transportation, among others. For establishing data communication links in a wide variety of environments, wireless systems are the most popular alternative due to their seamless operation, mobility support, and interoperability. However, these infrastructures are nearing an outage of capacity because of the congestion of the radio-frequency (RF) and microwave spectra, which has motivated the exploration of new alternatives using higher frequencies of the electromagnetic spectrum, such as millimeter waves and visible light, which provide more reusability and cell density since they face significant propagation losses and tend to cover only short ranges.

In addition to the constantly increasing demand for reliable and ubiquitous wireless communication infrastructures stimulated by user-end devices like smartphones, the new Internet of things (IoT) machines have emerged in the mass market. In most cases, IoT requires low data rate wireless machine-to-machine communication, which is recently becoming a considerable portion of the connections, raising, even more, the congestion of the RF and microwave spectra. The IoT devices usually consist of home, office, or industrial appliances that can connect to the Internet and provide extended functionalities and automation, potentially improving the efficiency of the processes and comfort of the users. In industrial contexts, there is often the requirement for sensors and actuators to be deployed in a wide variety of fields. The use of wireless sensor networks (WSNs) is relevant in environments that require mobile or semi-mobile machines that integrate

sensing with communications, or even in cases where deploying wired networks for static nodes is impractical.

The research for new wireless communication alternatives has increased the interest in visible light communications (VLC) and optical camera communication (OCC), a subset of optical wireless communication (OWC) technologies that utilize photosensitive devices such as digital cameras to detect wireless data streams generated by intensity-modulated lights based on light-emitting diodes (LEDs). OCC and VLC have been extensively developed in recent years for indoor applications and can be a complementary alternative to wireless communication systems in homes and offices, with technologies known as light fidelity (LiFi), which are already included in standardization by the Institute of Electrical and Electronics Engineers (IEEE) and the International Telecommunications Union (ITU) through the standard IEEE 802.15.7 and the recommendation ITU G.9991.

Although the development of OCC and VLC applications for indoors is considerably advanced, their operation outdoors is still limited. As in all OWC systems, the atmospheric conditions play a significant role in the degradation of the wireless optical channel due to the effects of aerosols, turbulence, and other meteorologic phenomena, which are uncontrollable and vaguely predictable. Evaluating these events' influence over the wireless optical channel is currently a challenge to be addressed in the research field of OCC, which may open a wide variety of applications in Smart Cities that can take advantage of existing infrastructures, such as car lamp-to-dash camera vehicular communication, advertising display-to-phone, and mobile or static node-to-surveillance camera links, among others.

This thesis experimentally evaluated the feasibility of deploying outdoor low data rate OCC links in harsh atmospheric conditions both emulated in a laboratory chamber and in real scenarios, using commercially available cameras and LED components. In most experimental OCC setups in research, the only photographic parameters considered are the exposure

time and the frame rate, whereas, in this work, the impact of varying the analog gain was studied. This led to a novel methodology for optimizing the communication quality in terms of the signal-to-noise ratio (SNR) by reducing the analog-to-digital conversion noise. Finally, in this thesis, an innovative topology of sub-pixel OCC is proposed, which has the potential to effectively provide communication re-utilizing camera hardware by using small optical front-ends of transmitters and receivers, ensuring minimal use of the field of view of the camera for communications, leaving the video frame free for general image purposes.

Among the highlighted results obtained from the experimentation in harsh atmospheric conditions, it was seen that the scattering caused by aerosols deviates energy from non-line of sight rays to the image sensor of the camera, making the transmitters appear bigger than expected and allowing to obtain more information in every frame, increasing the achievable data rate compared to in clear conditions. Although OCC systems can take advantage of the apparent widening of the transmitters in the presence of aerosols, the intensity of the light signal is still attenuated, reducing the SNR and increasing the bit error rate consequently. It was seen that using the analog amplifier built in the image sensor of the camera receiver could help to overcome the effect of fog and dust in the experiments in low visibilities.

The vast majority of the experimental OCC setups in recent research have taken advantage of the rolling shutter acquisition that most commercially available cameras perform. However, this technique requires the use of large portions of the camera's field of view to be assigned for communications. In this sense, OCC cannot re-utilize available hardware if it needs it to be fully dedicated for communications. In order to address this issue, the sub-pixel OCC experiment as mentioned above was carried out. Two transmitters employing a single 5 mm LED component were deployed at about 100 m of the camera, achieving around 20 dB of SNR. Although the data rate per node was relatively low (8 bps), the sub-pixel topology allows

increasing the number of transmitters to several hundreds of them. If some of the applications of WSN are considered, such as in precision farming, where relatively stable variables need to be measured, the potential application of sub-pixel OCC shows adequate capabilities and has the potential to become a new alternative for WSN and IoT applications.

Las infraestructuras de telecomunicaciones han cobrado relevancia para todos los servicios que se ofrecen actualmente en nuestra sociedad: automatización, mensajería, *streaming*, acceso a datos, seguridad, transporte, entre otros. Los sistemas inalámbricos son la alternativa más popular para establecer enlaces de comunicación de datos en una amplia variedad de entornos gracias a su funcionamiento transparente, movilidad e interoperabilidad. Sin embargo, estas infraestructuras están experimentando el agotamiento de su capacidad a causa de la congestión de los espectros de radiofrecuencia (RF) y microondas, lo que ha motivado la exploración de nuevas alternativas que utilicen frecuencias más altas del espectro electromagnético, como las ondas milimétricas y la luz visible, que proporcionan una mayor reutilización y densidad celular, ya que se enfrentan a grandes pérdidas de propagación y tienden a cubrir sólo cortas distancias.

Además de la demanda cada vez mayor de infraestructuras de comunicaciones inalámbricas fiables y ubicuas, estimulada por los dispositivos móviles de uso personal, han surgido en el mercado las nuevas máquinas del Internet de las cosas (IoT, *Internet of Things*), que en la mayoría de los casos, requieren una comunicación inalámbrica de máquina a máquina (M2M) de baja velocidad, que últimamente se están convirtiendo en una parte considerable de las conexiones, lo que aumenta, aún más, la congestión de los espectros de RF y microondas. Los dispositivos IoT suelen consistir en aparatos domésticos, de oficina o industriales que mediante la comunicación M2M pueden proporcionar funcionalidades ampliadas y automatización, mejorando potencialmente la eficiencia de los procesos y la comodidad de los usuarios. En contextos industriales, a menudo se

demanda el despliegue de sensores y actuadores en una amplia variedad de condiciones. El uso de redes de sensores inalámbricos (WSN, *Wireless Sensor Networks*) es relevante en entornos que requieren máquinas móviles o semimóviles que integren el sensado con las comunicaciones, o incluso en casos que los nodos aún en estático prefieren conectividad inalámbrica pues el uso de redes cableadas no es práctico.

La búsqueda de nuevas alternativas de comunicación inalámbrica ha aumentado el interés en desarrollar las comunicaciones por luz visible (VLC, *Visible Light Communications*) y la comunicación óptica basada en cámaras (OCC, *Optical Camera Communications*), un subconjunto de tecnologías de comunicación óptica inalámbrica (OWC, *Optical Wireless Communications*) que utilizan dispositivos fotosensibles, como las cámaras digitales o fotodiodos, para la demodulación de datos transmitidos por luces de intensidad modulada basadas en diodos emisores de luz (LED, *Light-emitting Diodes*) y monitores.

Las OCC y VLC se han desarrollado ampliamente en los últimos años para aplicaciones de interior y pueden ser una alternativa complementaria a los sistemas de comunicación inalámbricos en hogares y oficinas, con tecnologías conocidas como *Light Fidelity (LiFi)*, que ya están incluidas en la estandarización del Instituto de Ingenieros Eléctricos y Electrónicos (IEEE) y la Unión Internacional de Telecomunicaciones (UIT) a través de la norma IEEE 802.15.7 y la recomendación ITU G.9991. Aunque el desarrollo de las aplicaciones OCC y VLC para interiores está considerablemente avanzado, su funcionamiento en exteriores es todavía limitado.

Como en todos los sistemas OWC, las condiciones atmosféricas tienen un efecto considerable en la degradación del canal óptico inalámbrico debido a fenómenos meteorológicos, que son incontrolables y poco predecibles, tales como la presencia de aerosoles o partículas en suspensión y la turbulencia inducida por diferencias de temperatura, entre otros. La evaluación de la influencia de estos eventos sobre el canal óptico inalámbrico es actualmente

un reto a abordar en el campo de la investigación de OCC, que podría abrir una amplia variedad de aplicaciones en las *Smart Cities*. Dichas aplicaciones tienen la ventaja de poder aprovechar ciertas infraestructuras existentes. Algunos ejemplos son la comunicación de coche a coche mediante faros y cámaras *dashcam*, enlaces desde otras luminarias a cámaras de vigilancia, transmisión desde pantallas publicitarias a móviles, entre otras.

En esta tesis se ha evaluado experimentalmente la viabilidad de desplegar enlaces OCC de baja velocidad en exteriores en condiciones atmosféricas adversas, tanto emuladas en laboratorio como en escenarios reales, utilizando cámaras y componentes LED disponibles en el mercado. En la mayoría de las configuraciones experimentales en el campo de investigación de OCC, los únicos parámetros fotográficos que se tienen en cuenta son el tiempo de exposición y la tasa de fotogramas. En este trabajo se estudió el impacto de la variación de la ganancia analógica, lo que condujo a una nueva metodología para optimizar la calidad de la comunicación en términos de la relación señal-ruido (SNR, *Signal-to-Noise Ratio*) mediante la reducción del ruido de conversión analógico-digital. Por último, en esta tesis se propone una nueva topología de OCC denominada sub-píxel, que tiene el potencial de proporcionar comunicación reutilizando el *hardware* de cámaras mediante el uso de pequeños dispositivos ópticos en transmisores y receptores, asegurando un uso mínimo del campo de visión de la cámara para las comunicaciones, dejando los fotogramas libres para uso fotográfico general.

## Objetivos

En base a los desafíos mencionados a los que se enfrentan las aplicaciones de OCC en exteriores, esta tesis se desarrolló considerando objetivos que se exponen a continuación.

- **Objetivo 1 (O1):** Evaluar el desempeño de sistemas OCC en condiciones atmosféricas adversas.
- **Objetivo 2 (O2):** Evaluar el impacto en la calidad de la señal de los parámetros fotográficos envueltos en la adquisición de imágenes.
- **Objetivo 3 (O3):** Implementar un banco de pruebas de OCC sub-píxel compuesto de dispositivos ópticos de pequeña escala en un entorno de exterior real.

## Conclusiones

Entre los resultados destacados que se obtuvieron de la experimentación en condiciones atmosféricas adversas, se vio que la dispersión causada por los aerosoles desvía la energía de rayos fuera de la línea de vista hacia el sensor de imagen de la cámara, haciendo que los transmisores parezcan más grandes de lo esperado y permitiendo obtener más información en cada fotograma, aumentando la tasa de datos alcanzable en comparación con atmósferas limpias. Sin embargo, aunque los sistemas OCC pueden aprovechar el aparente ensanchamiento de los transmisores en presencia de aerosoles, la intensidad de la señal luminosa es atenuada de todas maneras, reduciendo la SNR y aumentando en consecuencia la tasa de error de bit. En este trabajo se encontró que el uso del amplificador analógico incorporado en el sensor de imagen puede ayudar a superar el efecto de la atenuación en los experimentos realizados en condiciones de baja visibilidad.

Frecuentemente, los montajes experimentales de OCC aprovechan la adquisición *rolling shutter* que realizan la mayoría de las cámaras disponibles en el mercado. Esta técnica requiere el uso de grandes porciones del campo de visión para las comunicaciones. En este sentido, OCC no puede reutilizar el hardware disponible si necesita que esté totalmente dedicado a la recepción de datos. Para solucionar este problema, se llevó a cabo el experi-



mento de OCC sub-píxel mencionado anteriormente. Se desplegaron dos transmisores que empleaban un único LED de 5 mm a aproximadamente 100 m de la cámara, logrando hasta 20 dB de SNR. Aunque la tasa de datos por nodo era relativamente baja (8 bps), la topología de sub-píxel permite aumentar considerablemente el número de transmisores. Si se tienen en cuenta algunas de las aplicaciones de las WSN, como por ejemplo en la agricultura de precisión, en la que es necesario medir variables relativamente estáticas, la aplicación de OCC muestra unas capacidades adecuadas y potencialmente podría convertirse en una alternativa de comunicación inalámbrica para WSN e IoT.



# Contents

---

Dedication	v
Acknowledgments	vii
Abstract	ix
Resumen	xiii
Contents	xix
1 Introduction	1
1.1 Motivation	2
1.2 Hypotheses	3
1.3 Objectives	4
1.4 Organization of the document	5
1.5 List of publications	6
1.5.1 Journal articles	6
1.5.2 Conference proceedings	7
1.5.3 Collaborations	7
2 State of the Art	9
2.1 Outdoor applications	10
2.2 Challenges	10
2.2.1 Outdoor wireless channel challenges	11
2.2.2 Multiple-transmitter topologies challenges	11
3 Theoretical Framework	13
3.1 Fundamentals	13
3.1.1 Channel modelling	13
3.1.2 On-off keying	14
3.2 Technologies	15
3.2.1 Light-emitting diode-based transmitter	15
3.2.2 Digital camera-based receiver	16
4 Methodology	19
4.1 Experimental setups	19
4.1.1 Transmitter equipment	19
4.1.2 Receiver equipment	20
4.1.3 Channel conditions considered	21
4.2 Processing	22

5	Experimental Results	25
5.1	Publication 1 (P1) . . . . .	25
5.2	Publication 2 (P2) . . . . .	41
5.3	Publication 3 (P3) . . . . .	50
5.4	Summary . . . . .	69
6	Conclusions and Future Works	71
	Bibliography	75
A	Journal article	79
B	Conference proceedings.	89
C	Scripts developed	111

The radiofrequency (RF) and microwave spectra are currently the primary communication resources used by wireless systems to carry information between nodes of different tiers of the Internet (wireless wide area, local area, and personal area networks, known as WWAN, WLAN, and WPAN). However, the electromagnetic spectrum is limited, whereas the number of connected devices is growing steadily [1]. Thus, supporting an ever-growing ecosystem of mobile devices implies a constant exploration of new technologies that efficiently exploit the limited spectrum available.

Besides the user-end devices and backbone infrastructure, the recent growth of embedded computers and other microcontroller-based nodes offering automation, known as the Internet of things (IoT), is a trend in telecommunications. The IoT devices form wireless sensors and actuators networks in a broad range of environments, needing connectivity from machine-to-machine (M2M), not necessarily interfacing with humans during operation. They are currently based on RF technologies, such as Wi-Fi, Bluetooth, and Zigbee, and new technologies, such as narrow-band and low-power wide-area networks, otherwise known as NB-IoT and LP-WAN. The benefits of such sensor networks' availability to industry and society generally range from precise monitoring of processes and resources management to increased safety and automation beyond human awareness. For example, vehicular infrastructure can communicate with mobile nodes in cars, alerting drivers of dangerous situations and alternative routes with continuous traffic monitoring. As shown in Fig. 1.1, wireless connections for M2M represent the most significant growth in device share, from 13% of the connections in 2018 to an expected 34% in 2023, unlike other kinds of connection, that will either maintain or reduce their share.

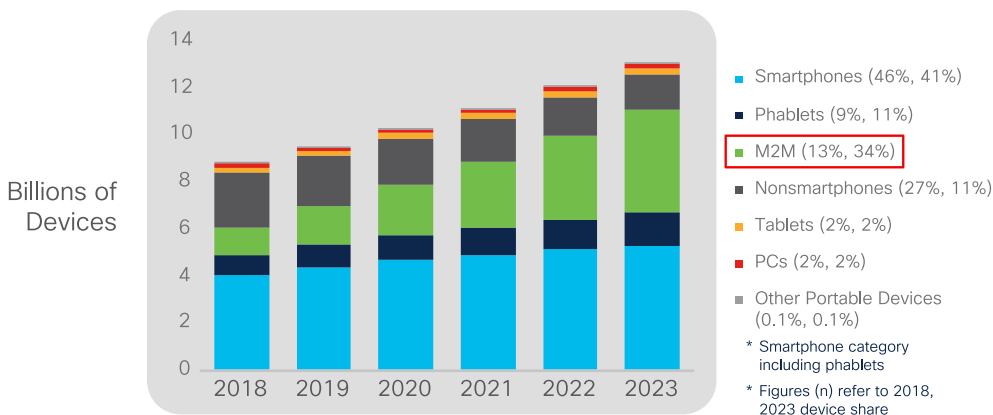


**Figure 1.1:** Global growth of mobile (wireless) devices per type, highlighting machine-to-machine (M2M) connections, that are predicted to have the highest share by the year 2023. Source: Cisco annual report [1].

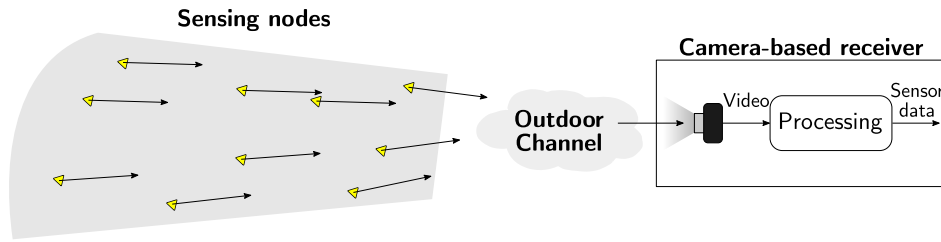


**Figure 1.2:** Diagram of potential applications of optical camera communication to wireless sensor networks. Source: [4].

Optical camera communication (OCC) technologies are part of visible light communication (VLC), a subset of optical wireless communications (OWC) that use light-emitting diodes (LEDs) and cameras as transmitting and receiving interfaces, respectively. The OCC schemes have emerged in the context of RF spectral scarcity and the growing demand for wireless connectivity supported by the ubiquity of digital cameras and solid-state lighting devices in smartphone and LED technologies. The OCC technologies extend the capabilities of cameras beyond photography and film-making and are envisioned to play a major role in IoT, providing data communication, localization, vehicular communications, among others [2], [3]. Since the camera-based OCC receivers do not need dedicated hardware for their implementation in smartphones and other portable devices, it is expected to be the first VLC scheme to be widespread.

As further developed in the following chapters, the VLC and OCC fields have a wide range of feasible and competitive applications, which can complement the current RF solutions for implementing more reliable heterogeneous networks. One of the highlighted applications envisioned for this technology and proposed in this work is the implementation of wireless sensing nodes featuring an LED-based transmitter that transfers data from the sensors to a camera, which monitors many simultaneous transmissions in the field and sends the data from the sensor network to a data acquisition center. Furthermore, these schemes have the potential to be applied in numerous industrial scenarios where automation is required. Figure 1.2 represents the potential scheme for the application of OCC to wireless sensor networks (WSNs). As an example, in precision farming, tens of sensing nodes in an area of about one hectare can harvest energy from sunlight, measure agricultural variables such as soil moisture, and send it to an OCC receiver which simultaneously monitors the field through video and acts as the gateway for the information to be acquired.

## 1.1 Motivation

The project entitled "Visible light-based Interoperability and Networking" (VisIoN), from Marie Skłodowska-Curie Actions (grant agreement No. 764461), focuses on the research and development of novel functionalities of LEDs on top of illumination. It recognizes the growing interest from academic and industrial research groups worldwide in the emerging area of VLC and acts as a training community

for new researchers who will lead the area. The project's background is based on photonics, wireless communications, modulation, and physical and upper-layer protocols. The project's methodology is to train early-stage researchers (ESRs) in co-supervised projects grouped by selected applications, making significant contributions in the technical and scientific levels through publications and dissemination, and enrolling the ESRs in Ph.D. programs, dedicated tutorials, and workshops held by the network. The consortium is formed additionally by industrial partners that help integrate theory with know-how, giving the ESRs technical training.

The target application areas that divide the VisIoN project into work packages are Smart Cities, Homes and Offices (SCOH), Smart Transportation, and Manufacturing and Medical. In particular, the project ESR2 Optical Camera Communications for Sensor Networking is part of the work package SCOH, aiming to use commercial cameras as receivers for low-speed VLC and implement an experimental test-bed to study the influence of atmospheric conditions in outdoor scenarios.

The Institute for Technological Development and Innovation in Communications (IDeTIC) belongs to the University of Las Palmas de Gran Canaria (ULPGC) and has six divisions, among which the Division of Photonics Technology and Communications holds the ESR2 project from VisIoN. In this division, multiple research projects related to VLC have been under development with international and national funding since the emergence of this field. In addition, industrial participation through Lightbee, which is tightly related to the division, has carried out the technological transfer of VLC into the market. In this context, the project ESR2 is supported by highly active and pioneering members of the field.

Some of the past research at IDeTIC that has laid the groundwork for the development of this thesis has focused on feasible experimental implementations of VLC for high and low-speed data transmission using existing infrastructures, such as street lamps, in-flight lighting, or car lamps, among others [5]–[7], different modulation schemes exploiting the colored sources and sensitive devices [8], [9], and the applications to Smart Cities, vehicular communications and underwater optical wireless communications [10]–[14]

## 1.2 Hypotheses

Taking into account the continuous advances in camera equipment development, their high sensitivity and accuracy, and assuming that the capabilities of modern commercial cameras can be exploited to establish outdoor OCC links, the hypotheses of this work are stated as follows.

### Hypothesis 1 (H1)

*OCC links can be established in outdoor scenarios using general-purpose cameras.*

The implementation of novel VLC applications in outdoor scenarios requires the links to overcome unpredictable changes in the optical wireless channel due to dynamic atmospheric conditions, degradation of the optical interfaces, and the presence of external sources of light. Furthermore, the image-forming optics

of cameras give OCC an advantage over photodiode (PD)-based VLC systems to establish communication links in outdoor scenarios due to the broader field of view and higher sensitivity of cameras. Although the bandwidth is lower compared to PD-based receivers, it is suitable for IoT applications.

### Hypothesis 2 (H2)

*The digital signal processing can be optimized in commercial camera-based OCC by controlling the variables involved in the image acquisition.*

OCC systems implemented using commercial camera equipment need to exploit the settings available by the hardware and firmware controllers. In this sense, since camera equipment is intended for photographic purposes, OCC can optimize the image parameters such as the capture timings by software-defined exposure time and the hardware's fixed rolling shutter row-shift time, as well as the image sensor's analog gain, to improve the communication signal's quality.

### Hypothesis 3 (H3)

*OCC can be established in the outdoor wireless channel with small optical devices, allowing re-utilization of the camera output for simultaneous video monitoring and communication.*

The feasibility of OCC has been successfully tested on an increasing number of commercial and research-oriented camera equipment. However, the scenarios considered use large optical devices or very short ranges, assuming a large portion of the image sensor area is impinged by the transmitter's light, limiting the video monitoring field of view and dedicating a considerable part to communications. By using smaller optical devices, such as single LEDs and microlens cameras, OCC can be established in outdoor conditions with projections of the transmitter over the image sensor under the pixel area size.

## 1.3 Objectives

As stated by the VisIoN project's Grant Agreement (No. 764461), the main objective of the thesis' tasks is the following:

*"Using commercial cameras as  $R_x$  for low-speed communications, combining signal processing modulation techniques with optical processing. Demonstration for validation."*

According to these guidelines, we have pursued the following specific objectives.

### Objective 1 - (O1)

*To evaluate the performance of OCC systems in outdoor environments under atmospheric conditions.*

In order to demonstrate H1 and potentially expand the spectrum of available applications of VLC and OCC, experimentation in outdoor scenarios needs to be carried out. Design constraints can be included in further developments by studying the atmospheric influence on the optical wireless channel.



## Objective 2 - (O2)

*To evaluate the impact of the camera acquisition parameters for maximizing the communication signal quality in OCC.*

The control of software-defined parameters and the use of different lens arrays have an impact on the optical communication signal quality, which can be measured and estimated using the signal-to-noise ratio and bit error rate as metrics. The experimental evaluation of the influence of these parameters may contribute to optimizing the signal quality in OCC.

## Objective 3 - (O3)

*To implement a sub-pixel OCC link test-bed, using small LED and camera devices in a real outdoor scenario.*

The implementation of a test-bed for OCC, comprised of a CMOS camera and LED components with small optical dimensions, controlled by programmable logic as in an IoT device, with link ranges of several tens of meters or above the hundred-meter range has the potential to allow simultaneous communication and video applications using OCC in outdoors with re-utilized camera equipment. Furthermore, the combination of long ranges and small optics falls in the category of sub-pixel OCC, where the region of interest (ROI) considered can be reduced to single pixels since the projection of the transmitters over the image sensor is of sub-pixel areas.

## 1.4 Organization of the document

This thesis consists of a compendium of indexed-journal publications, which are presented as the core experimental contributions in this document. Each of them is included in their final version of post-prints using the journal's format. In order to contextualize the project and its methodologies, give a review of the available literature, explain the principles of the development of this work, and describe the experimental design of the experiments carried out, this thesis includes the necessary chapters before the compendium of articles is presented.

This document is structured as shown in Figure 1.3 and is developed as follows. After contextualizing the author's project, stating the objectives of this work in Chapter 1, a review of the state of the art in OCC is presented in Chapter 2, highlighting the applications and challenges of the research field. Next, the fundamentals of OCC and the technologies employed in this thesis are developed in Chapter 3. Then, the materials and methods are detailed in Chapter 4, describing the experimental design and the digital signal processing (DSP) employed. Then, as it was aforementioned, the results of this work are shown by means of the compendium of publications in Chapter 5, where the experiments using OCC in emulated and real atmospheric conditions are analyzed. Finally, the conclusions obtained and the future works prospected from this research are summarized in Chapter 6.

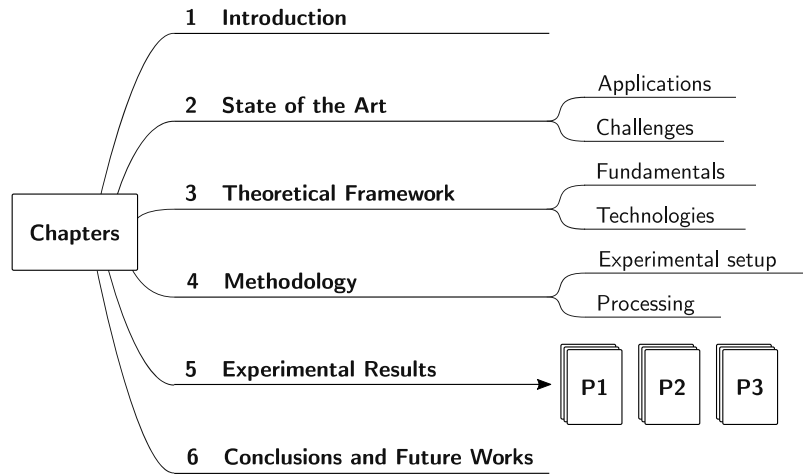


**Figure 1.3:** Structure of the document, highlighting the contributions of each chapter.

## 1.5 List of publications

The works developed in this thesis led to the editing of four publications in indexed journals and five articles in conference proceedings. In addition, the author collaborated with other researchers to publish four journal articles and two conference proceedings as a secondary contributor. In the following sections, all the mentioned articles are listed.

### 1.5.1 Journal articles

The publications included in the compendium (See Chapter 5 and Appendix A) are entitled as follows:

- **Matus, V.,** Eso, E., Teli S. R., Perez-Jimenez, R., Zvanovec, S. (2020). “Experimentally Derived Feasibility of Optical Camera Communications under Turbulence and Fog Conditions,” *MDPI Sensors*, 20(3), 757-771.
- **Matus, V.,** Guerra, V., Zvanovec, S., Rabadan, J., Perez-Jimenez, R. (2021). “Sandstorm effect on experimental optical camera communication,” *OSA Applied Optics*, 60(1), 75-82.
- **Matus, V.,** Guerra, V., Jurado-Verdu, C., Rabadan, J., and Perez-Jimenez, R. (2021). “Demonstration of a Sub-pixel Outdoor Optical Camera Communication Link,” *IEEE Latin America Transactions*, 19(10), 1798–1805.
- **Matus, V.,** Guerra, V., Jurado-Verdu, C., Zvanovec, S., and Perez-Jimenez, R. (2021). “Wireless Sensor Networks Using Sub-Pixel Optical Camera Communications: Advances in Experimental Channel Evaluation,” *MDPI Sensors*, 21(8), 2739–2757.

### 1.5.2 Conference proceedings

The camera-ready conference proceedings are included in Appendix B, and are entitled as follows:

- **Matus, V.**, Azurdia-Meza, C. A., Cespedes, S., Ortega, P., Montejo-Sanchez, S., Rojas, J., Soto, I., "Implementation of a Low-Cost Vehicular VLC System and CAN Bus Interface" in *2018 11th IEEE/IET International Symposium on Communication Systems, Networks and Digital Signal Processing (CSNDSP)*, Budapest, Hungary, 18-20 July 2018.
- **Matus, V.**, Guerra, V., Jurado-Verdu, C., Rabadan, J., Perez-Jimenez, R., "Simulation of Rolling Shutter Acquisition in Optical Camera Communications" in *2019 15th International Conference on Telecommunications (ConTEL)*, Graz, Austria, 3-5 July 2019.
- **Matus, V.**, Guerra, V., Jurado-Verdu, C., Shivani Rajendra Teli, Zvanovec, S., Rabadan, J., Perez-Jimenez, R., "Analog Gain Optimization in Rolling Shutter Optical Camera Communications" in *2020 12th IEEE/IET International Symposium on Communication Systems, Networks and Digital Signal Processing (CSNDSP)*, Porto, Portugal, 20-22 July 2020.
- **Matus, V.**, Shivani Rajendra Teli, Guerra, V., Jurado-Verdu, C., Zvanovec, S. and Perez-Jimenez, R., "Evaluation of Fog Effects on Optical Camera Communications Link," in *3rd West Asian Symposium on Optical and Millimeter-wave Wireless Communication (WASOWC)*, Tehran, Iran, 24-25 November 2020.
- **Matus, V.**, Guerra, V., Jurado-Verdu, C., Zvanovec, S., Rabadan, J., Perez-Jimenez, R., "Design and Implementation of an Optical Camera Communication System for Wireless Sensor Networking in Farming Fields" in *2021 IEEE International Symposium on Personal, Indoor and Mobile Radio Communications (PIMRC)*, Helsinki, Finland, 13-16 September 2021.

### 1.5.3 Collaborations

The following list contains the articles developed by researchers from IDeTIC and the VisIoN project, where the author has participated as a collaborator.

- Jurado-Verdu, C., **Matus, V.**, Rabadan, J., Guerra, V., Perez-Jimenez, R. (2019). "Correlation-based receiver for optical camera communications." *OSA Optics Express*, 27(14), 19150–19155.
- Jurado-Verdu, C., Guerra, V., **Matus, V.**, Rabadan, J., Perez-Jimenez, R., Luis Gomez-Pinchetti, J., Almeida, C. (2020). "Application of Optical Camera Communication to Microalgae Production Plants." *2020 12th International Symposium on Communication Systems, Networks and Digital Signal Processing (CSNDSP)*, Porto, Portugal, 20-22 July 2020.

- Teli, S. R., **Matus, V.**, Zvanovec, S., Perez-Jimenez, R., Vitek, S., Ghassemlooy, Z. (2020). "The First Study of MIMO Scheme Within Rolling-shutter Based Optical Camera Communications." *2020 12th International Symposium on Communication Systems, Networks and Digital Signal Processing (CSNDSP)*, Porto, Portugal, 20-22 July 2020.
- Jurado-Verdu, C., Guerra, V., **Matus, V.**, Almeida, C., Rabadan, J. (2021). "Optical Camera Communication as an Enabling Technology for Microalgae Cultivation." *MDPI Sensors*, 21(5).
- Teli, S. R., **Matus, V.**, Zvanovec, S., Perez-Jimenez, R., Vitek, S., Ghassemlooy, Z. (2020). "Optical Camera Communications for IoT–Rolling-Shutter Based MIMO Scheme with Grouped LED Array Transmitter." *MDPI Sensors*, 20(12), 3361.
- Jurado-Verdu, C., Guerra, V., **Matus, V.**, Rabadan, J., and Perez-Jimenez, R. (2021). "Convolutional autoencoder for exposure effects equalization and noise mitigation in optical camera communication." *OSA Optics Express*, 29, 22973-22991.

In this chapter, the latest advances in the OCC field are cited, focusing on the outdoor applications and the technologies used. The major challenges for the deployment of OCC in outdoor scenarios are outlined and discussed.

The OCC field, which is considered a subset of VLC [15]–[17], has gained interest in recent years after the first proposals of camera-based VLC receivers were reported [18]–[20]. These technologies essentially combine low data rate LED-based transmitters and camera-based receivers. However, they can also consider other light sources such as image displays, monochromous displays, and controllable mirrors, as well as other image sensor technologies such as multispectral cameras [3], [21]–[26].

The rapid development of these techniques can be attributed to the fact that multiple digital cameras are included in smartphones and other portable devices, in contrast to VLC, which requires the adoption of dedicated photodiode (PD) hardware, acting as a limitation for its deployment. The most available cameras use CMOS image sensors, which are less expensive than charge-coupled device (CCD) technology and, depending on their electronic architecture, their image acquisition mechanism can be either rolling shutter (RS) or global shutter (GS), as considered by the Institute of Electrical and Electronics Engineers (IEEE) 802.15.7 standard [27]. The shutter acquisition mode impacts the achievable data rate and linkspan of OCC systems, as it will be discussed in Chapter 3.

Similar to the feature of VLC technologies that exploit existing LED infrastructures to provide simultaneous illumination and communication, OCC can provide simultaneous video capture and communication. These premises make both technologies attractive for marketing and cost-neutral implementation. Contemporary research on OCC focuses on its application to vehicular communications [15], [28]–[30], positioning [31], and sensor networking in industrial and medical facilities [16], [32].

In sub-meter ranges, OCC and VLC can benefit from large projections of the transmitter surface into the photo-sensitive devices in receivers, achieving higher data rates, enabling inter-chip communications and dense IoT networks [33]. The implementation of OCC in smartphones can be reduced to an app based on computer vision, allowing applications such as private and sensitive transmissions needed for identification and secure payment or facility access control [34], as an alternative to RF identification (RFID) cards and quick-response (QR) codes. Furthermore, indoor wireless access to high-speed Internet is already commercially available using VLC technologies, otherwise known as Light Fidelity (LiFi), serving as an alternative to RF-based systems. However, since the achievable data rate of camera-based receivers depends on the image sensor frame rates, which are usually about 30 or 60 fps, such high-speed systems remain based on PD receivers. The OCC applications in the short-range can achieve low data rates, which does

not necessarily mean they are less attractive. For example, indoor location services have gained interest recently, where LED lamps in buildings can provide positioning information to mobile entities or wearables [31], [35], [36].

## 2.1 Outdoor applications

Some VLC and OCC-based solutions for Smart Cities have been proposed and developed over the last years, despite the challenging conditions of the wireless channel in outdoor scenarios. For example, the incorporation of dash cameras in vehicles, which is becoming mandatory in some countries for safety reasons, along with the rich road surveillance infrastructure, sets a potential for the implementation of OCC-based vehicular communications [28], [37], [38]. In other rural and industrial fields, the extensive use of sensors and actuators and the need for machine-to-machine communications has led to the development of WSNs for covering long ranges without the availability of wired infrastructures and for providing connectivity to mobile devices. Other mature technologies in the OWC field used in backbone networks and satellite communications are the free-space optics (FSO) [39], which use high-precision mechanics to direct laser beams carrying information among ground stations, aircraft, and spacecraft [40].

As proposed in this thesis, a potential application of OCC is to provide connectivity in outdoor sensor networks, such as in precision farming, where agricultural sensors and actuators in an energy-restricted node need low data rate communication to supervisory control and data acquisition. The technologies used nowadays for these networks are based on RF and can require licenses for operation and complex hardware implementation. As a complementary alternative, VLC transmitters based on single LEDs and minimal hardware, as shown in Fig. 2.1 can be used to transmit data to a camera monitoring the field.

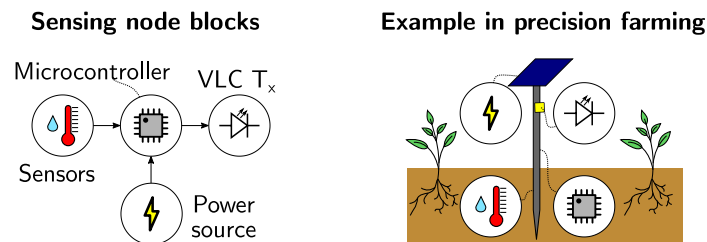


**Figure 2.1:** Example of a use case of visible light communication (VLC) front-end transmitter for applying VLC to wireless sensor networks in precision farming.

## 2.2 Challenges

As previously mentioned, the short-range implementations of OCC have achieved the highest data rates reported in the literature thanks to the clear and stable channel in closed environments and the higher optical power impinging the receiver

photo-sensitive devices. However, outdoor applications remain in lower development due to dynamic meteorologic phenomena that change the atmospheric conditions and cause perturbations of the received signal and the loss of energy in more extensive ranges. Nevertheless, the inherent capacity of cameras to spatially divide light sources open the possibility to implement multiple-transmitter topologies, achieving higher overall data rates.

### 2.2.1 Outdoor wireless channel challenges

When deploying OWC systems outdoors, the main challenges arise from meteorological phenomena in long ranges and the mobile node discovery and tracking issues. In addition, particularly in RS OCC, since the data rate depends on the number of pixels containing information, either the size of transmitters or the focal length of the optical lens in the receivers need to be large, blocking significant areas of the image sensor and reducing the field of view (FOV) of the camera, which limits the simultaneous video monitoring and communication capabilities. These issues are depicted in Fig. 2.2.

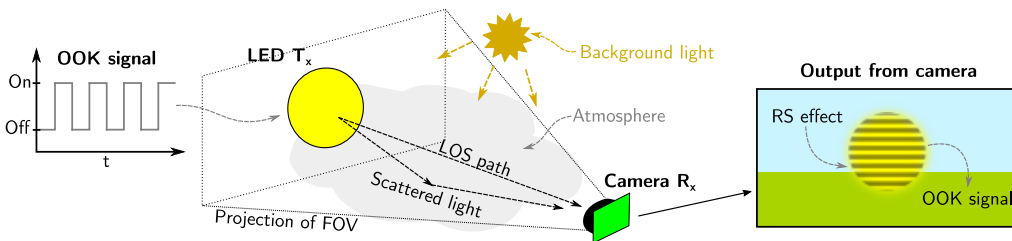


**Figure 2.2:** Rolling shutter (RS) OCC in outdoor applications.

Meteorological phenomena, such as rain, fog, pollution, turbulence, snow, have a negative impact on optical signals because they cause attenuation, scattering, or refraction, perturbations that ultimately can reduce the received power in all OWC systems. Those phenomena are uncontrollable and dynamic over time, and, consequently, no fixed strategy will mitigate the whole spectrum of possible atmospheric conditions. They must be responsive and automated so that the system adapts to the situation and optimizes its performance with the best effort.

### 2.2.2 Multiple-transmitter topologies challenges

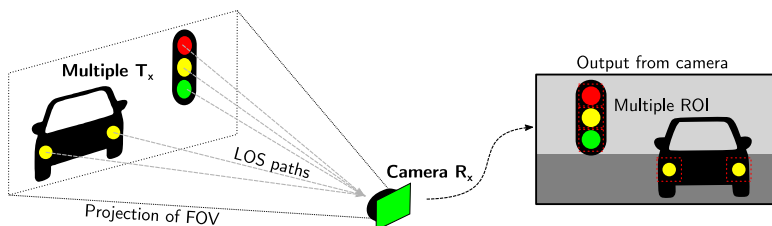


**Figure 2.3:** Example of a use case of optical camera communication using vehicle's dash camera equipment and multiple LED-based transmitters spatially divided

In indoor scenarios, screen-to-camera communications using LED or organic LED (OLED)-based displays and other multi-transmitter schemes have been developed, including simultaneous display and communication using codification embedded invisibly in the images, otherwise known as steganography [41]–[43].

The issues of node discovery and tracking, *i.e.*, finding the projection of transmitters over the image sensor in the frames acquired by the camera in OCC, become more relevant in multiple-transmitter topologies with separated and mobile nodes, as in WSN and vehicular applications, that exploit the image forming optics and inherent spatial division of the camera, as shown in Fig. 2.3. These schemes require algorithms based on pattern recognition through correlation or other statistical or machine learning strategies that efficiently find each transmitter's ROI in the image. The computational load of such algorithms could negatively impact the latency of the links, which is critical in vehicular environments.



This chapter compiles the basic technical knowledge needed for the development of the OCC systems used in this thesis and the most relevant aspects of the LED and CMOS technologies. The principles described include the optical wireless channel modeling, the capture process of camera equipment, and the modulation schemes that exploit the acquisition mechanisms of commercially available cameras.

### 3.1 Fundamentals

In the following sections, the principles of communication theory applied to the scenario of outdoor OCC are derived, considering a half-duplex scheme employing a light source as the transmitter and a camera as the receiver. The key aspects of OCC

#### 3.1.1 Channel modelling

In outdoor OWC systems, the rays of light generated by the emitter surface in the transmitter nodes travel through the atmosphere, which contains particles of different types of gases and aerosols. In addition, the air and ground surface temperatures change due to sunlight and other heat sources. These perturbations cause scattering, absorption, and turbulence, which have drawbacks in OWC systems. However, it has been demonstrated that pointing errors are reduced by multiple scattering since bright objects appear more extensive than in clear atmospheres [44], which in OCC translates into a bigger ROI, and thus a larger amount of pixels from which data can be decoded.

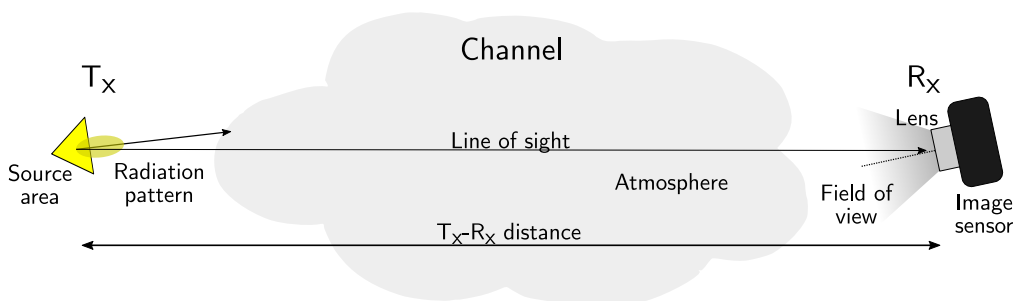


**Figure 3.1:** Diagram of visible light signal transmission in outdoor optical wireless channel.

Considering the phenomena mentioned above, an LED-based transmitter in the field of view (FOV) of a camera-based receiver sends a luminous signal through

the atmosphere, as depicted in Fig. 3.1, and the signal received by the camera in the OCC system ( $P_{Rx}(t)$ ) can be represented as:

$$P_{Rx}(t) = P_{Tx}(t) \cdot R(\theta_{out}, \phi_{out}) \cdot e^{-K_{ext}(\lambda) \cdot d} \cdot \frac{A_{lens} \cos \theta_{in}}{d^2}, \quad (3.1)$$

where  $P_{Tx}(t)$  is the power of the transmitter,  $R(\theta, \phi)$  is its radiation pattern, a spatial profile of the intensity distribution, which depends on the optical end of the LED light. It considers the emission angles  $\theta_{out}$ , and  $\phi_{out}$ . The extinction coefficient  $K_{ext}(\lambda)$  models the loss at every wavelength  $\lambda$ . The distance  $d$  is the link span,  $A_{lens}$  is the camera's main lens' area,  $\theta_{in}$  is the angle of incidence of the light at the camera.

In most embedded digital cameras, the lens is actually an array of tens of lenses with an equivalent focal distance ( $D$ ), focal length ( $f$ ), and a field of view (FOV) measured in degrees. The lens array is designed to form an image on the sensor plane, focused at a distance that depends on the relative positions of the lenses in the array, which can be adjusted using electromechanical devices.

One important property of image forming optics is the preservation of the energy density of sources. As their distance to the camera increases, the area they illuminate in the sensor plane is reduced as fast as the energy decays by distance (quadratically). Thus, without considering the effects of the atmosphere, the channel gain  $H(0)$ , as derived in [45], is given by:

$$H(0) = \frac{A_{px}^2 A_{lens}}{f^2 A_{tx}} R(\theta_{out}, \phi_{out}), \quad (3.2)$$

where  $A_{px}$  is the pixel area,  $A_{Tx}$  the transmitter's radiant area. The radiation pattern is evaluated at the angles of the LOS path  $\theta_{in}$  and  $\phi$  in spherical coordinates relative to the LED. Whenever transmitter's projection falls within the image sensor and is bigger than a single pixel, the intensity read by the pixels has no direct dependence on  $d$

### 3.1.2 On-off keying

Since one of the objectives of this thesis is to study the channel and the impact of the camera parameters, a rather basic structure of the modulator and demodulator blocks have been employed, and more advanced techniques have been considered out of the scope of this particular development.

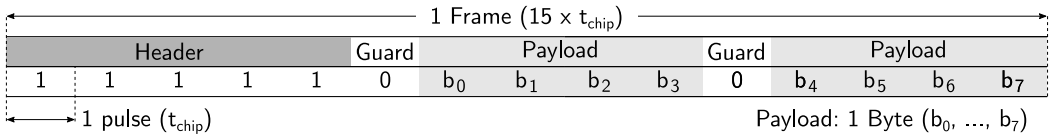


**Figure 3.2:** Frame structure in an on-off keying setting that allows the OCC receiver to detect the phase of the packet.

The on-off keying scheme consists of pulses of on and off-states of the lamp of a fixed time of chip  $t_{chip}$  that are consecutively sent by the transmitter. In order

for the receiver to be able to synchronize with the data, a packet structure may be defined, as shown in Fig. 3.2, in which different guard chips and header or trailer allow the phase of the transmission to be recognized. In OCC systems, the value of  $t_{chip}$  is defined depending on the shutter acquisition mode, and for GS, it can be around hundreds of ms, assuming the camera frame rate is about 30 fps, allowing one pulse every three frames. On the other hand, in RS can be reduced down to tens of  $\mu s$ , in the order of the row-shift time of the image sensor, allowing one pulse every few rows of the image.

## 3.2 Technologies

This section focuses on the technical aspects of the LED and digital camera technologies that allow the implementation of OCC transmitters and receivers. First, the LED capabilities are described, and the main VLC  $T_x$  blocks are described. Finally, the most prominent digital camera technologies described and the image sensor blocks involved in photographic capture that OCC can exploit are characterized.

### 3.2.1 Light-emitting diode-based transmitter

The LED technology has enabled the deployment of efficient lamps in all kinds of facilities and devices, displacing from the mass markets older technologies such as halogen in car lamps, fluorescent tubes in homes and offices, and high-intensity discharge lamps in streets and industrial infrastructures, among others. The LED-based lamps are preferred due to their long lifespan, robustness, inexpensiveness, efficiency, small size, and rapid response to switching. The latter feature is of interest for communications, as it will be explained below.

Depending on the composition of the diode and by using phosphor-based coatings or colored filters, LEDs can radiate different spectrums of visible, ultraviolet, or infrared light. By mixing them, a variety of colors can be obtained from LED sources, especially red, green, and blue, allowing the development of image displays that can be found in large and small screens. Some of the available LED substrate compositions are indium-gallium nitride (InGaN), and long-chain organic polymers or small organic molecules grouped as organic LEDs (OLED) used in display technology and OLED-based VLC [43].

The VLC systems exploit the fast switching capability of LEDs to transmit light pulses at rates of up to several hundreds of MHz, along with the color varieties of the substrates available to create simultaneous streams of data of different frequencies originating at the same LED-based lamp or display. In addition, camera-based receivers with color channels allow both the spatial and frequency division of the sources.

In most cases, LEDs need a power supply unit comprised of a fixed current source, known as the LED driver, whereas in others, the diode can be fed by a voltage source. In turn, VLC transmitters need a signal combining circuit (SCC) to feed the LED with a constant current and a varying current according to the modulation employed. The SCC can be a passive bias-tee or an active circuit based on transistors. As shown in Fig. 3.3, the SCC receives the signal created by a

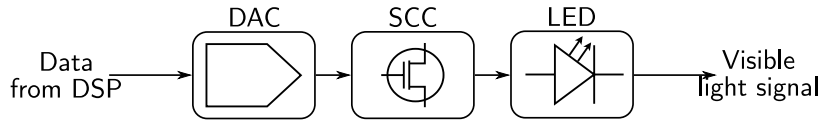


**Figure 3.3:** Visible light communication transmitter model. Input data coming from the digital signal processing (DSP) unit is digitalized by the digital-to-analog converter (DAC) and fed to the LED through a signal combining circuit (SCC) which adds a bias direct current to the alternating current signal.

digital-to-analog converter (DAC) and powers the LED accordingly, generating the visible light signal.

### 3.2.2 Digital camera-based receiver

Digital cameras are based on the use of electronic image sensors and an array of image-forming lenses that can create two-dimensional representations of the scenes in their field of view. As mentioned in previous chapters, they have become widely available in consumer electronics and urban infrastructures and are a potential alternative for the implementation of optical wireless communications. This section will focus on the basic aspects of CMOS camera equipment employed in the experimental setups described in the following chapters.

#### Acquisition mechanisms

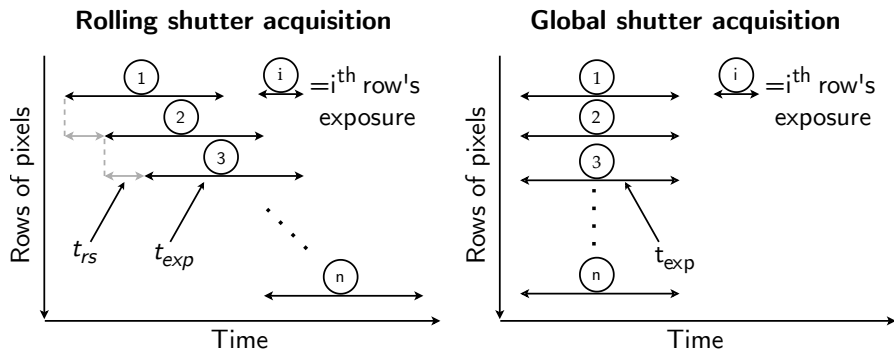


**Figure 3.4:** Row-by-row and simultaneous frame exposure in rolling shutter (RS) and global shutter (GS) acquisition mechanisms.

In addition to the technology of the pixel circuitry, CCD and CMOS image sensors may implement different mechanisms for acquisition that maximize the photographic quality or minimize the cost and complexity of the blocks in charge of the digitalization of the signals. The two main strategies, known as the rolling shutter (RS) and global shutter (GS) [46], as depicted in Fig. 3.4, consist of a row-by-row exposure and a simultaneous whole frame exposure, respectively. The RS technique allows the re-utilization of amplification and analog-to-digital conversion blocks per column of pixels, making the image sensor less expensive. Nevertheless, the photographic distortion this procedure generates can be significant in some

applications, such as in the video capture of fast-moving objects that demand simultaneous exposure, as employed in GS image sensors.

For OCC purposes, the RS cameras generate image frames with rows captured in different time windows, which translates into a matrix with several different states of the lamp during its switching. In turn, since GS exposes the entire frame simultaneously, the frames only contain one state of the lamp and can only decode one symbol from each photogram [22].

#### Pixel hardware

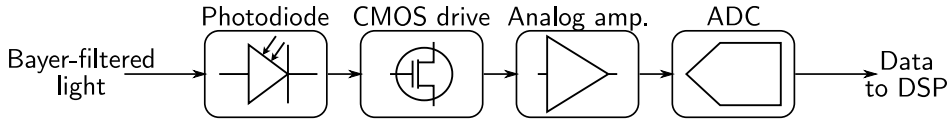


**Figure 3.5:** Typical configuration of Complementary Metal-Oxide-Semiconductor (CMOS) camera sub-pixels.

The usual implementation of a CMOS camera circuit is, as described in [47] contains a PD that receives light and is constantly generating a current  $i_{pd}$ . A CMOS drive turns  $i_{pd}$  into a voltage signal  $V_{px}$ . An analog amplifier with gain  $G$  is set by software and outputs a signal  $V' = G \cdot V$  that is sampled by the analog-to-digital converter (ADC). Here, the ADC induces a noise ( $\sigma_{adc}^2$ ). Other noise sources are the thermal noise ( $\sigma_{th}^2$ ), the shot noise ( $\sigma_{sh}^2$ ). The SNR can be approximated by [48]:

$$SNR_{px} \approx \frac{G^2 \cdot i_{pd}^2}{G(\sigma_{th}^2 + \sigma_{sh}^2) + \sigma_{adc}^2}, \quad (3.3)$$

when the pixel is illuminated by the optical communication signal without external interfering sources.

As it will be shown in Chapter 5, the relative value of  $\sigma_{adc}^2$  can be reduced, improving the value of SNR by  $\Delta SNR \approx 1 + \sigma_{adc}^2 / \sigma_{th}^2$  unless the ADC is saturated. This can be exploited for improving the SNR in harsh atmospheric conditions.



Since the main objectives of this thesis are to demonstrate the feasibility of establishing OCC links in harsh atmospheric conditions, control the photographic parameters of the camera for signal quality optimization, and ultimately build an OCC testbed that allows simultaneous video monitoring and communication, this chapter focuses on the materials and methods developed in this thesis. First, the transmitter and receiver hardware implemented is described, and the channel conditions considered to demonstrate the feasibility of OCC in harsh atmospheric conditions are specified. Finally, the processing techniques used on the receiver side are detailed. Note that the precise methodology of each of the experiments carried out is included in each publication covered in Chapter 5.

## 4.1 Experimental setups

The transmitter and receiver nodes developed in this project consist of LED lights and CMOS cameras, respectively, with different optical front-ends using commercially available components. The nodes were implemented using the optical components and cases made using three-dimensional printing manufacturing techniques. The scenarios in which these nodes were tested ranged from fog and turbulence conditions emulated in a laboratory chamber to different real atmospheric conditions, including clear weather and a heavy sandstorm event. The transmitters, receivers, and channel conditions, the main parts of the OCC system implemented, are described in the following sections.

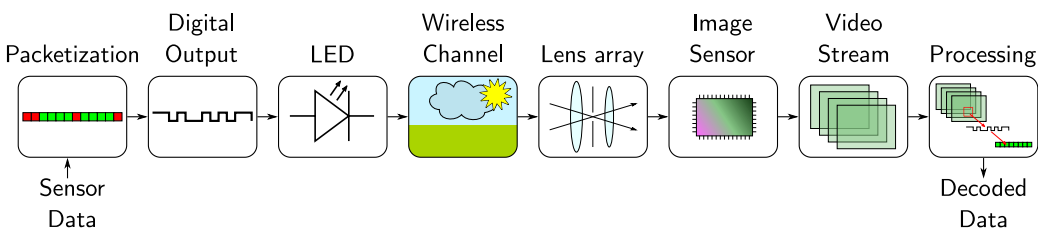


**Figure 4.1:** General block diagram of the OCC systems implemented.

### 4.1.1 Transmitter equipment

The transmitter nodes were implemented using white and red-green-blue (RGB) LEDs, along with an embedded microcontroller development board (Arduino Nano) featuring an Atmel ATmega328p chip [49]. The Arduino translates the modulation technique software into a digital signal, as shown in Fig. 4.2. The modulated signal varies according to the input data using the on-off keying (OOK) modulation technique, which switches the LEDs between on and off states using

a transistor-based driver, which serves as the signal combining circuit **fary\_VLC**. The visible-light signal produced by the LEDs is transmitted through the channel using the optical lens embedded in the LEDs resin encapsulation, and, in some cases, white methacrylate screens were included as diffusers.

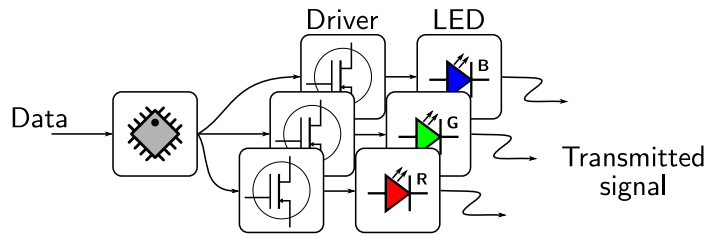


**Figure 4.2:** Transmitter hardware diagram

As detailed in Table 4.1, two kinds of transmitters were implemented, with larger and smaller emitter surfaces, and using white resin-encapsulated and red-green-blue (RGB) surface-mount device (SMD) LEDs, respectively. The different configurations allow the evaluation of the impact of the emitter size and the color-channel division in OCC. In Figure 4.3, the  $T_x$  nodes are shown during operation.

**Table 4.1:** Key parameters of the transmitter nodes.

Feature	Description
Large transmitter ( $LT_x$ ) dimensions	4.2 cm × 45 cm
$LT_x$ average source radiance	10 W/m <sup>2</sup>
$LT_x$ LED components	RGB LED strips (108 × 5050 SMD chips)
$LT_x$ dominant wavelengths [nm]	630 (R), 530 (G), 475 (B)
Small transmitter ( $ST_x$ ) dimensions	5 mm (radius)
$ST_x$ LED component	Vishay white non-diffused LED <b>vishay</b>

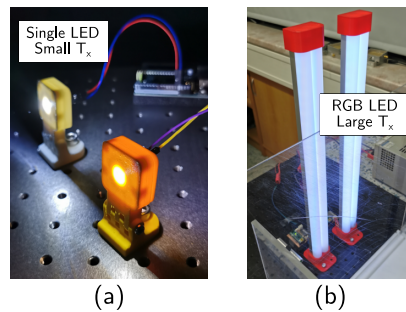


**Figure 4.3:** Transmitter ( $T_x$ ) equipment developed. **(a)** shows the single white LED small  $T_x$ . **(b)** shows the multi-color (red-green-blue) LED large  $T_x$ .

#### 4.1.2 Receiver equipment

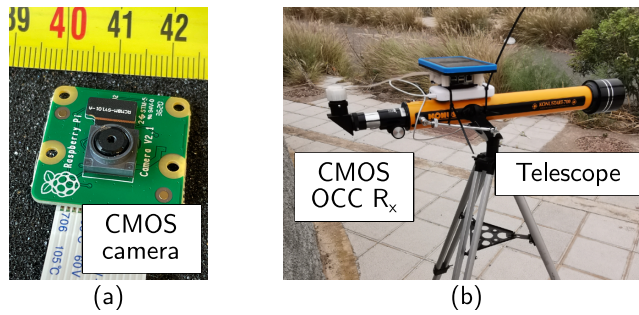
The receiver equipment used in this work consisted of a development camera component (Raspberry Pi Camera Module v2) featuring an 8-megapixel CMOS



image sensor (Sony IMX219 [50]), a lens array, and the interfacing circuitry for readout using Raspberry Pi computers. This camera allows recording video and images at different standard resolutions, such as full high definition (Full HD) 1920-by-1080 px at 30 frames-per-second (fps). In addition, an ocular adapter was built to attach the camera to the larger optics of a telescope, increasing the camera's focal length and allowing the OCC system to cover larger link spans. The key parameters of the  $R_x$  nodes are detailed in Table 4.2.

**Table 4.2:** Camera-based receiver parameters.

Feature	Description
Image sensor (IS)	Sony IMX219 [50]
IS resolution employed	1920 px $\times$ 1080 px (FullHD)
IS frame rate at FullHD	30 fps
IS analog gain range	0 to 20.6 dB
Rolling shutter delay ( $t_{rs}$ )	18.904 $\mu$ s
Built-in lens equivalent focal length ( $f$ )	3.04 mm
Built-in lens focal aperture ( $D$ )	$f/2.0$
Telescope focal length ( $f'$ )	700 mm
Telescope focal aperture ( $D'$ )	$f'/11.6$



**Figure 4.4:** Receiver ( $R_x$ ) equipment developed. (a) shows the camera board with built-in lens array for small  $R_x$ . (b) shows the implementation of large  $R_x$  using telescope.

### 4.1.3 Channel conditions considered

The wireless channel was studied using three different settings. First, the weather conditions were emulated in a laboratory chamber with a glycerine machine and heated-air blowers that allow generating the conditions of fog and turbulence, respectively. The key features of the chamber are detailed in Table 4.3. Second, to measure the levels of fog and turbulence, the experiment was equipped with a laser-optical power meter link and an array of temperature sensors that allow estimating the meteorologic visibility and the refractive index structure parameter, respectively.

The experiments in laboratory conditions were later extended to natural harsh atmospheric conditions, taking advantage of a sandstorm event that occurred in the Canary Islands archipelago, which registered historical levels of low visibility

**Table 4.3:** Key parameters of the laboratory chamber employed for the emulation of fog and turbulence.

Feature	Description
Chamber dimensions [m]	length 4.910, width 0.378, height 0.368
Link span	4.68 m
Temperature sensors	20 × Papouch Corp. TQS3-E (range: $-55$ to $+125^{\circ}\text{C} \times 0.1^{\circ}\text{C}$ )
LASER source	Thorlabs HLS635 (635 nm) F810APC
Optical power meter	Thorlabs PM100D S120C
Heat blowers	2 × Sencor SFH7010, 2000 W
Fog machine	Antari F-80Z, 700 W

due to the presence of dust suspended in the air, as reported by the United States National Aeronautics and Space Administration (NASA) Earth Observatory [51]. The factors at the time of the experiment, as measured by the Barcelona Dust Forecast Center from the Spanish State Meteorological Agency (AEMET) [52], are detailed in the Table 4.4.

**Table 4.4:** Key parameters considered for the emulated wireless outdoor channel in harsh atmospheric conditions during the sandstorm event of February 23<sup>rd</sup> in the Canary Islands, Spain.

Factor	Description
Link spans	100 m, 200 m
Aerosol Optical Depth (AOD <sub>550</sub> )	3.2 to 6.4 ( $\lambda = 550$ nm)
Dust surface concentration [ $\mu\text{g}/\text{m}^3$ ]	500 to 2000
Dust dry deposition [ $\text{mg}/\text{m}^2$ ]	100 to 400

Finally, the OCC systems were deployed outdoors using small optical front-ends in the transmitter and receiver sides and link spans of 90 m and 130 m in clear weather conditions, which fall into the category of sub-pixel OCC, in which the projection of the source over the image sensor is smaller than the area of a pixel if the focus and scattering are neglected, allowing the re-utilization of the video monitoring for communication.

## 4.2 Processing

This section gives an overview of the experimental setup's digital signal processing techniques implemented on the receiver and transmitter sides. Although each practical work in this thesis comprised different specific stages, a general scheme is explained as follows, taking into account the diagram shown in Fig. 4.5.

As it was presented in [53], the rolling shutter acquisition mechanism in combination with low exposure times creates a series of horizontal bands in the area of the projection of VLC transmitters over the image sensor. In contrast, in a global shutter scheme, the different states of the transmitter are captured in image frames of the video stream generated by the camera.

Regardless of the demodulation scheme, OCC systems require the detection of

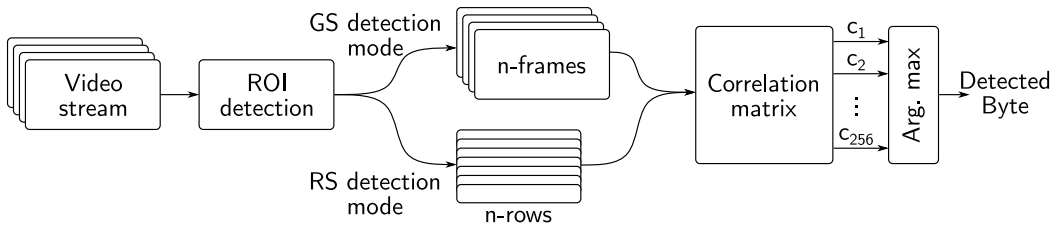


**Figure 4.5:** Flow diagram of the main processing stages involved in OCC receivers' detection.

pixels containing projections of the light rays coming from the transmitter to the image sensor area. These pixels, known as the region of interest (ROI), constantly vary over time unless the scenario is static. For this thesis, a pre-selection of the ROI was done arbitrarily for a lower computational load. Later, pre-cut ROI frames were processed into the final ROI using two different techniques, the Pearson's correlation coefficient and the two-Gaussian mixture model (GMM), as reported in [54] and [48], respectively. Correlation-based techniques have the advantage that correlators are easy to implement and can be used for other computer vision purposes. The graph in Fig. 4.6 shows a GMM model applied to the probability density function (PDF) of the pixel intensities, as estimated by a histogram plot. The GMM procedure, as derived in [48], outputs the maximum likelihood threshold, which segregates background from on states of the transmitter.

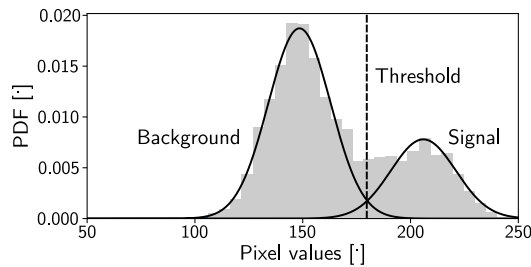


**Figure 4.6:** Two Gaussian scheme for data and background segregation in images.

Once the ROI has been detected, it can be assumed that the pixels contain the intensity of the received signal. Depending on the shutter mode employed, the packets are detected either from series of rows of the ROI or from series of ROIs cut from consecutive packets. Since the packet structure is known beforehand, the receiver can employ a bank correlation in parallel to obtain the highest match, which corresponds to the decoded data. If the packet structure presented in Chapter 3 is considered, each iteration of this process returns 1 Byte payload.



In this chapter, the compendium of publications is presented. Each article is commented as follows. First, the topic developed is introduced. Then the importance of the challenge addressed in the article is discussed, highlighting the research gap intended to be solved and summarizing the results obtained. Finally, a global summary of the contributions of each publication is given.

### 5.1 Publication 1 (P1)

The work presented in the article entitled “*Experimentally Derived Feasibility of Optical Camera Communications under Turbulence and Fog Conditions*” [54] focuses on the influence of heat-induced turbulence and attenuation by aerosols in fog. Two primary atmospheric conditions that affect OWC which were evaluated using the small receiver and large transmitter developed in this thesis. The phenomenon of turbulence induced by heat, which is present in roads and other industrial environments, where surfaces exposed to sunlight or high temperatures induce random variations of the air’s refractive index, affecting light beams propagation paths. The attenuation in turn, caused by fog and other aerosols in the atmosphere occurs especially in cold weathers and in areas with pollution in the air. Since meteorologic phenomena are dynamic, the atmospheric conditions change unpredictably, degrading the wireless communication channel, posing a significant challenge for outdoor optical networks that need to be prepared for overcoming these perturbations.

A 5 m-long laboratory chamber was used in this work, where the fog and heat-induced turbulence levels can be emulated. Although the control of these variables is imprecise due to the manual actuation of the heaters and the glycerin machine used to generate the virtual atmospheric conditions, the impact of each device can be measured using the following sensors: a laser link that measures the attenuation and consequent loss of meteorological visibility caused by the aerosols in the chamber, and a thermometer array, that measures the Rytov variance and the refractive index.

One of the main contributions of this work is that the exploitation of the amplification block of CMOS image sensors was reported for the first time, up to the authors’ knowledge. It was seen that by varying the analog gain, the highly attenuated signal quality was improved, whereas, in clear conditions, the gain causes saturation of the ADC. The SNR was estimated to measure the signal quality by computing the Pearson’s correlation coefficient between ROIs detected in clear conditions and heavy fog. The influence of fog was shown to be mitigated by feeding the ADC with an amplified signal, which is less affected by quantification noise compared to signals with similar amplitudes to the ADC discrete levels.



Article

# Experimentally Derived Feasibility of Optical Camera Communications under Turbulence and Fog Conditions

Vicente Matus <sup>1,\*</sup> , Elizabeth Eso <sup>2</sup> , Shivani Rajendra Teli <sup>3</sup> , Rafael Perez-Jimenez <sup>1</sup> and Stanislav Zvanovec <sup>3</sup>

<sup>1</sup> Institute for Technological Development and Innovation in Communications, Universidad de Las Palmas de Gran Canaria, 35001 Las Palmas, Spain; rafael.perez@ulpgc.es

<sup>2</sup> Optical Communications Research Group, Northumbria University, Newcastle-upon-Tyne NE1 7RU, UK; elizabeth.eso@northumbria.ac.uk

<sup>3</sup> Department of Electromagnetic Field, Faculty of Electrical Engineering, Czech Technical University in Prague, Technicka, 16627 Prague, Czech Republic; telishiv@fel.cvut.cz (S.R.T.); xzvanove@fel.cvut.cz (S.Z.)

\* Correspondence: vicente.matus@ulpgc.es

Received: 30 November 2019; Accepted: 28 January 2020; Published: 30 January 2020

**Abstract:** Optical camera communications (OCC) research field has grown recently, aided by ubiquitous digital cameras; however, atmospheric conditions can restrict their feasibility in outdoor scenarios. In this work, we studied an experimental OCC system under environmental phenomena emulated in a laboratory chamber. We found that the heat-induced turbulence does not affect our system significantly, while the attenuation caused by fog does decrease the signal quality. For this reason, a novel strategy is proposed, using the camera's built-in amplifier to overcome the optical power loss and to decrease the quantization noise induced by the analog-digital converter of the camera. The signal quality has been evaluated using the Pearson's correlation coefficient with respect to a reference template signal, along with the signal-to-noise ratio that has been empirically evaluated. The amplification mechanism introduced allows our system to receive the OCC signal under heavy fog by gradually increasing the camera gain up to 16 dB, for meteorological visibility values down to 10 m, with a correlation coefficient of 0.9 with respect to clear conditions.

**Keywords:** optical camera communications (OCC); CMOS image sensor; rolling shutter; fog attenuation; heat-induced turbulence; meteorological visibility; refractive index structure parameter

## 1. Introduction

Digital cameras are ubiquitous consumer electronics and are being explored to deliver extra capabilities beyond traditional photography and video. A new optical communication technique using cameras as receivers has been studied in the IEEE 802.15 SG7a within the framework of optical wireless communications and considered as a candidate of IEEE 802.15.7r1, which is called Optical Camera Communication (OCC). OCC has been investigated as one of the Visible Light Communication (VLC) schemes [1]. OCC implemented within internet of things (IoT) environments provides multiple functionalities of vision, data communications, localization and motion detection (MD) [2,3] used in various IoT-based network applications including device-to-device communications [4], mobile atto-cells [5], vehicular communications [6–8], and smart cities, offices, and homes (SCOH) [9].

The majority of new generation smart devices have built-in Complementary Metal-Oxide-Semiconductor (CMOS) image sensors, providing the ability to capture photos and videos [10,11]. The strategy behind using a CMOS camera for OCC is that the image sensor performs an acquisition mechanism known as Rolling Shutter (RS), in which it sequentially integrates light on rows of pixels [12]

starting the scanning of each line with a delay with respect to the previous one. In other words, the timings of the line-wise scanning make the imaging sensor to capture different windows of time of the optical signal coming from a Light Emitting Diode (LED) transmitter ( $T_x$ ). Then, each line of the image can hold a distinct portion of information.

The use of LEDs available in SCOH's lighting infrastructures, along with optical receivers, for making VLC systems is particularly challenging in outdoor environments. The potential applications of OCC in these scenarios are related to the creation and improvement of communication networks for the vehicular and pedestrian infrastructures [13], where a large number of LED lights and CMOS cameras can be found. The desirable distance coverage of the different services that can take advantage of OCC ranges from a few meters for hand-held receiver devices based on smartphones, and tens of meters for vehicular networks that support Intelligent Transportation Systems (ITS). The achievable link distance in OCC depends partly on the signal-to-noise ratio (SNR) at the receiver, which in turn depends on the transmitted power, the attenuation caused by the channel, the optical lens array of the camera and various sources of noise and interference. In the case of RS-based systems, the maximum link distance is also restricted by the number of lines of pixels covered by the transmitter. For this, the geometry of the transmitting surface, as well as the image forming lens array configuration, determine the image area in pixels [14]. The modulation and packet scheme may have an impact on the maximum link distance if the image frames must contain a number of visible symbols for demodulation. Depending on the case of application, the LED and camera-based transceivers can either have static or mobile positions and orientations, making mobility support essential, which relies on the effective detection of the pixels that have an SNR level suitable for demodulation.

The vehicular VLC (VVLC) are a significant application case with challenging conditions of relative position and motion between nodes. An analysis based on a comparison of VVLC with radio frequency (RF) vehicle-to-vehicle (V2V) links in terms of channel time variation was proposed in [15]. It was shown that the VVLC links have much slower channel time variation as compared to RF V2V links. On the other hand, the VVLC investigation in [16] obtained link duration for VVLC between neighboring vehicles are more than 5 s while in certain other cases the average link duration can be up to 15 s. The safety regulations in [17,18] provide the speed limits and inter-vehicle distance in different weather conditions for the estimation of the desired distance of coverage. Table 1 shows the speed limit based on the European Commission regarding mobility and transport standards, which may vary slightly from one European country to the other. The inter-vehicle distances outlined have been calculated based on the 2 s driving rule for good to bad weather conditions, according to the Government of Ireland, which recommends that a driver maintains a minimum of two seconds apart from the leading vehicle for good weather conditions, which is doubled to four seconds in bad weather.

**Table 1.** Inter-vehicle distances based on the weather condition based on regulations in [17,18].

Weather condition	Speed Limits [km/h]		Inter-Vehicle Distance [m]	
	Motor ways	Rural roads	Motor ways	Rural roads
Good weather	120–130	80–90	67–72	44–50
Bad weather ( $V_M = 50$ m)	50	50	56	56

The performance of intensity-modulation and direct-detection method employed by LED-to-Photodiode (PD) VLC [9,19], is highly restricted by external light sources such as sunlight, public lighting, and signaling. Moreover, weather conditions, such as the presence of fog, or high temperatures, cause substantial optical distortions [20]. Addressing these challenges, authors in [21] derived a path-loss model for PD-to-LED VLC using Mie's theory and simulating rain and fog conditions in a vehicular VLC setting. They determined the maximum achievable distances as a function of the desired bit-error-ratio (BER) using pulse amplitude modulation (PAM). They found that, for a 32-PAM system, the maximum distance achievable for the desired BER of  $10^{-6}$  is reduced from 72.21 m in clear weather, to 69.13 m in rainy conditions, and 52.85 m and 25.93 m in foggy conditions of different densities. The same Mie's theory is also used in [22] to evaluate a PD-based

VLC link under maritime fog conditions. Scattering and phase functions are derived, as well as the spectrum of the attenuation of optical signals for different distances. In [23], the authors experimented with a LED-to-PD VLC link of 1 m distance based on a single 1 W red LED and multiple PDs attached to a Fresnel lens under dense fog conditions in a laboratory chamber. The lens allows them to maintain a 25 dB signal-to-noise ratio (SNR) varying the optical gain it provides to compensate the attenuation due to the fog presence.

Atmospheric turbulence, and oceanic turbulence in the case of Underwater Wireless Optical Communication (UWOC), has been extensively studied. Guo et al. introduced the traditional lognormal model into a simulated VLC link for ITS [24]. The authors proved that VLC wavelengths in ITS performed worse than longer ones (e.g., 1550 nm), which is straightforward, taking into account that the turbulence measured by Rytov's variance has a dependence on the wavelength. In the case of UWOC, in which the use of visible-range wavelengths is mandatory due to the water absorption spectrum, Kolmogorov's turbulence spectrum is substituted by Nikishov's [25]. This turbulence spectrum fits better with the experimental measurements since it takes into account not only temperature but salinity variations.

Although the impact of turbulence has been characterized for classical optical detectors, its effect on OCC systems has not been adequately addressed yet. Works addressing channel characterization in outdoor OCC links [20] are still scarce compared to the amount of research on PD-based VLC. In the previous work [26], we evaluated the feasibility of a global shutter-based OCC link under fog conditions by the success rate of bits of vehicular link experimentally tested with a red brake light and a digital reflex camera. For a modulation index of 75%, the system showed high reliability under dense fog conditions up to a meteorological visibility of 20 m.

The contribution of this paper is to experimentally derive the feasibility of OCC in emulated outdoor conditions of fog and heat-induced turbulence using commercially available LEDs and cameras. This work is the first to report an experimental investigation on the effects of such conditions on an RS-based system. The experiments carried out for this work were done using a laboratory chamber, and the conditions emulated were of heat-induced turbulence and the presence of fog in the air. The refractive index structure parameter ( $C_n^2$ ) [27] is used to estimate the level of turbulence and the meteorological visibility ( $V_M$ ) as a measure of the level of fog. The fog experiments are especially relevant because we utilize the camera's built-in amplifier to overcome the fog attenuation and mitigate the relative contribution of the quantization noise induced by the analog-to-digital conversion stage, ensuring an improvement of the signal quality without increasing the exposure time, and, thus, keeping a high bandwidth.

This paper is structured as follows. Section 2 describes the used methodology, including the channel modeling, the model for the meteorological phenomena studied, and it presents the experimental design. Section 3 presents the experimental setup, describing the laboratory chamber and the OCC system employed. Section 4 shows the obtained results for heat-induced turbulence and fog experiments and performs an in-depth discussion. Finally, conclusions are drawn in Section 5.

## 2. Methodology

In this section, we describe the relevant processes involved in the CMOS camera mechanism of acquisition in RS-based OCC employed by our system and derive the analytical tools used for the evaluation of its performance in the experimental setting.

### 2.1. Channel Modelling

In CMOS image sensors, the red-green-blue (RGB) light from a Bayer filter impinges the subpixels. These entities are integrated by PDs and their driving circuit and are grouped by rows connected in parallel to amplifiers and analog/digital converter (ADC) units that are shared by columns. The output of these hardware blocks are image matrices that are sent to the camera digital signal processor (DSP), where data is compressed and delivered to the user as a media file. The sensor performs



RS acquisition, in which the start and end of the exposure of each row of pixels are determined by the circuit's fixed row-shift time ( $t_{rs}$ ) and the software-defined exposure time ( $t_{exp}$ ) [28]. The time parameters and circuitry mentioned are shown in Figure 1. Since  $t_{rs}$  is fixed, in order to increase the data rate,  $t_{exp}$  must be set as low as possible to make the sensor capture the highest diversity of states of the transmitter within each frame. The received power  $P_{Rx}(t)$  at a camera coming from a Lambertian light source of order  $m$  and transmitted power  $P_{Tx}(t)$  can be expressed as

$$P_{Rx}(t) = P_{Tx}(t) \cdot \frac{m+1}{2\pi} \cdot \cos^m \theta \frac{A_{lens} \cos \Psi}{d^2}, \quad (1)$$

where  $\theta$  and  $\Psi$  are the emission and incident angles, respectively,  $A_{lens}$  is the area of the camera's external lens, and  $d$  is the link span. From the RS mechanism shown in Figure 1, we can express the energy  $E_i$  captured by the  $i^{th}$  row as

$$E_i = \int_{i \cdot t_{rs}}^{i \cdot t_{rs} + t_{exp}} \frac{P_{Rx}(t)}{\sum_v^v \sum_k^h M_{j,k}} dt, \quad (2)$$

where  $h$  (columns),  $v$  (rows) are the dimensions of the image sensor, and  $M_{[v \times h]}$  is the mask of pixels where the source shape is projected. From the integral limits, it can be derived that the bandwidth of the  $R_x$  system decreases with the augment of the exposure time. In other words, the longer is  $t_{exp}$ , the more lines are simultaneously exposed, and the received signal is integrated in longer and less diverse time windows. For this reason, frames in OCC have to be acquired within short periods.

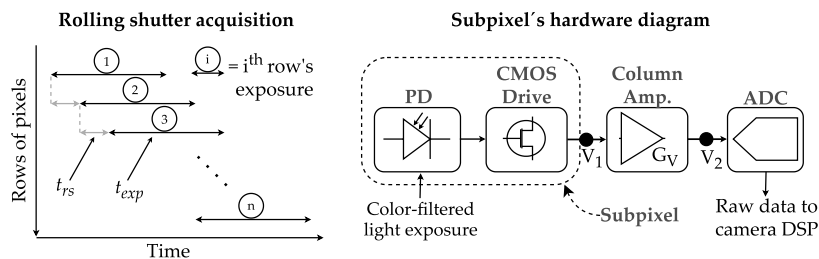


**Figure 1.** Typical configuration of Complementary Metal-Oxide-Semiconductor (CMOS) camera sub-pixels.

Note that low values of  $t_{exp}$ , along with the attenuation factor in outdoor channels caused by the presence of particles such as fog or by the light refraction by turbulence can result in  $E_i$  lower than the sensor's lowest threshold of detection. For overcoming this, we can take advantage of the amplifying stage in the subpixel circuitry shown in Figure 1. The voltage-ratio gain  $G_V$  of the column amplifier block behaves as

$$G_V(dB) = 20 \log_{10}(V_2/V_1), \quad (3)$$

where  $V_1$  is the voltage obtained from the pixel integration of light during exposure, and  $V_2$  is the voltage value that is sampled by the ADC. In the case of the IMX219 sensor and of other CMOS sensors with the architecture shown in Figure 1, a software-defined analog gain configuration can set the value of  $G_V$  for each capture. The typical values of  $G_V$  range from 0 dB to 20.6 dB, as shown in [29].

The column gain  $G_V$  of the CMOS sensor amplifies the received signal  $P_{Rx}$  and all the noises up to the ADC. This includes the shot noise at the PD, and the thermal noises of the circuits, which can be modeled as random variables of Normal distributions with variances  $\sigma_{sh}^2$ , and  $\sigma_{th}^2$ , as:

$$\sigma_{sh}^2 = 2q_e \left( i_{pd}(x, y, c) + i_d + i_{bg} \right) B, \quad (4)$$

$$\sigma_{th}^2 = \frac{4k_B T_n B}{G_V}, \quad (5)$$

where  $k_B$  is the Boltzmann's constant,  $T_n$  is noise temperature,  $B = 1/t_{rs}$  is the bandwidth,  $q_e$  is the electron charge,  $i_d$  is the dark current of the camera's pixels, and  $i_{pd}(x, y, c)$  is the PD current at pixel  $(x, y)$  in the color band  $c \in \{R, G, B\}$ . This current is determined by the emitted spectrum of the light source, the corresponding Bayer filter, and the substrate's responsivity. Finally,  $i_{bg}$  models the contribution of the background illumination level to the shot noise. Nonetheless, since reduced exposure times are generally used, the contribution of  $i_{bg}$  can be neglected.

The signal is then sampled by the ADC, introducing quantization noise ( $\sigma_{adc}^2$ ), that is usually modeled as a zero-mean random normal contribution whose variance depends on the resolution of the converter. This results in the SNR, which is referred at the DSP's input as:

$$SNR \approx \frac{G_V \cdot i_{pd}^2(x, y, c)}{G_V (\sigma_{th}^2 + \sigma_{sh}^2) + \sigma_{adc}^2}. \quad (6)$$

Considering the SNR as a function of  $G_V$ , it can be observed that it has an increasing behaviour with an upper asymptote given by  $i_{pd}^2(x, y, c) / (\sigma_{th}^2 + \sigma_{sh}^2)$ . Especially in the cases when the signal entering the ADC is weak, e.g., as in high attenuation scenarios such as in the presence of dense fog, the relative loss due to quantization noise can be minimized by increasing the column amplification. In other words, the SNR can be optimized by the camera analog gain, unless the ADC is saturated.

Our system employs an On-off keying (OOK) modulation for each of the color bands with a fixed data input that is used as a beacon signal. For bit error ratio (BER) derivation, let us assume the system now works with a random data input of  $p_0 = p_1 = 0.5$  as the probabilities of value 0 and 1, respectively. The Maximum Likelihood Estimator (MLE) threshold  $\mu_{mle}$  at the detection stage of the OOK demodulation is given by

$$\mu_{mle} = (\mu_0 + \mu_1) / 2, \quad (7)$$

where  $\mu_0$  and  $\mu_1$  are the expected values of the received signal for the cases of transmitted signal equal to bits 0 and 1, respectively. If the receiver's DSP applied a digital gain  $k_d$ , the resulting MLE threshold would be  $\widetilde{\mu}_{mle} = k_d(\mu_0 + \mu_1) / 2$ . In this case, if  $\mu_1 < 2^{n_{bit}}$ , where  $n_{bit}$  is the bit depth, and  $2^{n_{bit}}$  is the maximum digital value of the signal coming from the ADC, the BER would tend to the worst case of a coin flip (error probability equal to 0.5).

## 2.2. Meteorological Phenomena

The presence of fog particles and turbulence in the air are known as relevant sources of signal distortion in outdoor optical systems. These conditions can be emulated in a laboratory chamber, and well-known parameters can estimate their degree, as explained in the following derivations.

Beer's law [30] can describe the attenuation of propagating optical signals caused by fog. Generally, in optical systems, visibility  $V_M$  in km is used to characterize fog attenuation ( $A_f$ ). Using the Mie's scattering model [31],  $A_f$  can be related to  $V_M$  as:

$$A_f = \frac{3.91}{V_M} \left( \frac{\lambda}{550} \right)^{-q}, \quad (8)$$

where  $\lambda$  denotes wavelength in nm and parameter  $q$  is the distribution size of scattering particles given by Kim's model [32], which is in the short range of visibility ( $< 0.5$  km) considered equal to zero. Thus,  $V_M$  is given by:

$$V_M = \frac{3.91}{A_f}. \quad (9)$$

The channel coefficient for fog  $h_f$  can be determined by applying Beer's law describing light scattering and absorption in a medium as:

$$h_f = e^{-A_f d}. \tag{10}$$

Consequently, the average received optical power for the LOS link at the  $R_x$  under fog is expressed as:

$$P_{Rxf}(t) = P_{Rx}(t)h_f + n(t), \tag{11}$$

where  $n(t)$  denotes the addition of noises associated with  $\sigma_{th}^2$  and  $\sigma_{sh}^2$ .

The coefficient  $h_f$  depends on the value of the product of fog-attenuation and distance ( $A_f \cdot d$ ), which is known as the optical density of the link. This variable can have the same value for different combinations of fog level and link span, allowing to infer the influence of both variables varying only one of them.

The heat-induced turbulence of air results from variations in temperature and pressure of the atmosphere along the path of transmission. Consequently, this leads to variations of the refractive index of the air, resulting in amplitude and phase fluctuations of the propagating optical beam [33]. For describing the strength of atmospheric turbulence, the parameter most commonly used is the refractive index structure parameter ( $C_n^2$ ) (in units of  $m^{-2/3}$ ) [34,35], given by:

$$C_n^2 = \left(79 \cdot 10^{-6} \frac{P}{T^2}\right)^2 \cdot C_T^2 \tag{12}$$

where  $T$  represents temperature in Kelvin,  $P$  is pressure in millibar,  $C_T^2$  is the temperature structure parameter which is related to the universal 2/3 power law of temperature variations [35] given by:

$$D_T = \langle (T_1 - T_2)^2 \rangle = \begin{cases} C_T^2 \cdot L_P^{2/3} & l_0 \ll L_P \ll L_0 \\ C_T^2 \cdot l_0^{-4/3} \cdot L_P^2 & 0 \ll L_P \ll l_0 \end{cases}, \tag{13}$$

where  $|T_1 - T_2|$  is the temperature difference between two points separated by distance  $L_P$ , while the outer and inner scales of the small temperature variations are denoted by  $L_0$  and  $l_0$ , respectively.

### 2.3. Experimental Design

For the OCC system to be tested under emulated meteorological phenomena, the following conditions were considered. The signal transmitted by the VLC lamp was chosen to be a repetitive beacon, formed by a sequence of on-off pulses of each of the RGB channels, and followed by a black (off state) pulse denoted as K, then, the beacon was arbitrarily set to the following: G-R-B-K. The K pulse allows measuring the dark intensity in the pixels that cover the lamp image, while the pure color pulses allow to estimate the inter-channel cross-talk between the LED RGB colors and the RGB subpixels of the camera, as explained in our previous work [36]. The  $R_x$  camera equipment was configured to take captures with fixed  $t_{exp}$  and different  $G_V$  sequentially. After taking reference measurements, the atmospheric conditions were emulated while the beacon transmission and capture processes were sustained. The reference and test image sequences are processed through the stages shown in Figure 2, including the extraction of relevant pixels area in the picture, the estimation and enhancing of inter-channel cross-talk, and finally, the computation correlation between the signals obtained in clear conditions and under emulated weather conditions.

The extraction of the relevant group of pixels in OCC image frames, known as Region of Interest (ROI) detection, consists of locating the projection of the source in the image. In this case, we first manually locate and extract the ROI from the reference sequence. Then, since the test group is taken with the same alignment, the ROI stays fixed. Thus, the same coordinates of it are re-utilized. The pixels containing data are then averaged by row, giving the three-channel (RGB) signal  $T_{[M \times 3]}$ , where  $N$  is the number of rows of the ROI. From the reference ROI, a template of one G-R-B-K beacon signal is saved as  $R_{[N \times 3]}$ , where  $M$  is the number of rows used by one beacon in the RS acquisition.

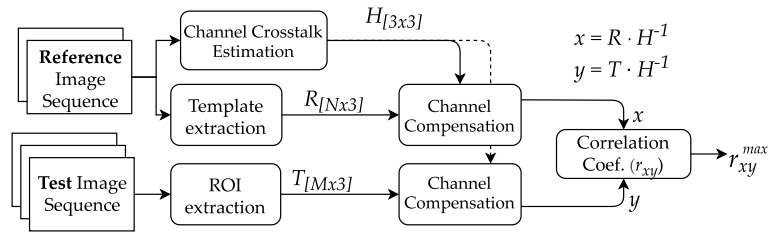


Figure 2. Flow diagram of the offline processing of data captured by cameras.

As shown in previous work [36], the inter-channel cross-talk (ICCT), which is caused by the mismatch between the LEDs and the camera’s Bayer filter spectra, is estimated from clear frames and then compensated in all datasets. We separately analyze R, G, and B pulses from the beacon signal. A matrix  $H_{[3 \times 3]}$  is obtained by averaging the contribution of each pure-LED pulse at the three RGB subpixels. In other words, a component  $h_{ij}$  from  $H_{[3 \times 3]}$  is the average measure from the  $j^{th}$  subpixel when the  $i^{th}$  LED is illuminating it, where  $i, j \in \{R, G, B\}$ . The inverse matrix  $H_{[3 \times 3]}^{-1}$  is used to clean all the datasets from ICCT found at this configuration. Finally, ICCT cleaned signals  $x = (R \cdot H^{-1})_{[N \times 3]}$  and  $y = (T \cdot H^{-1})_{[M \times 3]}$  are compared using the Pearson’s correlation coefficient  $r_{xy}$ , which is defined as:

$$r_{xy} = \frac{\sum_{i=1}^N (x_i - \bar{x})(y_i - \bar{y})}{\sqrt{\sum_{i=1}^N (x_i - \bar{x})^2} \sqrt{\sum_{i=1}^N (y_i - \bar{y})^2}}, \quad (14)$$

where  $x_i$  are the reference sample points from  $R$ , of size  $N$ ,  $y_i$  are  $N$  consecutive samples of  $T$ , and  $\bar{x}, \bar{y}$  are the mean values. The correlation is calculated for all possible consecutive subsets  $y_j, y_{j+1}, \dots, y_{j+N-1}$ ,  $(j + N - 1) < M$  and the maximum value  $r_{xy}^{max}$  is considered the similarity of the frame compared to the reference.

### 3. Experimental Setup

In this section, we describe the full setup of our experiments, which is shown in Figure 3, including the laboratory chamber used, the tools used for emulating hot and foggy weather conditions, the measurement devices used for estimating the levels of each condition, and the  $T_x$  and  $R_x$  devices that comprise the OCC link. The key experiment parameters are listed in Table 2 and the block diagram of the experimental setup is shown in Figure 4.

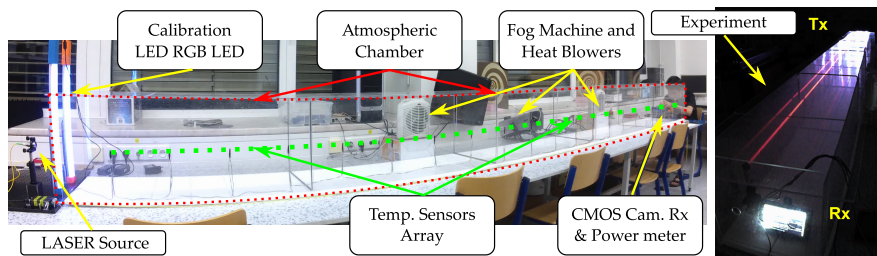


Figure 3. Photos of the laboratory setup utilized in the experiments.

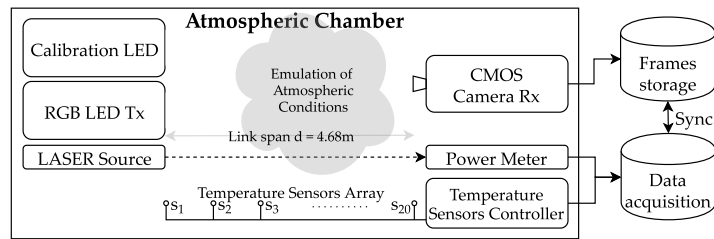


Figure 4. Block diagram of the experimental setup.

Table 2. Experiment key parameters.

Parameter	Value
Transmitter	
Device	12 V DC RGB LED strips (108 × 5050 SMD chips)
Front-end device	Microcontroller Atmel ATmega328p [37]
Idle power [W]	4.76
Dominant wavelengths [nm]	630 (Red), 530 (Green), 475 (Blue)
$T_{chip}$ [s]	1/8400
Receiver	
Camera	Picamera V2 module (Sony IMX219)
Resolution	3280 × 2464 px
$t_{exp}$ [μs]	60
Gain ( $G_V$ ) [dB]	0, 1, ..., 16
Frame rate [fps]	30
Laboratory chamber	
Dimensions [m]	4.910 × 0.378 × 0.368
Temperature sensors	20 × Papouch Corp. TQS3-E (range: −55 to +125°C × 0.1°C)
LASER source	Thorlabs HLS635 (635 nm) F810APC
Optical power meter	Thorlabs PM100D S120C
Heat blowers	2 × Sencor SFH7010, 2000 W
Fog machine	Antari F-80Z, 700 W

### 3.1. Laboratory Chamber

The atmospheric chamber set up for measurements in the facilities of the Czech Technical University in Prague [27] features two heater fans, and one Glycerine machine, that can blow hot air and fog into the chamber, respectively. For the characterization of turbulence and light scintillation in the chamber, an array of 20 temperature sensors were set up equidistantly. A laser source of 625 nm and 2 mW, and an optical power meter placed on each end of the chamber are used to measure the fog attenuation.

### 3.2. OCC System

The transmitter unit was built using strips of RGB LEDs connected to a microcontroller (model ATmega328p [37]) through a switching circuit based on transistors. The LED arrays were installed on aluminum rails with a white meth-acrylate diffuser. The circuitry makes the RGB channels to emit the beacon signal (idle state) repeatedly, or to send arbitrary data coming from a serial port (this feature was not used in this experiment). The chip time  $t_{chip}$  or the pulse width is set by software in the microcontroller. In the case of the experiments, this parameter was set to 1/8400 s.

The receiver was made using an Element14 Raspberry Pi board with its official camera device PiCamera V2. The firmware allows to set  $G_V$  from 1 to 16 dB and exposure time from 20 ns up to the time elapsed between frame captures, which in case of 30 fps video is approximately 33.3 ms. The fixed internal structure of the CMOS sensor (Sony IMX219) featured by the PiCamera is set to have a row-shift time  $t_{rs} = 18.904 \mu\text{s}$  [29]. The exposure time was set to  $t_{exp} = 60 \mu\text{s}$ .

Given the hardware configuration of our system in the laboratory, as shown in Figure 3, each of the image frames can contain up to 64 symbols. Since the modulation uses RGB channels, each symbol then is formed by 3 bits. The maximum throughput of this configuration at 30 fps is then 5.76 kbps.

#### 4. Results

In this section, we show the results from the analysis of the images obtained from heat-turbulence and fog experiments carried out, as shown in Section 3. The maximum values of the correlation coefficient were computed between the ICCT-compensated reference image sequence and the images captured under different conditions, as explained in Section 2. The  $r_{xy}^{max}$  values obtained are analyzed together with the experimental parameters set:  $C_n^2$  in the case of heat-induced turbulence, and  $V_M, G_V$ , in the case of fog.

##### 4.1. Heat-Turbulence Experiments

The heat-turbulence experiment's reference image sequence was captured using the chamber heaters off at a stabilized laboratory temperature of 21.7 °C. Thus, the template signal extracted from these captures is the result of operating the system under a negligible level of turbulence. The remaining test image sequence was captured under the thermal influence of channel in two parts, one under a higher laboratory temperature of 32.3 °C, and a second part with the heaters of the chamber working at full power, setting another turbulence level. The  $C_n^2$  parameter value is then calculated using the temperature sensors samples. The  $r_{xy}^{max}$  values between the frames of the test image sequence and the template are calculated. With these values, we infer the influence of this phenomenon.

The refractive index structure parameter values during the first part of the test image sequence capture ranged from  $C_n^2 = 1.86 \cdot 10^{-11} \text{ m}^{-2/3}$  to  $2.51 \cdot 10^{-11} \text{ m}^{-2/3}$  in high room temperature with the heaters off. In the second part, the range of turbulence increased to  $4.69 \cdot 10^{-11} \text{ m}^{-2/3} \leq C_n^2 \leq 7.13 \cdot 10^{-11} \text{ m}^{-2/3}$ . The obtained  $r_{xy}^{max}$  between the signals from each part of the experiment and the template are shown as histograms in Figure 5. To estimate the similarity between the  $r_{xy}^{max}$  data from the reference and from each part of the test image sequence, a Kolmogórov-Smirnov (KS) statistical test was done, which consists of a non-parametric tool that estimates if two data sets are samples from the same distribution with a confidence  $p$ -value [38]. The result is that the first part of the test image sequence has  $p = 0.81$  confidence value of having the same distribution as the reference, and the second has  $p = 0.83$ . It can be seen an almost negligible influence of turbulence on OCC systems.

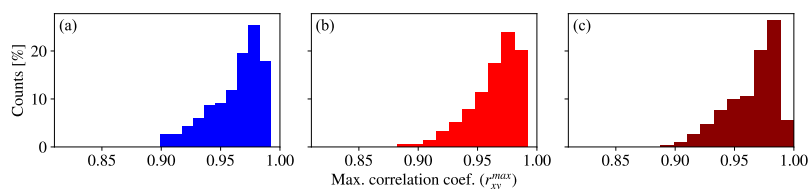


**Figure 5.** Distribution of maximum correlation coefficient values of image sequences taken (a) under a cool room temperature of 21.7 °C (no turbulence), (b) under a warm room temperature of 32.3 °C and with heaters off, and (c) with turbulence induced by the heaters.

The different ranges of turbulence analyzed presumably have the same distribution of  $r_{xy}^{max}$  values, according to the KS statistical test, and also the vast amount of them meet that  $r_{xy}^{max} > 0.9$ , which means that the experimental setup's behavior is considerably similar to the reference, regardless of the turbulence ranges that were induced. This robustness of the system can be attributed to the short link distance and the big field of view of the camera. Both make the refraction effects unnoticeable in the received signal of our system.

4.2. Fog Experiments

For the fog emulation experiment, the reference image sequence was taken under clear air in the laboratory chamber while the optical power meter measured the power of the laser without fog attenuation. The test image sequence was taken while the chamber was arbitrarily supplied with fog from the Antari F-80Z, while the laser power was measured in synchronicity in order to label each image with the current  $V_M$ . The value of  $G_V$  of the images was sequentially modified from 0 to 16 dB by steps of 1 dB during the test image sequence, while for the reference, it was set to zero as default.

The  $r_{xy}^{max}$  values obtained for the test images sequence varying  $G_V$  and  $V_M$  are shown as a contour plot in Figure 6. The high correlation area ( $r_{xy}^{max} > 0.9$ ) determines three important regions (highlighted in Figure 6 by dashed circles). For the high values of visibility, the signal coming from the transmitter is not affected by the fog attenuation and is received with the highest power. Then, the increase of gain causes saturation of the ADC, affecting the correlation. In the low visibility region, the presence of dense fog attenuates the received signal and lowers the correlation. It can be seen that, in this low-visibility region, the increase of gain gives a high correlation, meaning that the camera amplifier compensates the attenuation from fog. The region in between, around 50 m visibility, shows high values of correlation regardless of the variations of gain. The three regions described are shown in Figure 7, and a non-parametric locally estimated scatterplot smoothing (LOESS) regression [39] is performed with parameter span  $s = 0.5$  to show the trend of the data points. Examples of the ROI extraction from test images sequence are included to depict the effect of visibility and gain over the frames.

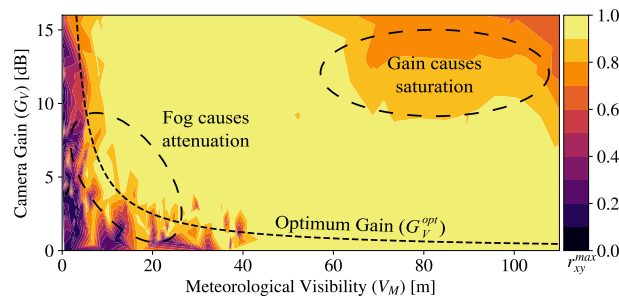


Figure 6. Maximum correlation between test and reference signals varying camera gain under emulated fog conditions of different values of meteorological visibility.

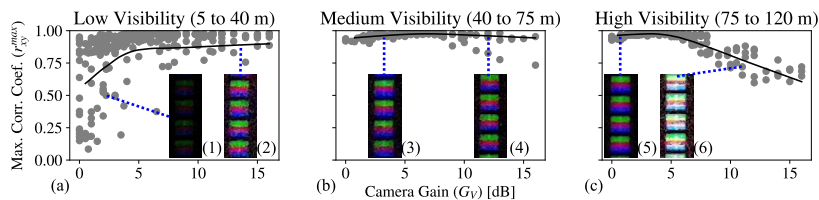


Figure 7. Maximum correlation data (gray dots) from fog-emulation experiments, separated by levels of (a) low, (b) medium, and (c) high visibility and their respective locally estimated scatterplot smoothing (LOESS) regression for  $s = 0.5$  (black curves). The area encircled in (a) is the region of image frames affected by the fog attenuation and in (b) by gain saturation. Insets are Region of Interest (ROI) extraction examples: (1) for low visibility and low gain, (2) low visibility and high gain, (3) medium visibility and low gain, (4) medium visibility and high gain, (5) high visibility and low gain, and (6) high visibility and high gain.

From the minimum gain values in the area of  $r_{xy}^{max} > 0.9$ , an optimum gain curve  $G_V^{opt}$  is derived providing that there is an inverse proportionality relationship between meteorological visibility and camera gain as follows:

$$G_V^{opt}(V_M) = \frac{k_v}{V_M}, \tag{15}$$

where  $k_v$  is an empirical parameter. Using curve fitting, the value  $k_v = 0.0497$  dB·km was derived for our experimental setup.

In order to calculate the SNR from the empirical data obtained, we have considered that OOK modulation is used. The following approximation of the SNR has been derived (note the 1/2 factor due to OOK):

$$SNR = \frac{1}{2} \frac{E^2[X_{ROI}]}{V[X_{ROI}]}, \tag{16}$$

where  $X_{ROI}$  comprises the samples of pixels that fall within the ROI mask  $M_{[v \times h]}$  as described in Equation (2), which was determined from reference images and since the  $T_x$  and  $R_x$  are static it is the same for the whole experiment.  $E[\cdot]$ , and  $V[\cdot]$  denote the statistical expected value and variance, respectively.

The empirical SNR definition was calculated for all the image sequences of the fog experiments. The results for the frames taken with  $G_V = 11$  dB are shown in Figure 8 for the three RGB channels. This value of gain was chosen because, as shown in Figure 6, the level  $G_V = 11$  dB is affected by the dense fog and also by the saturation. The SNR values in Figure 8 are plotted against optical density in logarithmic scale. They show that higher attenuation  $A_f$  values, or alternatively, longer link spans, cause a decay of the SNR. Therefore, a curve fitting was carried out assuming that the SNR decays at a rate of  $\alpha$  dB per decade of optical density, as follows:

$$SNR(A_f d) = SNR(1) + \alpha \cdot \log(A_f d), \tag{17}$$

where  $SNR(1)$  is the estimated signal-to-noise ratio at unitary optical density.

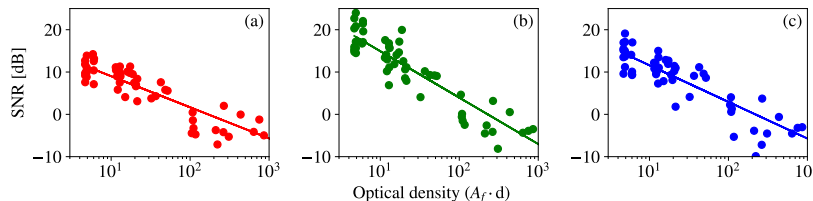


**Figure 8.** Empirical signal-to-noise ratio (SNR) values obtained from captures at  $G_V = 11$  dB plotted against optical density values at fixed link range  $d$  and with  $A_f$  values emulated by the presence of fog. The plot in (a) corresponds to R channel, (b) to G channel, and (c) to B channel, and their respective fitted curves.

The SNR values obtained from the image sequences were also evaluated on their influence over  $r_{xy}^{max}$ , as shown in Figure 9. A LOESS regression also shows the trend of the scatterplots in the figure, and it can be seen that  $r_{xy}^{max}$  increases with the SNR, except for the highest SNR values in the blue channel, which are affected by saturation of the ADC. It can also be seen that SNR values higher than 5 dB make  $r_{xy}^{max} > 0.9$  for most of the samples. From this, it can be concluded that  $r_{xy}^{max}$  is a valid metric for the quality of the signal in OCC, although SNR is more robust.



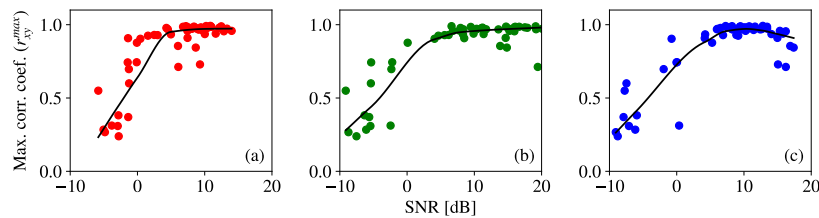


**Figure 9.** Values of  $r_{xy}^{max}$  from test image sequence of the fog-emulation experiment plotted against empirical SNR. The values are for frames taken with  $G_V = 11$  dB. The scatter plot in (a) corresponds to R channel, (b) to G channel, and (c) to B channel, and the curves in black are their corresponding LOESS regression for span value  $s = 0.7$ .

The results obtained in this experiment show that the fog attenuation can make the power of the optical signal weaken down to the point that the noise induced by the ADC considerably affects the SNR. In other words, the conversion to digital corrupts the weak optical signal from dense fog conditions or long link spans. In these cases, the column amplifier of the camera is crucial to keep a high amplitude input at the ADC and reduce the effect of quantization.

## 5. Conclusions

In this paper, we presented an experimental study of the influence of two kinds of atmospheric conditions over an RS-based OCC link: the heat-induced turbulence due to random fluctuations of the refractive index of the air along the path, and the attenuation caused by the presence of fog particles in the air. The image sequences captured under the two different conditions were compared to a reference sequence of images taken under clear conditions. For this, we used the maximum value of Pearson's correlation coefficient  $r_{xy}^{max}$  to determine their similarity. We have also evaluated the signal quality by the empirical SNR obtained from the image frames and showed its relationship with  $r_{xy}^{max}$  and its dependence on the product between fog attenuation and link span, known as the optical density. The most important findings in this work are, first, that the turbulence levels emulated do not affect the signal quality considerably. For the fog experiments, we have derived an expression for the theoretical SNR as a function of the analog camera gain, showing that a CMOS camera-based OCC system can improve the SNR by using the column amplifier. In the fog experiments, the correlation  $r_{xy}^{max}$  was impaired in two different cases: for high values of  $V_M$ , when the gain is increased, the correlation drops because of the saturation of the signal, and, for low visibility, the attenuation caused by the fog impairs the similarity to the reference when the gain is low, because of the loss due to quantization noise at the ADC. It was found for the latter case that by increasing the gain of the camera, the attenuation can be compensated, allowing the OCC link to receive signal with a  $r_{xy}^{max} > 0.9$  for  $V_M$  values down to 10 m. Our findings show that there is an inverse proportionality relationship between the optimum camera gain and the visibility, and that the empirical SNR decays at a rate  $\alpha$  with the optical density. This utilization of the CMOS camera's built-in amplifier opens a new possibility for OCC systems, extending the control strategy, and allowing to keep low exposure times and, thus, a high bandwidth, even in dense fog scenarios.

**Author Contributions:** The contributions of the authors in this paper are the following: conceptualization, V.M., S.R.T., E.E.; investigation, V.M., S.R.T.; methodology, V.M., E.E.; project administration, S.Z., R.P.-J.; software V.M.; and validation, S.Z., R.P.-J. All authors have read and agreed to the published version of the manuscript.

**Funding:** This project has received funding from the European Union's Horizon 2020 research and innovation program under the Marie Skłodowska-Curie grant agreement No 764461, and from the Spanish Research Administration (MINECO project: OSCAR, ref.: TEC 2017-84065-C3-1-R)

**Acknowledgments:** V. M. thanks the technical support given by Jan Bohata, Petr Chvojka, and Dmytro Suslov at the Czech Technical University in Prague, and by Víctor Guerra, and Cristo Jurado-Verdu at IDETIC - Universidad de Las Palmas de Gran Canaria.

**Conflicts of Interest:** The authors declare no conflict of interest. The funders had no role in the design of the study; in the collection, analyses, or interpretation of data; in the writing of the manuscript, or in the decision to publish the results.

## References

1. Cahyadi, W.A.; Kim, Y.H.; Chung, Y.H.; Ahn, C.J. Mobile phone camera-based indoor visible light communications with rotation compensation. *IEEE Photonics J.* **2016**, *8*, 1–8. [[CrossRef](#)]
2. Teli, S.R.; Zvanovec, S.; Ghassemlooy, Z. Performance evaluation of neural network assisted motion detection schemes implemented within indoor optical camera based communications. *Opt. Express* **2019**, *27*, 24082–24092. [[CrossRef](#)] [[PubMed](#)]
3. Chavez-Burbano, P.; Vitek, S.; Teli, S.; Guerra, V.; Rabadan, J.; Perez-Jimenez, R.; Zvanovec, S. Optical camera communication system for Internet of Things based on organic light emitting diodes. *Electron. Lett.* **2019**, *55*, 334–336. [[CrossRef](#)]
4. Tiwari, S.V.; Sewaiwar, A.; Chung, Y.H. Optical bidirectional beacon based visible light communications. *Opt. Express* **2015**, *23*, 26551–26564. [[CrossRef](#)] [[PubMed](#)]
5. Pergoloni, S.; Biagi, M.; Colonnese, S.; Cusani, R.; Scarano, G. Coverage optimization of 5G atto-cells for visible light communications access. In Proceedings of the 2015 IEEE International Workshop on Measurements & Networking (M&N), Coimbra, Portugal, 12–13 October 2015; pp. 1–5.
6. Boban, M.; Kousaridas, A.; Manolakis, K.; Eichinger, J.; Xu, W. Connected roads of the future: Use cases, requirements, and design considerations for vehicle-to-everything communications. *IEEE Veh. Technol. Mag.* **2018**, *13*, 110–123. [[CrossRef](#)]
7. Yamazato, T.; Takai, I.; Okada, H.; Fujii, T.; Yendo, T.; Arai, S.; Andoh, M.; Harada, T.; Yasutomi, K.; Kagawa, K.; et al. Image-sensor-based visible light communication for automotive applications. *IEEE Commun. Mag.* **2014**, *52*, 88–97. [[CrossRef](#)]
8. Takai, I.; Ito, S.; Yasutomi, K.; Kagawa, K.; Andoh, M.; Kawahito, S. LED and CMOS image sensor based optical wireless communication system for automotive applications. *IEEE Photonics J.* **2013**, *5*, 6801418. [[CrossRef](#)]
9. Ghassemlooy, Z.; Alves, L.N.; Zvanovec, S.; Khalighi, M.A. *Visible Light Communications: Theory and Applications*; CRC Press: Borarton, FL, USA, 2017.
10. Boubezari, R.; Le Minh, H.; Ghassemlooy, Z.; Bouridane, A. Smartphone camera based visible light communication. *J. Lightwave Technol.* **2016**, *34*, 4121–4127. [[CrossRef](#)]
11. Nguyen, T.; Islam, A.; Hossan, T.; Jang, Y.M. Current status and performance analysis of optical camera communication technologies for 5G networks. *IEEE Access* **2017**, *5*, 4574–4594. [[CrossRef](#)]
12. Nguyen, T.; Hong, C.H.; Le, N.T.; Jang, Y.M. High-speed asynchronous Optical Camera Communication using LED and rolling shutter camera. In Proceedings of the 2015 Seventh International Conference on Ubiquitous and Future Networks, Sapporo, Japan, 7–10 July 2015; pp. 214–219.
13. Chavez-Burbano, P.; Guerra, V.; Rabadan, J.; Perez-Jimenez, R. Optical camera communication for smart cities. In Proceedings of the 2017 IEEE/CIC International Conference on Communications in China (ICCC Workshops), Qingdao, China, 22–24 October 2017; pp. 1–4. [[CrossRef](#)]
14. Chavez-Burbano, P.; Guerra, V.; Rabadan, J.; Rodriguez-Esparragon, D.; Perez-Jimenez, R. Experimental characterization of close-emitter interference in an optical camera communication system. *Sensors* **2017**, *17*, 1561. [[CrossRef](#)] [[PubMed](#)]
15. Cui, Z.; Wang, C.; Tsai, H.M. Characterizing channel fading in vehicular visible light communications with video data. In Proceedings of the 2014 IEEE Vehicular Networking Conference (VNC), Paderborn, Germany, 3–5 December 2014; pp. 226–229.
16. Wu, L.C.; Tsai, H.M. Modeling vehicle-to-vehicle visible light communication link duration with empirical data. In Proceedings of the 2013 IEEE Globecom Workshops (GC Wkshps), Atlanta, GA, USA, 9–13 December 2013; pp. 1103–1109.

17. Mobility and Transport (European Commission). Current Speed Limit Policies. Available online: [https://ec.europa.eu/transport/road\\_safety/specialist/knowledge/speed/speed\\_limits/current\\_speed\\_limit\\_policies\\_en](https://ec.europa.eu/transport/road_safety/specialist/knowledge/speed/speed_limits/current_speed_limit_policies_en) (accessed on 28 January 2020).
18. Road Safety Authority (Government of Ireland). The Two-Second Rule. Available online: [http://www.rotr.ie/rules-for-driving/speed-limits/speed-limits\\_2-second-rule.html](http://www.rotr.ie/rules-for-driving/speed-limits/speed-limits_2-second-rule.html) (accessed on 28 January 2020).
19. Kim, Y.h.; Chung, Y.h. Experimental outdoor visible light data communication system using differential decision threshold with optical and color filters. *Opt. Eng.* **2015**, *54*, 040501. [CrossRef]
20. Islam, A.; Hossan, M.T.; Jang, Y.M. Convolutional neural networkscheme-based optical camera communication system for intelligent Internet of vehicles. *Int. J. Distrib. Sens. Netw.* **2018**, *14*, 1550147718770153. [CrossRef]
21. Elamassie, M.; Karbalayghareh, M.; Miramirkhani, F.; Kizilirmak, R.C.; Uysal, M. Effect of fog and rain on the performance of vehicular visible light communications. In Proceedings of the 2018 IEEE 87th Vehicular Technology Conference (VTC Spring), Porto, Portugal, 3–6 June 2018; pp. 1–6.
22. Tian, X.; Miao, Z.; Han, X.; Lu, F. Sea Fog Attenuation Analysis of White-LED Light Sources for Maritime VLC. In Proceedings of the 2019 IEEE International Conference on Computational Electromagnetics (ICCEM), Shanghai, China, 20–22 March 2019; pp. 1–3. [CrossRef]
23. Kim, Y.H.; Cahyadi, W.A.; Chung, Y.H. Experimental demonstration of VLC-based vehicle-to-vehicle communications under fog conditions. *IEEE Photonics J.* **2015**, *7*, 1–9. [CrossRef]
24. Guo, L.-d.; Cheng, M.-j.; Guo, L.-x. Visible light propagation characteristics under turbulent atmosphere and its impact on communication performance of traffic system. In Proceedings of the 14th National Conference on Laser Technology and Optoelectronics (LTO 2019), Shanghai, China, 17 May 2019; p. 1117047. [CrossRef]
25. Nikishov, V.V.; Nikishov, V.I. Spectrum of Turbulent Fluctuations of the Sea-Water Refraction Index. *Int. J. Fluid Mech. Res.* **2000**, *27*, 82–98. [CrossRef]
26. Eso, E.; Burton, A.; Hassan, N.B.; Abadi, M.M.; Ghassemlooy, Z.; Zvanovec, S. Experimental Investigation of the Effects of Fog on Optical Camera-based VLC for a Vehicular Environment. In Proceedings of the 2019 15th International Conference on Telecommunications (ConTEL), Graz, Austria, 3–5 July 2019; pp. 1–5.
27. Bohata, J.; Zvanovec, S.; Korinek, T.; Abadi, M.M.; Ghassemlooy, Z. Characterization of dual-polarization LTE radio over a free-space optical turbulence channel. *Appl. Opt.* **2015**, *54*, 7082–7087. [CrossRef] [PubMed]
28. Kuroda, T. *Essential Principles of Image Sensors*; CRC Press: Borarton, FL, USA, 2017.
29. IMX219PQH5-C Datasheet. Available online: <https://datasheetspdf.com/pdf/1404029/Sony/IMX219PQH5-C/1> (accessed on 28 January 2020)
30. Weichel, H. *Laser Beam Propagation in the Atmosphere*; SPIE Press: Bellingham, WA, USA, 1990; Volume 3.
31. Henniger, H.; Wilfert, O. An Introduction to Free-space Optical Communications. *Radioengineering* **2010**, *19*, 203–212.
32. Kim, I.I.; McArthur, B.; Korevaar, E.J. Comparison of laser beam propagation at 785 nm and 1550 nm in fog and haze for optical wireless communications. In Proceedings of the Optical Wireless Communications III. International Society for Optics and Photonics, Boston, MA, USA, 6 February 2001; pp. 26–37.
33. Ghassemlooy, Z.; Popoola, W.; Rajbhandari, S. *Optical Wireless Communications: System and Channel Modelling with Matlab*; CRC Press: Borarton, FL, USA, 2019.
34. Nor, N.A.M.; Fabyiyi, E.; Abadi, M.M.; Tang, X.; Ghassemlooy, Z.; Burton, A. Investigation of moderate-to-strong turbulence effects on free space optics—A laboratory demonstration. In Proceedings of the 2015 13th International Conference on Telecommunications (ConTEL), Graz, Austria, 13–15 July 2015; pp. 1–5.
35. Andrews, L.C.; Phillips, R.L. *Laser Beam Propagation Through Random Media*; SPIE Press: Bellingham, WA, USA, 2005; Volume 152.
36. Jurado-Verdu, C.; Matus, V.; Rabadan, J.; Guerra, V.; Perez-Jimenez, R. Correlation-based receiver for optical camera communications. *Opt. Express* **2019**, *27*, 19150–19155. [CrossRef] [PubMed]
37. Atmel Corporation. *ATmega328p, 8-bit AVR Microcontroller with 32K Bytes In-System Programmable Flash, Datasheet*; Atmel Corporation: San Jose, CA, USA, 2015.

38. Massey, F.J., Jr. The Kolmogorov-Smirnov Test for Goodness of Fit. *J. Am. Stat. Assoc.* **1951**, *46*, 68–78. [[CrossRef](#)]
39. Cleveland, W.S.; Devlin, S.J. Locally weighted regression: an approach to regression analysis by local fitting. *J. Am. Stat. Assoc.* **1988**, *83*, 596–610. [[CrossRef](#)]



© 2020 by the authors. Licensee MDPI, Basel, Switzerland. This article is an open access article distributed under the terms and conditions of the Creative Commons Attribution (CC BY) license (<http://creativecommons.org/licenses/by/4.0/>).

## 5.2 Publication 2 (P2)

The publication entitled “*Sandstorm effect over experimental optical camera communication*” [48] studied the effect of real sandstorms, a phenomenon that is originated in extended arid regions and deserts of the planet and can affect urban areas up to thousands of kilometers away with high concentrations of fine particulate matter. The lightweight dust particles travel carried by gusts and winds, and their concentrations can affect humans’ respiratory system and other forms of life, while the visibility can be reduced to the point that airports and other services cannot operate. Furthermore, in these scenarios, the reliability of all outdoor OWC systems is affected by dust due to the aerosol-induced scattering, fouling over surfaces, and abrasion of the optical front-end’s material.

The implementation of VLC links in such conditions was simulated by Ebrahim *et al.* [55] but not previously tested. Works by Arnon, Kedar *et al.* exploited the widening of the FOV produced by multiple scattering along the path in FSO links in the presence of aerosols [56]. OCC can also benefit from ROI expansion. This work provides an experimental analysis of OCC employed in a real sandstorm event. It provides an evaluation of the effects of the sandstorm, impairing the SNR and improving the size of ROI.

One of the highlighted findings in this work is the empirical demonstration of the expansion of ROI as the linkspan was increased, showing that theoretically, OCC systems can exploit the scattering produced by the aerosols in the dust of the sandstorm by considering larger amounts of pixels containing information compared to clear conditions. Similar effects have already been reported in other demonstrations in the FSO field [56], and in OCC using the camera’s focus to cause similar expansions of ROIs [57].



# Sandstorm effect on experimental optical camera communication

VICENTE MATUS,<sup>1,\*</sup> VICTOR GUERRA,<sup>1</sup> STANISLAV ZVANOVEC,<sup>2</sup> JOSE RABADAN,<sup>1</sup> AND RAFAEL PEREZ-JIMENEZ<sup>1</sup>

<sup>1</sup>DeTIC, Universidad de Las Palmas de Gran Canaria, Spain

<sup>2</sup>Czech Technical University in Prague, Czech Republic

\*Corresponding author: vmatus@idetec.eu

Received 11 September 2020; revised 20 November 2020; accepted 29 November 2020; posted 1 December 2020 (Doc. ID 405952); published 21 December 2020

Sandstorms can severely affect the reliability of outdoor optical wireless communications (OWC) by diminishing large regions' visibility. In this work, the effect of a real sandstorm on optical camera communications (OCC) links is experimentally evaluated. Two link ranges are essayed using a cost-efficient telescope-based camera setup with commercial LEDs. Using on-off keying modulation, a data rate of 1035 and 630 bps with error probabilities of  $9.14 \cdot 10^{-5}$  and  $4.1 \cdot 10^{-3}$  for 100 m and 200 m, respectively, can be achieved. The signal-to-noise ratio of the links was optimized by tuning the analog amplifier's gain of the camera, increasing it by up to 9 dB. It is shown that scattering due to the sandstorm can even be beneficial for increasing the data rate in OCC (contrary to classical photodetector-based OWC links), thanks to an increment of 33% on the region of interest dimensions compared to the expected clear air link. © 2020 Optical Society of America

<https://doi.org/10.1364/AO.405952>

## 1. INTRODUCTION

Optical camera communication (OCC) is an essential sub-field of visible light communication (VLC). It is based on the use of image sensors as receivers of the optical data signal. The ubiquity of camera devices in consumer electronics (e.g., smartphones, tablets, and laptops) is expected to bring this technology to the mass market earlier than other VLC systems that need a photodiode (PD) or multiple PDs as receivers, which are not available in commercial off-the-shelf devices. OCC is currently part of the Institute of Electrical and Electronics Engineers (IEEE) 802.15.7r1 standard [1], defining several transmission modes that take into account the particular characteristics of the image sensor, such as the rolling shutter (RS) and global shutter (GS) scanning methods. RS exploits the complementary metal-oxide-semiconductor (CMOS) sensor's progressive scanning of the image, which is done on a row-by-row basis, meaning that each row's exposure starts after the previous one's by a delay known as the row-shift time, and it enables communications up to several kilobits per second (kbps) [2]. GS is used in charge-coupled device (CCD) sensors, which expose the whole frame simultaneously. Thus, the frame rate limits GS's throughput to tens or hundreds of bits per second (bps). RS techniques provide higher data rates compared to GS since each image frame can contain several rows capturing different states of the transmitter. RS's achievable data rate is then highly dependent on the optical source's projection over the image

sensor's scanning axis because this size determines the number of detectable bits in the image frame [3]. The camera's optical system can augment the projection by, for example, defocusing and magnifying the image [4].

This low-speed technology has been proposed as suitable for many indoor applications such as visible light positioning, wireless monitoring of patients' sensors in hospitals, peer-to-peer data sharing, among others [2]. Furthermore, OCC is capable of operating in outdoor environments using the appropriate settings of the camera [5,6]. Its potential use on vehicular communications has been recurrently reported in the literature [2,7]. Moreover, cameras' inherent spatial multiplexing capability has been exploited to define sensor monitoring applications in Smart Cities [8]. The vehicular application of VLC has been studied in [9], where different scenarios of atmospheric conditions have been simulated. The PD-based receiver link achieves a maximum distance of about 40 m in clear weather conditions for a vehicle-to-vehicle communication scenario if a  $10^{-4}$  bit error rate (BER) is required. In harsh conditions, the maximum achievable distance drops to around 35 m, which is shown to increase to about 90 m with optical gain techniques such as increasing the focal aperture.

Free space optics (FSO) employing PDs and lasers are one of the most advanced optical wireless communications (OWC) for outdoor applications, with data rates around 10 Gbps and proven reliability even using mobile nodes in link spans from a

few hundred meters to tens of kilometers (km) [10,11]. Despite its very low data rates, OCC can still be competitive due to its cost-effectiveness. This technology can use inexpensive and already-deployed devices such as light-emitting diode (LED) lighting and ubiquitous digital cameras, as in most of the aforementioned applications.

Atmospheric conditions that may affect OWC and FSO performance are uncontrollable, but they must be considered when designing outdoor optical systems. The most studied phenomena are fog, mist, turbulence, aerosols, and precipitations (rain and snow). The joint impact of atmospheric turbulence and particle-related scattering in FSO communications at infrared wavelengths has been extensively measured by Libich *et al.* in [12], emulating smog particles and turbulence conditions in a laboratory chamber, using sand and ashes at different densities, and airflow at different velocities. Real outdoor scenarios have been experimentally studied for OCC in [4,8]. Chavez-Burbano *et al.* employed a GS camera under clean atmospheric conditions, and a 328-m-long link achieved a data rate of 15 bps with an error of approximately 4%. Eso *et al.* established a 400-m-long link with 450 bps data rate and null error using an RS in clear weather. The camera lens was used to defocus the image and obtain a bigger projection of the object in the image sensor plane.

The experimental work on overcoming the attenuation of the VLC link caused by atmospheric conditions has been implemented using optical gain by Kim *et al.* [13]; despite that, the field-of-view of the photodetector-based receiver is reduced. A different strategy has been developed for OCC in [5,14], where the use of the camera's analog gain was evaluated in the laboratory under fog conditions. The results showed that this parameter's optimization could significantly improve the signal quality in scenarios subject to high fog attenuation and particles scattering.

In high mobility scenarios such as OCC's vehicular application, the region of interest (ROI) detection is an essential feature for reliable links. The ROI consists of the image pixels that contain data, i.e., where the light rays from the transmitter impinge at the camera's image sensor, which can only be known beforehand in scenarios where the node positions are fixed. The use of neural networks (NN) to detect the ROI by finding well-known signals contained in an image frame has allowed researchers to implement physical layer modes from IEEE 802.15.7r1 (TG7r1) [15]. The system architecture proposed includes a two-stage NN to decode bits in pictures taken with an RS camera, although it has not been tested in real-world conditions. The effect of a sandstorm on VLC links was simulated by Ebrahim *et al.* in [16]. The authors studied the use case of vehicular-to-road communication under different particle types of sandstorms, which differed in size and density. High-density clay particles of 2  $\mu\text{m}$  diameter lowered the maximum achievable span to 90 m in the simulation. On the other hand, Ghassemlooy *et al.* replicated sandstorm conditions in a laboratory environment for evaluating the effect of this phenomenon on FSO links [17]. Contrary to VLC or FSO, this phenomenon has never been theoretically addressed nor experimentally evaluated for OCC systems.

This paper provides the first experimental investigation, to the best of our knowledge, that analyzes the impact of a

sandstorm event on an OCC link at long ranges. The main contribution is to measure and prove the effects of the phenomenon in the optical wireless channel for the OCC link and define the essential blocks for the camera's digital signal processor that ensure the detection of data containing pixels in the ROI of the image frames. This assessment is fundamental for OCC applications in Smart Cities to be developed and deployed.

This paper is organized as follows. Section 2 explains the channel model for the RS OCC, considering the presence of sandstorm conditions. In Section 3, we characterize the experimental scenario and derive the data analysis flow. Section 4 shows the outcome of the deployed OCC experiment in real sandstorm conditions. Finally, conclusions are summarized in Section 5.

## 2. CHANNEL MODEL

In this section, the optical wireless channel is modeled for an outdoor setting regarding the signal's attenuation due to sandstorm particles. The signal quality metrics are derived from the configuration of the transmitter ( $T_x$ ) and receiver ( $R_x$ ) units, taking into consideration the ROI dimensions of width and height.

The light pulses of varying wavelength  $\lambda$  generated by the transmitter are propagated through the medium and suffer from attenuation  $a(\lambda)$ , as modeled by Beer's law [18], and from scattering  $b(\lambda)$  caused by the particles [19,20]. The extinction coefficient  $K_{\text{ext}}(\lambda)$  of an optical wireless channel is then modeled as

$$K_{\text{ext}}(\lambda) = a(\lambda) + b(\lambda). \quad (1)$$

Note that the multiple particles along the path can cause non-line-of-sight rays of light to eventually impinge on the receiver's surface, which can be advantageous for FSO links, as reported by Kedar and Arnon in [21], and potentially for OCC. In the case of OCC in multiple-scattering scenarios, the overall received signal may be improved by expanding the apparent dimensions of bright objects. The power signal at the receiver  $P_{R_x}(t)$  can be modeled as

$$P_{R_x}(t) = P_{T_x}(t) \cdot e^{-K_{\text{ext}}(\lambda) \cdot d} \cdot R(\theta, \phi) \cdot \frac{A_{\text{lens}} \cos \Psi}{d^2}, \quad (2)$$

where the transmitter is modeled as a source of light with a predetermined radiation pattern  $R(\theta, \phi)$  and power  $P_{T_x}(t)$ , located at a distance  $d$  of the receiver. The variables  $\theta$  and  $\phi$  are the emission angles,  $\Psi$  is the incident angle,  $A_{\text{lens}}$  is the area of the receiver's external lens. The extinction coefficient at 550 nm can be related to visibility (V) [14] as

$$V = \frac{3.94}{K_{\text{ext}}(\lambda = 550 \text{ nm})}. \quad (3)$$

In order to determine the signal quality, the signal-to-noise ratio (SNR) was computed using the ROI detected within the image frame. The RS camera captures (in line of sight) an on-off keying (OOK) modulated transmitted signal. The approximation of the SNR has been derived (note the 1/2 factor due to OOK) as

$$\text{SNR} = \frac{1}{2} \frac{M_2[X_{\text{ROI}} - \mu_b]}{V[X_{\text{ROI}}]}, \quad (4)$$

where  $X_{\text{ROI}}$  are the values of pixels that fall within the ROI,  $\mu_b$  is the mean of the background offset, and  $M_2[\cdot]$  and  $V[\cdot]$  denote the second-order momentum and variance, respectively.

According to the expected theoretical BER [22], the OOK system's error rate is then given by

$$\text{BER} = \frac{1}{2} \text{erfc} \left( \sqrt{\frac{\text{SNR}}{2}} \right), \quad (5)$$

where  $\text{erfc}(\cdot)$  is the complementary error function.

If the architecture of the camera pixels is taken into account, the main noise sources are the thermal noise ( $\sigma_{\text{th}}^2$ ), shot noise ( $\sigma_{\text{sh}}^2$ ), and quantization noise ( $\sigma_{\text{adc}}^2$ ) induced by the analog-digital Converter (ADC). Considering that the camera has an amplifier with analog gain  $G_V$ , the SNR at any pixel is expressed as

$$\text{SNR}_{\text{px}} \approx \frac{G_V \cdot i_{\text{pd}}^2}{G_V (\sigma_{\text{th}}^2 + \sigma_{\text{sh}}^2) + \sigma_{\text{adc}}^2}, \quad (6)$$

where  $i_{\text{pd}}$  is the current generated by the PD of the pixel when it is illuminated by the optical communication signal without external interfering sources.

It can be seen that by increasing the analog gain of the camera, the relative contribution of  $\sigma_{\text{adc}}^2$  can be reduced, and the SNR can reach an asymptotic value of  $i_{\text{pd}}^2 / (\sigma_{\text{th}}^2 + \sigma_{\text{sh}}^2)$  in case the ADC is not saturated. This can be exploited for improving the SNR in highly attenuated scenarios when the received signal is weak and the quantization noise needs to be lowered. Furthermore, the maximum theoretical SNR improvement is given by

$$\Delta \text{SNR} \approx 1 + \frac{\sigma_{\text{adc}}^2}{\sigma_{\text{th}}^2 + \sigma_{\text{sh}}^2}. \quad (7)$$

Using the model and metrics stated in this section, the experimental validation was carried out in the sandstorm scenario following the methodology detailed in Section 3.

### 3. METHODOLOGY

In this section, the scenario of experimentation in the real conditions of a sandstorm is described. The OCC system used for the assessment of signal quality is characterized as well. Other well-known mathematical tools used in the data-processing flow are also introduced.

A sandstorm severely hit the Canary Islands archipelago from the Sahara desert for several days at the end of February 2020. The V dropped to tens of meters in some places, according to the United States' National Aeronautics and Space Administration (NASA) Earth Observatory [23]. The airport of Gran Canaria reported a V minimum of around 0.4 km, affecting more than 300 flights in the island and more than 800 in the whole archipelago. This event, known as "Calima" by the islanders, was said to be the worst in four decades.

The experimental setup shown in Fig. 1 and detailed in Table 1 was deployed outdoors near the Institute for Technological Development and Innovation in

**Table 1. Parameters of the Experiment Modules**

Module	Parameter	Value
$T_x$	Emitter dimensions	4.2 cm × 45 cm
	Average source radiance	10 W/m <sup>2</sup>
	Transmitting devices	RGB LED strips (108 × 5050 SMD chips)
Channel	LED dominant wavelengths [nm]	630 (R), 530 (G), 475 (B)
	Distance (d)	100 m, 200 m
	Aerosol optical depth (AOD <sub>550</sub> )	3.2 to 6.4 ( $\lambda = 550$ nm)
	Dust surface concentration [μg/m <sup>3</sup> ]	500 to 2000
	Dust dry deposition [mg/m <sup>2</sup> ]	100 to 400
$R_x$	Telescope focal length (f)	700 mm
	Telescope focal aperture (D)	f/11.6
	Image sensor model	Sony IMX219 [24]
	Image sensor resolution	2592 × 1952 px
	RS row-shift time ( $t_{rs}$ )	18.904 μs
	Camera gain ( $G_V$ )	0, ..., 20.6 dB
	Exposure time ( $t_{\text{exp}}$ )	85 μs

Communications (IDeTIC) from the University of Las Palmas de Gran Canaria (ULPGC), whose location is shown in Fig. 2. The system consisted of a LED transmitter and a telescope and CMOS camera receiver. The emitter was based on a rectangular lamp with red, green, and blue (RGB) LED strips with a white diffuser on top and controlled by an OOK signal generator, programmed to send a fixed and repetitive pattern or beacon of pure RGB pulses followed by a black pulse during the experiments easing both pre-processing and data analysis tasks since a well-known signal is expected. On the other hand, a CMOS image sensor was used as a receiver. A Galilean telescope with a focal length of 700 mm was coupled to the camera in order to reach the target distances of the experiment of  $d_1 = 100$  m and  $d_2 = 200$  m.

Regarding the channel conditions at the time of experimentation, and according to the Barcelona Dust Forecast Center from the Spanish State Meteorological Agency (AEMET), the key parameters of the sandstorm, as modeled as an aerosol particle of median size of 2.524 μm and 2.0 geometric standard deviation [25], are the following. The dust aerosol optical depth at  $\lambda = 550$  nm (AOD<sub>550</sub>) was between 3.2 and 6.4. This parameter increases with the particles' concentration in the air, and clear air values are usually below 0.1. The dust surface concentration was between 500 and 2000 μg/m<sup>3</sup>, with a dry deposition from 100 to 400 mg/m<sup>2</sup>.

The experiment's main target was to observe the sandstorm's impact on an outdoor OCC link's performance. As it occurs in other environments where the medium presents significant particle concentrations, sandstorm-impaired OCC links will suffer from multiple scattering. Hence, it was expected that the pixel SNR diminished with distance and that the point spread function (PSF) of the emitter-receiver pair widened with distance, resulting in a greater-than-expected ROI.



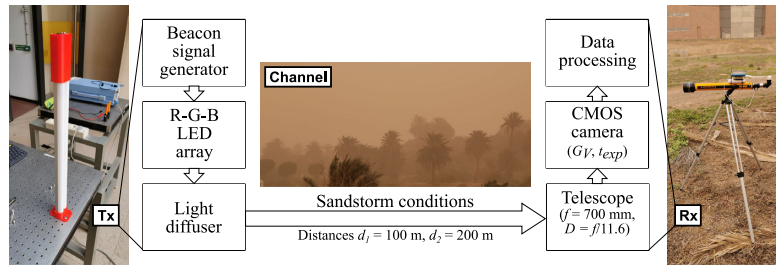


**Fig. 1.** Block diagram and pictures of the experimental setup of this work.

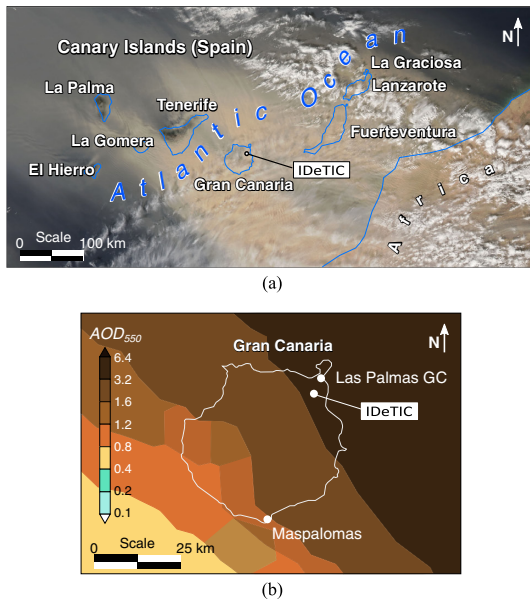


**Fig. 2.** Maps from the sandstorm event in the Canary Islands, 23 February 2020. (a) Satellite image from NASA Moderate Resolution Imaging Spectroradiometer (MODIS) showing the dust in real colors. (b) Map of aerosol optical depth at 550 nm ( $AOD_{550}$ ) at the time of experimentation, provided by AEMET. Approximate location of the IDEtIC facilities is shown in the maps.

The experimental evaluation was divided into three phases: data acquisition, pre-processing, and data analysis. Data acquisition was automated using a script on the receiver side, obtaining 50 images per analog gain  $G_V$ . Due to the emitter's shape, long

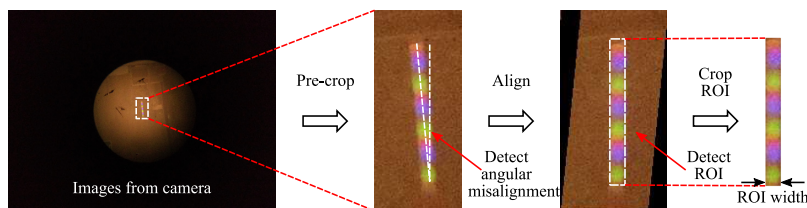


**Fig. 3.** Pre-processing stages of the images obtained with the  $R_x$  module.

link range, and weather conditions, the captured images showed the emitter in variable positions and rotations (caused by the wind perturbations). In order to solve this and provide only the dependence of the sandstorm scattering, semi-supervised pre-processing of the images was carried out. The emitter rotations were estimated using image-processing software, and the rows were shifted according to the estimated angular deviation of up to  $4^\circ$ . Figure 3 illustrates the pre-processing stage with the removal of angular misalignment due to wind perturbations, which also included an arbitrary pre-ROI crop. Finally, all of the image database was batch-processed (in terms of  $G_V$ ), estimating both the average pixel SNR and the ROI's size.

In order to obtain the pixel SNR, the ROI needed to be distinguished between the background and the transmitted signal. After empirically analyzing the shape of the image histograms, such as the plot in Fig. 4, it was observed that a Gaussian mixture model (GMM) could be used to separate the two stated classes (background and signal). The fitted probability density function (PDF) can be described as

$$f_{gmm}(x) = \frac{\alpha}{\sigma_b \sqrt{2\pi}} \exp\left(-\frac{(x - \mu_b)^2}{2\sigma_b^2}\right) + \frac{1 - \alpha}{\sigma_s \sqrt{2\pi}} \exp\left(-\frac{(x - \mu_s)^2}{2\sigma_s^2}\right), \quad (8)$$

where  $\mu$  is the mean, and  $\sigma$  is the standard deviation of the Gaussian functions. The sub-indices  $b$  and  $s$  label the background and signal classes, respectively. The parameter  $\alpha = 0.9$  is an arbitrary weight of the fitting.

From the PDF description, it is straightforward to obtain the optimal decision threshold  $x_{th}$  attending to the maximum likelihood criterion, which results in a second-order equation:

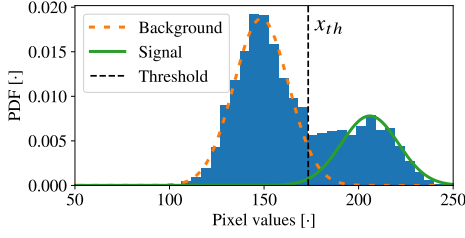


**Fig. 4.** Red channel histogram and fitted GMM curves of an arbitrary image frame captured at  $d_1 = 100$  m and  $G_V = 17.5$  dB.

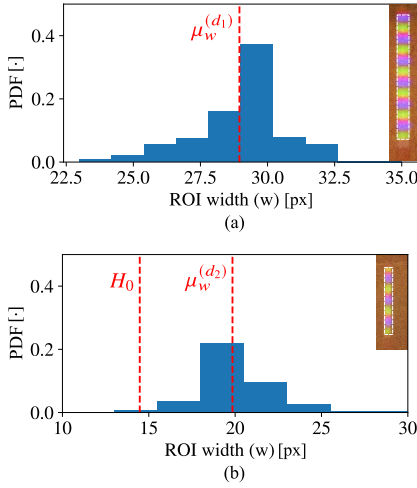


**Fig. 5.** Histograms showing the PDF of ROI width variation due to multiple scattering, where (a) corresponds to the results at distance  $d_1 = 100$  m and (b)  $d_2 = 200$  m. Insets in the graphs are examples of processed images, framing the detected ROI with a white dashed line.

$$0 = (\sigma_b^2 - \sigma_s^2) x_{th}^2 + 2(\mu_b \sigma_s^2 - \mu_s \sigma_b^2) x_{th} + \mu_s^2 \sigma_b^2 - \mu_b^2 \sigma_s^2 + 2\sigma_s^2 \sigma_b^2 \ln \left( \frac{\alpha}{1 - \alpha} \frac{\sigma_s}{\sigma_b} \right). \quad (9)$$

Using the calculated  $x_{th}$ , all of the pixels were classified into background or signal classes. The ROI was estimated as the total number of contiguous samples belonging to the signal class (on the  $x$  axis) with the maximum cardinality. This implies statistical filtering that avoids possible glitches on the classification of the actual background samples. The ROI height was estimated as the number of correctly detected beacons using a template-matching correlator.

As was aforementioned, the PSF would vary by a widening factor as a function of distance. However, in a multiple-scattering-free atmospheric link, the product of the ROI width  $w$  and the link distance is constant. Due to the experiment's nature, Welch's T-Test was performed to prove the expected non-linearity. The T-Test outputs a  $p$  value  $\in (0, 1)$ , which is

closer to zero when the null hypothesis is more likely to be incorrect. Equation (10) describes the null hypothesis (two-tailed test), in which  $\mu_w^{(d)}$  is the average ROI width of the population at distance  $d$ :

$$H_0 : d_1 \cdot \mu_w^{(d_1)} = d_2 \cdot \mu_w^{(d_2)}. \quad (10)$$

The ROI width expansion was assessed only for the green channel (530 nm) without loss of generality. Particle size distributions during sandstorms [26] present modal diameters much larger than 1  $\mu\text{m}$ , which is the upper limit for considering wavelength-dependent scattering effects (Mie or Rayleigh). Moreover, the probability of finding a particle with a diameter below this limit is much smaller than finding large particles. Hence, the ROI width would not significantly vary with respect to wavelength.

Regarding the pixel SNR, Eq. (4) showed its mathematical description. As commented, in order to have a good approximation, the background level (lamp OFF state) must be obtained. The parameter  $\mu_b$  is reused to estimate the level. All of the pixels classified into the signal class during the GMM procedure were used to estimate both signal and noise powers.

Finally, Pearson's correlation coefficient  $r_{xy}$ , which was used as a link quality estimator as in [14], because its value increases with the SNR, is calculated as

$$r_{xy} = \frac{E[XT] - E[X]E[T]}{\sigma_X \sigma_T}, \quad (11)$$

where  $X$  is the received signal or the detected ROI, and  $T$  is a template of the expected waveform contained in the ROI, which is known because the  $T_x$  module in this experiment is set to transmit a repetitive pattern. The coefficients  $\sigma_X$  and  $\sigma_T$  are the standard deviations of the signal and the template, respectively. Note that in this case,  $\sigma_T$  is constant and greater than zero since the template is a series of RGB pulses. The operator  $E[\cdot]$  refers to the expected value.

#### 4. RESULTS AND DISCUSSION

In this section, the outcome of the processes explained in Section 3 are shown and reviewed, including the dust's impact on the ROI width, SNR calculations, and correlator outputs as measures of the signal quality.

In Fig. 5 it can be observed that the ROI is approximately 33% greater than  $H_0$  in clear air, proving the assumption that multiple scattering significantly expands the PSF and ROI consequently. The width expansion can be used for reducing the noise by taking the average value of the ROI pixels in the same row. These advantages are similar to the effect of camera defocusing employed by *Eso et al.* in [4]. According to the OOK modulation scheme employed, the image frames at  $d_1$  contain up to 23 OOK symbols for each channel, while at  $d_2$ , they contain up to 14 symbols instead of 11 symbols of the theoretical clear air conditions. Due to the high resolution of the images and the image sensor's  $t_{rs}$ , a practical camera frame rate would be 15 fps, which is available in most commercial cameras. The achievable data rate of the system is then 1035 bps and 630 bps at 100 m 200 m, respectively. These values confirm the positive impact of the ROI expansion due to multiple scattering because,

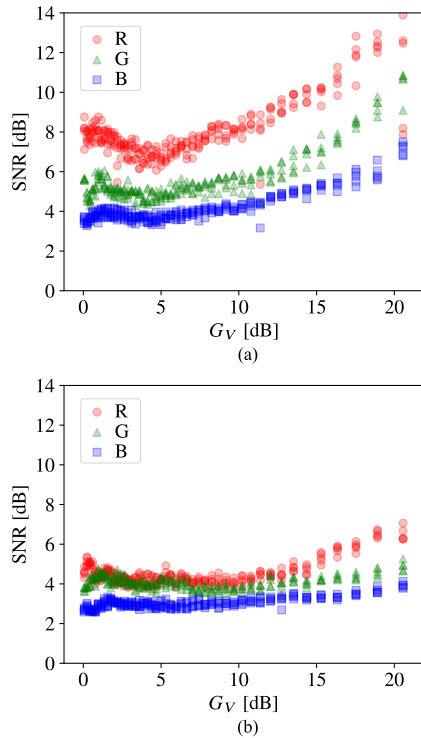


**Fig. 6.** Scatter plots of the RGB channels' SNR versus the camera analog gain ( $G_V$ ), where (a) corresponds to the results at distance  $d_1 = 100$  m and (b)  $d_2 = 200$  m.

at long distances, the apparently larger transmitter surface contains more symbols than in a scatter-free scenario (clear air).

The image frames captured by the camera (at both 100 m and 200 m and using different values of gain allowed by the CMOS sensor) were processed to detect the OOK symbols, from which the SNR for each color channel was then calculated, as shown in the plots of Fig. 6. The channel extinction coefficients were computed from the symbol intensities at both distances using Eq. (2) and assuming  $K_{\text{ext}}(\lambda)$  was constant during the experiments. The resulting extinction coefficients under V of 0.57 km are shown in Table 2. An SNR improvement of up to  $\Delta\text{SNR} \approx 9$  dB at  $d_1$  and 3 dB at  $d_2$  shows that the camera's analog gain positively impacts the SNR. The consequent BER values for each link span, according to Eq. (5), are then  $9.14 \cdot 10^{-5}$  and  $4.1 \cdot 10^{-3}$  for 100 m and 200 m, respectively. The optimal gain in this high optical extinction scenario is the highest allowed by the camera of 20.6 dB. The reason  $G_V$  improves the SNR, in this case, is the high quantization noise due to the low received power, as explained by Eq. (6).

The correlation values obtained by applying Eq. (11) to the image frames and the expected-waveform template are shown in Fig. 7. The correlation is observed to reach a *plateau* at high gains, which is always below 1.0 (perfect correlation). This occurs because SNR is finite, and Pearson's correlation coefficient can be statistically modeled as a ratio distribution between

**Table 2.** Extinction Coefficient Values under Sandstorm Measurements

Channel	$\lambda$ [nm]	$K_{\text{ext}}(\lambda)$ [ $\text{m}^{-1}$ ]
Red	630	$7.2 \cdot 10^{-3}$
Green	530	$6.9 \cdot 10^{-3}$
Blue	475	$5.6 \cdot 10^{-3}$

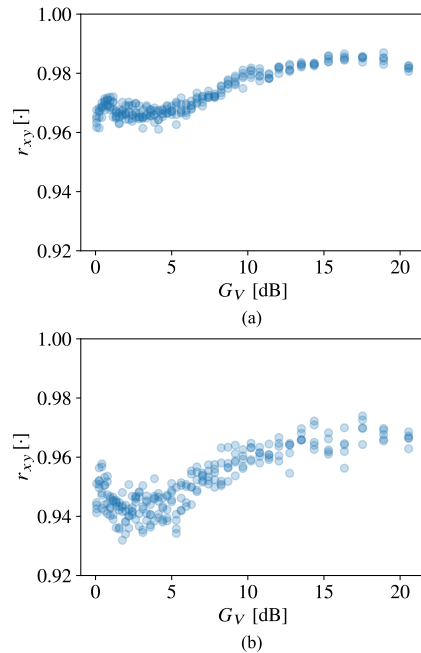


**Fig. 7.** Scatter plots for the correlation ( $r_{xy}$ ) versus the camera analog gain ( $G_V$ ), where (a) corresponds to the results at distance  $d_1 = 100$  m and (b)  $d_2 = 200$  m.

correlated numerator (first-order moment) and denominator (square root of a second-order moment). Furthermore, the resulting high correlation values occur because the template is large (44 pixel rows height), reducing the data variance.

The results presented show that the decoding stage can take advantage of the ROI expansion caused by the scattering and the improved image quality generated by the analog gain.

## 5. CONCLUSIONS

An OCC link using a commercial RS camera module receiver coupled to a telescope and a low-power RGB LED transmitter was experimentally tested, during the sandstorm event that occurred on 23 February 2020, in the Canary Islands archipelago. During this experiment, the  $\text{AOD}_{550}$  reached values between 3.2 and 6.4, while the V dropped to approximately 0.57 km. A comprehensive set of measurements was carried out, comprising image captures varying the camera analog gain at two target distances of 100 m and 200 m. The link in these

conditions can achieve data rates of 1035 bps and 630 bps, respectively.

A channel model was derived for attenuated optical wireless signals in multiple-scattering scenarios. The SNR computation for these types of links was used to assess sandstorms' effect on the evaluated OCC links. It is shown that SNR depends not only on shot noise but also on quantization noise, which can be mitigated by both the optical and camera's analog gain. This occurs because, for severely attenuated optical signals, the effective number of bits in the analog-to-digital conversion are dramatically reduced. When electrically amplifying these signals, the extra noise due to the amplifier's noise figure is compensated by a higher ADC resolution. It was shown that the analog gain of the CMOS sensor improved the SNR under high attenuation conditions, approximately 9 dB in the 100 m experiment and 3 dB in the 200 m experiment.

In order to accurately estimate SNR, a binary classification procedure based on a GMM was performed. This SNR calculation relies on the correct binary classification of ROI signal pixels versus the background. As it was experimentally demonstrated in [14], correlation-based metrics, on top of aiding the detection of ROI, can provide quick estimations about the signal quality. In this work, the same trends apply. It was observed that as the SNR increases, the values of  $r_{xy}$  increase as well. The template-matching correlations obtained in this work are more than 0.92 because of its relatively large dimensions, despite the optical distortions caused by the sandstorm.

It was observed that the GMM procedure, joint to a template-based correlation, is suitable for detecting the ROI and estimating its dimensions. Taking advantage of this method, it was proved that sandstorms might generate ROI expansion due to multiple scattering. Concretely, during these experiments, the ROI was 33% larger than expected. Considering that an RS-OCC system's maximum achievable data rate depends on the projected ROI size, this effect may be positive despite the increased path loss.

A highlighted finding of this work is that the scattering produced by the sandstorm particles allows for expanding the effective area of the source projected in the image sensor. This provides room for allocating more symbols in the ROI than in a scatter-free scenario, thus increasing the achievable data rate.

**Funding.** H2020 Marie Skłodowska-Curie Actions (764461).

**Acknowledgment.** The authors thank Jaime Ticay and Cristo Jurado-Verdu from IDeTIC-ULPGC for the technical support. This project received funding from the European Union's Horizon 2020 research and innovation programme. This project has received funding from the European Union's Horizon 2020 research and innovation programme under the Marie Skłodowska-Curie grant agreement No 764461.

**Disclosures.** The authors declare no conflicts of interest.

## REFERENCES

1. IEEE Standard Association, "IEEE standard for local and metropolitan area networks-part 15.7: short-range wireless optical communication using visible light," 802.15.7-2011 (2011), pp. 1–309.
2. N. Saeed, S. Guo, K.-H. Park, T. Y. Al-Naffouri, and M.-S. Alouini, "Optical camera communications: survey, use cases, challenges, and future trends," *Phys. Commun.* **37**, 100900 (2019).
3. C. Jurado-Verdu, V. Matus, J. Rabadan, V. Guerra, and R. Perez-Jimenez, "Correlation-based receiver for optical camera communications," *Opt. Express* **27**, 19150–19155 (2019).
4. E. Eso, S. Teli, N. B. Hassan, S. Vitek, Z. Ghassemlooy, and S. Zvanovec, "400 m rolling-shutter-based optical camera communications link," *Opt. Lett.* **45**, 1059–1062 (2020).
5. V. Matus, V. Guerra, C. Jurado-Verdu, S. Teli, S. Zvanovec, J. Rabadan, and R. Perez-Jimenez, "Experimental evaluation of an analog gain optimization algorithm in optical camera communications," in *12th International Symposium on Communication Systems, Networks Digital Signal Processing (CSNDSP)* (2020), pp. 1–5.
6. E. Eso, A. Burton, N. B. Hassan, M. M. Abadi, Z. Ghassemlooy, and S. Zvanovec, "Experimental investigation of the effects of fog on optical camera-based VLC for a vehicular environment," in *15th International Conference on Telecommunications (ConTEL)* (IEEE, Graz, Austria, 2019), pp. 1–5.
7. N. Saha, M. S. Iftekhar, N. T. Le, and Y. M. Jang, "Survey on optical camera communications: challenges and opportunities," *IET Optoelectron.* **9**, 172–183 (2015).
8. P. Chavez-Burbano, V. Guerra, J. Rabadan, and R. Perez-Jimenez, "Optical camera communication for smart cities," in *IEEE/CIC International Conference on Communications in China (ICCC Workshops)* (2017), pp. 1–4.
9. M. Karbalayghareh, F. Miramirkhani, H. B. Eldeeb, R. C. Kizilirmak, S. M. Sait, and M. Uysal, "Channel modelling and performance limits of vehicular visible light communication systems," *IEEE Trans. Veh. Technol.* **69**, 6891–6901 (2020).
10. M. A. Khalighi and M. Uysal, "Survey on free space optical communication: a communication theory perspective," *Commun. Surveys Tuts.* **16**, 2231–2258 (2014).
11. J. Horwath, D. D. Gonzalez, L. M. Navajas, A. L. Souto, V. Semerjyan, G. Raju, J. Grabowsky, C. Garcia, Y. Lai, T. Bähr, C.-C. Chen, F. Haque, A. Grier, H. Harding, M. Hunwardsen, E. Booen, and H. Hemmati, "Test results of error-free bidirectional 10 Gbps link for air-to-ground optical communications," *Proc. SPIE* **10524**, 105241F (2018).
12. J. Libich, J. Perez, S. Zvanovec, Z. Ghassemlooy, R. Nebuloni, and C. Capsoni, "Combined effect of turbulence and aerosol on free-space optical links," *Appl. Opt.* **56**, 336–341 (2017).
13. Y. H. Kim, W. A. Cahyadi, and Y. H. Chung, "Experimental demonstration of VLC-based vehicle-to-vehicle communications under fog conditions," *IEEE Photon. J.* **7**, 7905309 (2015).
14. V. Matus, E. Eso, S. R. Teli, R. Perez-Jimenez, and S. Zvanovec, "Experimentally derived feasibility of optical camera communications under turbulence and fog conditions," *Sensors* **20**, 757 (2020).
15. T. Nguyen, A. Islam, and Y. M. Jang, "Region-of-interest signaling vehicular system using optical camera communications," *IEEE Photon. J.* **9**, 7900720 (2017).
16. K. J. Ebrahim and A. Al-Omary, "Sandstorm effect on visible light communication," in *9th IEEE-GCC Conference and Exhibition (GCCCE)* (2017), pp. 1–7.
17. Z. Ghassemlooy, J. Perez, and E. Leitgeb, "On the performance of FSO communications links under sandstorm conditions," in *Proceedings of the 12th International Conference on Telecommunications* (2013), pp. 53–58.
18. H. Henniger and O. Wilfert, "An introduction to free-space optical communications," *Radioengineering* **19**, 203–212 (2010).
19. B. Cochenour, L. Mullen, and J. Muth, "Effect of scattering Albedo on attenuation and polarization of light underwater," *Opt. Lett.* **35**, 2088–2090 (2010).

20. D. Kedar and S. Arnon, "Urban optical wireless communication networks: the main challenges and possible solutions," *IEEE Commun. Mag.* **42**(5), S2–S7 (2004).
21. D. Kedar and S. Arnon, "The positive contribution of fog to the mitigation of pointing errors in optical wireless communication," *Appl. Opt.* **42**, 4946–4954 (2003).
22. H. Le Minh, W. Popoola, and Z. Xu, "Techniques for enhancing the performance of VLC systems," in *Visible Light Communications: Theory and Applications* (2017), pp. 195.
23. M. Carlowicz, "Dust blankets the canary islands," <https://earthobservatory.nasa.gov/images/146337/dust-blankets-the-canary-islands>.
24. Sony Corporation, IMX219PQH5-C, Diagonal 4.60 mm (Type 1/4.0) 8 Mega-Pixel CMOS Image Sensor with Square Pixel for Color Cameras, Datasheet (2014).
25. C. Pérez, K. Hausteijn, O. Jorba, Z. Janjic, N. Huneus, J. Baldasano, T. Black, S. Basart, S. Nickovic, and R. L. Miller, "Atmospheric dust modeling from MESO to global scales with the online NMMB/BSC-dust model—part 1: model description, annual simulations and evaluation," *Atmos. Chem. Phys.* **11**, 13001–13027 (2011).
26. J. Shao and J. Mao, "Dust particle size distributions during spring in Yinchuan, China," *Adv. Meteorol.* **2016**, 1–8 (2015).

### 5.3 Publication 3 (P3)

The last article included in this compendium is entitled “Wireless Sensor Networks Using Sub-Pixel Optical Camera Communications: Advances in Experimental Channel Evaluation” [58]. The application of OCC to WSN is proposed by analyzing the experimental works up to date presented by the authors on the optical wireless channel evaluation. The importance of this topic is that it summarizes the key aspects of modulation schemes, the topology of the network, and utilization of LED and CMOS technologies for establishing multi-point-to-point links with commercially available hardware.


Outdoor OCC links often require large optical devices to work, such as lenses of several hundred mm focal length and transmitter surfaces of around a few m<sup>2</sup>. These requirements pose a limitation to the implementation of VLC systems using existing infrastructures and the simultaneous illumination and communication capabilities, which are some of the key features that have brought these technologies into markets. Likewise, OCC systems exploit existing camera equipment for cost-effective deployment. Nevertheless, the re-utilization of video captures for simultaneous imaging and communication restricts OCC decoding techniques because they rely on large ROI dimensions for improved data and error rates.

This article presents a novel approach to implementing outdoor OCC links using small optical devices, introduced as sub-pixel since the projection of the transmitter falls into the area of a single pixel if the camera is focused according to the linkspan and the atmosphere is clear of aerosols. This approach serves as an alternative to large-optical systems, allowing the re-utilization of the camera images for video monitoring and data decoding simultaneously.

In this paper, a feasible solution for spatially divided transmitters in outdoor conditions is studied under sub-pixel distances. The experiments presented achieved error-free low-datarate communication at distances up to 130 m. Furthermore, although the processing at the receiver is done offline, the image can contain multiple transmitters captured in a single video stream, which demonstrates the feasibility of implementing multipoint-to-point topologies in OCC.

Article

# Wireless Sensor Networks Using Sub-Pixel Optical Camera Communications: Advances in Experimental Channel Evaluation <sup>†</sup>

Vicente Matus <sup>1,\*</sup> , Victor Guerra <sup>1</sup> , Cristo Jurado-Verdu <sup>1</sup> , Stanislav Zvanovec <sup>2</sup>  and Rafael Perez-Jimenez <sup>1</sup> 

<sup>1</sup> Institute for Technological Development and Innovation in Communications (IDeTIC), University of Las Palmas de Gran Canaria, 35001 Las Palmas, Spain; vguerra@idetic.eu (V.G.); cjurado@idetic.eu (C.J.-V.); rperez@idetic.eu (R.P.-J.)

<sup>2</sup> Department of Electromagnetic Field, Faculty of Electrical Engineering, Czech Technical University in Prague, Technicka, 16627 Prague, Czech Republic; xzvanove@fel.cvut.cz

\* Correspondence: vmatus@idetic.eu

<sup>†</sup> This paper is an extended version of our paper published in 3rd West Asian Symposium on Optical and Millimeter-wave Wireless Communications (WASOWC), Tehran, Iran, 24–25 November 2020.

**Abstract:** Optical wireless communications in outdoor scenarios are challenged by uncontrollable atmospheric conditions that impair the channel quality. In this paper, different optical camera communications (OCC) equipment are experimentally studied in the laboratory and the field, and a sub-pixel architecture is raised as a potential solution for outdoor wireless sensor networks (WSN) applications, considering its achievable data throughput, the spatial division of sources, and the ability of cameras to overcome the attenuation caused by different atmospheric conditions such as rain, turbulence and the presence of aerosols. Sub-pixel OCC shows particularly adequate capabilities for some of the WSN applications presented, also in terms of cost-effectiveness and scalability. The novel topology of sub-pixel projection of multiple transmitters over the receiver using small optical devices is presented as a solution using OCC that re-uses camera equipment for communication purposes on top of video-monitoring.

**Keywords:** optical camera communication (OCC); wireless sensor networks (WSNs); channel characterization; farming 4.0; intelligent transportation systems (ITS); visible light communication (VLC)



check for updates

**Citation:** Matus, V.; Guerra, V.; Jurado-Verdu, C.; Zvanovec, S.; Perez-Jimenez, R. Wireless Sensor Networks Using Sub-Pixel Optical Camera Communications: Advances in Experimental Channel Evaluation. *Sensors* **2021**, *21*, 2739. <https://doi.org/10.3390/s21082739>

Academic Editor: David Plets

Received: 18 March 2021

Accepted: 9 April 2021

Published: 13 April 2021

**Publisher's Note:** MDPI stays neutral with regard to jurisdictional claims in published maps and institutional affiliations.



**Copyright:** © 2021 by the authors. Licensee MDPI, Basel, Switzerland. This article is an open access article distributed under the terms and conditions of the Creative Commons Attribution (CC BY) license (<https://creativecommons.org/licenses/by/4.0/>).

## 1. Introduction

Optical camera communications (OCC), the sub-field of visible light communications (VLC) in which receivers ( $R_x$ ) are implemented using image sensors [1], has excellent potential to be part of the evolution of new technologies beyond the fifth generation of cellular networks (5G). The use of cameras represents a low integration cost due to their massive availability in end-user devices such as smartphones, public infrastructure surveillance cameras, and vehicular security dash cameras. Moreover, transmitters ( $T_x$ ) in VLC, in general, are implemented using light-emitting diode (LED) technology, which is widely spread and presents low power consumption and a long lifespan. OCC arises from exploiting the digital cameras, considerably more abundant than individual photodiodes (PDs), but at the same time with limitations on the achievable data rates. For example, PD-based VLC systems exceeding Gbps throughput have been reported [2,3]. In contrast, the frame rate of conventional cameras poses an inherent limitation to OCC's data rate, but the image-forming optics and the ability to visualize different objects within the field-of-view (FOV) can be exploited to increase the throughput [1,4–6].

OCC has been incorporated into the Institute of Electrical and Electronics Engineers (IEEE) 802.15.7r1 standard [7], which shows the interest of the scientific community in its development. The standard contemplates the two fundamental strategies for implementing

these systems, which vary according to the camera's image acquisition technique: global shutter (GS) and rolling shutter (RS) systems. The first mainly use charge-coupled device (CCD) image sensors that simultaneously expose all their pixels when acquiring a new image. On the other hand, RS systems are mainly based on complementary metal-oxide-semiconductor (CMOS) technology and scan the image sequentially line by line of pixels, with a fixed overlap [8]. Although CCD sensors are built using a GS structure, it is important to note that the image acquisition mechanism is not strictly related to the sensor's manufacturing technology, and CMOS hardware can be built using RS or GS strategies in the readout circuitry. Moreover, OCC systems employing RS hardware can perform GS techniques for the post-processing of the image and the demodulation of data, as shown in this work.

In indoor scenarios (offices, homes, and medical or industrial facilities), VLC systems can already provide high-speed Internet, taking advantage of the short distances and the moderate presence of interfering sources. If the use of cameras is considered, one of the most prominent applications of indoor OCC is in the field of visible light positioning (VLP), which combines data transmission and image processing to recognize the geometry of the environment and monitor interactions between mobile nodes [9–11]. Other applications of interest have been proposed for OCC, such as wireless patient monitoring in hospitals, where the use of radiofrequency (RF) signals may interfere with the proper performance of the instrumentation and the RF spectrum is more limited than in other kinds of facilities; and peer-to-peer (P2P) data exchange using optical beacons as an alternative to near-field communications [4].

When considering the use of surveillance cameras in outdoor scenarios for Smart Cities applications and sensor networking, the presence of uncontrollable adverse atmospheric phenomena such as heat-induced turbulence, the presence of small particles in suspension (aerosols, water vapor, pollutants, dust), and rain and snow precipitation, must be taken into account. These phenomena cause light to be absorbed and dispersed, producing both attenuation and time dispersion of the signal in the link's direction, increasing the communication error rate. Different solutions have been proposed to cope with the challenging conditions; these can be divided into ones that alter the camera's optics and others that effectively adjust the image sensor's internal parameters.

However, in all these works mentioned above, it is assumed that the projected area of the light source in the image affects a high number of pixels, as shown in Figure 1. In this case, the lamp's geometric projection occupies a significant portion of the image [12,13]. This previous consideration has a final impact on the maximum distance of the link, making it necessary either to use luminous surfaces with an extensive area or to use telescopic lenses, which reduce the FOV, as mentioned before. Nonetheless, these approaches make it impossible to exploit the cameras as video and communication devices simultaneously. In contrast, the use of smaller and more numerous transmitters can be exploited in OCC for transmitting multiple data streams to the same receiver. This technique of spatial division has been proposed for intelligent transportation systems (ITS) [4] but is challenged by the need for computer vision algorithms capable of discovering the sources within the image during motion and determining the region of interest (ROI), i.e., the pixels that contain data. Figure 2 shows how multiple sources can potentially convey information to an OCC  $R_x$  on a car.

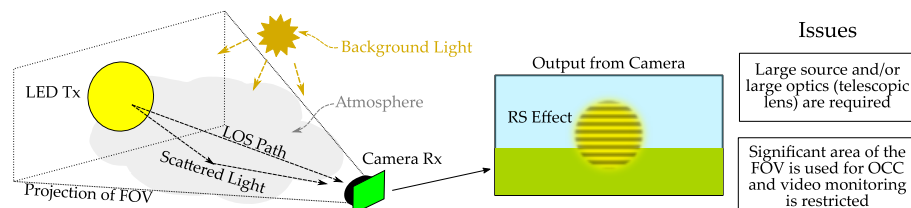


**Figure 1.** Diagram of the implementation of optical camera communication (OCC) using rolling shutter (RS) techniques in outdoor scenarios and the inherent issues associated with field-of-view (FOV) use in long distance setups.



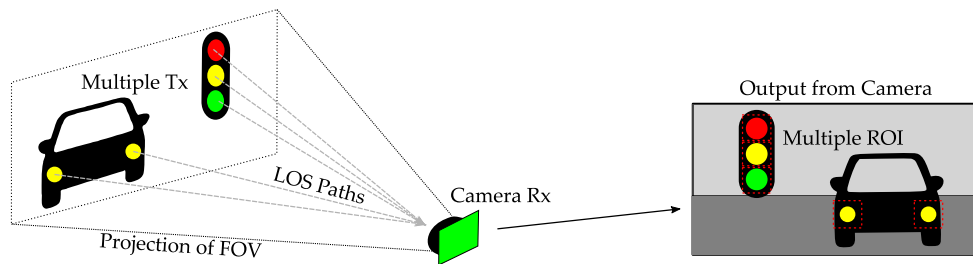


**Figure 2.** Vehicular visible light communication using OCC is an example of segregation of spatially divided data inputs that is feasible by virtue of the image-forming nature of cameras.

This work extends from our previous conference paper in [14]. An OCC link under emulated fog conditions in a laboratory chamber was studied to evaluate the effects of the impairment of visibility over the process of correlation-based signal detection. The OCC camera's output image sequences were offline processed to detect the ROI and how its dimensions varied according to the different levels of meteorological visibility produced by the presence of fog. It was shown that the correlation process was considerably affected by values under 40 m of visibility. The ROI dimensions presented a negligible change in these conditions.

Further experimentation has been carried out, including the effects of heat-induced turbulence and exploiting the camera's analog gain in [15,16]. Real conditions of a sand-storm were experimentally studied in [17]. In this work, the previous experiments are compared and analyzed. Further theoretical analysis of the channel and the detection using correlation-based processing for ROI detection is shown in this paper.

This work's main contribution is to demonstrate the feasibility of outdoor OCC links, in which communication happens from using not just large optical devices but also to employing small optical devices in long distances, falling into the sub-pixel level. The term sub-pixel refers to the fact that the source's projection area is smaller than the area of one pixel, and it should not be confused with the color-sensitive components of an image sensor pixel, also called subpixels [18]. In a preliminary discussion, it could be assumed that the link is not viable because the light emitted only impinges partly one pixel. However, this work shows that the energy emitted by the LED affects the adjacent pixels for reasons ranging from the scattering in the atmosphere, and the optical focus, so that the signal can be successfully recovered by considering a larger number of pixels. This paper provides a comprehensive compilation of the authors' highlighted findings in evaluating experimental outdoor OCC. It proposes the sub-pixel approach, discussing the viability of OCC's real outdoor applications in the IoT and WSN fields. The OCC devices presented in this paper have been implemented using off-the-shelf components, and their designs are available for replication.

This paper is structured as follows. Section 2 summarizes the scientific contributions towards implementing optical IoT and WSN using outdoor OCC systems. In Section 3, a proposal of an architecture of OCC-based sensor networks is developed, according to the WSN key requirements and OCC capabilities. Section 4 outlines the methodology and results of the experimental evaluations done and the implications of the results obtained. Conclusions and future lines are addressed in Section 5.

## 2. Related Works

In this section, the applications and challenges of OCC and related systems are summarized, focusing on the fact that most OWC technologies, including PD-based and camera-based VLC systems, have been proposed for outdoor Smart Cities, and WSN applications [1,2,19], although some important indoor applications are mentioned as well. Specifically, regarding the implementation of sub-pixel systems for WSN as proposed in this paper, the authors are not aware of other works where an equivalent functionality is

reported. It is worth noting that the sub-pixel scenario can be considered to be a VLC system based on individual PDs since camera pixels are based on such devices [18]. However, as will be seen in the following sections, the camera optics and light scattering provide an opportunity to enhance communication using the other contiguous pixels of the camera.

### 2.1. Spatial Division of Transmitters

Some of OCC's advantages over single PD-based systems come from the image-forming nature of cameras that allow the spatial separation of the light sources as in [20–22]. This technique can substantially improve the data rates achievable by OCC systems if there is the possibility to extend the number of transmitters in space, as in the deployment of sensors.

One of the interesting applications that takes advantage of the spatial division is VLP [10,11,23,24]. These systems take advantage of the high precision achievable, of the order of tens of centimeters, compared to satellite positioning systems that can be tens of meters. VLP systems are robust in enclosed spaces and have been explored in outdoor vehicular settings [25] where more precision than provided by satellite localization means is needed. Furthermore, positioning systems relate to another important application, intelligent transportation systems (ITS), which has been proposed as an application of VLC [23,26–28]. ITS aim to improve road safety and the communication between vehicles and infrastructures. As mentioned before, vehicular VLC systems can exploit the spatial division of sources in OCC. This application has the potential to improve the performance of autonomous vehicles, an important sub-field of ITS where the use of machine learning techniques exploiting different sources of sensor data are used for lateral and longitudinal motion control of passenger cars [29]. Although many kinds of sensors are being studied, camera equipment is considered fundamental for capturing information from the environment in most approaches. In [25], computer vision and OCC techniques are combined to determine the position of a vehicle with errors below 20 cm.

OCC's main limitations can be grouped in three categories: those related to the image-forming capability, where the distortions caused by the optics are a source of interference and noise, especially relevant in screen-to-camera communications [30]; issues related to the timing of capturing and the synchronization with transmission [12,13], in which the slight variations of the camera frame along with the gaps between frame acquisitions induce errors in data decodification; and the important challenges related to the discovery of nodes and their tracking in motion [31], where the time elapsed by computer vision algorithms in the detection of the ROI can have a considerable impact on the latency.

### 2.2. Atmospheric Phenomena in Optical Wireless Communication

Outdoor scenarios, where the weather and other atmospheric phenomena play an important role in the propagation of optical signals [32], have been experimentally investigated in the OWC field and recently in VLC, as summarized in [33]. In [34], an outdoor link of approximately 400 m was experimentally validated, which exploited defocusing the camera, allowing the surface of the LED to be extended and the transfer rate to be increased to 450 bps (bits per second). In the experiments of [26,35], other examples show how the channel's effect is compensated by modifying the optical parameters, specifically by using magnification lenses. The first work focused on an application for a vehicular environment based on PDs instead of cameras, achieving a link distance of 40 m in ideal weather conditions. In [35], a GS camera was used to establish a link with a luminous sign located at a distance of 328 m with an effective transmission rate of 15 bps with a 4% error. Finally, Ref. [8] shows the use of a Fresnel lens for establishing a VLC vehicular link in a laboratory emulated environment is demonstrated. Nonetheless, these approaches are impractical if it is considered that the FOV of the receiver optics is drastically reduced. As a solution for maintaining the camera's original FOV, in previous works [15,16] it is demonstrated that the signal attenuation produced by turbulence and fog phenomena can

be overcome by increasing the analog gain of the image sensor without the need to alter the camera optics.

### 3. Proposal of Optical Camera Communication-Based Sensor Networks Architecture

In this section, the basic architecture of a WSN based on OCC is proposed. First, the wireless channel is derived for the case of the novel sub-pixel transmitter projection scheme, considering the outdoor scenario, where the presence of particles in the air causes both the absorption and scattering of light. A discussion of heat-induced turbulence models found in the literature is done further in this section, and it is finished by summarizing the technical requirements and potential applications of the OCC-based WSN proposed.

#### 3.1. Optical Wireless Channel

As in any OWC system, the power received in an OCC system can be modeled using the solid angle differential approach (Equation (1)) [36]. Since this work focuses on outdoor links, an extinction loss term  $K_{ext}(\lambda)$  has been added to the medium (absorption and scattering) which depends on the wavelength  $\lambda$  [37–39]:

$$P_{rx} = P_{tx}R(\theta, \varphi) \frac{A_{lens}}{d^2} \cos(\Psi)e^{-K_{ext}(\lambda)d} \tag{1}$$

where  $P_{rx}$  is the received power,  $P_{tx}$  the transmitted power and  $R(\theta, \varphi)$  is the radiation pattern of the source (assumed constant over its entire area) for the elevation  $\theta$  and azimuth  $\varphi$  angles. The received power depends on the area of the main lens  $A_{lens}$  projected over the angle of incidence  $\Psi$  and the link distance  $d$ .

Nevertheless, since cameras are used as optical receivers, image-forming optics must be considered in this type of system. In general, terms and disregarding any blurring effect, a priori, OCC systems have been based on conserving pixel energy density with distance, i.e., the energy of each pixel has no direct dependence on  $d$ , as long as the optical emitter’s projection is greater than a single pixel, as derived in [40]:

$$H_p(0) = \frac{A_{px}^2 A_{lens}}{f^2 A_{tx}} R(\theta, \varphi), \tag{2}$$

where  $f$  is the focal length of the lens of the camera, and  $A_{px}$  and  $A_{tx}$  are the area of a pixel of the image sensor and the transmitter LED, respectively. The concept behind this property is the compensation of spherical propagation losses with the focus of the image. Although less energy reaches the camera’s main optics as the distance increases (quadratic decrease), the number of pixels on which the emitter is projected also decreases in the same order, compensating for the effects and keeping the surface energy density constant on the image sensor.

For long distances, it is easy to demonstrate that the number of pixels  $N_{px}$  on which an emitter with area  $A_{tx}$  is projected depends on the camera’s FOV and image sensor resolution as:

$$N_{px} = \frac{NM}{FOV_n FOV_m} \frac{A_{tx}}{d^2}, \tag{3}$$

where  $N$  and  $M$  define the horizontal and vertical resolution of the sensor, respectively, and  $FOV_n$  and  $FOV_m$  define the horizontal and vertical fields of vision of the receiver, respectively. By joining Equations (1) and (3), and projecting the energy over the area of a pixel, Equation (4) is obtained, which summarizes the average energy of a pixel:

$$P_{px} = P_{tx}R(\theta, \varphi) \frac{A_{lens}}{A_{tx}} \cos(\Psi)e^{-K_{ext}(\lambda)d} \zeta_{xy} A_{px}, \tag{4}$$

where for convenience, the angular resolution of the sensor  $\zeta_{xy}$  represents the ratio of its FOV to the sensor resolution. However, when the emitter’s projection decreases below a single pixel, the above equation is no longer valid and the system can start to be modeled as

a PD-based OWC link, where the received power is directly proportional to the photodiode area illuminated by the projection (this projection is less than  $A_{px}$  and no image can be formed). The power received in a sub-pixel situation ( $P_{subpx}$ ) is given by:

$$P_{subpx} = P_{px} \times N_{px} = P_{rx} \times A_{px}. \quad (5)$$

It must be understood that  $N_{px}$  (the number of pixels of the transmitter's projection) in the equation above acts as a coefficient of adjustment referred to the percentage of illuminated pixels. It is clear that  $P_{subpx}$  loses its independence from distance and starts behaving as in case of a traditional OWC link. Once the arrival power to the sensor is specified, the conversion process must be taken into account when describing the OCC signal within the captured image. CMOS cameras work by converting the incident photons into electrons, storing them and encoding them sequentially row by row [18]. Therefore, it is convenient to carry out a unit conversion that takes into account this particularity. The number of stored electrons ( $E_{px}$ ) during the exposure time of the capture  $T_{exp}$  (valid for any situation) is obtained by [41]:

$$E_{px} = T_{exp} \int_{\lambda} P_{px}(\lambda) EQE(\lambda) \frac{E_{ph}(\lambda)}{q} d\lambda \quad (6)$$

Please note that the concept of pixel arrival power has been extended to include the emission spectrum of the optical source.  $EQE(\lambda)$  is the external quantum efficiency of the receiver substrate (usually silicon),  $E_{ph}(\lambda)$  is the energy of the photon at each wavelength, and  $q$  is the charge of the electron. Although theoretically, a small emitter located at a long distance will appear as a single bright spot in the capture, the image-forming optics are not perfect, and there is some spatial dispersion of the energy. This dispersion is modeled by the point spread function (PSF) of the system, denoted as  $h[n, m]$  already in the image domain, where  $n$  denotes the horizontal coordinate, and  $m$  the vertical coordinate. In essence,  $h[n, m]$  is the system's spatial impulse response and is usually dependent on the distance of the link. Any projection must be convoluted with it, so in a sub-pixel situation, the illuminated region can be modeled as:

$$s[n, m] = G_V \mathfrak{K}(E_{px}) \times h[n - n_0, m - m_0] \quad (7)$$

where  $\mathfrak{K}(\times)$  is a function that includes analog-to-digital conversion,  $G_V$  is the analog gain of the CMOS camera's reading circuitry and  $n_0$  and  $m_0$  are the coordinates of the pixels where the emitter is projected. It must be noted that in an ideal situation  $h[n, m]$  has unit energy, so if there is energy dispersion, the theoretical pixel level of the projection will be lower than expected.

Regarding the signal-to-noise ratio (SNR) of an OCC link, Equation (8) summarizes it, being applicable to both sub-pixel and generally studied situations, as:

$$SNR = \frac{G_V^2 E_{px}^2}{G_V^2 (\sigma_{sh}^2 + \sigma_{th}^2) + \sigma_{adc}^2}. \quad (8)$$

It has been assumed that the correction factor  $\gamma$  [18] of the camera is unitary for simplicity and without loss of generality, as well as that the link is not saturated (number of stored electrons less than the full-well capacity of the circuitry). The three main contributions to the noise of the OCC link are shot noise ( $\sigma_{sh}^2$ ), thermal noise ( $\sigma_{th}^2$ ) and quantization noise ( $\sigma_{adc}^2$ ). The effect of the latter can be minimized by applying the optimal analog gain value, as demonstrated in [15]. Among the noises of shot nature, the most significant contributions are the dark noise, the shot noise of the generated signal itself, and the readout noise. In outdoor links there is another phenomenon that can have a substantial impact on system performance. The background level can vary, at least in a sub-pixel situation where the speed is determined by the camera's capture rate, comparable to the transmission time of a frame. This effect will be analyzed experimentally in Section 4.

As derived in [15,42,43], turbulence is a consequence of the heterogeneous values of temperature and pressure in the atmosphere. The refractive index of the air changes randomly over time and space, affecting the amplitude and phase of optical signals [36]. The refractive-index structure parameter ( $C_n^2$ ) (in  $m^{-2/3}$ ), is used to characterize the strength of optical turbulence. It typically ranges from  $10^{-17} m^{-2/3}$  or less for weak turbulence, and above  $10^{-13} m^{-2/3}$  for strong turbulence. It is given by [43–45]:

$$C_n^2 = \left(79 \times 10^{-6} \frac{P}{T^2}\right)^2 \times C_T^2, \tag{9}$$

where  $P$  and  $T$  are the average values of the air’s pressure in millibar and temperature in Kelvin, respectively.  $C_T^2$  is the temperature structure parameter, which can be calculated by measuring the temperature of two or more points in the space separated by a distance  $R$ . It is derived from the random processes’ general definition of the structure function  $D_T$ , given by [45]:

$$D_T = \langle (T_1 - T_2)^2 \rangle = \begin{cases} C_T^2 \times l_0^{-4/3} \times R^2 & 0 \ll R \ll l_0 \\ C_T^2 \times R^{2/3} & l_0 \ll R \ll L_0 \end{cases} \tag{10}$$

where  $|T_1 - T_2|$  is the temperature difference between two points, and  $l_0$  is the minimum air heterogeneity characterized by Kolmogorov’s theory of turbulence [45], whereas  $L_0$  is the maximum.

3.2. Technical Requirements and Potential Applications of OCC-Based Wireless Sensor Networks

As mentioned before, OCC has many potential applications in different scenarios. This technology is cost-effective and allows simultaneous communication with a significant number of remote nodes, providing dedicated time-frequency channels to each of them thanks to optical cameras’ inherent spatial division multiplexing capabilities. A general-purpose scheme of an OCC-based WSN has been defined and it is depicted in Figure 3. This baseline description includes simple low power receiver-less remote nodes, the deployment scenario, the camera-based gateway, and a cloud-based endpoint. Depending on the use case characteristics, the sensors’ information may be extracted on-the-edge by processing the captured frames in situ (at the camera side) or processing them in the cloud endpoint after streaming the captured video signal. Some remarkable application fields have been identified and are discussed in the following subsections.

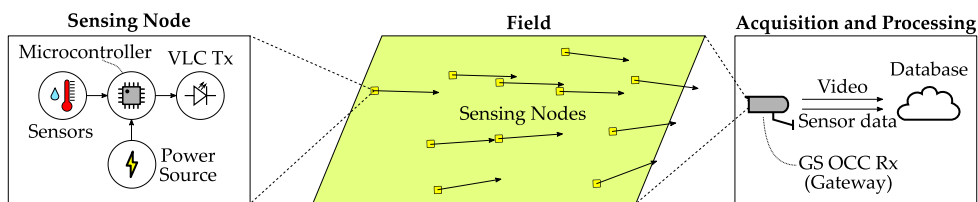


Figure 3. Proposal of the OCC equipment for Wireless Sensor Networks.

IoT technology is beginning to impact the agriculture industry, providing unforeseen capabilities that comprise, among others, local or remote data acquisition, communication between critical agents, and cloud-based intelligent decision making. These capabilities are expected to improve not only the yields but also optimize essential resources such as land and water and even help the workforce. According to [46], the main applications of Smart Agriculture are the monitoring of water, soil, bugs, crop health, machinery, and the environment. These applications rely on several services such as irrigation, fertilization, or soil preparation, which ultimately make intensive use of sensors that have particular connectivity demands.

Communication in Farm Area Networks (FANs) is being carried out using the available cellular infrastructures, IEEE 802.15.4-based technologies such as Bluetooth or Zigbee, LoRa, or Sigfox. Regarding the use of 2G-4G technology, the availability of these deployments is a primary concern in rural areas, and the use of Low Power Wide Area Network (LPWAN) technologies such as LoRa [47], or Sigfox [48] are mainly being adopted in the industry. This communications layer is usually the lowest level of a four-layer architecture, including Medium Access Layer (MAC), Network Layer, and Transport Layer. Notwithstanding, following the proposed scheme of Figure 3, an OCC-enabled FAN using sub-pixel links would need only a physical layer implementation in the first mile, while the camera would act as a data-aggregating agent which could have traditional interfaces such as the mentioned ones. The advantages of integrating OCC in this use case are the unlicensed spectrum, the potential capability of simultaneously monitoring hundreds of devices without MAC protocol, and the simplicity of the node design.

#### 4. Experimental Evaluation

In this section, the experimentation using different OCC equipment is detailed by describing their key parameters and modulation scheme and presenting the experimental setups and the results obtained in various realistic scenarios.

##### 4.1. Physical Layer Strategies

The transmitters and receivers developed for the experiments shown in this section consist of LED modules and CMOS cameras with different optics, respectively. They can be separated into two categories of small and large optical devices. The small devices consist of discrete off-the-shelf components, and the large devices have been developed for an extended vertical dimension (for the case of  $T_x$ ) and for a longer focal distance (for the case of  $R_x$ ). The large transmitters have also been implemented using multi-channel red-green-blue (RGB) LEDs, for exploiting more parallel data streams, with a higher power consumption in consequence. Figure 4 shows the implementation of these devices, while Table 1 shows their key parameters.

**Table 1.** Description of the  $T_x$  and  $R_x$  key features.

Feature	Description
<b>RGB LED Large Transmitter</b>	
Device	12 V DC RGB LED strips (108 × 5050 SMD chips)
Front-end device	Microcontroller Atmel ATmega328p [49]
<b>Single LED Small Transmitter</b>	
Device	3.7 V DC White LED 5 mm
Front-end device	Microcontroller Atmel ATmega328p [49]
<b>CMOS Camera Receiver</b>	
Camera	Picamera V2 module (Sony IMX219 [50])
Max resolution	3280 × 2464 px
Gain ( $G_V$ ) max. value	16 dB
Frame rate	30 fps

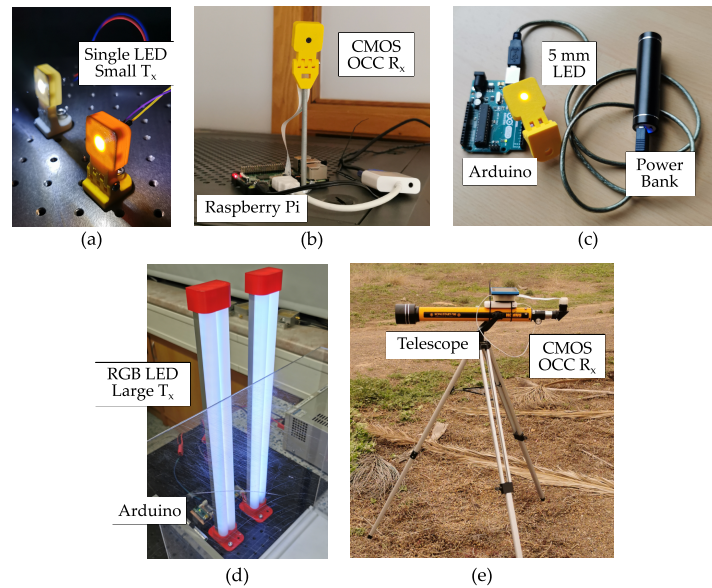


**Figure 4.** Hardware and equipment developed for the OCC experiments. (a) Single LED small transmitters. (b) CMOS camera-based OCC receiver. (c) Standalone implementation of the single LED small transmitters. (d) RGB LED large transmitters. (e) Large optics (telescope) CMOS-based receiver.

The modulation scheme used by the transmitters is on-off keying (OOK), and takes advantage of the switching outputs available in most microcontrollers and only requires the use of a transistor for driving high power LEDs without complex front-end devices. In the case of low power LEDs, the switching output can usually directly drive the LED. The packet structure proposed for GS detection is depicted in Figure 5, with a symbol rate of 7.5 baud for cameras using 30 fps frame rate. In the case of RS detection, much higher symbol rates can be employed, proportional to the row-shift time, as described in [13]. The RS experiment used a symbol rate of  $8.4 \times 10^3$  baud, and exploited the color channels of the camera, with three parallel data streams using RGB LEDs.

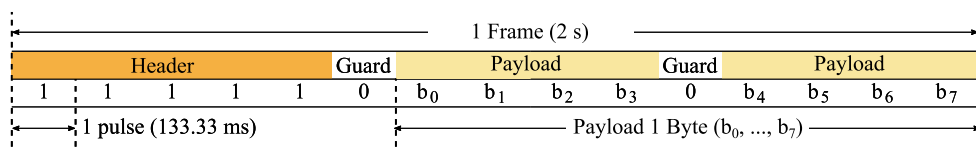


**Figure 5.** Frame format used by both of the  $T_x$  devices of the sub-pixel experiment, assuming a global shutter demodulation at the  $R_x$ .

#### 4.2. Description of the Experiments

The experiments carried out range from laboratory setups emulating outdoor scenarios [14–16] to real outdoor scenarios with different conditions [17], as summarized in Table 2 and described in the following sections. The OCC equipment was developed using off-the-shelf components, such as arrays of RGB LEDs in strip format and standard resin-encapsulated 5 mm white LED for the transmitters, and a RS CMOS camera with a built-in microlens. In the case of [17], the camera was attached to a telescope for covering distances up to 200 m.

**Table 2.** Summary of the experiments carried out, with their key contributions on methodology and results.

Experiment	Design	Processes	Metrics	Highlighted Findings
Exp. 1.1 [16]	Attenuation emulated in laboratory. 0.46 m link.	Rolling Shutter, Gain control algorithm.	Pearson's Corr. Coef.	Automated gain optimization.
Exp. 1.2 [14,15]	Fog and turbulence emulation in chamber, 4.68 m link.	Rolling Shutter, RGB cross-talk compensation, ROI detection.	SNR, Pearson's Corr. Coef.	Influence of camera gain.
Exp. 2 [17]	Sandstorm real outdoor scenario. 100 m, 200 m link.	Rolling Shutter, Large optical zoom, Tilt compensation, Gaussian Mixture Model, ROI detection.	SNR, BER.	ROI expansion due to scattering.
Exp. 3	Sub-pixel real outdoor scenario. 90 m, 130 m link.	GS detection with RS hardware, Small optical devices.	SNR, BER, PSF.	Re-use, PSF enhance, Scalability.

#### 4.2.1. Emulation of Atmospheric Conditions in Laboratory

These experiments, labeled as 1.1 and 1.2 in Table 2, consisted of testing the large transmitters and the CMOS  $R_x$  in laboratory settings emulating two important atmospheric conditions: fog and turbulence. First, in Experiment 1.1, only attenuation of the signal was emulated using a white methacrylate sheet in different configurations. The different optical powers received by the camera were captured changing its analog gain, and a control algorithm was derived in [16] to automatically set the gain by using the Pearson's correlation coefficient ( $r_{x,y}$ ) as an estimator of the image quality, alternative to the SNR. This coefficient is defined as:

$$r_{xy} = \frac{\sum_{i=1}^N (x_i - \bar{x})(y_i - \bar{y})}{\sqrt{\sum_{i=1}^N (x_i - \bar{x})^2} \sqrt{\sum_{i=1}^N (y_i - \bar{y})^2}}, \quad (11)$$

where  $x_i$  are reference of  $N$  samples of an expected signal or template (a header of a packet, for example),  $y_i$  are  $N$  consecutive samples of the input signal, and  $\bar{x}, \bar{y}$  are their mean values.

In the Experiment 1.2 (See Table 2), the CMOS  $R_x$  and large  $T_x$  (See Table 1) were tested using the laboratory chamber at the facilities of the Czech Technical University in Prague. Conditions of fog and turbulence were generated using a glycerin machine and two heater-blowers, respectively. The features of the chamber are listed in Table 3. The level of fog was studied by means of the meteorological visibility (V) [51] measured by a laser source-power meter couple aligned across the chamber, parallel to the OCC link, and the turbulence level was estimated by the well-known refractive-index structure parameter, as derived in [42], using an array of 20 temperature sensors set up equidistantly across the chamber. The diagram of the setup is shown in Figure 6.

**Table 3.** Laboratory chamber parameters and equipment.

Feature	Description
Dimensions	4.9 m (length), 0.4 m (width), 0.4 m (height)
Temperature sensors	20 × Papouch Corp. TQS3-E (precision 0.1 °C)
LASER source	Thorlabs HLS635 (635 nm) F810APC
Optical power meter	Thorlabs PM100D S120C
Heat blowers	2 × Sencor SFH7010, 2000 W
Fog machine	Antari F-80Z, 700 W



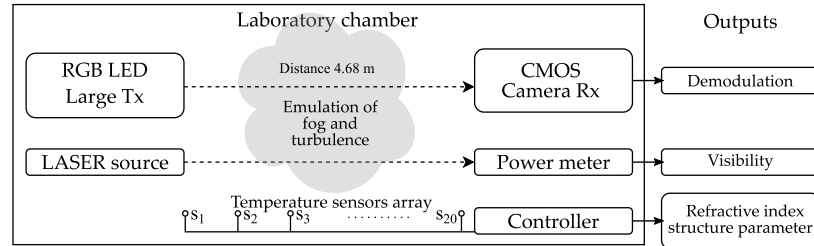


Figure 6. Diagram of the laboratory chamber employed for emulation of atmospheric conditions.

From the experimentation under heat-induced turbulence of values of  $4.69 \times 10^{-11} \text{ m}^{-2/3} \leq C_n^2 \leq 7.13 \times 10^{-11} \text{ m}^{-2/3}$ , these conditions showed negligible influence over the OCC system performance. Contrarily, under fog conditions, the OCC system showed susceptibility to being affected by the attenuation caused by the aerosol generated by the glycerin machine. In [14] it was shown that the meteorological visibility under 40 m would make  $r_{xy}$  to drop, as shown in Figure 7a. The combined effect of the low values of visibility and the low values of camera exposure cause the ADC input to be considerably low. In [15], the same visibilities were analyzed varying the camera’s analog gain, and it was shown that  $G_V$  could overcome this issue without the need for large optics in the range of 4.68 m link distance and visibility under 40 m, which could be compared to dense fog weather. It was seen that for better visibilities, above 50 m, the gain can also cause saturation of the ADC, inducing noise. Then, between 40 and 50 m of visibility, the gain control algorithm mentioned before could use a fuzzy or adaptive threshold from which the analog gain would take high or low values, as depicted in Figure 7b.

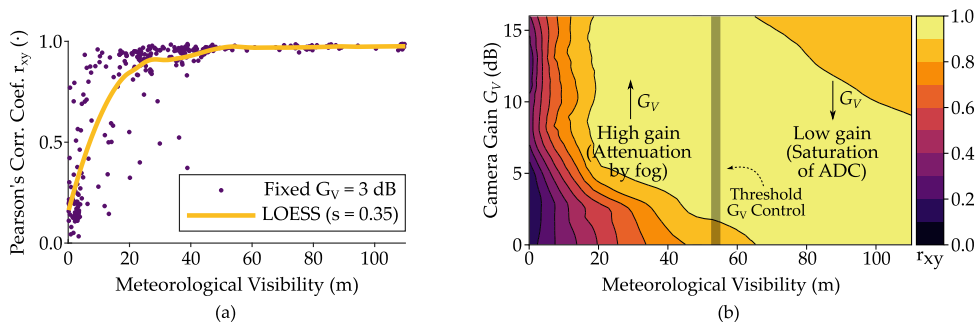
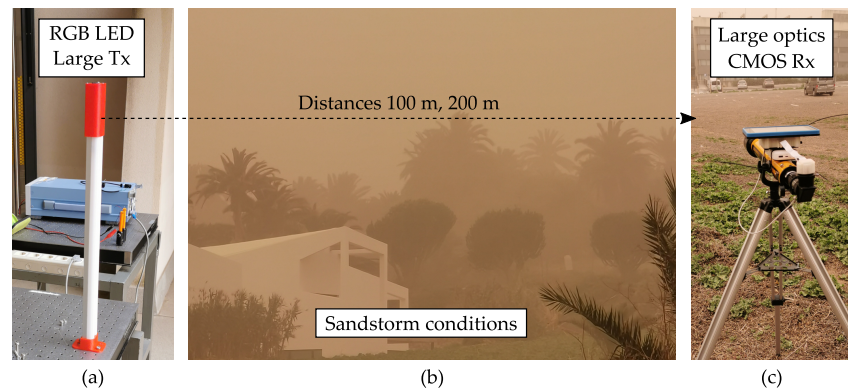


Figure 7. Results using the Pearson’s correlation coefficient between reference signal and images taken in Experiment 1.2 under different visibility conditions. (a) Scatterplot of the  $r_{xy}$  values obtained using fixed gain of 3 dB. The red line is the non-parametric locally estimated scatterplot smoothing (LOESS) of span = 0.35 [52]. (b) Contour plot LOESS of span = 0.15 of  $r_{xy}$  values changing the camera gain. The shaded vertical line corresponds to a fuzzy threshold determined by the analog gain control algorithm.

#### 4.2.2. Real Conditions of Sandstorm Using Large Optical Devices

In the previous work, [17], Experiment 2 (See Table 2), a transmission using the large RGB LED transmitter, and the CMOS receiver attached to a 700 mm Galilean telescope was performed at distances of 100 m and 200 m during a sandstorm event in the nearby area of the IDeTIC facilities, as shown in Figure 8. The large optics used ensure a considerable area of projection over the image sensor, allowing use of RS decoding. A Gaussian Mixture Model (GMM) was used to for the accurate segregation of background and signal. It was observed that the ROI expanded in the presence of aerosols due to scattering, allowing the decoding of around 30% more lines involved in the RS detection, compared to clear conditions.



**Figure 8.** Photographs of the Experiment 3 setup under sandstorm conditions [17]. (a) Transmitter side using large RGB LED. (b) Surroundings of the experiment affected by the sand particles. (c) Receiver side using the CMOS camera attached to a telescope.

The visibility during the experiment was estimated to be about 0.57 km. The estimated  $K_{ext}(\lambda)$  values for the RGB channels studied are shown in Table 4. In this high optical extinction scenario, the camera gain has a favorable effect on the SNR, improving it by up to  $\Delta SNR \approx 9$  dB at 100 m and 3 dB at 200 m. The obtained BER values for each link span are  $9.14 \times 10^{-5}$  and  $4.1 \times 10^{-3}$  for 100 m and 200 m, respectively.

**Table 4.** Extinction coefficient values under sandstorm measurements.

Channel	$\lambda$ [nm]	$K_{ext}(\lambda)$ [ $\text{m}^{-1}$ ]
Red	630	$7.2 \times 10^{-3}$
Green	530	$6.9 \times 10^{-3}$
Blue	475	$5.6 \times 10^{-3}$

#### 4.2.3. Real Outdoor Scenario in Sub-Pixel Setting

In the sub-pixel conditions of Experiment 3 (See Table 2), the small LED transmitters' projection is less than a single camera pixel. When using image-forming optics, the emitters' physical size is a critical aspect in establishing the links. However, at long distances, the use of emitters that are projected onto several pixels perceptible by the human eye is unfeasible since this magnitude increases quadratically with distance.

Two nodes were programmed to send OOK signals in loop transmission frames with the structure shown in Figure 5 containing 1 Byte of payload in which the values from 0x00 to 0xFF were transmitted sequentially. The bit time defined for the experiments was 133.33 ms, offering a bit rate of 4 bps. Both units were anchored to two posts located at  $d_1 = 90$  m and  $d_2 = 130$  m away from the camera respectively, as shown in Figure 9. Once the nodes were activated and started transmitting data, a 10-min video was recorded using 85  $\mu\text{s}$  of exposure time, a minimum analog gain and no digital gain. The camera's capture rate was set to 30 frames per second, so each transmitted bit was spread over 4 frames. Once the video was captured showing the emissions of both nodes simultaneously, the regions of interest of both transmitters were defined manually, since the elaboration of a discovery procedure was not the objective of this work. Both regions of interest were statistically analyzed to obtain signal-to-noise ratio (SNR) and PSF estimates.

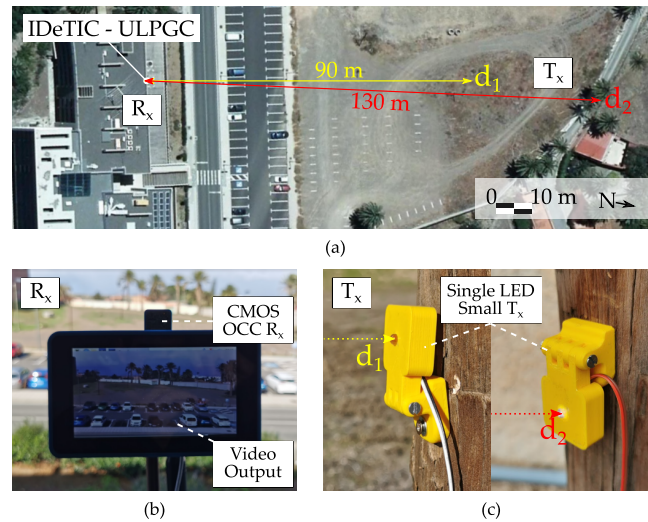


**Figure 9.** Photographs of the communication devices deployed for the sub-pixel experiments at the facilities of IDeTIC. (a) Satellite image from Cartográfica de Canarias (Grafcan) [53]. (b) CMOS camera receiver. (c) single LED small transmitter.

To carry out the SNR analysis, a 150-sample sliding window was processed in which a Gaussian Mixture Model (GMM) was set as:

$$G_2(x) = \frac{\alpha}{\sigma_0\sqrt{2\pi}} e^{-\frac{(x-\mu_0)^2}{2\sigma_0^2}} + \frac{1-\alpha}{\sigma_1\sqrt{2\pi}} e^{-\frac{(x-\mu_1)^2}{2\sigma_1^2}} \tag{12}$$

where  $G_2(x)$  is a Gaussian mixture,  $\alpha$  is the ratio of the first Gaussian,  $\mu_i$  denotes the expected value and  $\sigma_i$  is the standard deviation.

The SNR is then calculated as:

$$SNR = \frac{1}{2} \frac{|\mu_1 - \mu_0|^2}{\alpha\sigma_0^2 + (1-\alpha)\sigma_1^2} \tag{13}$$

The SNR of each of the samples resulting from applying the slider window was stored to estimate the system’s expected SNR afterward. Assuming that the transmission is OOK, the theoretical error rate for each experimentally estimated SNR was calculated using:

$$BER = \frac{1}{2} \operatorname{erfc}\left(\sqrt{\frac{SNR}{2}}\right), \tag{14}$$

where  $\operatorname{erfc}(\times)$  is the complementary error function. Both SNR and BER calculations were carried out for each color of the image sensor (R, G and B) and for an average emphasized with the PSF approximation (Equation (15)). The goal of spatial averaging is to improve the SNR by reducing the effective variance of noise.

$$y = \frac{\sum_{i=0}^{I-1} \sum_{j=0}^{J-1} r_{xy}[i, j] \times x[i, j]}{\sum_{i=0}^{N-1} \sum_{j=0}^{M-1} r_{xy}[i, j]}, \tag{15}$$

where  $I$  and  $J$  are the height and width of the ROI considered for averaging,  $y_{mean}$  is the signal resulting from the arithmetic mean,  $y$  is the signal resulting from the emphasized averaging,  $s[i, j]$  is the original signal in the coordinate  $(i, j)$ .

The location of the transmitters in the captured images was selected arbitrarily and reinforced by the correlation process to estimate the PSF. The image processing is depicted

in Figure 10, showing the photograms obtained by the camera, and the ROI of the sources. The PSFs estimated are plotted in a region of 7-by-7 px in which it can be seen the numerous pixels that have a considerable correlation to the sub-pixel projection. The results of SNR and BER for both  $T_x$  are summarized in Table 5. The RGB channels do not show considerable difference. The SNR at  $d_1$  reaches 20.0 dB for the green channel, and at  $d_2$  it is 13.0 dB for the red channel. The experimental BER values obtained do not reflect the theoretic expected values possibly due to the non-stationary behavior of the background light level, and the limited amount data analyzed.

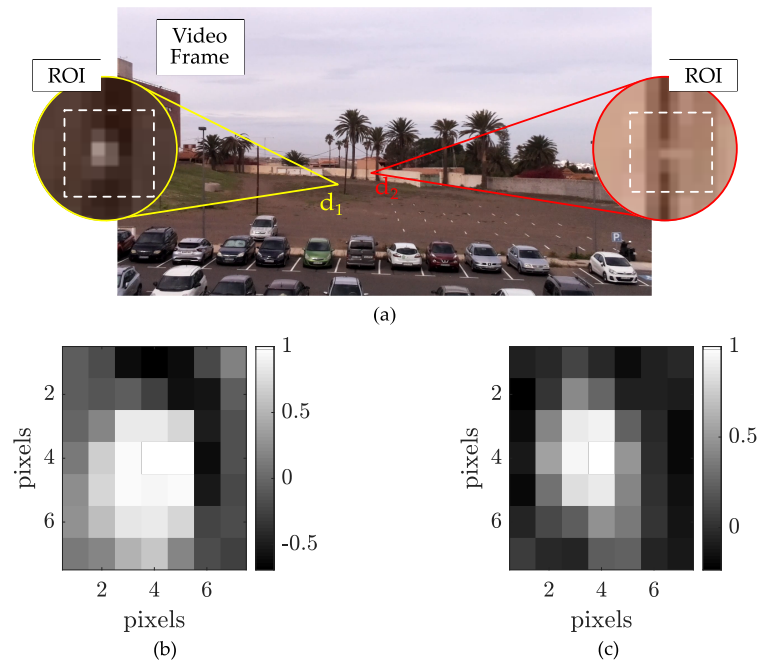


**Figure 10.** Image processing results from the experimentation using the sub-pixel setting. (a) Example of a frame obtained by the camera during experimentation, with insets of the regions of projection of each transmitter. (b) Estimated point spread function (PSF) for  $d_1$ . (c) Estimated PSF for  $d_2$ .

**Table 5.** Signal-to-noise (SNR) ratio and bit error rate (BER) results by channel using point spread function weighted scheme in sub-pixel experiments.

Metric	Position	Channel R	Channel G	Channel B
SNR (experimental)	$d_1$	19.7 dB	20.0 dB	19.8 dB
	$d_2$	13.0 dB	12.9 dB	12.5 dB
BER (theoretical)	$d_1$	$<10^{-12}$	$<10^{-12}$	$<10^{-12}$
	$d_2$	$3.97 \times 10^{-6}$	$5.03 \times 10^{-6}$	$1.24 \times 10^{-5}$
BER (experimental)	$d_1$	$<3.33 \times 10^{-3}$	$<3.33 \times 10^{-3}$	$<3.33 \times 10^{-3}$
	$d_2$	$9.60 \times 10^{-3}$	$9.60 \times 10^{-3}$	$7.20 \times 10^{-3}$

#### 4.3. Discussion of the Results

One of OCC technology's recurring promises is the possibility of using cameras in Smart Cities for massive sensor monitoring applications. However, until now, OCC systems have been based on the use of large lamps, complemented with high-gain optics (telescopes or focal length lenses of hundreds of mm) or short distances, to make use of RS techniques. However, in the cases of use in WSN, the transmission speed is a non-critical factor, so it allows the exploitation of the inherent spatial multiplexing capacity of the cameras.

The sub-pixel system achieved a relatively equal SNR for the red, green, and blue channels, with values of approximately 20 dB and 13 dB for 90 m and 130 m, respectively, using the emphasized PSF enhancement. Considering that the NRZ-OOK technique was used, the theoretical BER level was estimated for each distance, and it can be observed that the experimental BER is considerably far for the  $d_2$  case since the channel is non-stationary. For the case  $d_1$ , no errors were found during the experiments. The channel fluctuations are an issue for the successful segregation of the signal of interest and could become critical for mobile nodes and outdoor conditions.

## 5. Conclusions

In this paper, a network architecture based on OCC for WSN and IoT applications is developed from the advances in experimental channel evaluation in emulated and real conditions. The experimental setup used for the proof-of-concept of the network strategy was implemented using two transmitters at 90 m and 130 m communicating simultaneously to one CMOS camera at 8 bps each, with the potential to expand the number of  $T_x$  nodes to several tens of them covering considerable areas, such as crop fields, streets, parks, industrial facilities, among others. WSNs are envisioned in this paper as a field in which sub-pixel OCC has a significant potential to become a competent alternative. Although the achievable data rate is relatively low, signaling sensor data through OCC with single LEDs is cost and energy-efficient, and camera-based receivers can be reused for video recording and communications simultaneously in these settings.

The analysis of previous works analyzed, in which RS-OCC systems were evaluated in emulated and real outdoor scenarios, showed significant limitations of RS schemes. Although the achieved data rate (several hundred bps), distances (hundreds of m), and cost-effectiveness of the equipment are positive aspects of RS-OCC, the need to use large optical devices is an issue. The use of large LED  $T_x$  or long focal distance lenses are requirements that limit the camera equipment to only be used as a communication device at the expense of their video-monitoring capabilities. The sup-pixel approach uses only small optical devices, i.e., a microlens CMOS camera, and single 5 mm standard LEDs, allowing more transmitters to input data into the receiver, taking advantage of the spatial division that is inherent in the camera equipment, and allowing the images to be used for video-monitoring of the scenario. This re-use of camera equipment for communication and video-monitoring enables the opportunity to apply these schemes to camera systems that are already deployed, e.g., surveillance cameras.

Future works should include further experimentation in the sub-pixel scenario that supports the capabilities of the OCC-based WSN proposal envisioned in this work, including a larger number of nodes and more extended data transmissions. Other important issues to be addressed include the characterization of the channel background light in a long-term measurement, the mobility support and node discovery, which are critical for the latency of the communications. Please note that node detection in this work was done arbitrarily and offline. However, an online correlation-based detection should be implemented for automatic node discovery and for covering mobility and perturbations that might displace the transmitters' projections on the image sensor. Furthermore, multi-hop schemes and OWC downlink from the network gateway to the sensing nodes could also be developed, although the cost of implementing optical receiver equipment in the sensing nodes can involve a high energy consumption. Finally, the experimental setup in outdoor conditions shown here can be extrapolated to small indoor environments of SCOH, and the sub-pixel context can be kept by using micro-LED devices, which are more power-efficient.

**Author Contributions:** Conceptualization, V.M., V.G. and R.P.-J.; Formal analysis, V.M. and V.G.; Funding acquisition, S.Z. and R.P.-J.; Investigation, V.M. and V.G.; Methodology, V.M., V.G. and C.J.-V.; Resources, S.Z. and R.P.-J.; Software, V.M., V.G. and C.J.-V.; Supervision, S.Z. and R.P.-J.; Visualization, V.M., V.G. and S.Z.; Writing—original draft, V.M., V.G. and S.Z.; Writing—review & editing, V.M., V.G. and S.Z. All authors have read and agreed to the published version of the manuscript.

**Funding:** This project has received funding from the European Union’s Horizon 2020 research and innovation program under the Marie Skłodowska-Curie grant agreement No 764461. This article is based upon work from COST Action CA19111 (European Network on Future Generation Optical Wireless Communication Technologies, NEWFOCUS), supported by COST (European Cooperation in Science and Technology).

**Conflicts of Interest:** The authors declare no conflict of interest. The funders had no role in the design of the study; in the collection, analyses, or interpretation of data; in the writing of the manuscript, or in the decision to publish the results.

## References

- Cahyadi, W.A.; Chung, Y.H.; Ghassemlooy, Z.; Hassan, N.B. Optical Camera Communications: Principles, Modulations, Potential and Challenges. *Electronics* **2020**, *9*, 1339.
- Pathak, P.H.; Feng, X.; Hu, P.; Mohapatra, P. Visible light communication, networking, and sensing: A survey, potential and challenges. *IEEE Commun. Surv. Tutor.* **2015**, *17*, 2047–2077.
- Almadani, Y.; Plets, D.; Bastiaens, S.; Joseph, W.; Ijaz, M.; Ghassemlooy, Z.; Rajbhandari, S. Visible Light Communications for Industrial Applications—Challenges and Potentials. *Electronics* **2020**, *9*, 2157.
- Saeed, N.; Guo, S.; Park, K.H.; Al-Naffouri, T.Y.; Alouini, M.S. Optical camera communications: Survey, use cases, challenges, and future trends. *Phys. Commun.* **2019**, *37*, 100900.
- Saha, N.; Iftekhar, M.S.; Le, N.T.; Jang, Y.M. Survey on optical camera communications: Challenges and opportunities. *IET Optoelectron.* **2015**, *9*, 172–183.
- Le, N.T.; Hossain, M.; Jang, Y.M. A survey of design and implementation for optical camera communication. *Signal Process. Image Commun.* **2017**, *53*, 95–109.
- Jang, M. IEEE 802.15 WPAN 15.7 Amendment-Optical Camera Communications Study Group (SG 7a). 2019. Available online: <https://www.ieee802.org/15/pub/SG7a.html> (accessed on 12 April 2021).
- Kim, Y.H.; Cahyadi, W.A.; Chung, Y.H. Experimental Demonstration of VLC-Based Vehicle-to-Vehicle Communications Under Fog Conditions. *IEEE Photonics J.* **2015**, *7*, 1–9.
- Chaudhary, N.; Alves, L.N.; Ghassemlooy, Z. Current Trends on Visible Light Positioning Techniques. In Proceedings of the 2019 2nd West Asian Colloquium on Optical Wireless Communications (WACOWC), Tehran, Iran, 27–28 April 2019; pp. 100–105.
- Chaudhary, N.; Younus, O.I.; Alves, L.N.; Ghassemlooy, Z.; Zvanovec, S.; Le-Minh, H. An Indoor Visible Light Positioning System Using Tilted LEDs with High Accuracy. *Sensors* **2021**, *21*, 920.
- Palacios Játiva, P.; Román Cañizares, M.; Azurdia-Meza, C.A.; Zabala-Blanco, D.; Dehghan Firoozabadi, A.; Seguel, F.; Montejo-Sánchez, S.; Soto, I. Interference Mitigation for Visible Light Communications in Underground Mines Using Angle Diversity Receivers. *Sensors* **2020**, *20*, 367.
- Jurado-Verdu, C.; Matus, V.; Rabadan, J.; Guerra, V.; Perez-Jimenez, R. Correlation-based receiver for optical camera communications. *OSA Opt. Express* **2019**, *27*, 19150–19155.
- Jurado-Verdu, C.; Guerra, V.; Rabadan, J.; Perez-Jimenez, R.; Chavez-Burbano, P. RGB Synchronous VLC modulation scheme for OCC. In Proceedings of the 2018 11th International Symposium on Communication Systems, Networks and Digital Signal Processing (CSNDSP), Budapest, Hungary, 18–20 July 2018; pp. 1–6.
- Matus, V.; Teli, S.R.; Guerra, V.; Jurado-Verdu, C.; Zvanovec, S.; Perez-Jimenez, R. Evaluation of Fog Effects on Optical Camera Communications Link. In Proceedings of the 2020 3rd West Asian Symposium on Optical Wireless Communications (WASOWC), Tehran, Iran, 24–25 November 2020; pp. 1–5.
- Matus, V.; Eso, E.; Teli, S.R.; Perez-Jimenez, R.; Zvanovec, S. Experimentally Derived Feasibility of Optical Camera Communications under Turbulence and Fog Conditions. *Sensors* **2020**, *20*, 757.
- Matus, V.; Guerra, V.; Jurado-Verdu, C.; Teli, S.; Zvanovec, S.; Rabadan, J.; Perez-Jimenez, R. Experimental Evaluation of an Analog Gain Optimization Algorithm in Optical Camera Communications. In Proceedings of the 2020 12th International Symposium on Communication Systems, Networks and Digital Signal Processing (CSNDSP), Porto, Portugal, 20–22 July 2020; pp. 1–5.
- Matus, V.; Guerra, V.; Zvanovec, S.; Rabadan, J.; Perez-Jimenez, R. Sandstorm effect on experimental optical camera communication. *OSA Appl. Opt.* **2021**, *60*, 75–82.
- Kuroda, T. *Essential Principles of Image Sensors*; CRC Press: Boca Raton, FL, USA, 2017.
- Khalighi, M.A.; Uysal, M. Survey on Free Space Optical Communication: A Communication Theory Perspective. *IEEE Commun. Surv. Tutor.* **2014**, *16*, 2231–2258.
- Teli, S.R.; Zvanovec, S.; Perez-Jimenez, R.; Ghassemlooy, Z. Spatial frequency-based angular behavior of a short-range flicker-free MIMO-OCC link. *OSA Appl. Opt.* **2020**, *59*, 10357–10368.
- Teli, S.R.; Matus, V.; Zvanovec, S.; Perez-Jimenez, R.; Vitek, S.; Ghassemlooy, Z. The First Study of MIMO Scheme Within Rolling-shutter Based Optical Camera Communications. In Proceedings of the 2020 12th International Symposium on Communication Systems, Networks and Digital Signal Processing (CSNDSP), Porto, Portugal, 20–22 July 2020; pp. 1–5.

22. Le, N.-T.; Jang, Y.M. Performance evaluation of MIMO Optical Camera Communications based rolling shutter image sensor. In Proceedings of the 2016 8th International Conference on Ubiquitous and Future Networks (ICUFN), Vienna, Austria, 5–8 July 2016; pp. 140–144.
23. Gonçalves, A.L.R.; Maia, Á.H.A.; Santos, M.R.; de Lima, D.A.; de Miranda Neto, A. Visible Light Positioning and Communication Methods and Their Applications in the Intelligent Mobility. *IEEE Lat. Am. Trans.* **2021**, *100*, 2174–2185.
24. Iturralde, D.; Azurdiá-Meza, C.; Krommenacker, N.; Soto, I.; Ghassemlooy, Z.; Becerra, N. A new location system for an underground mining environment using visible light communications. In Proceedings of the 2014 9th International Symposium on Communication Systems, Networks and Digital Signal Processing (CSNDSP), Manchester, UK, 23–25 July 2014; pp. 1165–1169.
25. Hossan, M.; Chowdhury, M.Z.; Hasan, M.; Shahjalal, M.; Nguyen, T.; Le, N.T.; Jang, Y.M. A new vehicle localization scheme based on combined optical camera communication and photogrammetry. *Mob. Inf. Syst.* **2018**, *2018*, 8501898.
26. Karbalayghareh, M.; Miramirkhani, F.; Eldeeb, H.B.; Kizilirmak, R.C.; Sait, S.M.; Uysal, M. Channel Modelling and Performance Limits of Vehicular Visible Light Communication Systems. *IEEE Trans. Veh. Technol.* **2020**, *69*, 6891–6901.
27. Marè, R.M.; Marte, C.L.; Cugnasca, C.E.; Sobrinho, O.G.; dos Santos, A.S. Feasibility of a Testing Methodology for Visible Light Communication Systems Applied to Intelligent Transport Systems. *IEEE Lat. Am. Trans.* **2020**, *100*, 515–523.
28. Elamassie, M.; Karbalayghareh, M.; Miramirkhani, F.; Kizilirmak, R.C.; Uysal, M. Effect of Fog and Rain on the Performance of Vehicular Visible Light Communications. In Proceedings of the 2018 IEEE 87th Vehicular Technology Conference (VTC-Spring), Porto, Portugal, 3–6 June 2018, pp. 1–6.
29. Kuutti, S.; Bowden, R.; Jin, Y.; Barber, P.; Fallah, S. A Survey of Deep Learning Applications to Autonomous Vehicle Control. *IEEE Trans. Intell. Transp. Syst.* **2021**, *22*, 712–733.
30. Ashok, A.; Jain, S.; Gruteser, M.; Mandayam, N.; Yuan, W.; Dana, K. Capacity of pervasive camera based communication under perspective distortions. In Proceedings of the 2014 IEEE International Conference on Pervasive Computing and Communications (PerCom), Budapest, Hungary, 24–28 March 2014; pp. 112–120.
31. Shi, J.; He, J.; Jiang, Z.; Zhou, Y.; Xiao, Y. Enabling user mobility for optical camera communication using mobile phone. *OSA Opt. Express* **2018**, *26*, 21762–21767.
32. Beshr, M.; Michie, C.; Andonovic, I. Evaluation of Visible Light Communication system performance in the presence of sunlight irradiance. In Proceedings of the 2015 17th International Conference on Transparent Optical Networks (ICTON), Budapest, Hungary, 5–9 July 2015; pp. 1–4.
33. Georlette, V.; Bette, S.; Brohez, S.; Pérez-Jiménez, R.; Point, N.; Moeyaert, V. Outdoor Visible Light Communication Channel Modeling under Smoke Conditions and Analogy with Fog Conditions. *Optics* **2020**, *1*, 259–281.
34. Eso, E.; Teli, S.; Hassan, N.B.; Vitek, S.; Ghassemlooy, Z.; Zvanovec, S. 400 m rolling-shutter-based optical camera communications link. *OSA Opt. Lett.* **2020**, *45*, 1059–1062.
35. Chavez-Burbano, P.; Guerra, V.; Rabadan, J.; Perez-Jimenez, R. Optical camera communication for smart cities. In Proceedings of the 2017 IEEE/CIC International Conference on Communications in China (ICCC Workshops), Qingdao, China, 22–24 October 2017; pp. 1–4.
36. Ghassemlooy, Z.; Popoola, W.; Rajbhandari, S. *Optical Wireless Communications: System and Channel Modelling with Matlab*; CRC Press: Boca Raton, FL, USA, 2019.
37. Ishimaru, A. *Electromagnetic Wave Propagation, Radiation, and Scattering: From Fundamentals to Applications*; John Wiley & Sons: Hoboken, NJ, USA, 2017.
38. Kedar, D.; Arnon, S. Urban optical wireless communication networks: The main challenges and possible solutions. *IEEE Commun. Mag.* **2004**, *42*, S2 – S7.
39. Kedar, D.; Arnon, S. The positive contribution of fog to the mitigation of pointing errors in optical wireless communication. *Appl. Opt.* **2003**, *42*, 4946–4954.
40. Yamazato, T.; Kinoshita, M.; Arai, S.; Souke, E.; Yendo, T.; Fujii, T.; Kamakura, K.; Okada, H. Vehicle Motion and Pixel Illumination Modeling for Image Sensor Based Visible Light Communication. *IEEE J. Sel. Areas Commun.* **2015**, *33*, 1793–1805.
41. Guerra, V.; Ticay-Rivas, J.R.; Alonso-Eugenio, V.; Perez-Jimenez, R. Characterization and Performance of a Thermal Camera Communication System. *Sensors* **2021**, *20*, 3288.
42. Bohata, J.; Zvanovec, S.; Korinek, T.; Abadi, M.M.; Ghassemlooy, Z. Characterization of dual-polarization LTE radio over a free-space optical turbulence channel. *OSA Appl. Opt.* **2015**, *54*, 7082–7087.
43. Libich, J.; Perez, J.; Zvanovec, S.; Ghassemlooy, Z.; Nebuloni, R.; Capsoni, C. Combined effect of turbulence and aerosol on free-space optical links. *OSA Appl. Opt.* **2017**, *56*, 336–341.
44. Nor, N.A.M.; Fابيي, E.; Abadi, M.M.; Tang, X.; Ghassemlooy, Z.; Burton, A. Investigation of moderate-to-strong turbulence effects on free space optics—A laboratory demonstration. In Proceedings of the 2019 15th International Conference on Telecommunications (ConTEL), Graz, Austria, 13–15 July 2019.
45. Andrews, L.C.; Phillips, R.L. *Laser Beam Propagation through Random Media*; SPIE Press: Bellingham, WA, USA, 2005; Volume 152.
46. Ayaz, M.; Ammad-Uddin, M.; Sharif, Z.; Mansour, A.; Aggoune, E.M. Internet-of-Things (IoT)-Based Smart Agriculture: Toward Making the Fields Talk. *IEEE Access* **2019**, *7*, 129551–129583.
47. Zhu, N.; Xia, Y.; Liu, Y.; Zang, C.; Deng, H.; Ma, Z. Temperature and Humidity Monitoring System for Bulk Grain Container Based on LoRa Wireless Technology. In *Lecture Notes in Computer Science, Proceedings of the Cloud Computing and Security, Haikou, China, 8–10 June 2018*; Sun, X., Pan, Z., Bertino, E., Eds.; Springer International Publishing: Cham, Switzerland, 2018; pp. 102–110.

48. Mekki, K.; Bajic, E.; Chaxel, F.; Meyer, F. Overview of Cellular LPWAN Technologies for IoT Deployment: Sigfox, LoRaWAN, and NB-IoT. In Proceedings of the 2018 IEEE International Conference on Pervasive Computing and Communications Workshops (PerCom Workshops), Athens, Greece, 19–23 March 2018; pp. 197–202.
49. Atmel Corporation. *ATmega328p, 8-bit AVR Microcontroller with 32K Bytes In-System Programmable Flash, Datasheet*; Atmel Corporation: San Jose, CA, USA, 2015.
50. IMX219PQH5-C Datasheet. Available online: <https://datasheetspdf.com/pdf/1404029/Sony/IMX219PQH5-C/1> (accessed on 7 April 2021).
51. Eso, E.F.; Burton, A.; Hassan, N.B.; Abadi, M.M.; Ghassemlooy, Z.; Zvanovec, S. Experimental Investigation of the Effects of Fog on Optical Camera-based VLC for a Vehicular Environment. In Proceedings of the 2019 15th International Conference on Telecommunications (ConTEL), Graz, Austria, 13–15 July 2019.
52. Cleveland, W.S.; Devlin, S.J. Locally Weighted Regression: An Approach to Regression Analysis by Local Fitting. *J. Am. Stat. Assoc.* **1988**, *83*, 596–610.
53. Cartográfica de Canarias (GRAFCAN). Sistema de Información Territorial de Canarias. Available online: <https://grafcan.es/v0kq90T> (accessed on 12 April 2021).



## 5.4 Summary

As was presented in this chapter, three different experimental OCC systems were tested under challenging channel conditions to evaluate the feasibility of implementing OCC WSNs. The key materials and methods and contributions of each publication are listed in Table 5.1. From P1, the main contribution is to introduce the control of gain in the camera configuration, which can use the Pearson's correlation coefficient for rapid estimation of the SNR, as in [59]. In P2, large optics were employed to allow the use of RS detection techniques, whereas, in P3, the size of the optical ends was reduced to allow the re-utilization of the camera video employing GS techniques, which was defined as sub-pixel topology.

**Table 5.1:** Summary of the key contributions on methodology and results of the publications of the compendium.

	<b>Design</b>	<b>Processes</b>	<b>Metrics</b>	<b>Findings</b>
P1	Fog* and turbulence* 0.46m link large Tx, small Rx	Rolling shutter Gain variation ROI detection	SNR Pearson's corr. coef.	Analog gain
P2	Sandstorm 100m, 200m link large Tx, large Rx	Rolling shutter ROI detection Gaussian mixture	SNR, BER	ROI expansion
P3	Clear outdoor 90 m, 130 m small Tx, small Rx	Global shutter PSF detection	SNR, BER Pearson's corr. coef.	Sub-pixel topology PSF ehancement Re-utilization

\*: Emulated using laboratory chamber.



This chapter summarizes the major contributions of this work to the channel characterization of outdoor OCC systems in the context of WSNs. First, based on the objectives for the development of this thesis, a discussion of the achievements is given, supported by the experimental results presented. Second, the potential new lines of research derived from this work are described.

## Conclusions

This doctoral thesis entitled “Contribution to the Experimental Channel Evaluation of Optical Camera Communication for Wireless Sensor Networks” presented the development and analysis of experimental works on evaluating the influence of atmospheric conditions over the optical wireless communication channel in outdoor OCC links. It was elaborated upon three main objectives that aimed to demonstrate the feasibility of outdoor OCC links in harsh atmospheric conditions, develop strategies for the photographic parameters optimization and their influence on the signal quality, and deploy a practical OCC testbed in natural outdoor conditions employing commercially available cameras and LED components.

The works presented in the previous chapter as a compendium of publications [48], [54], [58] addressed the three objectives mentioned above by implementing experimental OCC systems in emulated and real meteorologic phenomena, including the presence of aerosols such as fog and dust from a sandstorm, as well as turbulence induced by heat, and in a clear atmosphere. The final contribution of this work was to demonstrate the feasibility of sub-pixel OCC links in a realistic scenario.

One of the recurring commitments of the OCC technologies is the possibility of using cameras in Smart Cities for massive sensor monitoring applications. However, so far, experimental OCC systems like in [10], [48], [54], [57] have relied on the use of large-size lamps, complemented with large lenses in the receiver side to allow the use of RS techniques. Nevertheless, in the use cases proposed in this work, the transmission rate is a non-critical factor, thus allowing the use of GS techniques instead, which provide more re-usability of the image frames for general photographic and video purposes. In summary, the exploitation of RS detection in outdoor scenarios likely requires dedicated hardware, whereas GS detection has more potential to re-utilize existing infrastructures.

The main characteristics of the OCC receiver employed are the following. First, the camera was based on CMOS Sony IMX219 [50] image sensor, which features a maximum resolution of 3280 by 2464 pixels with a maximum analog gain of 20.6 dB. Second, the rolling shutter acquisition mechanism that it performs is done with a row-shift time of 18.904  $\mu$ s, and the exposure times used ranged from 60 to 180  $\mu$ s. Finally, in the case of the Element14 Raspberry Pi Camera V2, its built-in

lens is a manual focus with an equivalent focal length  $f = 3.04$  mm and aperture  $f/20$ . This optical end was extended with a telescope of  $f' = 700$  mm of focal length with an aperture  $f'/11.6$ . The experiments were done using either only the built-in lens or coupled to the telescope. Depending on the size of the ROI achieved, the decoding stages considered RS or GS techniques. The characteristics of this camera are similar to those of smartphones and other devices available in the mass market. Then, the results obtained in the experimentation of this work are considered representative for most situations.

The experiments done in a 5 m laboratory chamber presented in P1 [54] emulated dense fog conditions and high turbulence and employed an RS-based OCC link. The effect of the fog was modeled as an attenuation caused by the aerosol particles in the air. The heat-induced turbulence, in turn, was considered to be stochastic variations of the refractive index of the air in the chamber, as in other works in the OWC field [60]. From these experiments, a negligible compromise of the signal quality was found in turbulent conditions.

In all the experiments carried out, the CMOS camera performed the OCC receiver acquisition tasks. Its circuitry was controlled from software to evaluate the impact of changing photographic parameters. Optimizing variables such as the exposure time and the analog gain allowed the SNR to increase for different visibility values. In particular, the experiments under emulated fog in P1 showed two important effects of the analog gain of the camera. In low visibilities, high values of gain helped to reduce the relative power of quantization noise, whereas in high visibilities, it caused saturation. These opposite effects of the increased analog gain led to the development of a control algorithm, as presented in [59] and included in P3 [58]. The automatic selection of gain to improve signal quality was based on the estimation of the SNR through Pearson's correlation coefficient, which is involved in other blocks of the processing workflow of the RS and GS detection, and thus, its re-utilization is computationally neutral.

The experimentation in real sandstorm conditions was the first in the OCC field, up to the author's knowledge, to establish an OCC link in a severe sandstorm event. In this work, an RGB led transmitter reached up to 200 m linkspan with the CMOS camera coupled to the telescope reached. The system was tested at 100 m, reaching 1035 bps, which would be extrapolated to about 500 bps at 200 m. Nevertheless, an interesting effect of the sandstorm let the longer link reach 630 bps. As reported in [44], the scattering effect of aerosols lets non-LOS rays to reach the OWC receiver's surface, which in P2 [48] let the 200 m linkspan setup detect an ROI size around 33% bigger, increasing the achievable datarate consequently.

The final outdoor OCC experiment was implemented using 5 mm white LEDs and the CMOS camera with its 3.04 mm built-in lens in a linkspan of around 100 m. Given these magnitudes, the projection of the transmitters falls in the sub-pixel area. Although the GS decoding techniques compromise the datarate of the links, this novel topology implies a negligible use of the FOV of the camera, effectively providing simultaneous video monitoring and communication, contrary to most RS systems.

It was seen that despite the sub-pixel projection of the sources, the adjacent pixels could be considered part of the ROI in case the transmitter is out of the

depth of the focused area or if the atmosphere induces scattering. Both effects were reduced using the PSF representation, which correlators can estimate, allowing to increase the SNR by a weighted average of the ROI, obtaining nearly 20 dB in the experiments presented in P3. The results obtained make sub-pixel OCC systems potentially attractive for the application to WSNs. LED-based nodes at distances of several tens of meters could upload low-speed data to a camera-based node that could simultaneously be surveillance equipment since the frames contain both the data and the image or video of the environment.

## Future works

The contributions mentioned above have the potential to open new research works in the course of applying OCC to WSNs in outdoor scenarios. The new lines of research envisioned by the author are the following.

From the experimentation in harsh outdoor scenarios, since only the effect of aerosols and turbulence were addressed in this thesis, all the meteorologic phenomena that are known to degrade OWC links are worth modeling, characterizing, and evaluating specifically for OCC systems, including rain conditions, different cloudy weathers, and the effect of sunlight at different times of the day, among others. Furthermore, the long-term characterization of all atmospheric conditions would serve as a base for the efficient design of optical ends, modulation schemes, and photographic parameter control algorithms.

Since the decoding stages in this work were performed over offline video captures, their migration to online implementation, including the automated control of the analog gain, is valuable for transferring the OCC research to real technology and optimizing the potential latency issues. In this regard, the aforementioned RS schemes requiring large FOV portions dedicated to communications or considerably low exposure times that limit hardware re-utilization could benefit from rapid alternating photographic parameters to work virtually parallel to video monitoring functionalities. Moreover, an online correlation-based detection should be implemented for automatic node discovery and for covering mobility and perturbations that might displace the transmitters' projections on the image sensor.

The sub-pixel topology presented in this work can be extended by increasing the number of transmitter nodes and using higher frame rates, reaching bit rates on the order of tens of kbps shared between nodes. Furthermore, the energy efficiency of LEDs and the simple implementation of OOK modulation can potentially reduce the complexity and energy consumption of transmitter nodes compared to other RF and microwave-based technologies that require highly integrated hardware. The outdoor sub-pixel scheme presented in this thesis could also be adopted in indoor scenarios, at short ranges, taking advantage of even lower power consumption micro-LED lights, for IoT machine monitoring applications in home and office environments.



# Bibliography

---

- [1] Cisco Systems, **Cisco annual internet report (2018–2023) white paper**, Cisco Systems, Tech. Rep., 2020 (see page 1).
- [2] P. Chavez-Burbano, S. Vitek, S. Teli, V. Guerra, J. Rabadan, R. Perez-Jimenez y S. Zvanovec, **Optical camera communication system for internet of things based on organic light emitting diodes**, *Electronics Letters*, vol. 55: no. 6, 334–336 (see page 2).
- [3] N. Saeed, S. Guo, K.-H. Park, T. Y. Al-Naffouri y M.-S. Alouini, **Optical camera communications: Survey, use cases, challenges, and future trends**, *Physical Communication*, vol. 37, 100900, ISSN: 1874-4907 (see pages 2, 9).
- [4] V. Matus, V. Guerra, C. Jurado-Verdu, R. Jose y P.-J. Rafael, **Design and implementation of an optical camera communication system for wireless sensor networking in farming fields**, in *2021 IEEE International Symposium on Personal, Indoor and Mobile Radio Communications*, vol. 1, 2021, 107–111 (see page 2).
- [5] C. Quintana, V. Guerra, J. Rufo, J. Rabadan y R. Perez-Jimenez, **Reading lamp-based visible light communication system for in-flight entertainment**, *IEEE Transactions on Consumer Electronics*, vol. 59: no. 1, 31–37. DOI: [10.1109/TCE.2013.6490238](https://doi.org/10.1109/TCE.2013.6490238) (see page 3).
- [6] J. Rufo, J. Rabadan, F. Delgado, C. Quintana y R. Perez-Jimenez, **Experimental evaluation of video transmission through led illumination devices**, *IEEE Transactions on Consumer Electronics*, vol. 56: no. 3, 1411–1416. DOI: [10.1109/TCE.2010.5606277](https://doi.org/10.1109/TCE.2010.5606277) (see page 3).
- [7] R. Perez-Jimenez, J. Rufo, C. Quintana, J. Rabadan y F. J. Lopez-Hernandez, **Visible light communication systems for passenger in-flight data networking**, in *2011 IEEE International Conference on Consumer Electronics (ICCE)*, 2011, 445–446. DOI: [10.1109/ICCE.2011.5722675](https://doi.org/10.1109/ICCE.2011.5722675) (see page 3).
- [8] J. Luna-Rivera, R. Perez-Jimenez, J. Rabadan-Borjes, J. Rufo-Torres, V. Guerra y C. Suarez-Rodriguez, **Multiuser csf scheme for indoor visible light communications**, *Opt. Express*, vol. 22: no. 20, 24256–24267. DOI: [10.1364/OE.22.024256](https://doi.org/10.1364/OE.22.024256). [Online]. Available: <http://www.opticsexpress.org/abstract.cfm?URI=oe-22-20-24256> (see page 3).
- [9] J. F. Rufo Torres, **Contribución al estudio de servicios soportados sobre redes vlc (visible light communications)**, Ph.D. dissertation, 2016 (see page 3).
- [10] P. X. Chávez Burbano, **Optical camera communication for internet of things in urban environments**, Ph.D. dissertation, 2021 (see pages 3, 71).
- [11] P. Chavez-Burbano, V. Guerra, J. Rabadan, D. Rodriguez-Esparragon y R. Perez-Jimenez, **Experimental characterization of close-emitter interference in an optical camera communication system**, *Sensors*, vol. 17: no. 7, 1561, ISSN: 1424-8220. DOI: [10.3390/s17071561](https://doi.org/10.3390/s17071561) (see page 3).
- [12] V. Guerra Yáñez, **Contribution on the study of underwater wireless optical links: Channel prediction and energy efficiency**, Ph.D. dissertation, 2016 (see page 3).
- [13] P. Wang, Z. Sun, M. C. Vuran, M. A. Al-Rodhaan, A. M. Al-Dhelaan e I. F. Akyildiz, **Topology analysis of wireless sensor networks for sandstorm monitoring**, in *2011 IEEE International Conference on Communications (ICC)*, Jun. 2011, 1–5 (see page 3).
- [14] R. Perez-Jimenez, J. Rabadan, J. Rufo, E. Solana y J. M. Luna-Rivera, **Visible light communications technologies for smart tourism destinations**, in *2015 IEEE First International Smart Cities Conference (ISC2)*, 2015, 1–5. DOI: [10.1109/ISC2.2015.7366193](https://doi.org/10.1109/ISC2.2015.7366193) (see page 3).
- [15] P. H. Pathak, X. Feng, P. Hu y P. Mohapatra, **Visible light communication, networking, and sensing: A survey, potential and challenges**, *IEEE communications surveys & tutorials*, vol. 17: no. 4, 2047–2077 (see page 9).

- [16] Y. Almadani, D. Plets, S. Bastiaens, W. Joseph, M. Ijaz, Z. Ghassemlooy y S. Rajbhandari, **Visible light communications for industrial applications—challenges and potentials**, *Electronics*, vol. 9: no. 12, ISSN: 2079-9292 (see page 9).
- [17] Z. Ghassemlooy, L. N. Alves, S. Zvanovec y M.-A. Khalighi, **Visible light communications: theory and applications**. CRC press, 2017 (see page 9).
- [18] Z. Ghassemlooy, W. Popoola y S. Rajbhandari, **Optical wireless communications: system and channel modelling with Matlab**. CRC press, 2019 (see page 9).
- [19] Y. Tanaka, S. Haruyama y M. Nakagawa, **Wireless optical transmissions with white colored led for wireless home links**, in *11th IEEE International Symposium on Personal Indoor and Mobile Radio Communications. PIMRC 2000. Proceedings (Cat. No.00TH8525)*, vol. 2, 2000, 1325–1329 vol.2. DOI: [10.1109/PIMRC.2000.881634](https://doi.org/10.1109/PIMRC.2000.881634) (see page 9).
- [20] C. Danakis, M. Afgani, G. Povey, I. Underwood y H. Haas, **Using a cmos camera sensor for visible light communication**, in *2012 IEEE Globecom Workshops, 2012*, 1244–1248. DOI: [10.1109/GLOCOMW.2012.6477759](https://doi.org/10.1109/GLOCOMW.2012.6477759) (see page 9).
- [21] W. A. Cahyadi, Y. H. Chung, Z. Ghassemlooy y N. B. Hassan, **Optical camera communications: Principles, modulations, potential and challenges**, *Electronics*, vol. 9: no. 9, ISSN: 2079-9292 (see page 9).
- [22] N. T. Le, M. A. Hossain e Y. M. Jang, **A survey of design and implementation for optical camera communication**, *Signal Processing: Image Communication*, vol. 53, 95–109, ISSN: 0923-5965 (see pages 9, 17).
- [23] D. Moreno, J. Rufo, V. Guerra, J. Rabadan y R. Perez-Jimenez, **Optical multispectral camera communications using led spectral emission variations**, *IEEE Photonics Technology Letters*, vol. 33: no. 12, 591–594 (see page 9).
- [24] —, **Effect of temperature on channel compensation in optical camera communication**, *Electronics*, vol. 10: no. 3, ISSN: 2079-9292 (see page 9).
- [25] D. Moreno, B. Majlesein, J. Rufo, V. Guerra, J. Rabadan y R. Perez-Jimenez, **Thermally-induced spectral variations of led applied to optical multispectral camera communications**, in *2020 12th International Symposium on Communication Systems, Networks and Digital Signal Processing (CSNDSP), 2020*, 1–6 (see page 9).
- [26] V. Guerra, J. R. Ticay-Rivas, V. Alonso-Eugenio y R. Perez-Jimenez, **Characterization and performance of a thermal camera communication system**, *Sensors*, vol. 20: no. 11 (see page 9).
- [27] IEEE Standard Association, **IEEE standard for local and metropolitan area networks-part 15.7: Short-range wireless optical communication using visible light**, *IEEE: Piscataway, NZ, USA*, 1–309 (see page 9).
- [28] M. Karbalayghareh, F. Miramirkhani, H. B. Eldeeb, R. C. Kizilirmak, S. M. Sait y M. Uysal, **Channel modelling and performance limits of vehicular visible light communication systems**, *IEEE Transactions on Vehicular Technology*, vol. 69: no. 7, 6891–6901 (see pages 9, 10).
- [29] M. Elamassie, M. Karbalayghareh, F. Miramirkhani, R. C. Kizilirmak y M. Uysal, **Effect of fog and rain on the performance of vehicular visible light communications**, in *2018 IEEE 87th Vehicular Technology Conference (VTC Spring), Jun. 2018* (see page 9).
- [30] M. K. Hasan, N. T. Le, M. Shahjalal, M. Z. Chowdhury e Y. M. Jang, **Simultaneous data transmission using multilevel led in hybrid occ/lifi system: Concept and demonstration**, *IEEE Communications Letters*, vol. 23: no. 12, 2296–2300. DOI: [10.1109/LCOMM.2019.2945758](https://doi.org/10.1109/LCOMM.2019.2945758) (see page 9).
- [31] N. Chaudhary, O. I. Younus, L. N. Alves, Z. Ghassemlooy, S. Zvanovec y H. Le-Minh, **An indoor visible light positioning system using tilted leds with high accuracy**, *Sensors*, vol. 21: no. 3, ISSN: 1424-8220 (see pages 9, 10).
- [32] E. A. Jarchlo, E. Eso, H. Doroud, A. Zubow, F. Dressler, Z. Ghassemlooy, B. Siessegger y G. Caire, **Fdla: A novel frequency diversity and link aggregation solution for handover in an indoor vehicular vlc network**, *IEEE Transactions on Network and Service Management*, vol. 18: no. 3, 3556–3566. DOI: [10.1109/TNSM.2021.3075476](https://doi.org/10.1109/TNSM.2021.3075476) (see page 9).



- [33] C. Jurado-Verdu, V. Guerra, V. Matus, C. Almeida y J. Rabadan, **Optical camera communication as an enabling technology for microalgae cultivation**, *Sensors*, vol. 21: no. 5, ISSN: 1424-8220 (see page 9).
- [34] L. Aguiar, P. de Saa, V. Guerra y R. Perez-Jimenez, **Survey of vlc and occ applications on tourism industry: Potentials amp; challenges**, in *2020 South American Colloquium on Visible Light Communications (SACVC)*, 2020, 1–6. DOI: [10.1109/SACVLC50805.2020.9129867](https://doi.org/10.1109/SACVLC50805.2020.9129867) (see page 9).
- [35] S. R. Teli, P. Chvojka, S. Vitek, S. Zvanovec, R. Perez-Jimenez y Z. Ghassemlooy, **A mimo hybrid visible light communication system for optical iot**, *IEEE Internet of Things Journal* (see page 10).
- [36] A. Dehghan Firoozabadi, C. Azurdia-Meza, I. Soto, F. Seguel, N. Krommenacker, D. Iturralde, P. Charpentier y D. Zabala-Blanco, **A novel frequency domain visible light communication (vlc) three-dimensional trilateration system for localization in underground mining**, *Applied Sciences*, vol. 9: no. 7, ISSN: 2076-3417 (see page 10).
- [37] A. Memedi y F. Dressler, **Vehicular visible light communications: A survey**, *IEEE Communications Surveys & Tutorials*, vol. 23: no. 1, 161–181 (see page 10).
- [38] H. B. Eldeeb, E. Eso, E. A. Jarchlo, S. Zvanovec, M. Uysal, Z. Ghassemlooy y J. Sathian, **Vehicular vlc: A ray tracing study based on measured radiation patterns of commercial taillights**, *IEEE Photonics Technology Letters*, 1–1. DOI: [10.1109/LPT.2021.3065233](https://doi.org/10.1109/LPT.2021.3065233) (see page 10).
- [39] M. A. Khalighi y M. Uysal, **Survey on free space optical communication: A communication theory perspective**, *IEEE Communications Surveys Tutorials*, vol. 16: no. 4, 2231–2258, ISSN: 1553-877X (see page 10).
- [40] J. Horwath, D. D. Gonzalez, L. M. Navajas, A. L. Souto, V. Semerjyan, G. Raju, J. Grabowsky, C. Garcia, Y. Lai, T. Bähr, C.-C. Chen, F. Haque, A. Grier, H. Harding, M. Hunwardsen, E. Booen y H. Hemmati, **Test results of error-free bidirectional 10 Gbps link for air-to-ground optical communications**, in *Free-Space Laser Communication and Atmospheric Propagation XXX*, H. Hemmati y D. M. Boroson, Eds., vol. 10524, International Society for Optics y Photonics, SPIE, 2018, 417–430 (see page 10).
- [41] G. Blinowski, **Security of visible light communication systems—a survey**, *Physical Communication*, vol. 34, 246–260, ISSN: 1874-4907. DOI: <https://doi.org/10.1016/j.phycom.2019.04.003>. [Online]. Available: <https://www.sciencedirect.com/science/article/pii/S1874490718304786> (see page 12).
- [42] S. R. Teli, V. Matus, S. Zvanovec, R. Perez-Jimenez, S. Vitek y Z. Ghassemlooy, **Optical camera communications for iot–rolling-shutter based mimo scheme with grouped led array transmitter**, *Sensors*, vol. 20: no. 12, ISSN: 1424-8220 (see page 12).
- [43] Z. N. Chaleshtori, P. Chvojka, S. Zvanovec, Z. Ghassemlooy y P. A. Haigh, **A survey on recent advances in organic visible light communications**, in *2018 11th International Symposium on Communication Systems, Networks Digital Signal Processing (CSNDSP)*, 2018, 1–6. DOI: [10.1109/CSNDSP.2018.8471788](https://doi.org/10.1109/CSNDSP.2018.8471788) (see pages 12, 15).
- [44] D. Kedar y S. Arnon, **The positive contribution of fog to the mitigation of pointing errors in optical wireless communication**, *Applied Optics*, vol. 42: no. 24, 4946–4954 (see pages 13, 72).
- [45] T. Yamazato, I. Takai, H. Okada, T. Fujii, T. Yendo, S. Arai, M. Andoh, T. Harada, K. Yasutomi, K. Kagawa y S. Kawahito, **Image-sensor-based visible light communication for automotive applications**, *IEEE Communications Magazine*: no. 7 (see page 14).
- [46] N. Saha, M. S. Ifthekhar, N. T. Le e Y. M. Jang, **Survey on optical camera communications: Challenges and opportunities**, English, *IET Optoelectronics*, vol. 9, 172–183(11), ISSN: 1751-8768 (see page 16).
- [47] T. Kuroda, **Essential Principles of Image Sensors**. CRC Press, 2017, ISBN: 9781138074170 (see page 17).

- [48] V. Matus, V. Guerra, S. Zvanovec, J. Rabadan y R. Perez-Jimenez, **Sandstorm effect on experimental optical camera communication**, *Appl. Opt.*, vol. 60: no. 1, 75–82 (see pages 17, 23, 41, 71, 72).
- [49] Atmel Corporation, **ATmega328p, 8-bit AVR Microcontroller with 32K Bytes In-System Programmable Flash, Datasheet**. Atmel Corporation, 2015 (see page 19).
- [50] Sony Corporation, **IMX219PQH5-C, Diagonal 4.60 mm (Type 1/4.0) 8 Mega-Pixel CMOS Image Sensor with Square Pixel for Color Cameras, Datasheet**. Sony Corporation, 2014 (see pages 21, 71).
- [51] M. Carlowicz, **Dust blankets the canary islands**, <https://earthobservatory.nasa.gov/images/146337/dust-blankets-the-canary-islands> (see page 22).
- [52] C. Pérez, K. Hausteine, O. Jorba, Z. Janjic, N. Huneus, J. Baldasano, T. Black, S. Basart, S. Nickovic, R. L. Miller y et al., **Atmospheric dust modeling from meso to global scales with the online nmmb/bsc-dust model – part 1: Model description, annual simulations and evaluation**, *Atmospheric chemistry and physics*, vol. 11: no. 24, 13001–13027 (see page 22).
- [53] V. Matus, V. Guerra, C. Jurado-Verdu, J. Rabadan y R. Perez-Jimenez, **Simulation of rolling shutter acquisition in optical camera communications**, in *2019 15th International Conference on Telecommunications (ConTEL)*, 2019, 1–5. DOI: [10.1109/ConTEL.2019.8848549](https://doi.org/10.1109/ConTEL.2019.8848549) (see page 22).
- [54] V. Matus, E. Eso, S. R. Teli, R. Perez-Jimenez y S. Zvanovec, **Experimentally derived feasibility of optical camera communications under turbulence and fog conditions**, *Sensors*, vol. 20: no. 3, 757, ISSN: 1424-8220 (see pages 23, 25, 71, 72).
- [55] K. J. Ebrahim y A. Al-Omary, **Sandstorm effect on visible light communication**, in *2017 9th IEEE-GCC Conference and Exhibition (GCCCE)*, May 2017, 1–7 (see page 41).
- [56] D. Kedar y S. Arnon, **Urban optical wireless communication networks: The main challenges and possible solutions**, *Communications Magazine, IEEE*, vol. 42, S2–S7 (see page 41).
- [57] E. Eso, S. Teli, N. B. Hassan, S. Vitek, Z. Ghassemlooy y S. Zvanovec, **400 m rolling-shutter-based optical camera communications link**, *Opt. Lett.*, vol. 45: no. 5, 1059–1062 (see pages 41, 71).
- [58] V. Matus, V. Guerra, C. Jurado-Verdu, S. Zvanovec y R. Perez-Jimenez, **Wireless sensor networks using sub-pixel optical camera communications: Advances in experimental channel evaluation**, *Sensors*, vol. 21: no. 8, ISSN: 1424-8220. DOI: [10.3390/s21082739](https://doi.org/10.3390/s21082739). [Online]. Available: <https://www.mdpi.com/1424-8220/21/8/2739> (see pages 50, 71, 72).
- [59] V. Matus, V. Guerra, C. Jurado-Verdu, S. Teli, S. Zvanovec, J. Rabadan y R. Perez-Jimenez, **Experimental evaluation of an analog gain optimization algorithm in optical camera communications**, in *2020 12th International Symposium on Communication Systems, Networks Digital Signal Processing (CSNDSP)*, 2020, 1–5 (see pages 69, 72).
- [60] J. Bohata, S. Zvanovec, T. Korinek, M. M. Abadi y Z. Ghassemlooy, **Characterization of dual-polarization lte radio over a free-space optical turbulence channel**, *Applied optics*, vol. 54: no. 23, 7082–7087 (see page 72).

This appendix chapter includes the paper entitled entitled “Demonstration of a Sub-pixel Outdoor Optical Camera Communication Link”, published in Spanish, which presents the proof-of-concept of outdoor OCC links using small optical devices, where the projection of the transmitter falls into the sub-pixel area. This approach serves as an alternative to large-optical systems, allowing the re-utilization of the camera images for video monitoring and data decoding simultaneously.

# Demonstration of a Sub-Pixel Outdoor Optical Camera Communication Link

Vicente Matus, Victor Guerra, Cristo Jurado-Verdu, Jose Rabadan, and Rafael Perez-Jimenez

**Abstract**—Optical Camera Communication (OCC) is an Optical Wireless Communication (OWC) technology that relies on general-purpose cameras to perform not only image-related tasks but also to receive data from optical sources. In general terms, OCC has been extensively studied in indoor scenarios and can be a competent and cost-effective alternative solution for wireless data transmission in Smart Cities for medium to long links up to hundreds of meters. In this paper, the feasibility of establishing an outdoor sub-pixel communication link is demonstrated. In this experiment, single 5 mm white LED transmitters located at distances of 90 and 130 m send simultaneous optical codes to a receiver based on a commercial camera, achieving a signal-to-noise ratio of 20 dB and 13 dB, respectively. This work shows that although the geometrical projection within the transmitter's image is less than the pixel area, it is still possible to establish an effective communication link, with 8 bps per transmitter. At 130 m, the best performance was an error rate of  $7,2 \cdot 10^{-3}$ , and for 90 m, no errors were detected.

**Index Terms**—Optical Camera Communication, Outdoor Optical Communication, Visible Light Communication.

## I. INTRODUCCIÓN

Las comunicaciones ópticas usando cámaras (OCC - *Optical Camera Communications*) representan uno de los campos de investigación de mayor proyección dentro de las comunicaciones ópticas por luz visible (VLC - *Visible Light Communications*). Esta tecnología cuenta con un gran potencial para formar parte de la evolución de las nuevas redes *Beyond 5G*. En primer lugar, porque suponen un coste de integración muy bajo al utilizar tanto las cámaras fotográficas que actualmente están masivamente integradas en multitud de dispositivos finales de usuario (tales como *smartphones*, cámaras de vigilancia, *dashcam*, entre otros), como la tecnología led, que está ampliamente difundida por su bajo consumo y alta durabilidad.

Fruto de esta versatilidad, las OCC han sido incorporadas en el estándar IEEE 802.15.7r1 [1], donde se contemplan las dos estrategias fundamentales que se utilizan para el desarrollo de estos sistemas, y que varía en función de la técnica de adquisición de imágenes por parte de la cámara. Los sistemas *Global Shutter* (GS) y *Rolling Shutter* (RS). Los primeros utilizan principalmente sensores *Charge-Coupled Device* (CCD) que a la hora de adquirir una nueva imagen exponen todos sus píxeles de forma simultánea. Por el contrario, los sistemas *Rolling Shutter* (RS) basados principalmente en la tecnología

de transistores *Complementary Metal-Oxide-Semiconductor* (CMOS), realizan el escaneo de la imagen línea por línea de píxeles, de forma secuencial con un ligero solapamiento.

En escenarios interiores (oficinas, hogares), la aplicación más destacada para los sistemas OCC a día de hoy es la de posicionamiento por luz visible (VLP - *Visible Light Positioning*), en la que se combina la transmisión de datos y el procesado de imágenes para reconocer la geometría del entorno y vigilar las interacciones entre nodos móviles. Otras aplicaciones de interés son la monitorización inalámbrica de pacientes en hospitales, o en otras instalaciones donde el uso de señales de radiofrecuencia (RF) puede interferir el correcto desempeño de la instrumentación; y el intercambio de datos *peer-to-peer* (P2P) mediante balizas ópticas como alternativa a las comunicaciones de campo cercano (NFC - *Near Field Communications*) [2].

Cuando se plantea el uso de OCC en escenarios exteriores para aplicaciones de *Smart Cities* y control de redes de sensores, hay que tener en cuenta la presencia de fenómenos atmosféricos adversos no controlables tales como precipitaciones de lluvia y/o nieve, turbulencias inducidas por calor, presencia de partículas pequeñas en suspensión (aerosoles tales como vapor de agua, agentes contaminantes, polvo, etc.). Estos fenómenos producen tanto la atenuación como la dispersión temporal de la señal en la dirección del enlace, aumentando la tasa de error en la comunicación. Para hacer frente a estas condiciones se han propuesto distintas soluciones que se pueden dividir entre aquellas que alteran la óptica de la cámara, y las que ajustan de forma efectiva los parámetros internos de configuración del sensor de imagen.

En [3] se validó experimentalmente un enlace en exteriores de aproximadamente 400 m, que hace uso del desenfoque óptico de la cámara, lo que permitió extender la superficie del led emisor e incrementar la tasa de transferencia hasta los 450 bps (bits por segundo). En los experimentos de [4] y [5] se muestran otros ejemplos en los que se compensa el efecto del canal mediante el uso de lentes de magnificación. El primer trabajo, se centró en una aplicación para un entorno vehicular basado en fotodiodos (PD - *photo-diode*) en lugar de cámaras, consiguiendo una distancia de enlace de 40 m condiciones climáticas ideales. En el segundo artículo se utilizó una cámara GS para establecer un enlace con un cartel luminoso situado a una distancia de 328 m con una tasa de transmisión efectiva de 15 bps con un 4 % de error. Por último, en [6] se demuestra el uso de una lente de Fresnel para el establecimiento de un enlace vehicular VLC en un entorno emulado en laboratorio. En otros trabajos previos, [7], [8] se demuestra que el deterioro en la señal producido por la atenuación debida a fenómenos de turbulencia y neblina se pueden mitigar modificando la

V. Matus, V. Guerra, C. Jurado-Verdu, J. Rabadan and R. Perez-Jimenez are with the Institute for Technological Development and Innovation in Communications, Universidad de Las Palmas de Gran Canaria, Spain.

Corresponding author: V. Matus, vmatus@idetic.eu.

This project has received funding from the European Union's Horizon 2020 research and innovation programme under the Marie Skłodowska-Curie grant agreement No 764461.

ganancia analógica del sensor de imagen sin necesidad de alterar la óptica de la cámara.

Sin embargo, en todos estos trabajos anteriormente mencionados se parte de la premisa de que el área proyectada de la fuente luminosa en la imagen afecta un número alto de píxeles, lo que quiere decir, que la proyección geométrica de la lámpara ocupa una porción destacable en la imagen [9], [10]. Esta consideración previa repercute en la distancia máxima de enlace, haciendo que o bien se necesiten superficies luminosas de área muy extensa o el uso de lentes telescópicas lo cual se traduce en una reducción del campo de visión y, por tanto, una penalización en las capacidades de monitorización simultánea de dispositivos.

En este trabajo se demuestra la viabilidad de un enlace GS para exteriores en el que la comunicación sucede a nivel de sub-píxel. El término sub-píxel hace referencia a que el área de proyección de la fuente es menor al área de un píxel. En una discusión preliminar podría asumirse la no viabilidad del enlace en base a que la luz emitida incide únicamente en un píxel. Sin embargo, en este trabajo se demuestra que la energía emitida por el LED afecta a los píxeles contiguos de forma que la señal puede ser recuperada con éxito.

Este artículo se estructura como sigue. El estado del arte en el campo de investigación de OCC se resume en la Sección II. La sección III explica en detalle el modelo de canal OCC y la nueva definición propuesta en este trabajo respecto a los escenarios sub-píxel. La sección IV presenta el diseño experimental y las métricas de interés, mientras que la sección V muestra los resultados obtenidos. Finalmente, en la sección VI se extraen las conclusiones y el potencial impacto de los hallazgos de este trabajo.

## II. ESTADO DEL ARTE

La rama de OCC surge a partir de un subcampo de las comunicaciones ópticas inalámbricas (OWC - *Optical Wireless Communications*) [11] que emplean todo tipo de dispositivos en el espectro óptico incluyendo luz infrarroja, visible y ultravioleta. Destacan en este campo las comunicaciones en espacio libre (FSO - *Free-Space Optics*) [12] que se encuentra en un estado de desarrollo más avanzado y las VLC, que son un tema en creciente desarrollo en los últimos años desde la masificación de las luces LED. OCC aprovecha la vasta disponibilidad de las cámaras digitales, considerablemente más abundantes que PD individuales, pero a la vez con mayores limitaciones de tasa de datos alcanzables. Por ejemplo, se han reportado sistemas VLC basados en PD que sobrepasan los Gbps de rendimiento [13], [14], en cambio, para OCC la tasa de captura de fotogramas de las cámaras convencionales supone una limitante inherente [2], [15], [16]. Se pueden encontrar así trabajos en orientados a la explotación de sistemas de modulación avanzados [17]–[19] para alcanzar mayores tasas de datos.

Tanto sistemas VLC basados en PD, como sistemas OCC basados en cámaras se han propuesto para aplicaciones de *Smart Cities*. Una de las que destaca es posicionamiento (VLP - *Visible Light Positioning*) [20]–[23]. En estos sistemas se aprovecha la alta precisión alcanzable, del orden de decenas de

centímetros, comparada a sistemas de posicionamiento satelital que puede ser de decenas de metros. Los sistemas VLP tienen robustez en espacios cerrados. Estos sistemas además se relacionan con otra importante aplicación, los sistemas de transporte inteligentes utilizando VLC [4], [20], [24], [25].

Las ventajas de OCC frente a sistemas basados en PD se basan en la capacidad de las cámaras de formar imágenes y, por ende, de separar espacialmente las fuentes de luz [26]–[28]. Con esto se pueden mejorar sustancialmente las tasas de datos, si se emplea una topología multipunto-a-punto, como ciertos casos de redes de sensores y de Internet de las cosas (IoT - *Internet of Things*).

Las principales limitaciones de OCC están relacionadas con la formación de imagen y con las tasas de captura, como ya se mencionó. Entre ellas están las distorsiones causadas por la óptica [29], la sincronización entre los tiempos de captura y los de transmisión [9], [10]. Finalmente, en el procesamiento de la imagen surgen otros problemas importantes a considerar, donde destaca el descubrimiento de nodos y su seguimiento en movimiento [30].

Específicamente, sobre la implementación de sistemas sub-píxel como la se propone en este artículo, los autores no conocen otros trabajos donde se reporte una funcionalidad equivalente. Cabe destacar que el escenario sub-píxel se puede considerar como un sistema VLC basado en PD, si se considera que los píxeles de las cámaras están basados en dichos dispositivos [31]. Sin embargo, como se verá en las siguientes secciones, la óptica de la cámara y la dispersión de la luz proveen oportunidad de mejorar la comunicación utilizando los demás PD presentes en la cámara.

## III. MODELO DE CANAL EN OPTICAL CAMERA COMMUNICATION

Como en cualquier sistema OWC, la potencia recibida en un sistema OCC se puede modelar empleando la aproximación de ángulo sólido diferencial (Ecuación 1) [11]. Ya que este trabajo se centra en enlaces en exteriores, se ha añadido un término de pérdidas por extinción  $c(\lambda)$  en el medio (absorción y dispersión) que depende de la longitud de onda  $\lambda$  [32]–[34].

$$P_{rx} = P_{tx} R(\theta, \varphi) \frac{A_{lens}}{d^2} \cos(\Psi) e^{-c(\lambda)d}, \quad (1)$$

donde  $P_{rx}$  es la potencia recibida,  $P_{tx}$  es la potencia transmitida y  $R(\theta, \varphi)$  es el patrón de emisión de la fuente (asumido constante en toda su área) para los ángulos de elevación  $\theta$  y azimut  $\varphi$ . La potencia de llegada al receptor ( $R_x$ ) depende del área de la lente principal  $A_{lens}$ , proyectada según el ángulo de incidencia  $\Psi$  y de la distancia del enlace  $d$ .

En OCC debe considerarse la óptica formadora de imagen de las cámaras. En términos generales y despreciando cualquier efecto de desenfoque, a priori, los sistemas OCC han estado basados en la conservación de la densidad de energía de píxel con la distancia. Esto es, la energía de cada píxel es independiente de la distancia siempre y cuando la proyección de  $T_x$  sea superior a 1 píxel. El concepto subyacente a esta propiedad es la compensación de las pérdidas por propagación esférica con el enfoque de la imagen. Aunque llegue menos energía a la óptica principal de la cámara a medida que

la distancia aumenta (disminución cuadrática), el número de píxeles sobre los que  $T_x$  es proyectado también decrece con el mismo orden, manteniendo la densidad de energía constante sobre el sensor de imagen. Para largas distancias, es fácil demostrar que el número de píxeles  $N_{px}$  sobre los que se proyecta un  $T_x$  de área  $A_{tx}$  depende del campo de visión (FOV - *Field of View*) de la cámara y de la resolución del sensor de imagen, tal y como muestra la Ecuación 2.

$$N_{px} = \frac{N_x N_y}{FOV_x FOV_y} \frac{A_{tx}}{d^2} \quad (2)$$

$N_x$  y  $N_y$  definen la resolución del sensor, mientras que  $FOV_x$  y  $FOV_y$  definen los campos de visión horizontal y vertical de  $R_x$  respectivamente. Uniendo las Ecuaciones 1 y 2, y proyectando la energía sobre el área de un píxel ( $A_{px}$ ) se obtiene la Ecuación 3, la cual resume la energía promedio de un píxel.

$$P_{px} = P_{tx} R(\theta, \varphi) \frac{A_{lens}}{A_{tx}} \cos(\Psi) e^{-c(\lambda)d} \zeta_{xy} A_{px}, \quad (3)$$

donde por conveniencia se ha denominado  $\zeta_{xy}$  a la resolución angular del sensor denotada por el cociente entre sus FOV y la dimensión del mismo. Sin embargo, cuando la proyección de  $T_x$  disminuye por debajo de 1 píxel, el sistema puede comenzar a modelarse como un enlace OWC basado en PD, donde la potencia recibida es directamente proporcional al área de PD iluminada por la proyección (menor a  $A_{px}$ ). El concepto mencionado se resume como sigue:

$$P_{px}^{sub} = P_{px} \cdot N_{px} = P_{rx} \cdot A_{px} \quad (4)$$

Debe entenderse  $N_{px}$  en la Ecuación 4 como un coeficiente de ajuste referido al porcentaje de píxel iluminado. Se observa claramente que la potencia recibida en una situación sub-píxel ( $P_{px}^{sub}$ ) sí depende de la distancia y pasa a comportarse como un enlace OWC tradicional. Una vez concretada la potencia de llegada al sensor, el proceso de conversión debe tenerse en cuenta a la hora de describir la señal OCC dentro de la imagen captada. Las cámaras CMOS trabajan convirtiendo los fotones incidentes en electrones. Por tanto, es conveniente llevar a cabo una conversión de unidades que tenga en cuenta esta particularidad. En la Ecuación 5 se muestra el número de electrones almacenados ( $E_{px}$ ) durante el tiempo de exposición de la captura  $T_{exp}$  (válida para cualquier situación).

$$E_{px} = T_{exp} \int_{\lambda} P_{px}(\lambda) EQE(\lambda) \frac{E_{ph}(\lambda)}{q} d\lambda \quad (5)$$

Nótese que se ha extendido el concepto de potencia de llegada al píxel incluyendo el espectro de emisión de la fuente óptica.  $EQE(\lambda)$  es la eficiencia cuántica externa (EQE - *External Quantum Efficiency*) del sustrato del PD (silicio por lo general),  $E_{ph}(\lambda)$  es la energía del fotón a cada longitud de onda y  $q$  es la carga del electrón. A pesar de que teóricamente un  $T_x$  pequeño situado a larga distancia se presentará como un único punto brillante en la captura, la óptica formadora de imagen no es perfecta, y existe cierta dispersión espacial de la energía. Esta dispersión se modela a través de la *Point Spread Function* (PSF) del sistema, denotada como  $h[n, m]$  ya en el dominio imagen. En esencia,  $h[n, m]$  es la respuesta impulsiva

espacial del sistema, y depende por lo general de la distancia del enlace. Cualquier proyección debe ser convolucionada con ella, por lo que en una situación sub-píxel la región iluminada puede modelarse de la siguiente forma.

$$s[n, m] = G_V \mathfrak{R}(E_{px}) \cdot h[n - n_0, m - m_0] \quad (6)$$

$\mathfrak{R}(\cdot)$  es una función que incluye la conversión analógico-digital,  $G_V$  es la ganancia analógica de la cámara CMOS y  $n_0$  y  $m_0$  son las coordenadas de los píxeles donde  $T_x$  es proyectado. Debe tenerse en cuenta que en una situación ideal,  $h[n, m]$  tiene energía unitaria, por lo que si existe dispersión de energía, el nivel del píxel teórico de la proyección será menor de lo esperado.

En lo referente a la relación señal a ruido (SNR - *Signal-to-Noise Ratio*) de un enlace OCC, la Ecuación 7 la resume, siendo aplicable tanto a situaciones sub-píxel como a las generalmente estudiadas.

$$SNR = \frac{G_V^2 E_{px}^2}{G_V^2 (\sigma_{sh}^2 + \sigma_{th}^2) + \sigma_{adc}^2} \quad (7)$$

Se ha asumido que el factor de corrección  $\gamma$  de la cámara es unitario por simplicidad y sin pérdida de generalidad, así como que el enlace no está saturado (número de electrones almacenados menor que la capacidad del pozo). Las tres contribuciones principales al ruido del enlace OCC son el ruido *shot* ( $\sigma_{sh}^2$ ), el ruido térmico ( $\sigma_{th}^2$ ) y el ruido de cuantificación ( $\sigma_{adc}^2$ ). El efecto de este último puede ser minimizado aplicando el valor óptimo de ganancia analógica, tal y como se demostró en [7], [8]. Los ruidos *shot* se originan por la naturaleza discreta de las partículas que procesa el píxel: fotones y electrones, considerando su aparición aleatoria en el dominio del tiempo y del espacio. Dentro de los ruidos de *shot*, las contribuciones más significativas son el ruido de oscuridad, cuando se generan electrones sin excitación óptica, el ruido *shot* óptico de la propia señal generada por el fotodetector y el ruido de *readout* generado por los circuitos previos al conversor análogo-digital (ADC - *Analog-to-Digital Converter*) [31].

En los enlaces *outdoor* existe otro fenómeno que puede tener un impacto sustancial en el desempeño del sistema. El nivel de iluminación de fondo puede variar, al menos en una situación sub-píxel donde la velocidad viene determinada por la tasa de captura de la cámara, de manera comparable al tiempo de transmisión de una trama. Este efecto será analizado experimentalmente y discutido en la Sección V.

#### IV. METODOLOGÍA

El objetivo principal de este trabajo es demostrar experimentalmente la viabilidad de los enlaces OCC a larga distancia, donde la proyección de los emisores sea menor que un único píxel de la cámara. Como se ha comentado, la tecnología OCC ha sido propuesta como un habilitador para *Smart Cities* e IoT. Sin embargo, hasta la fecha no ha habido trabajos que validen su uso en escenarios realistas sujetos a condiciones como las que se plantean en este trabajo. A largas distancias, el uso de emisores que se proyecten en un gran número de píxeles es inviable.



Fig. 1. Fotos de los componentes del montaje experimental incluyendo vista satelital del escenario en las inmediaciones del IDeTIC obtenida de Cartográfica de Canarias (Grafcan) [35].

Para llevar a cabo la evaluación experimental del enlace sub-píxel, se diseñó un nodo  $T_x$  OCC (Figura 1) alimentado con batería y conmutado por un microcontrolador. Se programaron dos nodos para enviar en bucle tramas de transmisión con la estructura que se muestra en la Figura 2 que contenían 1 *Byte* de *payload* en los que se transmitía secuencialmente los valores desde 0x00 hasta 0xFF. El tiempo de pulso definido para los experimentos fue de 133.33 ms, ofreciendo una tasa binaria de 4 bps. Ambas unidades de transmisión fueron ancladas a dos postes situados a 90 metros y 130 metros de distancia de la cámara respectivamente.

Como  $R_x$  se empleó un sensor de imagen CMOS, modelo Sony IMX219, (RaspiCam v2) controlado por una Raspberry Pi v3. Se grabó la transmisión en un vídeo de 10 minutos de duración empleando un tiempo de exposición de 85  $\mu$ s a mínima ganancia analógica (0 dB) y sin ganancia digital. La tasa de captura de la cámara fue configurada a 30 fps con una resolución de 1920 x 1080 px. Los parámetros experimentales se muestran en la Tabla I.

TABLA I  
PARÁMETROS CLAVE DEL EXPERIMENTO

Módulo	Parámetro	Valor
$T_x$	Diámetro de $T_x$	5 mm
Canal	Dispositivo de transmisión	1 LED blanco estándar
	Distancia ( $d_1$ , $d_2$ )	90 m, 130 m
$R_x$	Sensor de imagen	Sony IMX219 [36]
	Resolución de fotografías	1920 x 1080 px
	Tasa de captura	30 fps
	Tiempo de exposición ( $t_{exp}$ )	85 $\mu$ s

Una vez capturado el vídeo mostrando las emisiones de ambos nodos simultáneamente, la región de interés (ROI - *Region of Interest*) de cada transmisor se definió manualmente, ya que la elaboración de un procedimiento de descubrimiento no era objetivo de este trabajo. Ambas ROI se analizaron estadísticamente para obtener estimaciones de la SNR y de la PSF.

La PSF del sistema en ambos nodos (cercano y lejano) se estimó empleando un procedimiento basado en la correlación. Para ello se detectó el píxel de mayor energía dentro de la ROI correspondiente, y se fijó como referencia. Posteriormente se calculó la correlación de Pearson de los píxeles adyacentes respecto a la referencia. Se observó que la correlación daba valores considerablemente cercanos a la unidad para una región aproximada de 3x3 píxeles, demostrando que la imperfección del sistema óptico puede beneficiar a un enlace OCC sub-píxel. A pesar de que el efecto del *background* subyace al cálculo

de la correlación, la matriz resultante fue asociada a la PSF como una aproximación.

Para llevar a cabo el análisis de la SNR se procesó una ventana deslizante de 150 muestras en la que se ajustó un *Gaussian Mixture Model* (GMM) como el de la Ecuación 8.

$$G_2(x) = \frac{\alpha}{\sigma_0\sqrt{2\pi}}e^{-\frac{(x-\mu_0)^2}{2\sigma_0^2}} + \frac{1-\alpha}{\sigma_1\sqrt{2\pi}}e^{-\frac{(x-\mu_1)^2}{2\sigma_1^2}}, \quad (8)$$

donde  $G_2(x)$  es una mezcla de dos Gaussianas,  $\alpha$  es la proporción de la primera Gaussiana,  $\mu_i$  denota valor esperado y  $\sigma_i$  es desviación típica. Este procedimiento ya ha sido empleado satisfactoriamente en otros trabajos como [37]. Se empleó debido a la alta variación del nivel de *background* en la imagen (Figura 4), la cual podría falsear la estimación de la SNR si se tuviese en cuenta toda la señal capturada para el cálculo. La Ecuación 9 muestra cómo se llevó a cabo la estimación de la SNR.

$$SNR = \frac{1}{2} \frac{|\mu_1 - \mu_0|^2}{\alpha\sigma_0^2 + (1-\alpha)\sigma_1^2} \quad (9)$$

Usando el valor de *background* obtenido en cada ajuste GMM, se calculó la SNR muestra a muestra para posteriormente obtener la SNR esperada del sistema (promedio). Asumiendo que la transmisión es *Non-Return to Zero On-Off Keying* (NRZ-OOK), la tasa de error teórica para cada SNR estimada experimentalmente se calculó empleando la Ecuación 10.

$$BER = \frac{1}{2} \operatorname{erfc} \left( \sqrt{\frac{SNR}{2}} \right), \quad (10)$$

donde  $\operatorname{erfc}(\cdot)$  es la función de error complementario. Tanto el cálculo de la SNR como de la BER fue llevado a cabo para cada color del sensor de imagen (R, G y B) y para tres esquemas de detección: píxel de máxima energía, media (Ecuación 11) y media enfatizada con la aproximación de la PSF (Ecuación 12). El objetivo del promediado espacial es mejorar la SNR al reducir la varianza efectiva de ruido.

$$y_{mean} = \frac{1}{NM} \sum_{i=0}^{N-1} \sum_{j=0}^{M-1} x[i, j] \quad (11)$$

$$y_{emph} = \frac{\sum_{i=0}^{N-1} \sum_{j=0}^{M-1} \rho[i, j] \cdot x[i, j]}{\sum_{i=0}^{N-1} \sum_{j=0}^{M-1} \rho[i, j]} \quad (12)$$

$N$  y  $M$  son el alto y ancho de la ROI considerada para el promediado,  $y_{mean}$  es la señal resultante de la media aritmética,  $y_{emph}$  es la señal resultantes del promediado enfatizado,  $s[i, j]$  es la señal original en la coordenada  $(i, j)$  y  $\rho[i, j]$  es la correlación descrita anteriormente.

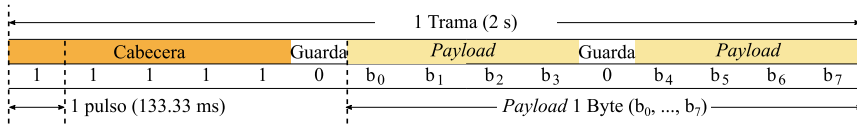


Fig. 2. Formato de trama empleado en el experimento.

IV-A. Algoritmo de detección OCC

Además de estimar la BER teórica, se implementó un algoritmo de detección basado en correladores, uno por cada posible trama enviada (256 en total). El algoritmo lleva a cabo una multiplicación matriz-vector con cada muestra adquirida, para posteriormente encontrar el índice asociado al valor máximo. La matriz de correladores,  $S$ , se formó a partir de la estandarización de los vectores asociados a cada una de las tramas posibles (Ecuación 13).

$$\hat{s}_i = \frac{N s_i - \|s_i\|_{L_0}}{\sqrt{(\|s_i\|_{L_0}) (N - \|s_i\|_{L_0})}}, \quad (13)$$

donde  $\hat{s}_i$  es el vector de la  $i$ -ésima trama, sometido a estandarización estadística, que fuerza la distribución a una de media y desviación típica igual a 0 y a 1, respectivamente.  $s_i$  es el vector original,  $N$  es el tamaño de la trama, el cual en este trabajo es 60 acorde al diseño de la trama y a la frecuencia de muestreo y  $\|\cdot\|_{L_0}$  es la norma  $L_0$  (número de elementos no nulos del vector). Al llevar a cabo la correlación de esta manera, únicamente debe hacerse una multiplicación matriz-vector de orden  $256 \times 60$ , la cual tiene un consumo computacional despreciable. Para que el resultado de la multiplicación se corresponda con la correlación de Pearson y poder definir umbrales en el proceso de sincronización, el *buffer* de longitud 60 sobre el que se aplica el producto es también sometido a estandarización estadística acorde a la Ecuación 14.

$$\hat{y} = \frac{y - \bar{y}}{\sigma_y} \quad (14)$$

Al igual que en el caso anterior,  $\hat{y}$  es el *buffer* de señal de entrada normalizado,  $y$  es el original,  $\bar{y}$  es la media aritmética y  $\sigma_y$  la desviación típica. Acorde a la definición de la correlación de Pearson, al hacer el producto  $S \cdot \hat{y}$  se obtiene un vector de correlaciones  $c$  que puede ser empleado para detectar el símbolo transmitido. La Figura 3 ilustra el proceso de detección.

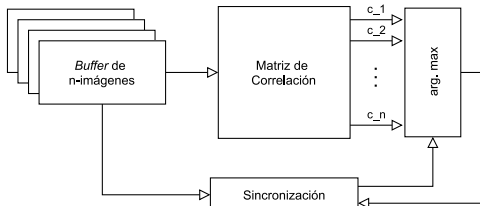


Fig. 3. Diagrama de flujo de  $R_x$ .

El esquema de sincronización empleado ha sido el siguiente. Una vez se llena el *buffer*, se espera a la primera trama

que supere la correlación umbral,  $c_{th}$  de 0.94. Este valor fue escogido de manera empírica, usando los procedimientos desarrollados en [7], [8]. El *Byte* transmitido se decodifica directamente buscando el argumento máximo del vector  $c$ . Tras dicha detección, se inhibe el proceso de decisión durante las siguientes 55 muestras y posteriormente se almacenan pares correlación-*Byte* decodificado para las siguientes 10 muestras. Dentro de ese *buffer* secundario se hace la búsqueda del instante de mayor correlación y se asume que el *Byte* asociado se corresponde a aquel con mayor verosimilitud. El número de muestras descartadas a partir de este momento será 50 más el índice del valor de máxima correlación encontrado en el *buffer* secundario.

V. RESULTADOS

Como se comentó anteriormente, se capturó un vídeo de 10 minutos en el que dos nodos OCC situados a dos distancias diferentes estuvieron enviando de manera consecutiva información desde el *Byte* 0x00 hasta el *Byte* 0xFF. La Figura 4 muestra, a modo de ejemplo, la forma de onda capturada para ambos nodos en el píxel de máxima energía. Como puede observarse, el nivel de *background* varió considerablemente durante la transmisión, además de la ganancia del canal, visible en la amplitud variable de la señal recibida.

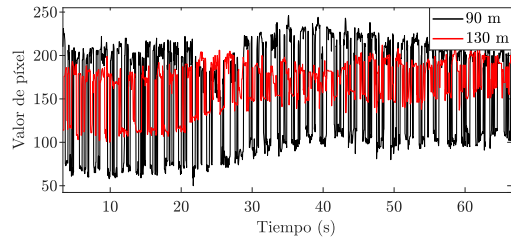


Fig. 4. Ejemplo de forma de onda capturada en el píxel de máxima energía para los dos nodos desplegados.

Al estar en una situación sub-píxel en la que el FOV de  $R_x$  es tan reducido (orden de miliestereoradianes), cualquier perturbación atmosférica o vibración que afecte al alineamiento puede tener un impacto en el enlace. Un ejemplo de imagen capturada con ambos nodos resaltados se muestra en la Figura 5. Este resultado demuestra que la pequeña dimensión de  $T_x$  y el amplio campo de visión de  $R_x$  permitirían el uso de OCC para la monitorización de una gran cantidad de sensores (varias centenas) de manera simultánea, explotando la capacidad de multiplexación espacial inherentes a las cámaras.

El procedimiento de aproximación de la PSF de los enlaces se aplicó a las señales capturadas en color convertidas a escala de grises (luminancia), obteniendo los resultados de la



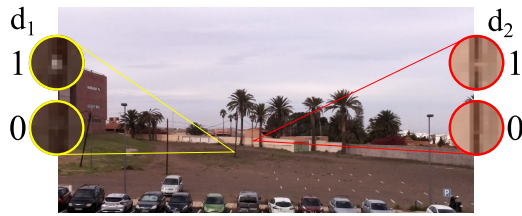


Fig. 5. Ejemplo de imagen capturada en el entorno de pruebas en exteriores. Las imágenes incrustadas en círculos muestran los estados encendido y apagado de ambos nodos.

Figura 6. Aunque la proyección de los nodos  $T_x$  (5 mm de diámetro) sobre el sensor de imagen es menor a un único píxel, se observa que existe una región en la cual la correlación es suficiente como para asegurar que existe señal. Esta dispersión en la energía ocurre debido a la imposibilidad de enfocar por completo toda la energía proveniente de un cierto ángulo sólido en un único píxel. Además, la PSF del enlace a 90 metros tiene mayor dispersión que la PSF a 130 metros, posiblemente debido a la distancia focal fijada durante la captura de los vídeos, así como a las imperfecciones del sistema de lentes.

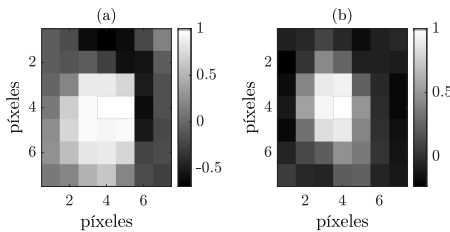


Fig. 6. Estimación de la PSF a partir de la correlación respecto al píxel de mayor energía. (a) PSF estimada a 90 metros. (b) PSF estimada a 130 metros.

La Figura 7 muestra las formas de onda asociadas a los píxeles (4,4) y (3,4) de la PSF para el enlace lejano. A medida que el píxel observado se aleja del de máxima energía, la correlación se pierde y la onda asociada al píxel queda únicamente definida por la variación de la iluminación de fondo de la imagen.

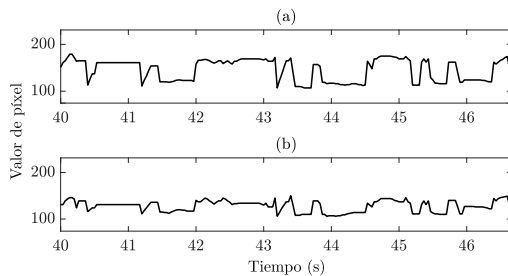


Fig. 7. Formas de onda para el nodo lejano (130 metros). (a) Píxel de máxima energía o (4,4) de la PSF. (b) Píxel (3,4) de la PSF.

Como se explicó en la Sección IV, se obtuvieron la SNR y la BER de ambos nodos, tanto teórica como experimental y empleando diferentes esquemas de promediado espacial. La Tabla II muestra los resultados para el esquema de detección basado en 1 píxel (de máxima energía), mientras que la Tabla III muestra los resultados para el esquema basado en la media de todos los píxeles de la región de la PSF y la Tabla IV muestra los resultados usando el esquema enfatizado por la PSF.

El nodo cercano alcanzó una SNR experimental máxima de 20 dB en el canal verde (G - Green) utilizando el método de promediado enfatizado usando la PSF estimada. Su peor valor de SNR alcanzado fue de 17,1 dB para el canal rojo (R - Red) usando el método de cálculo basado sólo en el píxel de mayor correlación en la PSF. La BER fue estimada teóricamente como inferior a  $10^{-12}$ , dados los altos valores de SNR. En el experimento no se encontraron errores con ninguno de los métodos de promediado (el \* indica que la BER es menor a  $3.33 \cdot 10^{-3}$ ). Esto se debe a que no se ejecutó un número suficiente de experimentos.

En el caso del nodo lejano, donde la proyección del píxel en el sensor es comparablemente menor, la SNR fluctuó entre 8,1 dB y 13 dB, para el canal G en esquema 1-píxel y el R en esquema enfatizado, respectivamente. La BER teórica estimada fue del orden de  $10^{-3}$ ,  $10^{-5}$  y  $10^{-6}$  para los esquemas 1-píxel, promediado y enfatizado, respectivamente. En este caso los valores de BER son más altos y por lo tanto, hacen falta menos experimentos por ejecutar. Las BER experimentales obtenidas para este experimento discreparon bastante de los niveles teóricos, siendo por ejemplo, una diferencia de 1 hasta 3 órdenes de magnitud. Ésto puede deberse a la naturaleza no-estacionaria del canal, que afecta más en este caso de baja SNR, relativamente, y que no es superada de manera efectiva por el sistema de detección.

TABLA II  
MÉTRICAS EN ESQUEMA 1-PÍXEL

Métrica	Posición	Canal R	Canal G	Canal B
SNR exp.	$d_1$	17,1 dB	17,3 dB	17,3 dB
SNR exp.	$d_2$	8,1 dB	8,1 dB	8,2 dB
BER teórica	$d_1$	$< 10^{-12}$	$< 10^{-12}$	$< 10^{-12}$
BER teórica	$d_2$	$5,50 \cdot 10^{-3}$	$5,50 \cdot 10^{-3}$	$5,10 \cdot 10^{-3}$
BER exp.	$d_1$	0*	0*	0*
BER exp.	$d_2$	$2,22 \cdot 10^{-2}$	$2,22 \cdot 10^{-2}$	$8,9 \cdot 10^{-3}$

TABLA III  
MÉTRICAS EN ESQUEMA PROMEDIADO

Métrica	Posición	Canal R	Canal G	Canal B
SNR exp.	$d_1$	19,6 dB	19,9 dB	19,7 dB
SNR exp.	$d_2$	12,6 dB	12,3 dB	12,3 dB
BER teórica	$d_1$	$< 10^{-12}$	$< 10^{-12}$	$< 10^{-12}$
BER teórica	$d_2$	$9,96 \cdot 10^{-6}$	$1,88 \cdot 10^{-5}$	$1,88 \cdot 10^{-5}$
BER exp.	$d_1$	0*	0*	0*
BER exp.	$d_2$	$1,20 \cdot 10^{-2}$	$1,20 \cdot 10^{-2}$	$9,60 \cdot 10^{-3}$

## VI. CONCLUSIONES

El objetivo fundamental de este trabajo es demostrar la viabilidad de los enlaces OCC sub-píxel a través de una

TABLA IV  
MÉTRICAS EN ESQUEMA ENFATIZADO

Métrica	Posición	Canal R	Canal G	Canal B
SNR exp.	$d_1$	19,7 dB	20,0 dB	19,8 dB
SNR exp.	$d_2$	13,0 dB	12,9 dB	12,5 dB
BER teórica	$d_1$	$< 10^{-12}$	$< 10^{-12}$	$< 10^{-12}$
BER teórica	$d_2$	$3,97 \cdot 10^{-6}$	$5,03 \cdot 10^{-6}$	$1,24 \cdot 10^{-5}$
BER exp.	$d_1$	0*	0*	0*
BER exp.	$d_2$	$9,60 \cdot 10^{-3}$	$9,60 \cdot 10^{-3}$	$7,2 \cdot 10^{-3}$

validación experimental en un escenario realista. Una de las promesas recurrentes de esta tecnología es la posibilidad de usar cámaras en *Smart Cities* para aplicaciones de monitorización masiva de sensores. Sin embargo, hasta ahora los sistemas OCC se han basado en el uso de lámparas de gran tamaño, complementadas con óptica de alta ganancia (objetivos de alta distancia focal), para poder hacer uso de las técnicas RS. No obstante, en los casos de uso que se proponen en este trabajo, la velocidad de transmisión es un factor no crítico, por lo que se permite la explotación de la inherente capacidad de multiplexación espacial de las cámaras.

Para validar la hipótesis de partida, se diseñó un sistema experimental en que la proyección de cada nodo emisor ( $T_x$ ) sobre el sensor de imagen fuese de menor tamaño que un único píxel. Se construyeron dos nodos transmisores alimentados con batería, transmitiendo una secuencia fácilmente decodificable modulada usando NRZ-OOK y un nodo  $R_x$  basado en una cámara comercial situada a larga distancia. Se probaron dos enlaces a distancias de 90 m y 130 m.

El sistema alcanzó una SNR relativamente igual para los canales rojo, verde y azul, con valores de aproximadamente 17 dB y 8 dB para 90 m y 130 m, respectivamente. Usando el mejoramiento por PSF enfatizado se incrementaron estos valores a 20 dB y 13 dB. Considerando que se utilizó la técnica NRZ-OOK se estimó la cota teórica de la BER para cada distancia y se puede observar que la BER experimental dista considerablemente para el caso  $d_2$  dado que el canal es no estacionario. Para el caso  $d_1$  no se encontró ningún error durante los experimentos.

El esquema de comunicación presentado en este trabajo puede escalarse mediante el aumento de nodos transmisores y el uso de mayores velocidades de captura de fotogramas, alcanzando tasas de bits del orden de decenas de kbps compartida entre los nodos. Las características que se muestran en este trabajo hacen a los sistemas OCC sub-píxel particularmente atractivos para su aplicación en *Smart Cities* como por ejemplo en la monitorización de sensores en entornos industriales, a distancias de varias decenas de metros y cargando datos a baja velocidad a un nodo central basado en una cámara comercial que podría ser simultáneamente un equipo de vigilancia, dado que los fotogramas contienen tanto los datos como la imagen del entorno. La eficiencia energética de los LED y la implementación simple de la modulación NRZ-OOK reducen la complejidad y consumo de los nodos transmisores, que en redes de sensores están limitados energéticamente. Además, este tipo de esquemas podría utilizarse en interiores, a pequeñas distancias, aprovechando luces micro-LED aún más

bajas en consumo, para aplicaciones IoT de monitorización de máquinas en entornos de hogar, oficina.

## REFERENCIAS

- [1] IEEE Standard Association, "IEEE standard for local and metropolitan area networks-part 15.7: short-range wireless optical communication using visible light," *IEEE: Piscataway, NJ, USA*, pp. 1–309, 2011.
- [2] N. Saeed, S. Guo, K.-H. Park, T. Y. Al-Naffouri, and M.-S. Alouini, "Optical camera communications: Survey, use cases, challenges, and future trends," *Physical Communication*, vol. 37, p. 100900, 2019.
- [3] E. Eso, S. Teli, N. B. Hassan, S. Vitek, Z. Ghassemlooy, and S. Zvanovec, "400 m rolling-shutter-based optical camera communications link," *Opt. Lett.*, vol. 45, pp. 1059–1062, Feb 2020.
- [4] M. Karbalayghareh, F. Miramirkhani, H. B. Eldeeb, R. C. Kizilirmak, S. M. Sait, and M. Uysal, "Channel modelling and performance limits of vehicular visible light communication systems," *IEEE Transactions on Vehicular Technology*, vol. 69, no. 7, pp. 6891–6901, 2020.
- [5] P. Chavez-Burbano, V. Guerra, J. Rabadan, and R. Perez-Jimenez, "Optical camera communication for smart cities," in *2017 IEEE/CIC International Conference on Communications in China (ICCC Workshops)*, pp. 1–4, 2017.
- [6] Y. H. Kim, W. A. Cahyadi, and Y. H. Chung, "Experimental demonstration of vlc-based vehicle-to-vehicle communications under fog conditions," *IEEE Photonics Journal*, vol. 7, no. 6, pp. 1–9, 2015.
- [7] V. Matus, V. Guerra, C. Jurado-Verdu, S. Teli, S. Zvanovec, J. Rabadan, and R. Perez-Jimenez, "Experimental evaluation of an analog gain optimization algorithm in optical camera communications," in *2020 12th International Symposium on Communication Systems, Networks Digital Signal Processing (CSNDSP)*, pp. 1–5, 2020.
- [8] V. Matus, E. Eso, S. R. Teli, R. Perez-Jimenez, and S. Zvanovec, "Experimentally derived feasibility of optical camera communications under turbulence and fog conditions," *Sensors*, vol. 20, p. 757, Jan 2020.
- [9] C. Jurado-Verdu, V. Matus, J. Rabadan, V. Guerra, and R. Perez-Jimenez, "Correlation-based receiver for optical camera communications," *Opt. Express*, vol. 27, pp. 19150–19155, Jul 2019.
- [10] C. Jurado-Verdu, V. Guerra, J. Rabadan, R. Perez-Jimenez, and P. Chavez-Burbano, "Rgb synchronous vlc modulation scheme for occ," in *2018 11th International Symposium on Communication Systems, Networks Digital Signal Processing (CSNDSP)*, pp. 1–6, July 2018.
- [11] Z. Ghassemlooy, W. Popoola, and S. Rajbhandari, *Optical wireless communications: system and channel modelling with Matlab*. CRC press, 2019.
- [12] M. A. Khalighi and M. Uysal, "Survey on free space optical communication: A communication theory perspective," *IEEE Communications Surveys Tutorials*, vol. 16, no. 4, pp. 2231–2258, 2014.
- [13] P. H. Pathak, X. Feng, P. Hu, and P. Mohapatra, "Visible light communication, networking, and sensing: A survey, potential and challenges," *IEEE communications surveys & tutorials*, vol. 17, no. 4, pp. 2047–2077, 2015.
- [14] Y. Almadani, D. Plets, S. Bastiaens, W. Joseph, M. Ijaz, Z. Ghassemlooy, and S. Rajbhandari, "Visible light communications for industrial applications—challenges and potentials," *Electronics*, vol. 9, no. 12, 2020.
- [15] N. Saha, M. S. Iftekhar, N. T. Le, and Y. M. Jang, "Survey on optical camera communications: challenges and opportunities," *IET Optoelectronics*, vol. 9, pp. 172–183(11), October 2015.
- [16] N. T. Le, M. Hossain, and Y. M. Jang, "A survey of design and implementation for optical camera communication," *Signal Processing: Image Communication*, vol. 53, pp. 95–109, 2017.
- [17] J. L. H. Rios, "Experimental validation of inverse mppm modulation for dimming control and data transmission in visible light communications," *IEEE Latin America Transactions*, vol. 100, no. 1e, 2020.
- [18] O. I. Younus, N. Bani Hassan, Z. Ghassemlooy, P. A. Haigh, S. Zvanovec, L. N. Alves, and H. L. Minh, "Data rate enhancement in optical camera communications using an artificial neural network equaliser," *IEEE Access*, vol. 8, pp. 42656–42665, 2020.
- [19] P. Haigh, P. Chvojka, Z. Ghassemlooy, S. Zvanovec, and I. Darwazeh, "Visible light communications: multi-band super-nyquist cap modulation," *Optics express*, vol. 27, no. 6, pp. 8912–8919, 2019.
- [20] A. L. R. Gonçalves, Á. H. A. Maia, M. R. Santos, D. A. de Lima, and A. de Miranda Neto, "Visible light positioning and communication methods and their applications in the intelligent mobility," *IEEE Latin America Transactions*, vol. 100, no. 1e, 2021.
- [21] N. Chaudhary, O. I. Younus, L. N. Alves, Z. Ghassemlooy, S. Zvanovec, and H. Le-Minh, "An indoor visible light positioning system using tilted leds with high accuracy," *Sensors*, vol. 21, no. 3, 2021.

- [22] P. Palacios Játiva, M. Román Cañizares, C. A. Azurdia-Meza, D. Zabala-Blanco, A. Dehghan Firoozabadi, F. Seguel, S. Montejo-Sánchez, and I. Soto, "Interference mitigation for visible light communications in underground mines using angle diversity receivers," *Sensors*, vol. 20, no. 2, 2020.
- [23] D. Iturralde, C. Azurdia-Meza, N. Krommenacker, I. Soto, Z. Ghassemlooy, and N. Becerra, "A new location system for an underground mining environment using visible light communications," in *2014 9th International Symposium on Communication Systems, Networks & Digital Sign (CSNDSP)*, pp. 1165–1169, IEEE, 2014.
- [24] R. M. Marè, C. L. Marte, C. E. Cugnasca, O. G. Sobrinho, and A. S. dos Santos, "Feasibility of a testing methodology for visible light communication systems applied to intelligent transport systems," *IEEE Latin America Transactions*, vol. 100, no. 1e, 2020.
- [25] M. Elamassie, M. Karbalayghareh, F. Miramirkhani, R. C. Kizilirmak, and M. Uysal, "Effect of fog and rain on the performance of vehicular visible light communications," in *2018 IEEE 87th Vehicular Technology Conference (VTC Spring)*, pp. 1–6, 2018.
- [26] S. R. Teli, S. Zvanovec, R. Perez-Jimenez, and Z. Ghassemlooy, "Spatial frequency-based angular behavior of a short-range flicker-free mimo-occ link," *Appl. Opt.*, vol. 59, pp. 10357–10368, Nov 2020.
- [27] S. R. Teli, V. Matus, S. Zvanovec, R. Perez-Jimenez, S. Vitek, and Z. Ghassemlooy, "The first study of mimo scheme within rolling-shutter based optical camera communications," in *2020 12th International Symposium on Communication Systems, Networks and Digital Signal Processing (CSNDSP)*, pp. 1–5, 2020.
- [28] Nam-Tuan Le and Yeong Min Jang, "Performance evaluation of mimo optical camera communications based rolling shutter image sensor," in *2016 Eighth International Conference on Ubiquitous and Future Networks (ICUFN)*, pp. 140–144, 2016.
- [29] A. Ashok, S. Jain, M. Gruteser, N. Mandayam, W. Yuan, and K. Dana, "Capacity of pervasive camera based communication under perspective distortions," in *2014 IEEE International Conference on Pervasive Computing and Communications (PerCom)*, pp. 112–120, IEEE, 2014.
- [30] J. Shi, J. He, Z. Jiang, Y. Zhou, and Y. Xiao, "Enabling user mobility for optical camera communication using mobile phone," *Optics express*, vol. 26, no. 17, pp. 21762–21767, 2018.
- [31] T. Kuroda, *Essential Principles of Image Sensors*. CRC Press, 2017.
- [32] A. Ishimaru, *Electromagnetic wave propagation, radiation, and scattering: from fundamentals to applications*. John Wiley & Sons, 2017.
- [33] D. Kedar and S. Arnon, "Urban optical wireless communication networks: The main challenges and possible solutions," *Communications Magazine, IEEE*, vol. 42, pp. S2 – S7, 06 2004.
- [34] D. Kedar and S. Arnon, "The positive contribution of fog to the mitigation of pointing errors in optical wireless communication," *Applied Optics*, vol. 42, no. 24, pp. 4946–4954, 2003.
- [35] Cartográfica de Canarias (GRAFCAN), "Sistema de información territorial de Canarias."
- [36] Sony Corporation, *IMX219PQH5-C, Diagonal 4.60 mm (Type 1/4.0) 8 Mega-Pixel CMOS Image Sensor with Square Pixel for Color Cameras, Datasheet*. Sony Corporation, 2014.
- [37] V. Matus, V. Guerra, S. Zvanovec, J. Rabadan, and R. Perez-Jimenez, "Sandstorm effect on experimental optical camera communication," *Appl. Opt.*, vol. 60, pp. 75–82, Jan 2021.



**Vicente Matus** obtuvo el grado de Ingeniero Eléctrico en 2018 en la Universidad de Chile. En la actualidad es un becario de doctorado en el proyecto Marie Skłodowska-Curie Innovative Training Network VisIoN (G.A. 764461) en Instituto Universitario IDETIC de la ULPGC, España. Su campo de investigación se enfoca en las comunicaciones ópticas mediante cámaras y sus aplicaciones en redes de sensores.



**Victor Guerra** MEng. en Telecomunicaciones (ULPGC, 2010), MSc. en Sistemas Inteligentes (ULPGC, 2012) y PhD (ULPGC, 2016). Premio Extraordinario de Doctorado en la Rama de Ingeniería y Arquitectura (ULPGC, 2018). Investigador de la División de Fotónica y Comunicaciones del Instituto Universitario IDETIC desde 2008. Ha participado en 4 proyectos H2020, 3 proyectos nacionales y 2 de carácter regional, además de en varios contratos con empresas privadas de alta relevancia. Ha publicado más de 50 artículos en revistas indexadas y comunicaciones en congresos. Sus intereses actuales de investigación son las comunicaciones ópticas inalámbricas (atmosféricas y submarinas), las comunicaciones ópticas por cámara y las aplicaciones de inteligencia artificial.



**Cristo Jurado-Verdu** obtuvo el máster en Ingeniería en Tecnologías de Telecomunicación en la ULPGC en 2019, España. Actualmente, está realizando su doctorado en comunicaciones ópticas inalámbricas en el Instituto Universitario IDETIC de la ULPGC. Su investigación está enfocada al desarrollo de potenciales aplicaciones de las comunicaciones ópticas basadas en cámara. Sus intereses están relacionados con la optimización de firmware embebido, la automatización industrial, y la implementación de aplicaciones de visión artificial.



**José Rabadan** es Ingeniero de Telecomunicación (1995) y Doctor (2000) por la Universidad de Las Palmas de Gran Canaria, donde actualmente es profesor e investigador adscrito al Instituto Universitario IDETIC. Sus intereses de investigación se enmarcan en el campo de las comunicaciones ópticas inalámbricas, en los sistemas de comunicación por luz visible y comunicaciones ópticas con cámaras, donde trabaja en esquemas de codificación y modulación de alto rendimiento y en técnicas de estimación de canales. Ha sido investigador en diferentes proyectos nacionales e internacionales financiados por administraciones y empresas nacionales y europeas. También es autor de 3 capítulos de libros, más de 30 artículos en revistas internacionales y más de 90 ponencias en congresos.



**Rafael Perez-Jimenez** Madrid 1965. Eng. y MSc. (UPM, 1991), PhD (ULPGC 1995 y ULL en 2020), catedrático en la ULPGC desde 2003. Director del Instituto Universitario IDETIC de la ULPGC entre 2008 y 2020. Ha participado en 9 proyectos de investigación internacionales, más de 20 proyectos nacionales y una veintena de contratos relevantes con empresas y administraciones. Ha publicado 4 libros docentes, 5 capítulos de libro y más de 250 artículos, comunicaciones y ponencias en congresos internacionales. Su área de especialización corresponde al desarrollo de sistemas de comunicaciones ópticas para redes de sensores y enlaces de media/baja velocidad, y a la caracterización de canales ópticos en interiores y en sistemas móviles. Actualmente es coordinador dentro del área de Tecnología de la Información y Comunicaciones de la Agencia Estatal de Investigación de España.



This appendix chapter includes the works presented by the author in conference proceedings during the development of this thesis. In the following pages, the camera-ready full papers are attached.

# Simulation of Rolling Shutter Acquisition in Optical Camera Communications

V. Matus, V. Guerra, C. Jurado-Verdu, J. Rabadan, and R. Perez-Jimenez  
 IDeTIC-ULPGC, PCT Tafira, 35017, Las Palmas de Gran Canaria, Spain.  
 Email: {vmatus, vguerra, cjurado, jrabadan, rperez}@idetec.eu

**Abstract**—The rolling shutter (RS) acquisition mechanism performed by the majority of the digital cameras included in portable devices has been exploited to make receivers for visible light communications (VLC). They are able to decode signals of frequencies higher than the frame rate of the camera, which is a limitation when using global shutter sensors. Based on experience with an experimental optical camera communications system, a simulation of rolling shutter receiver for OCC has been developed. This simulator uses a color-multiplexed on-off keying (OOK) modulation, along with a radiance pattern for the LED source, to generate transmitted signals. Then, a simplified camera optics model translates them into received signals, to which the RS simulation is applied, delivering synthetic camera frames.

**Index Terms**—Optical Camera Communications, Rolling Shutter

## I. INTRODUCTION

The opportunity of exploiting mobile camera technology as receivers for Visible Light Communications (VLC) has been explored in the recent years since the publication of seminal paper [1]. The principle is to take frames with the camera sensor and decode different states of modulated light sources after processing these frames.

The video-recording capabilities of cameras, yielding up to hundreds of frames per second (fps), along with the ability to run heavy image processing algorithms, have enabled researchers to implement links between low-speed VLC lamps and digital cameras. The decoding stages are purely based on software, making Optical Camera Communications (OCC) a technology that can take advantage of already deployed end-user devices such as Light Emitting Diodes (LED) and smartphones.

In this stage of OCC technology, simulating systems is a crucial step for designing and testing new devices and algorithms. CamComSim by A. Duque *et al.* [2] gives a tool for the estimation of bit and packet performance of OCC links, allowing the test of higher layer protocols. That work was experimentally validated with a test bed in which the alignment between transmitter and receiver is assumed perfect. In CamComSim, the distance between transmitter and receiver can be up to 40 cm. It allows to use only a circular shape for the LED (the diameter can be changed). In the level of the optical phenomena, [3] proposes a geometrical model for studying non-aligned LED and camera positions, along

This project has received funding from the European Union's Horizon 2020 research and innovation programme under the Marie Skłodowska-Curie grant agreement No 764461

with the use of a Point Spread Function (PSF) to model the blurriness of the picture by using parameters obtained from camera radiometric response database, obtaining simulated images of multiple LED sources.

In this paper a simulator of the rolling shutter mechanism of an OCC setting is presented. The work comprises computational models for transmitter radiance, channel propagation, camera optics, and the process of RS. The main objective is to reproduce the line-wise scanning of VLC sources and to output synthesized image frames. This simulator is a useful tool for testing and validating OCC algorithms and hardware since it allows to set up a variety of different scenarios while preserving the signal synchronization between the source and the receiver.

The next sections of this manuscript are distributed as follows. Section II shows the basic principles of the communications chain that is going to be simulated. Section III explains the way each block is simulated and what the computation delivers. Finally, Section IV exposes the conclusions of this work.

## II. SYSTEM DESCRIPTION

### A. Transmitter

The transmitters consist of red-green-blue (RGB)-LED light sources with arbitrary shape and radiation pattern, emitting OOK-encoded light signals independently over the three color channels. In the literature, the radiation pattern of an LED is assumed to be Lambertian [4], but it is important to notice that the commercial LED-based lamps usually integrate a variety of optical pieces, such as reflectors and lenses, that modify this pattern consequently. Nonetheless, it is possible to obtain radiation measurements of lighting devices from manufacturers under the Illuminating Engineering Society (IES) or EULUMDAT formats. These files provide a numerical definition of the lamps. Although in this work it has been assumed that the radiation pattern is uniform within the emitter area, generally it is defined as  $I(x, y, \theta, \phi)$ .

The shape of the emitter is important in OCC, since its projection over the sensor of the receiver determines the pixels that is going to illuminate. In this work, the shape of LED transmitters is assumed a flat area, and it has been defined by the perimeter line of it  $\Gamma_{Tx}$ , which is a tuple of vertices. Typical VLC systems consider the emitters as point sources since their areas are much smaller than the projected area of the receiver's Field Of View (FOV) at the emitter's plane.

Nevertheless, in OCC, since each pixel presents equivalent FOV in the range of several milliradians, the situation exposed above does not occur.

### B. Optics

Position and orientation of transmitters (Tx) and receivers (Rx) are modeled using linear algebra in order to create a realistic scene. The distance between Tx and Rx is assumed long enough to perform the differential solid angle approximation ( $d\Omega \approx A_{lens}/d^2$ ).

The optical system has been modeled using Ray Transfer Matrix (RTM) equations. The main limitation of this approach is that its accuracy is severely diminished for non-paraxial rays (incident angles above  $30^\circ$ ). RTM is based on  $2 \times 2$  matrices which model how optical rays travel through the optical system. Since RTM assumes that  $\sin \theta \approx \theta$ , and the refraction (or reflection) plane is conserved ( $\phi_{in} = \phi_{out}$ ), the output radial deviation  $y_o$  and angle  $\theta_o$  can be expressed as Eq. 1.

$$\begin{pmatrix} y_o \\ \theta_o \end{pmatrix} = \begin{pmatrix} A & B \\ C & D \end{pmatrix} \begin{pmatrix} y_i \\ \theta_i \end{pmatrix} \quad (1)$$

This ABCD matrix is the product of all the individual matrices which compose the optical system (Eq. 2).

$$\begin{pmatrix} A & B \\ C & D \end{pmatrix} = \prod_i \begin{pmatrix} A & B \\ C & D \end{pmatrix}_i \quad (2)$$

### C. Receivers

Cameras are essentially an imaging sensor attached to an image-forming array of lenses. It is assumed that the lens array of the camera can be reduced to one equivalent lens. Furthermore, all the incident power is projected over the sensor without losses. Equation 3 describes the incident power as follows:

$$P_{Rx} = P_{Tx} \frac{m+1}{2\pi} \cos \theta \cdot \frac{A_{lens} \cos \Psi}{d^2}, \quad (3)$$

where  $P_{Tx}$  is the transmitted power,  $m$  is the degeneration factor of the Lambertian pattern (directivity),  $\theta$  is the emission angle,  $A_{lens}$  is the main lens area,  $\Psi$  is the incident angle, and  $d$  the link range.

The projected area in pixels  $N_{px}$  of a distant source depends on the receiver's FOV and the sensor resolution. Several works treat this mathematically [5], but in this work, a generic simulation framework has been defined, and the projected area has been numerically calculated using Eq. 1 constrained to the optical axis ( $y_i = 0$ ). The resulting projection of  $\Gamma_{Tx}$  has been binarized, defining a mask of ones within the projected area and zeroes otherwise. Due to the conservation of the *etendue*, the optical power at each pixel is:

$$P_{px} = \frac{P_{Rx}}{N_{px}}. \quad (4)$$

The Point Spread Function (PSF) of an optical system is its spatial impulse response, which describes how energy is spread by the system. If no losses are taken into account,

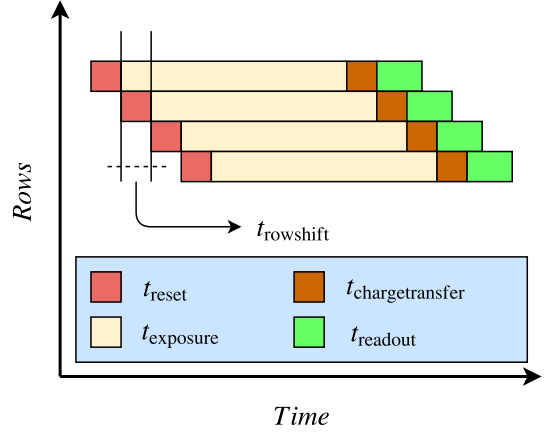


Fig. 1. Illustration of row-by-row timings in RS acquisition mode.

the energy of the PSF must be unitary. From the locality principle, it can be assumed that the PSF of each point of the surface is the same. Therefore, the resulting energy distribution  $I_{Rx}(x, y)$  is the convolution of the Mask  $M(x, y)$  with the PSF  $h(x, y)$ , weighed by the pixel power (Eq. 5).

$$I_{Rx}(x, y) = P_{px} \int_X \int_Y M(\alpha, \beta) h(x - \alpha, y - \beta) d\alpha d\beta \quad (5)$$

Finally, the input power is filtered by the Bayer filter array, separating the image spectrum into R, G, and B components. In addition, the optoelectrical conversion is carried out generating a photo-current dependent on the input spectrum. For each pixel, Eq. 6 is applied:

$$i(x, y, c) = I_{Rx}(x, y) \int_{\lambda} \bar{S}(x, y, \lambda) F_c(\lambda) R(\lambda) d\lambda, \quad (6)$$

where  $i(x, y, c)$  is the output pixel current at the  $c$ -th channel,  $\bar{S}(x, y, \lambda)$  is the pixel's energy-normalized input spectrum,  $F_c(\lambda)$  is the  $c$ -th channel filter response, and  $R(\lambda)$  is the substrate's responsivity (typically Silicon).

The majority of Complementary Metal-Oxide Semiconductor (CMOS) based imaging sensors for digital cameras operate in RS acquisition mode. In this mode, the sensor scans row-by-row of pixels (line-wise) the entire image, with a delay between each row. This scan process is tied to the system clock tick and limited by the sampling rate of the Analog to Digital converter, A/D. In this mode, the whole time the camera is on, the pixel sensors continuously integrates the light that falls into their surface, until a reset signal discharges them. This reset signal acts over an entire row of pixels during a short  $t_{reset}$  time. After resetting, the row of pixels is exposed during a  $t_{exposure}$  time. Finally every pixel is read out by the ADC,  $t_{readout}$ . This procedure is repeated for each row. The time between the start of one row to the consecutive one it is called  $t_{rowshift}$ , and is generally smaller than the exposure time, thus

producing an overlapping between the row scanning times, as shown in Fig. 1.

### III. IMPLEMENTATION

The implementation of the simulator has been carried out using Python (with Numpy, Scipy and Matplotlib libraries). The experimental setup shown in a previous work [6] was modified and used to define key parameters of the simulation. Real image frames were taken using an experimental setup, shown in Fig. 3, which is comprised by a Raspberry Pi computer equipped with its camera and display, and a self-made VLC lamp with RGB LED stripes and a front-end that allows using switching modulations like OOK.

In the following of this section, the main steps of the simulator are explained. The flow diagram shown in Fig. 2 is useful to understand the whole process. From the side of the receiver (camera) an image mask and the PSF from the source (LED) are calculated and convoluted into a power-spread or power distribution frame, as explained in Section II. From the side of the source (LED), random data is generated and converted into a time domain signal that travels through the channel and reaches the sensor. Finally, the RS process takes place by integrating the signal in various times, one for each line, as shown in Fig. 1.

#### A. Preparation of Energy Distribution Frame

The calculation of Mask and the PSF can be understood by the following point of view: the Mask is made from projecting the source's visible area over the frame through the center point of the lens of the camera, while the PSF is made from projecting one point of the source over the area of the frame. All the projections are made using the RTM of the system, where inputs  $y, \theta$  on the lens are computed using coordinates systems relative to source and destination, *i.e.*, calculating point-to-point vectors and using rotation-translation linear algebraic tools. The result is shown in Fig. 4, where Mask and PSF are plotted in units of pixels. The size of the PSF will vary depending on the focal length of the lens and the positions of Tx and Rx.

Note that both calculations use an area represented by a fine sweep of discrete points, then, to obtain pixel-sized values, an interpolation has to be carried out. Output at this point is obtained by the convolution of both Mask and PSF, and this is the power distribution over pixels of the sensor for a fixed position of Tx and Rx.

#### B. Transmitted Waveform

The data to be transmitted is randomly generated and then separated into three data streams, one for each channel (R, G, and B). Since the modulation used in this system is OOK and, for instance, no channel codes are being used, the binary stream is just translated into pulses of width  $t_{chip}$ . The time step width  $t_{step}$  for the simulation's global time variable at this point has to satisfy Eq. 7 in order to have enough resolution.

$$\frac{1}{t_{step}} > \max\left(\frac{2}{t_{chip}}, \frac{2}{t_{rowdelay}}, \frac{2}{t_{rowexposure}}\right) \quad (7)$$

The impulse response of the LED and its driver are neglected since the frequency  $t_{chip}^{-1}$  is small compared to a typical LED frequency response. The LED lamp used in the experimental setup is built by 5050 surface mount device (SMD) RGB chips. Their radiation pattern is available in .IES format [7]. For this format, a matrix of azimuth and elevation angles contains data of luminous flux per solid angle, or candelas. Since the distance between Tx and Rx is big enough, it can be assumed that light comes from the same solid angle.

Finally, the power impinging the camera's main lens is calculated using Eq. 3, and by using the empirical radiation pattern data as shown in Eq. 8:

$$P_{Rx} = P_{Tx}(\theta_{LED}, \phi_{LED}) \cdot \cos \theta_{camera} \cdot \frac{A_{lens}}{d^2}, \quad (8)$$

where,  $P_{Tx}(\theta_{LED}, \phi_{LED})$  is the power obtained from the LED radiation pattern at inclination and azimuth angles  $\theta_{LED}, \phi_{LED}$ , and  $\theta_{camera}$  is the incident inclination angle at the camera.

#### C. Rolling Shutter Acquisition

The experimental setup was built using a Raspberry Pi equipped with its original Camera V2 (Sony IMX219PQH5-C CMOS sensor [8]), and touchscreen display for easy input. For simulation, the power spreading or power distribution frame is amplified by ISO gain  $G_{ISO}$  by using  $G_{iso} = 10^{iso/10}$ , where iso is the ISO value.

The RS process is then carried out by generating frame trigger times. It can be considered that a frame is taken every  $1/fps$  seconds where  $fps$  is the frame rate. In a real situation, the frame trigger times are conditioned by the output buffer readout operation performed by the operative system. This leads to non-deterministic frame trigger times, which are modeled following a normal distribution.

Line acquisition triggers depend only on the camera's delay between row expositions  $t_{rowdelay}$ . In the case of the Raspberry Camera V2  $t_{rowdelay} = 18.904 \mu s$ . With these triggers, the received signal is integrated by windows of width  $t_{rowexposure}$  that can be set arbitrarily for the capture. It can be also thought as a moving average of length  $t_{rowexposure}$  and a stride of  $t_{rowdelay}$ . This operation has been performed numerically by convolving the transmission waveform with the exposure window, and then decimating the resulting signal by the appropriate factor (determined by  $t_{rowdelay}$ ). Equation 9 describes the moving average respect to the camera's parameters and the transmitted waveform  $f(t)$ .

$$v_{x,y,c} = G_{iso} \cdot i(x, y, c) \int_{y-t_{row}}^{y-t_{row}+t_{exp}} f(t) dt \quad (9)$$

To model different noise sources, such as shot noise, and thermal noise, it's assumed that all can be modelled by Normal distributions. A frame-size matrix of additive noise values per pixel  $N$  is defined by the sum of each noise's standard deviation as follows:

$$\delta_{x,y,c} = \sqrt{G_{iso}(\delta_{th}^2 + \delta_{sh}^2)}, \quad (10)$$



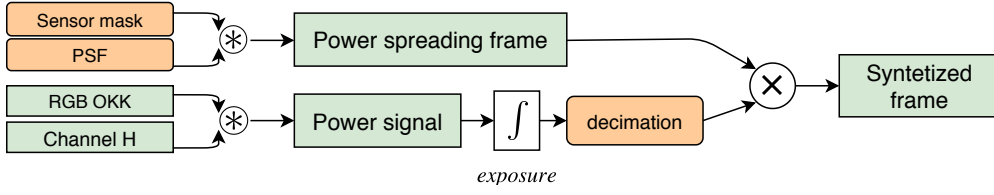


Fig. 2. Flow diagram of the simulator implementation.

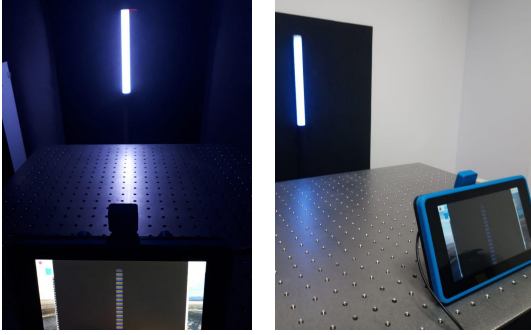


Fig. 3. Pictures of the real setup.

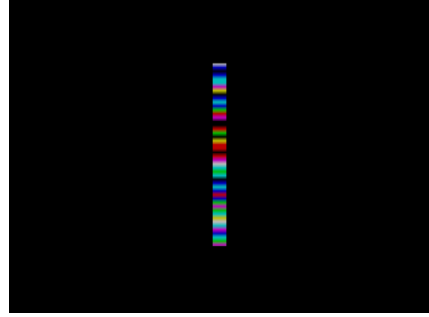


Fig. 5. Synthetic frame generated by the simulator.

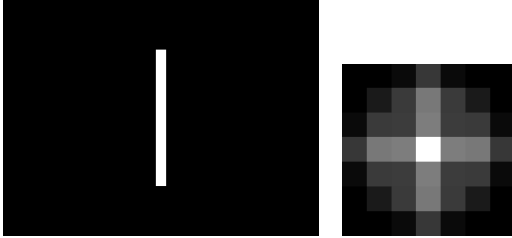


Fig. 4. Mask (left) and PSF (right) obtained to calculate power distribution.

where,  $\delta_{th}^2$  is associated to thermal noise and  $\delta_{sh}^2$  to shot noise. Thermal noise is independent to input, and it's defined by the following:

$$\delta_{th}^2 = \frac{4k_B T_n B}{G_{iso}}, \quad (11)$$

where,  $k_B$  is the Boltzmann's constant,  $T_n$  is the noise temperature, and  $B = 1/t_{rowdelay}$  is the bandwidth. The rest of the standard deviations depend on the input, and can be reduced to a single term  $\delta_{sh}$  calculated by using:

$$\delta_{sh}^2 = 2q_e (i(x, y, c) + i_d) B, \quad (12)$$

where,  $q_e$  is the elementary charge of the electron and  $i_d$  is the dark current of the camera's pixels. Finally, to obtain the synthesized frame, gamma correction is applied in the digital domain (although it can be performed also in the analog domain) to the image so that the final value of each pixel  $p_{x,y,c}$  is obtained by:

$$p_{x,y,c} = T_{adc} (v_{x,y,c} + N_{x,y,c})^\gamma, \quad (13)$$

TABLE I

KEY PARAMETERS OF THE EXPERIMENT'S SETUP

Key parameter	Value
Tx $t_{chip}$ ( $\mu$ s)	300
Tx height (cm)	24
Tx width (cm)	2.2
Test distance, $d$ (cm)	80
Sensor	Sony IMX219 [8]
Sensor resolution (pixels)	3280 $\times$ 2464
Pixel size ( $\mu$ m)	1.12
Camera	HFoV, VFoV
Focal length	3.04 mm
ISO	200
Analog gain	3.66
Digital gain	1
$t_{rowdelay}$ ( $\mu$ s)	18.904
$t_{rowexposure}$ ( $\mu$ s)	85, 293, 633

where  $N_{x,y,c}$  is the pixel noise and  $T_{adc}$  is the ADC conversion function.

The output of the simulator at this point are synthetic frames, like the one shown in Fig. 5. Using the parameters shown in Table I, the simulator and the experimental setup were ran to obtain real pictures, shown in Fig. 6 and synthesized frames, shown in Fig. 7.

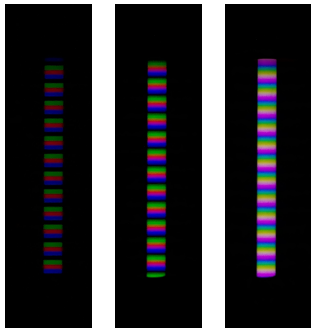


Fig. 6. Real pictures of LED Tx taken with experimental setup using  $t_{\text{rowexposure}} = 85 \mu\text{s}$ ,  $293 \mu\text{s}$ , and  $633 \mu\text{s}$  respectively.

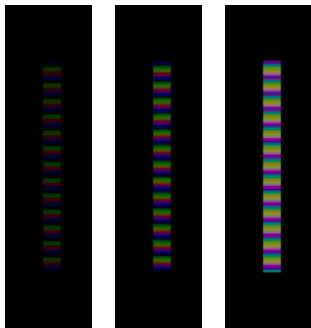


Fig. 7. Synthetic pictures of LED Tx made with simulator using  $t_{\text{rowexposure}} = 85 \mu\text{s}$ ,  $293 \mu\text{s}$ , and  $633 \mu\text{s}$  respectively.

#### IV. CONCLUSIONS

This paper shows the implementation of a simulator for the RS acquisition mechanism of the camera in an OCC setting, including a simplified model for optics of the system by means of RTM. The simulated system's parameters were tested on a real setup using Raspberry Pi Camera V2 and SMD 5050 RGB LED self-made lamp, enabling to compare the output synthesized image frames with real images.

The optical model reproduces the image formation in the camera based on the computation of the power distribution of the source's signal over the camera frame. The lens array of the camera is simplified by using RTM, which improves the computation load but reduces accuracy. To resemble the row-by-row scanning of the RS mode, the received signal is integrated by windows of wide equal to the arbitrarily selected exposure time of the camera.

The main contribution of this paper is the implementation of the RS simulation, which allows generating synthetic image frames of multiple low-speed VLC sources with arbitrary shapes. The synchronization of transmitters and receivers can be fixed while varying parameters of the simulation. This would enable, for example, to optimize the design of modulation schemes aided by machine learning.

#### REFERENCES

- [1] C. Danakis, M. Afgani, G. Povey, I. Underwood, and H. Haas, "Using a CMOS camera sensor for visible light communication," in *2012 IEEE Globecom Workshops, GC Wkshps 2012*, 2012.
- [2] A. Duque, R. Stanica, H. Rivano, and A. Desportes, "CamComSim: a LED-to-Camera Communication Simulator," INSA Lyon ; INRIA Grenoble - Rhône-Alpes ; CITI - CITI Centre of Innovation in Telecommunications and Integration of services ; Rtone, Tech. Rep. RR-9114, 10 2017. [Online]. Available: <https://hal.inria.fr/hal-01625734>
- [3] M. S. Iftekhar, M. A. Hossain, C. H. Hong, and Y. M. Jang, "Radiometric and Geometric Camera Model for Optical Camera Communications," in *2015 SEVENTH INTERNATIONAL CONFERENCE ON UBIQUITOUS AND FUTURE NETWORKS*, 2015, pp. 53–57.
- [4] Z. Ghassemlooy, L. N. Alves, S. Zvanovec, and M.-A. Khalighi, *Visible Light Communications: Theory and Applications*. CRC Press, 2017.
- [5] P. Chavez-Burbano, V. Guerra, J. Rabadan, D. Rodriguez-Esparragon, and R. Perez-Jimenez, "Experimental characterization of close-emitter interference in an optical camera communication system," *Sensors*, vol. 17, no. 7, p. 1561, 2017.
- [6] C. Jurado-Verdu, V. Guerra, J. Rabadan, R. Perez-Jimenez, and P. Chavez-Burbano, "RGB Synchronous VLC modulation scheme for OCC," in *2018 11th International Symposium on Communication Systems, Networks and Digital Signal Processing, CSNDSP 2018*, 2018.
- [7] FlexfireLEDs, *Photometric Testing Data and IES File Downloads*. FlexfireLEDs, 2017. [Online]. Available: <https://www.flexfireleds.com/photometric-data-ies-files/>
- [8] Sony Corporation, *IMX219PQH5-C Datasheet*, 2014.

# Experimental Evaluation of an Analog Gain Optimization Algorithm in Optical Camera Communications

Vicente Matus  
*IDeTIC-ULPGC,*  
Las Palmas de Gran Canaria, Spain  
vmatus@idetic.eu

Victor Guerra  
*IDeTIC-ULPGC,*  
Las Palmas de Gran Canaria, Spain  
vguerra@idetic.eu

Cristo Jurado-Verdu  
*IDeTIC-ULPGC,*  
Las Palmas de Gran Canaria, Spain  
cjurado@idetic.eu

Shivani Rajendra Teli  
*Czech Technical University*  
Prague, Czech Republic  
telishiv@fel.cvut.cz

Stanislav Zvanovec  
*Czech Technical University*  
Prague, Czech Republic  
xzvanove@fel.cvut.cz

Jose Rabadan  
*IDeTIC-ULPGC,*  
Las Palmas de Gran Canaria, Spain  
jrabadan@idetic.eu

Rafael Perez-Jimenez  
*IDeTIC-ULPGC,*  
Las Palmas de Gran Canaria, Spain  
rperez@idetic.eu

**Abstract**—The operation of Optical Camera Communication systems in outdoor conditions is challenged by interfering sources of light and optical attenuation induced by the atmosphere. The low signal power at the receiver is prone to be affected by the quantization noise at the analog-to-digital converter. In this paper, an algorithm for optimizing the camera's analog gain has been experimentally evaluated under laboratory conditions. The image quality improvement is estimated by Pearson's correlation coefficient to a template signal, and it is shown to improve the signal-to-noise ratio up to 27.8 dB.

**Index Terms**—Optical Camera Communications, analog gain, Pearson's correlation coefficient, signal-to-noise ratio.

## I. INTRODUCTION

Optical Camera Communication (OCC) is a group of schemes within the Visible Light Communication (VLC) field to be included in the IEEE 802.15.7r1 [1], and where the main principle is to use a digital camera as a receiver ( $R_x$ ), taking advantage of the low price of these devices. In OCC, the extensive use of Rolling Shutter (RS) cameras is based on their ability to scan lines of pixels delayed between each other by orders of tens of  $\mu\text{s}$  [2]. These cameras are the most available in commercial devices using Complementary Metal-Oxide-Semiconductor (CMOS) sensors [3], [4]. The signal coming from a Light Emitting Diode (LED) transmitter ( $T_x$ ) is captured by the lines of the sensor at different times, allowing the receivers to decode several symbols from each image frame.

Outdoor applications of OCC such as localization, Vehicular VLC, and Sensor Networks, face relevant challenges such as long link spans, optical degradation by atmospheric conditions [5], and require mobility support in most cases. Applications such as VLC positioning specifically rely on beacon signals, and

This project has received funding from the European Union's Horizon 2020 research and innovation programme under the Marie Skłodowska-Curie grant agreement No 764461.

most systems use packet structures with well-known patterns for the detection of Region of Interest (ROI) and synchronization. Correlators can be used for the recognition of such patterns [6].

The signal-to-noise ratio (SNR) at the receiver is crucial for allowing any communication link to have longer spans. The SNR depends on the transmitted power, on the attenuation factor of the channel, and in the case of OCC, it also depends on the optical lens array of the camera. In addition, an OCC system can be exposed to various sources of noise and interference. The area of the transmitter projected over the imaging sensor is also relevant in OCC, the maximum link distance is then bounded by the amount of sensor rows covered by the transmitter, in the case of RS-OCC. Geometrical derivations can estimate the image projected area [7]. The SNR can be estimated from the data-containing pixels

In this work, the use of an analog gain control algorithm for optimizing the SNR through a cost function based on the correlation is proposed. The correlation is extensively used for spatial synchronization and channel estimation in OCC. Therefore, the inclusion of this control algorithm will have little or no impact on computation performance of the  $R_x$  if the correlation is considered already a process of other algorithms. Several experiments involving different input powers, the algorithm's convergence iteration, and the SNR improvement are also provided.

The structure of this paper is the following. The OCC channel of an RS-based OCC system is modelled in II. The control algorithm for the optimization of the signal quality is derived in Section III. Both methodology and experimental design are described in Section IV. In Section V, the results obtained from the experiments are discussed. Finally, the conclusions of this work are drawn in Section VI.

## II. OCC CHANNEL

The simplified diagram of an outdoor OCC scenario is shown in Fig. 1 in which a VLC transmitter using On-Off Keying (OOK) modulation sends pulses of each of the red-green-blue (RGB) colors. The shape of the ROI or the pixels of the frame that are exposed to the transmitted signal is not necessarily known beforehand. The attenuation of some atmospheric conditions that might be present, *e.g.* in foggy weather, is modeled by  $A$  in dB/m. The link span  $d$  in m depends on the relative position of the source with respect to the camera and its orientation, which in most cases are constantly changing.

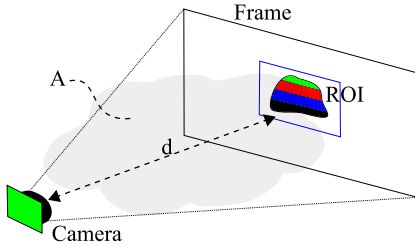


Fig. 1. Simplified diagram of the RS-OCC system considered.

The power signal at the receiver  $P_{Rx}(t)$  under an attenuated channel, when the transmitter is modeled as an  $m$ -order Lambertian source with power  $P_{Tx}(t)$ , can be expressed as

$$P_{Rx}(t) = P_{Tx}(t)e^{-Ad} \cdot \frac{m+1}{2\pi} \cdot \cos^m \theta \frac{A_{lens} \cos \Psi}{d^2}, \quad (1)$$

where  $\theta$  is the emission angle,  $\Psi$  is the incident angle, and  $A_{lens}$  is the area of the camera's external lens. From this expression, it can be seen that by varying either the transmitted power or the factor  $A \cdot d$ , known as the optical density, the received power can be affected alternatively, allowing to emulate the effect of the other parameters. Note that the projected area of the source over the camera sensor is mostly only dependent on  $d$ .

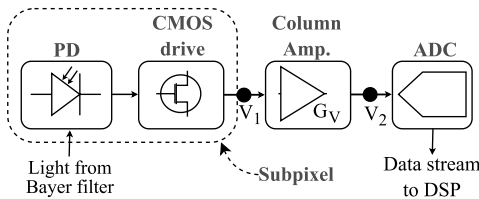


Fig. 2. Typical configuration of Complementary Metal-Oxide-Semiconductor (CMOS) camera sub-pixels.

In Fig. 2, the block diagram of a regular CMOS camera sub-pixel is shown, as described in [8]. The photodiode (PD) at position  $x, y$  and channel  $c \in \{R, G, B\}$  receives light from a colored Bayer filter and generates a current  $i_{pd}(x, y, c)$  which is turned into a voltage signal  $V_1$  by the CMOS drive. Since the sequential reading by rows allows it, an analog amplifier and analog-to-digital converter (ADC) are shared by each column of sub-pixels of the sensor. The gain of the analog amplifiers  $G_V$  is set globally by the software of the camera and the voltage

signal that is sampled by the ADC is given by  $V_2 = G_V \cdot V_1$ . The ADC induces a noise ( $\sigma_{adc}^2$ ), that can be modeled as a random Normal of mean zero with a variance that depends on the digitalization levels. The SNR of the signal that enters the digital signal processing (DSP) block can be modeled as

$$SNR \approx \frac{G_V^2 \cdot i_{pd}^2(x, y, c)}{G_V^2 (\sigma_{th}^2 + \sigma_{sh}^2) + \sigma_{adc}^2}, \quad (2)$$

where  $\sigma_{th}^2$  and  $\sigma_{sh}^2$  correspond to the thermal noise and shot noise of the process, respectively. Note that the noise induced by the ADC can be virtually reduced to zero by increasing  $G_V$  as

$$\lim_{G_V \rightarrow \infty} SNR = \frac{i_{pd}^2(x, y, c)}{\sigma_{th}^2 + \sigma_{sh}^2}, \quad (3)$$

nevertheless, the ADC has an upper bound for the input voltage, then  $G_V$  can only be increased up to the point  $V_2$  does not saturate the ADC.

In previous work [9], it was shown that the SNR can be obtained empirically from image frames. Nevertheless, its computation can be substituted by the calculation of the Pearson's correlation coefficient  $r_{xy}$  between the image frames and a well known template, which is used in some implementations of OCC for synchronization of the received signal in the images and also for ROI detection. The parameter  $r_{xy}$  is defined as

$$r_{xy} = \frac{\sum_{i=1}^N (x_i - \bar{x})(y_i - \bar{y})}{\sqrt{\sum_{i=1}^N (x_i - \bar{x})^2} \sqrt{\sum_{i=1}^N (y_i - \bar{y})^2}}, \quad (4)$$

where  $x_i$  are the rows of the template of size  $N$  rows,  $y_i$  are  $N$  consecutive rows of the image, and  $\bar{x}, \bar{y}$  are the mean values. The computation is iterated for all possible subsets  $y_j, y_{j+1}, \dots, y_{j+N-1}$ ,  $(j + N - 1) < M$  of consecutive rows of the frame. When the template is matched in phase with the signal it emulates, the maximum value  $r_{xy}^{max}$  is achieved. This value is considered the overall correlation between the image frame and the template, which has been shown to be closely related to the SNR, giving high values of  $r_{xy}^{max}$  when the signal quality is high [9].

## III. ANALOG GAIN CONTROL ALGORITHM

As it was aforementioned,  $r_{xy}^{max}$  is closely related to SNR, and may serve as a fast estimator of it. Therefore, optimizing the correlation using  $G_V$  would implicitly maximize SNR. The following paragraphs describe each one of the development of the algorithm for controlling  $G_V$  to maximize  $r_{xy}^{max}$  proposed in this work, which is based on the typical feedback-based design, as shown in Fig. 3.

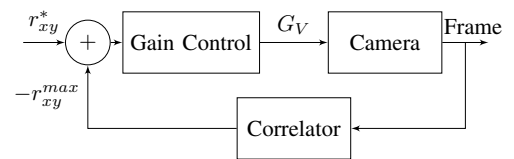


Fig. 3. Block diagram of the gain control algorithm.

The set point  $r_{xy}^*$  is the desired value for  $r_{xy}^{max}$  to be achieved by the controller, which is set to 1 in order to force the system to get the highest signal quality.

The camera block receives each updated value of  $G_V$  and sets this parameter on the physical device. Generally, camera's do not have a continuum of analog gains, but a discrete range of possible values. In this work, since Sony IMX219 image sensor is considered, the possible gains in linear units is defined by

$$G_V(X) = \frac{256}{256 - X}, \quad (5)$$

where  $X$  is an integer between 0 and 232 (233 possible analog gains). Due to the hyperbolic nature of  $G_V(X)$ , there is higher resolution at lower gain values. Furthermore, this quantization could be considered as an extra noise term, since each iteration will probably not coincide with valid values.

Finally, this block also captures the image and passes it to the correlation calculation block, which carries out Pearson's correlation coefficient with a parametric template. The maximum value of this operation is then forwarded to the gain control algorithm.

Mathematically, it is straightforward to define a cost function  $C(G_V)$  that optimizes  $r_{xy}^{max}$  as

$$C(G_V) = (1 - r_{xy}^{max})^2. \quad (6)$$

The performance of the control algorithm would significantly depend on the shape of the error curve. Nonetheless, in this work a simple squared difference scheme is proposed.  $C(G_V)$  can be easily optimized using an iterative approach via a gradient descent on  $G_V$ , yielding

$$G_V^{(i+1)} = G_V^{(i)} - \lambda \frac{C(G_V^{(i)})}{\partial C(G_V) / \partial G_V |_{G_V^{(i)}}}, \quad (7)$$

where  $\lambda$  is the learning rate or damping coefficient. It can be observed that the cost function's derivative can be reformulated as

$$\frac{\partial C(G_V)}{\partial G_V} = -2(1 - r_{xy}^{max}) \frac{\partial r_{xy}^{max}}{\partial G_V}. \quad (8)$$

Since there is no closed-form relationship between  $r_{xy}^{max}$  and  $G_V$ , its derivative must be numerically estimated. In this work, a N-points linear regression was performed to obtain the curve's slope on the point of interest. However, the neighbourhood of the starting point must be explored during the algorithm's initialization by forcing a fixed analog gain change until an N-size estimation buffer is full to begin with the linear regressions, where N = 4 has been chosen arbitrarily.

Finally, combining equations (7) and (8), it yields the final iterative scheme, expressed as

$$G_V^{(i+1)} = G_V^{(i)} + \frac{\lambda}{2} \frac{1 - r_{xy}^{max(i)}}{\partial r_{xy}^{max} / \partial G_V |_{G_V^{(i)}}}. \quad (9)$$

The performance of the proposed algorithm would highly depend on the estimation of  $r_{xy}^{max}$ 's slope. As it was commented, this magnitude will be calculated using a linear regression of N points. Hence, the accuracy of the denominator in Equation (9) depends on the curve's shape, which will not be linear *a priori*, and the separation between samples.

#### IV. METHODOLOGY

It has been shown that the Pearson's correlation coefficient is a computationally quick estimator of the signal quality. Moreover, the camera analog gain can optimize the SNR by reducing quantization noise. The objective of this work is to propose a control algorithm for  $G_V$  based on the  $r_{xy}$  values obtained from each image capture. In order to demonstrate this hypothesis, a series of experiments were carried out using the experimental setup shown in Fig. 4. The scenario comprises a commercial RGB lamp controlled by a general purpose microcontroller [10] and a receiver built using an Element14 Raspberry Pi board with a camera based on Sony IMX sensor [11]. The lamp transmits pulses of a period  $T_{chip}$  and consecutively repeats a sequence of G-R-B-K pulses, where K stands for black, meaning it is an off state of the lamp. Different conditions can be emulated varying the LED power source voltage and using a Methacrylate sheet in order to emulate channel loss (optical density). The  $T_x$  and  $R_x$  parameters can be observed in Table I.

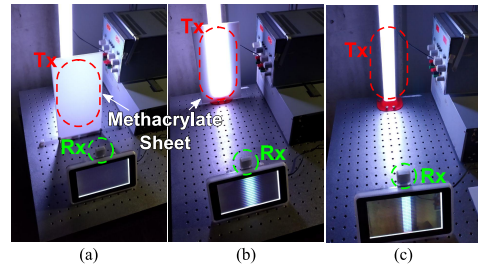


Fig. 4. Pictures of the experimental setup. In the experiments, the radiant energy at the camera position is  $3.39 \mu\text{W}/\text{cm}^2$  in (a),  $11.79 \mu\text{W}/\text{cm}^2$  in (b), and  $45.11 \mu\text{W}/\text{cm}^2$  in (c)

TABLE I  
Experiment key parameters.

Parameter	Value
Transmitter	
Device	12 V DC RGB LED strips
Front-end device	Atmel ATmega328p controller [10]
Power levels [W]	min = 1.8, max = 4.8
Dominant wavelengths [nm]	630 (Red), 530 (Green), 475 (Blue)
$T_{chip}$ [s]	1/3600
Receiver	
Camera	Picamera V2 module (Sony IMX219) [11]
Resolution	3280 × 2464 px
$t_{exp}$ [ $\mu\text{s}$ ]	300
Gain ( $G_V$ ) [dB]	0, ..., 20.6 (233 values)

The algorithm presented in Section III was evaluated for the three synthetic scenarios using different initial gain values ( $G_V^{(0)}$ ). Furthermore, the estimation of the correlation's slope was based on  $N = 4$  samples. The analyzed performance metric of the algorithms was the convergence iteration, estimated using:

$$r_{th} = r_{xy}^{max(\infty)} (1 \pm \varepsilon), \quad (10)$$

where  $r_{xy}^{max(\infty)}$  is the final value after convergence, and  $\varepsilon$  is the threshold's parameter (which was set 0.05 arbitrarily for all experiments). The parameter  $r_{th}$  is the final threshold value of the correlation.

## V. RESULTS AND DISCUSSION

The first step of experimentation consisted on the acquisition of frames at all the available  $G_V$  values, and under three conditions of received intensity of radiant energy ( $I$ ), as it is shown in Table II. These conditions were implemented by varying transmitted power and the channel attenuation, which derived in three different values of  $I$  at the receiver position. In each of the three conditions, the camera acquired images using the 233 available  $G_V$  values, repeating 50 times the acquisition, resulting in 11,650 frames under the same radiant energy conditions. These frames were processed to get the Pearson's correlation coefficient with respect to a template signal equal to the transmitted pulses of OOK.

TABLE II  
Experiments conditions.

	$I$ [ $\mu\text{W}/\text{cm}^2$ ]	Gains [dB]	No. of Captures
Experiment 1	3.39	0 - 20.6	50 per each $G_V$
Experiment 2	11.79	0 - 20.6	50 per each $G_V$
Experiment 3	45.11	0 - 20.6	50 per each $G_V$

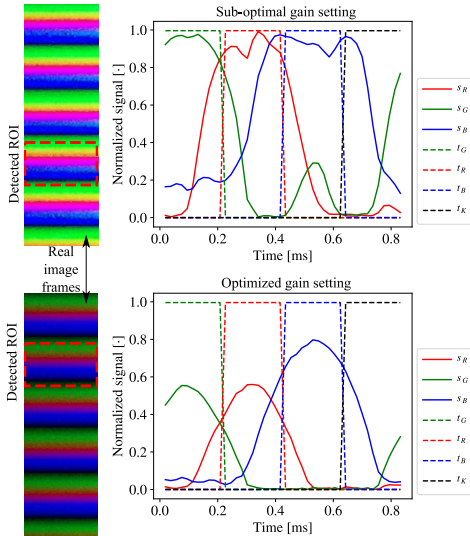


Fig. 5. Processing from two images obtained in the conditions of Experiment 3. The plot curves correspond to the  $R_x$  signal R-G-B channels, labeled as  $s_R$ ,  $s_G$ ,  $s_B$ , respectively, and the dashed curves to the template pulses G-R-B-K labeled as  $t_G$ ,  $t_R$ ,  $t_B$ ,  $t_K$ , respectively. The picture insets represent a portion of the actual images captured. The red dashed line highlights the detected ROI.

In order to illustrate the impact of the variation of  $G_V$  in the image frames captured by the camera, Fig. 5 shows two signals obtained in the conditions of Experiment 3. The sub-optimal gain setting image was captured using  $G_V = 15.3$  dB and the optimized gain setting image was captured using  $G_V = 2.0$  dB. The images obtained  $r_{xy}^{max} = 0.76$ , and  $r_{xy}^{max} = 0.85$ , respectively, and the SNR obtained was 27.8 dB and 24.2 dB, respectively.

In Fig. 6, the average results of  $r_{xy}^{max}$  obtained from data acquisition and correlation processing are shown for the three experiments. The lowest received intensity of radiant energy at Experiment 1 shows more fluctuations of the correlation, and it shows that the contribution of  $G_V$  is to improve the

signal quality since it is weak. In the other two experiments, a similar behaviour is seen. The high intensity of the received signal makes the gain to deteriorate the signal with saturation, which builds up mostly smoothly. In Experiments 2 and 3, the gain control algorithm should converge to the minimum gain values, and in Experiment 1, it should converge to the maximum gain. It is also important to note that none of the experiments have resulted in a  $r_{xy}^{max}$  curve with a maximum point at an intermediate value of  $G_V$ .

By setting arbitrary initial  $G_V$  values, the correlation data sets evaluated from Experiments 1, 2 and 3 were used to run the gain control algorithm for a fixed number of 150 iterations. In Fig. 7, the results of the chosen  $G_V$  at each iteration are shown. It can be seen that the Experiments 2 and 3 converge to the minimum gain, as expected, in which the correlation is the maximum. The convergence is obtained after about 25 iterations. For the case of Experiment 1, the algorithm takes longer to converge, after about 60 iterations.

The results obtained show that the gain control algorithm can successfully converge to the gain value that ensures maximum correlation available in each scenario. Considering a standard frame rate of 30 fps, and negligible delays at the DSP, the algorithm could converge in about 1 s.

## VI. CONCLUSIONS

This work shows the development an algorithm for the automated control of analog gain in a CMOS sensor camera used in an experimental RS-based OCC under laboratory conditions that emulated an optical attenuation of the signal across the channel. It was shown that the camera analog amplifier stage before the ADC can reduce the quantization noise only if it does not saturate the ADC, thus, the optimal value of  $G_V$  can vary depending on the transmitted power and the attenuation induced by the channel. In addition, the use of Pearson's correlation coefficient was shown to be an estimator of the signal quality at the  $R_x$ , as an alternative to the calculation of SNR. The algorithm was developed for the use of  $r_{xy}^{max}$  as the feedback, allowing to estimate the next capture's  $G_V$  to maximize the quality. It was found that in high received power cases, the algorithm converges to the optimal gain in about 25 iterations, whereas in low received power cases, it takes more than double the amount of iterations. With these values, and considering a standard 30 fps frame rate of the camera, the convergence time is between 1 and 2 s. In case of mobility or changing conditions, it would be necessary to repeatedly run the algorithm. For future work, the parameters of the control algorithm such as damping coefficient and gain seed need to be optimized in more realistic conditions. It is also necessary to demonstrate its convergence under conditions where the optimal  $G_V$  is an intermediate value.

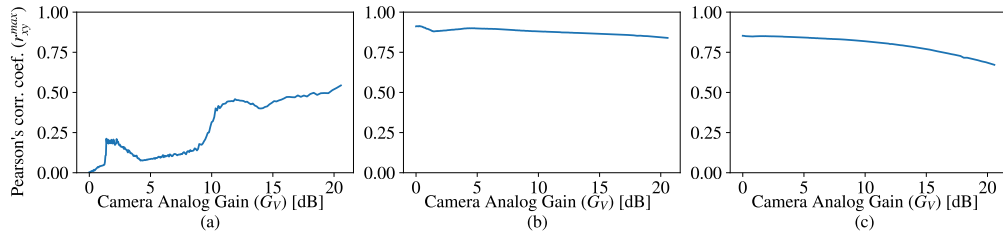


Fig. 6. Data acquisition average values of  $r_{xy}^{max}$  obtained varying  $G_V$  over all the available values. Results from Experiment 1 are shown in (a), Experiment 2 in (b), and Experiment 3 in (c).

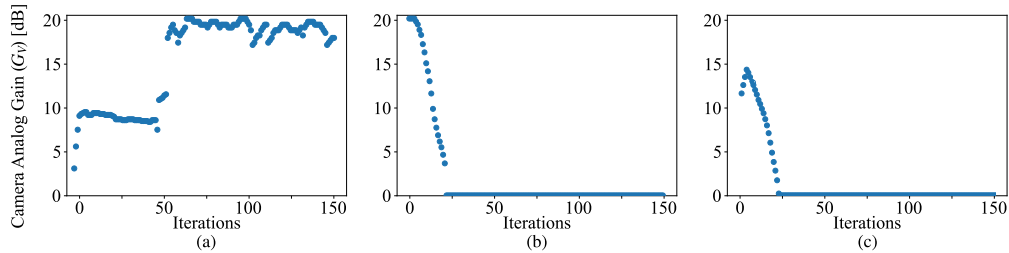


Fig. 7. Convergence of the algorithm in each of the experiments, where (a) corresponds to Experiment 1, (b) to Experiment 2, and (c) to Experiment 3.

#### REFERENCES

- [1] W. A. Cahyadi, Y. H. Kim, Y. H. Chung, and C. Ahn, "Mobile phone camera-based indoor visible light communications with rotation compensation," *IEEE Photonics Journal*, vol. 8, no. 2, pp. 1–8, April 2016.
- [2] T. Nguyen, Chang Hyun Hong, Nam Tuan Le, and Y. M. Jang, "High-speed asynchronous optical camera communication using led and rolling shutter camera," in *2015 Seventh International Conference on Ubiquitous and Future Networks*, July 2015, pp. 214–219.
- [3] R. Boubezari, H. Le Minh, Z. Ghassemlooy, and A. Bouridane, "Smart-phone camera based visible light communication," *Journal of Lightwave Technology*, vol. 34, no. 17, pp. 4121–4127, Sep. 2016.
- [4] T. Nguyen, A. Islam, T. Hossan, and Y. M. Jang, "Current status and performance analysis of optical camera communication technologies for 5g networks," *IEEE Access*, vol. 5, pp. 4574–4594, 2017.
- [5] A. Islam, M. T. Hossan, and Y. M. Jang, "Convolutional neural networks-based optical camera communication system for intelligent internet of vehicles," *International Journal of Distributed Sensor Networks*, vol. 14, no. 4, p. 1550147718770153, 2018.
- [6] C. Jurado-Verdu, V. Matus, J. Rabadan, V. Guerra, and R. Perez-Jimenez, "Correlation-based receiver for optical camera communications," *Opt. Express*, vol. 27, no. 14, pp. 19 150–19 155, Jul 2019.
- [7] P. Chavez-Burbano, V. Guerra, J. Rabadan, D. Rodríguez-Esparragón, and R. Perez-Jimenez, "Experimental characterization of close-emitter interference in an optical camera communication system," *Sensors*, vol. 17, no. 7, p. 1561, Jul 2017.
- [8] T. Kuroda, *Essential Principles of Image Sensors*. CRC Press, 2017.
- [9] V. Matus, E. Eso, S. R. Teli, R. Perez-Jimenez, and S. Zvanovec, "Experimentally derived feasibility of optical camera communications under turbulence and fog conditions," *Sensors*, vol. 20, no. 3, p. 757, Jan 2020.
- [10] Atmel Corporation, *ATmega328p, 8-bit AVR Microcontroller with 32K Bytes In-System Programmable Flash, Datasheet*. Atmel Corporation, 2015.
- [11] Sony Corporation, *IMX219PQH5-C, Diagonal 4.60 mm (Type 1/4.0) 8 Mega-Pixel CMOS Image Sensor with Square Pixel for Color Cameras, Datasheet*. Sony Corporation, 2014.

# Evaluation of Fog Effects on Optical Camera Communications Link

Vicente Matus\*, Shivani Rajendra Teli<sup>†</sup>, Victor Guerra\*,  
Cristo Jurado-Verdu\*, Stanislav Zvanovec<sup>†</sup>, Rafael Perez-Jimenez\*

\*IDeTIC-ULPGC, Las Palmas de Gran Canaria, Spain

<sup>†</sup>Czech Technical University in Prague, Czech Republic

vmatus@idetic.eu, telishiv@fel.cvut.cz, vguerra@idetic.eu,

cjurado@idetic.eu, xzvanove@fel.cvut.cz, rperez@idetic.eu

**Abstract**—The applications of Optical Camera Communications (OCC) have been tested for vehicular communications, Internet-of-things (IoT), and other outdoor scenarios due to the vast availability of standard camera equipment. The outdoor channel is, however, affected by atmospheric conditions, ranging from the presence of particles or water drops in the air to thermally induced fluctuations of the refractive index (turbulence). In this work, we experimentally investigate the influence of fog on an OCC link exploiting rolling shutter cameras and using red-green-blue (RGB) channels inside a laboratory chamber featuring a fog machine. The analysis is performed using the Pearson's correlation coefficient between test and reference signals as a measure of similarity or decay of the signal attenuation of fog associated with atmospheric visibility.

**Index Terms**—Optical camera communications (OCC), fog, meteorological visibility, experimental outdoor OCC.

## I. INTRODUCTION

Optical Camera Communications (OCC) using Complementary Metal-Oxide-Semiconductor (CMOS) camera as receiver (Rx) has been investigated as one of the Visible Light Communication (VLC) schemes [1]. OCC implemented within internet of things (IoT) environments provides multiple functionalities of vision, data communications, localization and motion detection [2]–[4] used in various IoT-based network applications including device-to-device communications [5], mobile atto-cells [6], vehicle-to-everything (V2X) [7], smart environments (cities, industries, offices, homes, surveillance), etc. [8]. A popular way to implement OCC in the Rx is by using the rolling shutter (RS) acquisition mechanism of CMOS, in which the sensor captures the image row-by-row with a delay between each line [9]. The camera captures a set of states of the signal from the VLC Light Emitting Diode (LED) transmitter (Tx) based on the timings of the RS scanning. These are governed by the CMOS chip's fixed row-shift time ( $t_{rs}$ ) and the software-defined exposure time ( $t_{exp}$ ) [10], as shown in Fig. 1.

The widespread use of LED as taillights, brake lights, headlights, traffic signals, lighting infrastructures, display communications, and cameras for safety and comfort applications has

reached into fields such as sensor networks, automotive and industrial facilities. In outdoor VLC environments, the intensity-based detection method [8], [11] fails to produce reliable data detection due to the presence of high-power external light sources such as sunlight. The communications performance is also strongly dependent on weather conditions over the optical channel, such as rain, snow, and fog, because these conditions cause a severe loss on the LED transmission quality. In particular, foggy weather causes either poor or no communication, thus making LED-photodetector (PD) based VLC impractical. A comprehensive study of VLC and OCC outdoor links in terms of atmospheric attenuation under fog conditions needs to be conducted. To this end, [12] investigated the success rate of received bits of an OCC link for vehicular communications between red brake light and camera varying the modulation index of On-off keying (OOK) setting. They experimentally tested the setup in a laboratory chamber. [13] studied the influence of rain and fog on VLC based V2V. They derived a path-loss model based on Mie's theory aided by Zemax software to create simulations. They obtained expressions for the maximum achievable distances for a desired value bit-error-ratio (BER). Authors in [14] experimentally investigated the effect of light and heavy fog employing a single red LED as Tx and three PD units and a Fresnel lens as the Rx. With this setup, they overcome the attenuation due to the gain the lens gives. In [15], the characterization of maritime fog and the effects on VLC is studied also using Mie's theory to model both scattering and phase functions since the size of water particles is proportional to the wavelengths of visible light. They obtained the attenuation over the spectrum of white LED employed for different distances.

OCC deployment in particular applications such as vehicle-to-vehicle (V2V), vehicle-to-infrastructure (V2I or I2V) and vehicle-to-everything (V2X or X2V) is of increased interest [16], [17], due possibly to the use of pre-existing camera-based infrastructures, such as traffic camera networks, security cameras, or the already installed car dashboard cameras. Authors in [16], [17] investigated the use of high-speed CMOS image sensors for automotive applications, with the primary aim of increasing the data throughput up to 10 Mbps. However, the concept was based on a custom-made combination of image pixels and communication pixels, not based on off-the-shelf

This paper has been supported by the European Union's Horizon 2020 research and innovation program under the Marie Skłodowska-Curie grant agreement No 764461 (VisIoN Project)



The 3<sup>rd</sup> International West Asian Symposium on Optical and Millimeter-wave Wireless Communications (WASOWC2020)

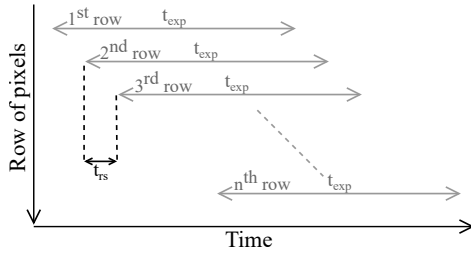


Fig. 1. Important parameters of line scan timing in rolling shutter CMOS camera.

CMOS cameras.

The recent OCC research is mainly focused on data rate enhancement and establishing reliable link qualities. However, OCC links, when deployed for outdoor applications, mainly need to focus on the effect of atmospheric conditions on the link performance, which is sparsely reported in the literature [18]. Works addressing channel characterization in outdoor OCC links are sparse compared to the vast research of this topic within Free Space Optics (FSO), which use collimated beams on particular wavelengths (850 nm or 1550 nm) instead of diffuse wideband light in the visible spectrum.

This paper aims to explore the capabilities of OCC in the presence of fog. The experiments carried out for this work were done using an atmospheric chamber, equipped with a laser source and power meter to estimate the fog level across the chamber by means of meteorological visibility ( $V_M$ ). A self-made red-green-blue (RGB) LED lamp with a VLC front-end, and a low-cost CMOS camera with RS acquisition comprise the system.

The content of this paper is structured as follows. Section II presents the experimental setup and describes the methodology used. Section III shows the results obtained from data processing and related discussion. Finally, conclusions are drawn in Section IV.

## II. EXPERIMENTAL SETUP AND METHODS

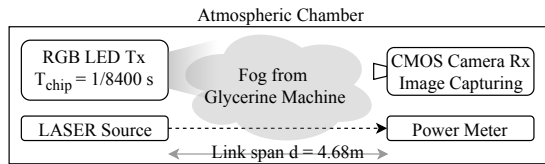


Fig. 2. Diagram of the experimental setup.

The effects of fog over an RS-based OCC unidirectional link were studied using a laboratory chamber at the facilities of the Czech Technical University in Prague. Since RS takes advantage of the line scanning, the impact of this atmospheric condition can be positive if the projection of the Tx area over the camera sensor increases its dimensions due to scattering. On the other hand, the attenuation associated with the presence

of particles in the air has a negative impact that must be studied.

A light source's radiation pattern can be modeled as a Lambertian function of order  $m$  [8], with a transmitted power  $P_{Tx}(t)$ . Then the received power  $P_{Rx}(t)$  can be expressed as:

$$P_{Rx}(t) = P_{Tx}(t) \cdot \frac{m+1}{2\pi} \cdot \cos\theta \frac{A_{lens} \cos\Psi}{d^2}, \quad (1)$$

where  $d$  is the Tx-Rx distance,  $\theta$  the emission angle,  $\Psi$  the incident angle, and  $A_{lens}$  is the area of the main lens of the camera. The RS mechanism makes the energy integrated by the  $i^{th}$  row  $E_i$  to be as:

$$E_i = \int_{i \cdot t_{rs}}^{i \cdot t_{rs} + t_{exp}} \frac{P_{Rx}(t)}{\sum_j^v \sum_k^h M_{j,k}} dt, \quad (2)$$

where  $h$  (columns) and  $v$  (rows), are the dimensions of the CMOS sensor, and  $M_{[v \times h]}$  is the mask of pixels where the shape of the transmitting surface is projected.

The emulation of fog in this work was done using a Glycerine machine. For evaluating the channel attenuation, the related meteorological visibility ( $V_M$ ), was derived from the measurement of laser power intensity of a 625nm and 2mW beam across the span of the chamber.

The VLC Tx lamp is set to transmit a beacon signal formed by pulses of each of the RGB colors, followed by a black (off state) pulse. The pure color pulses allows estimating the mismatch between the spectra of the LED and the Bayer filter of the camera, which causes an inter-channel cross-talk [19]. The Rx camera was programmed to make image captures at  $t_{exp} = 60\mu s$ . After taking reference measurements with clear conditions, we manipulated the atmospheric conditions while sustaining the beacon transmission and capture processes. The key experiment parameters are listed in Table I and the diagram of experimental setup is shown in Fig. 2.

TABLE I  
System parameters.

Description	Values
Capture device	Raspberry Pi + Picamera V2 module
camera resolution	3280 × 2464 px
shutter speed	60μs
Tx	RGB LED strips (5 × 5mm SMD chips)
Tx symbol rate	1/8400Hz
OCC link span	4.68m

Transmitters used were made out of arrays of RGB LED connected to a microcontroller model ATmega328p, and a switching circuit based on transistors. We installed the LED strips on aluminum rails with white meth-acrylate diffuser. The circuitry makes the RGB channels to repeatedly emit the beacon signal at a rate that is set by software in the microcontroller.

The receivers were made using the development board Raspberry Pi with PiCamera V2. The CMOS sensor (Sony IMX219QH5-C [20]) fixed internal structure is set to have a row-shift time  $t_{rs} = 18.904\mu s$ . The exposure time was set to  $t_{exp} = 60\mu s$ .

For the later analysis of data, the reference images and the captures taken in fog conditions, denoted as reference and test image sequences respectively, are taken through processes including the detection of region of interest (ROI) in the image, the estimation of inter-channel cross-talk, and the calculation of the Pearson's correlation coefficient ( $\rho_{XY}$ ) between test and reference image sequences as a measure of similarity between both.

The detection of ROI in OCC consists of determining the relevant group of pixels from which the Rx can decode information. The amount of rows forming this group is proportional to the number of different states of the lamp that can be decoded. Also, if multiple columns of pixels form the region of interest, the information inside the rows can be averaged, allowing to filter noise.

In this work, the ROI is first manually extracted from the reference group and, since the alignment is maintained, the test group's regions of interest are extracted re-using the coordinates. For estimating the impact of fog on the dimensions of the ROI, a detection algorithm is performed, and ROI limits are determined by finding the pixels with an intensity of 20% of the extinction ratio. We chose this limit after computing the algorithm for a range of values and selected the result with the minimum amount of results with dimensions smaller than the reference ROI, considered to be spurious.

Afterward, from the extraction of ROI,  $Signal_{[Nx3]}$  is obtained, where  $N$  is the number of rows of the ROI, and 3 is related to the RGB channels. From the reference ROI, a template of one beacon signal of the transmitter is saved as  $Ref'_{[Mx3]}$ , where  $M$  is the number of rows used by the beacon.

The cross-talk between RGB channels is then estimated by manually analyzing the reference pixels containing information from pure R, G, and B pulses of the LED. Then, the matrix  $H_{[3 \times 3]}^{-1}$  is used to clean all the data, giving the cleaned signals  $Ref'_{[Mx3]}$  and  $Signal'_{[Nx3]}$ . These are later evaluated by Pearson's correlation coefficient.

### III. RESULTS

One important impact of fog over OCC can be the expansion of ROI due to the scattering of light resulting in an apparent enlarged image of the transmitter. For this reason, the influence of fog on the dimensions of detected ROI were studied. In this case, the algorithm described in Section II was used to detect the width of ROI, as shown in Fig. 3. The algorithm was not used for the estimation of height or ROI since the black pulses of the beacon can be considered as pixels without information. Nevertheless, the expansion in one axis should be equal to the other one.

The ROI widths of the image sequences in different fog levels were estimated, and the difference of pixel columns with respect to reference ROI was obtained and is shown for different scales of  $V_M$  in Fig. 4. In this image, we can see that there is an expansion of the ROI at low visibility values,

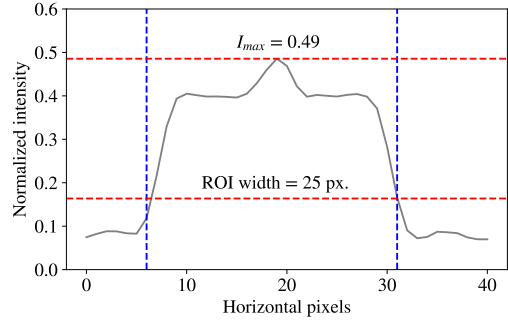


Fig. 3. Output from the estimation of ROI dimensions of an example test signal. Red lines are: (upper) peak intensity, and (lower) the decay of 20% of the extinction ratio. Blue lines are the intersection of red lines and the grayscale intensity profile of lamp (horizontal axis).

although minimal if it is compared to the dimensions of the ROI (229 by 25 pixels).

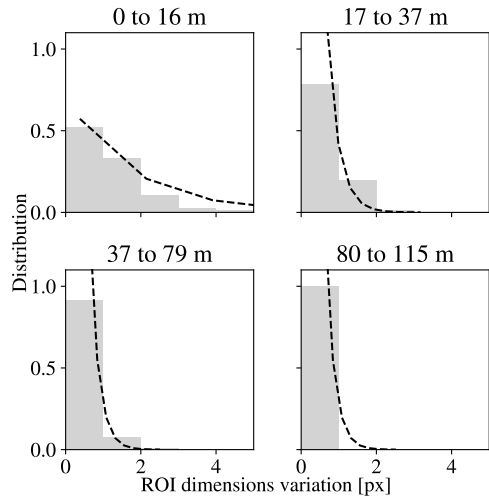


Fig. 4. Histograms and estimated distribution of the detected ROI dimensions variation with respect to reference, separated by equally sized groups according to the level of meteorological visibility  $V_M$  at the capture.

The analysis of Pearson's correlation coefficient between cleaned test data ( $Signal'_{[Nx3]}$ ) and cleaned reference data ( $Ref'_{[N \times 3]}$ ) was done all along the extracted ROI, giving a periodic curve in which the peaks correspond to the positions of the reference signal that match the phase of the test signal, as shown in Fig. 5. The highest value of  $\rho_{XY}$  is saved as the similarity of the picture compared to the reference image.

By saving the peak values of  $\rho_{X,Y}$  of each image, and meteorological visibility at capture, the relation of these two variables can be studied, as shown in Fig. 6. The scatter plot

The 3<sup>rd</sup> International West Asian Symposium on Optical and Millimeter-wave Wireless Communications (WASOWC2020)

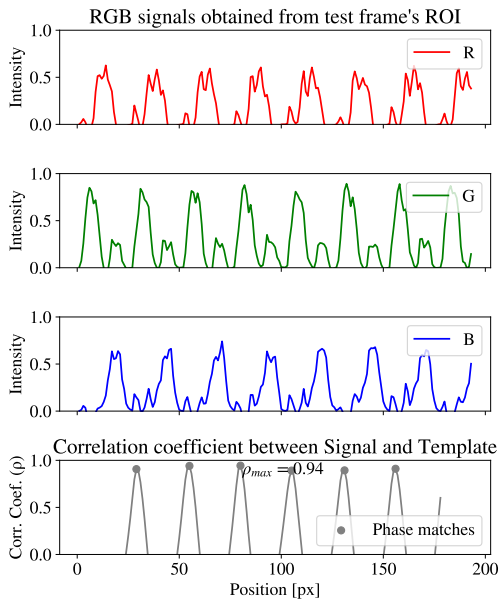


Fig. 5. Example of  $Signal'_{[N \times 3]}$  obtained from test frame and its correlation coefficient with  $Ref'_{[N \times 3]}$  along the height of ROI.

obtained shows an obvious trend of the correlation coefficient to decrease when  $V_M$  is low because the fog attenuates the signal and then the SNR must decrease, and then the similarity to the reference signal is lowered. The figure manifests that above the level of  $V_M \approx 40m$  the test signal remains similar to the reference. Then, below this level, the similarity is damaged. From the non-parametrical regression LOESS of parameter  $\alpha = 0.5$  [21], can be seen that the correlation coefficient drops fast below the level of  $V_M \approx 20m$ .

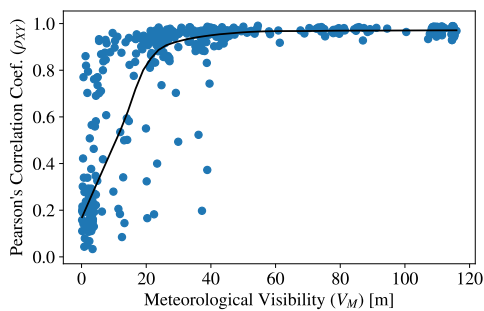


Fig. 6. Peak values of  $\rho_{X,Y}$  obtained from the test group with respect to  $Ref'_{[N \times 3]}$ , plotted against  $V_M$ . LOESS regression is shown for parameter  $\alpha = 0.5$  [21].

#### IV. CONCLUSIONS

This paper presents a study on the influence of the presence of fog over an experimental setup of an OCC unidirectional link in a 5-m-long laboratory chamber. From our results, it was shown that the presence of fog impaired the received signal's Pearson's correlation coefficient with respect to reference signals when the meteorological visibility falls below 40 m, and  $\rho_{X,Y}$  decreases severely when  $V_M$  is under 20 m. It was also presented that the ROI detection process delivered dimensions of the region of interest that were similar to the reference when the meteorological visibility decreased, although for values of  $V_M$  lower than 10 m the algorithm failed to detect the ROI dimensions consistently. With these results, we can assume that the presence of fog causes an attenuation that must be compensated for  $V_M$  values underneath 40 m, and that also the presence of fog does not make OCC able to use larger groups of pixels for signal detection.

#### ACKNOWLEDGMENT

V. M. thanks the help received from Jan Bohata, Petr Chvojka, and Dmytro Suslov at the Czech Technical University in Prague, and Elizabeth Eso from Northumbria University in Newcastle Upon Tyne.

#### REFERENCES

- [1] W. A. Cahyadi, Y. H. Kim, Y. H. Chung, and C. Ahn, "Mobile phone camera-based indoor visible light communications with rotation compensation," *IEEE Photonics Journal*, no. 2, April 2016.
- [2] M. J. Jang, "IEEE 802.15 WPAN 15.7 amendment - optical camera communications study group (SG 7a)," *IEEE 802.15 WPAN*, 2019 [Online accessed 5 October 2019].
- [3] S. R. Teli, S. Zvanovec, and Z. Ghassemlooy, "Performance evaluation of neural network assisted motion detection schemes implemented within indoor optical camera based communications," *Opt. Express*, no. 17, Aug 2019.
- [4] P. Chavez-Burbano, S. Vitek, S. R. Teli, V. Guerra, J. Rabadan, R. Perez-Jimenez, and S. Zvanovec, "Optical camera communication system for internet of things based on organic light emitting diodes," *Electronics Letters*, no. 6, 2019.
- [5] S. V. Tiwari, A. Sewaiwar, and Y. H. Chung, "Optical bidirectional beacon based visible light communications," *Opt. Express*, no. 20, Oct 2015.
- [6] S. Pergoloni, M. Biagi, S. Colonnese, R. Cusani, and G. Scarano, "Coverage optimization of 5G atto-cells for visible light communications access," in *2015 IEEE International Workshop on Measurements Networking (M N)*, Oct 2015.
- [7] M. Boban, A. Kousaridas, K. Manolakis, J. Eichinger, and W. Xu, "Connected roads of the future: Use cases, requirements, and design considerations for vehicle-to-everything communications," *IEEE Vehicular Technology Magazine*, no. 3, Sep. 2018.
- [8] Z. Ghassemlooy, L. N. Alves, S. Zvanovec, and M.-A. Khalighi, *Visible light communications: theory and applications*. CRC press, 2017.
- [9] T. Nguyen, Chang Hyun Hong, Nam Tuan Le, and Y. M. Jang, "High-speed asynchronous optical camera communication using led and rolling shutter camera," in *2015 Seventh International Conference on Ubiquitous and Future Networks*, July 2015.
- [10] T. Kuroda, *Essential Principles of Image Sensors*. CRC Press, 2017.
- [11] Y. H. Kim and Y. H. Chung, "Experimental outdoor visible light data communication system using differential decision threshold with optical and color filters," *Optical Engineering*, no. 4, 2015.
- [12] E. Fabiyi, A. Burton, N. B. Hassan, M. M. Abadi, Z. Ghassemlooy, and S. Zvanovec, "Experimental investigation of the effects of fog on optical camera-based vlc for a vehicular environment," in *2019 15th International Conference on Telecommunications (ConTEL)*, July 2019.

The 3<sup>rd</sup> International West Asian Symposium on Optical and Millimeter-wave Wireless Communications (WASOWC2020)

- [13] M. Elmassie, M. Karbalayghareh, F. Miramirkhani, R. C. Kizilirmak, and M. Uysal, "Effect of fog and rain on the performance of vehicular visible light communications," in *2018 IEEE 87th Vehicular Technology Conference (VTC Spring)*, June 2018.
- [14] Y. H. Kim, W. A. Cahyadi, and Y. H. Chung, "Experimental demonstration of VLC-based vehicle-to-vehicle communications under fog conditions," *IEEE Photonics Journal*, no. 6, Dec 2015.
- [15] X. Tian, Z. Miao, X. Han, and F. Lu, "Sea fog attenuation analysis of white-led light sources for maritime VLC," in *2019 IEEE International Conference on Computational Electromagnetics (ICCEM)*, March 2019.
- [16] T. Yamazato, I. Takai, H. Okada, T. Fujii, T. Yendo, S. Arai, M. Andoh, T. Harada, K. Yasutomi, K. Kagawa, and S. Kawahito, "Image-sensor-based visible light communication for automotive applications," *IEEE Communications Magazine*, no. 7, July 2014.
- [17] I. Takai, S. Ito, K. Yasutomi, K. Kagawa, M. Andoh, and S. Kawahito, "LED and CMOS image sensor based optical wireless communication system for automotive applications," *IEEE Photonics Journal*, no. 5, Oct 2013.
- [18] A. Islam, M. T. Hossan, and Y. M. Jang, "Convolutional neural network scheme-based optical camera communication system for intelligent internet of vehicles," *International Journal of Distributed Sensor Networks*, no. 4, 2018.
- [19] C. Jurado-Verdu, V. Matus, J. Rabadan, V. Guerra, and R. Perez-Jimenez, "Correlation-based receiver for optical camera communications," *Opt. Express*, no. 14, Jul 2019.
- [20] Sony Corporation, *IMX219PQH5-C, Diagonal 4.60 mm (Type 1/4.0) 8 Mega-Pixel CMOS Image Sensor with Square Pixel for Color Cameras, Datasheet*. Sony Corporation, 2014.
- [21] W. S. Cleveland and S. J. Devlin, "Locally weighted regression: An approach to regression analysis by local fitting," *Journal of the American Statistical Association*, no. 403, 1988.

# Design and Implementation of an Optical Camera Communication System for Wireless Sensor Networking in Farming Fields

Vicente Matus\*, Victor Guerra\*, Cristo Jurado-Verdu\*,  
Stanislav Zvanovec†, Jose Rabadan\*, Rafael Perez-Jimenez\*

\*IDeTIC-ULPGC, Las Palmas de Gran Canaria, Spain

†Czech Technical University in Prague, Czech Republic

vmatus@idetic.eu, vguerra@idetic.eu, cjurado@idetic.eu, xzvanove@fel.cvut.cz, jrabadan@idetic.eu, rperez@idetic.eu

**Abstract**—Optical camera communication (OCC) is an innovative set of optical wireless communication that exploits the ever-increasing availability of cameras and solid-state lighting equipment to establish low data rate optical links. This paper evaluates the feasibility of implementing OCC links between sensor nodes in a field outdoors and a camera connected to the cloud in an emulated farming environment. The power efficiency and low maintenance constraints of wireless sensor networks (WSN) are considered in the hardware design of the nodes, which include an energy harvesting system. The system is capable of transmitting 7.5 bps per node at distances of about 100 m. The proposed system is considered a cost-effective and scalable solution for WSN in precision farming.

**Index Terms**—Optical Camera Communication; Visible Light Communication; Smart Farming; Agriculture 4.0; Energy Harvesting.

## I. INTRODUCTION

Digital cameras and solid-state lighting are abundant and continuously growing technologies in urban environments. The techniques for establishing optical wireless communication (OWC) [1] links using these technologies have been denominated optical camera communications (OCC) [2]–[4], which consists of interfaces using light-emitting diode (LED)-based transmitters ( $T_x$ ), and charge-coupled device (CCD) or complementary metal-oxide-semiconductor (CMOS)-based receivers ( $R_x$ ). OCC is closely related to visible light communications (VLC) [5]–[7] because in practice, the most popular OCC implementations reuse cameras and lights that are intended to be used in the visible light spectrum. Nevertheless, some other interesting schemes of OCC have been reported using hyperspectral and thermal cameras [8]–[11].

In addition to the image sensor technology, OCC considers the acquisition mechanism as well, as included in the 802.15.7 standard by the Institute of Electrical and Electronics Engineers (IEEE) [12], which divides them into two categories: global shutter (GS) and rolling shutter (RS) systems. The main difference between both is the time window when the

pixels integrate light. In GS cameras, the whole frame is captured simultaneously, whereas, in RS, it is done on a row-by-row basis, meaning that each horizontal line of pixels in the images is created with a delay with respect to the previous one. For photographic purposes, this difference compromises quality, although the difference is negligible in most cases since the delay between rows is around tens of microseconds. Regarding the hardware complexity, RS allows sparing whole circuit blocks between rows of the sensor, reducing the cost, and making CMOS-sensor RS cameras more prominent in the market. Finally, for communication purposes in OCC, the RS-GS difference compromises the achievable data rate of the system, since each frame in RS can contain more than one state of the transmitter's lamp [13], [14], and GS, in turn, can only decode one symbol per image frame (photogram) [15].

It is worth mentioning that RS techniques require considerable amounts of pixel rows containing data in the region of interest (ROI) of the photograms. Increasing the number of rows is only possible using either large transmitter surfaces, large optical lenses with the camera [16], or by defocusing the lens to widen the transmitter's projection [15]. These requirements necessarily reduce the camera vision, making it impossible to re-utilize existing infrastructure.

Current research on OCC focuses on its applications to the Internet of things (IoT) and Smart Cities, where the most prominent ones are vehicular VLC [5], [17], [18], visible light positioning (VLP) [19] and communication systems in industrial and medical facilities [20], [21] where the radiofrequency spectrum availability is restricted. In this paper, the focus is brought into the application of OCC to precision farming using wireless sensor networks (WSN) [22]. As depicted in Fig. 1, low-energy sensing nodes are deployed in crop fields, measuring physical and biochemical conditions and reporting them to a control system that monitors the farm and manages the nutrients, irrigation, and the dosage of agricultural chemicals [23], [24]. This scenario is particularly interesting since the data rates required are low, nodes are primarily static, sunlight is inherently available for energy harvesting, and surveillance cameras can be re-utilized, as demonstrated in previous works [25], [26].

This work was supported by the European Union's Horizon 2020 research and innovation programme under the Marie Skłodowska-Curie grant agreement no 764461 (VisIoN). It is also based upon work from COST Action CA19111 NEWFOCUS, supported by COST (European Cooperation in Science and Technology).

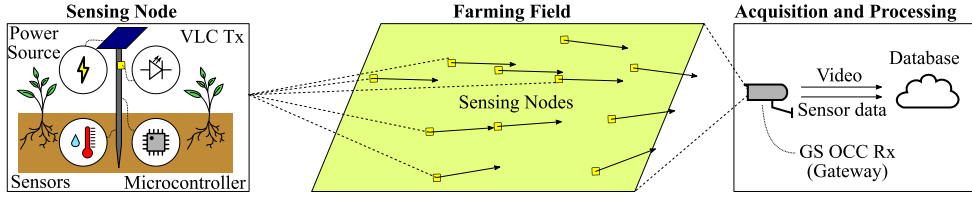


Fig. 1. Basic architecture of a wireless sensor network (WSN) based on an optical camera communication (OCC) scheme.

Hardware constraints and environmental conditions must be considered in farming scenarios. Energy harvesting with single-cell solar panels as input and ultracapacitors (otherwise known as supercapacitors) and lithium-ion batteries for storage [27] can meet the relaxed data rate and latency constraints with a low-cost [28]. For long stops between packet transmissions, sleep mode in the nodes' microcontrollers is required, which requires the receivers to have synchronization strategies. Furthermore, the effects of degradation of the hardware due to the action of chemicals and dust- and bio-fouling must be considered to ensure a lifespan of several years for the nodes to be unattended.

In this paper, an experimental setup is developed and tested in an outdoor field as a proof-of-concept of OCC application to WSN in precision farming systems and its feasibility. The contribution of this work is to propose a novel application of OCC, discussing the design and implementation challenges of developing a multipoint-to-point network of sensing nodes transmitting to a camera monitor node in outdoor conditions and experimentally evaluating the connection of a node.

This paper is structured as follows. Section II develops a model for the wireless optical channel in the scenario of OCC applied to the WSN needed in precision farming scenarios. In Section III, the simulations and the real experimental setup of this work are described. Section IV shows and discusses the results obtained from the experimentation, and Section V, summarizes the conclusions of this work, as well as the further works prospected.

## II. CHANNEL MODEL

In this section, the main parameters of the wireless channel and the OCC devices are considered to develop a channel model. The further theoretical background has been presented in previous works [25], [26], [29] to include more aspects of the channel, such as atmospheric conditions of heat-induced turbulence and the presence of aerosols that produce scattering and absorption of the optical signal. However, in this paper, the influence of these conditions and the background noise produced by the sun and reflections are neglected, and only line-of-sight signal is considered.

Consider a LED-based  $T_x$  pointing towards a camera-based  $R_x$  in a wireless channel. For communication systems as OCC, the image-forming optics theory helps to describe the reception of signals carried by light. OCC systems have exploited the fact that the pixel energy density is preserved with distance.

That is, as long as the transmitter's projection over the image sensor is bigger than one pixel, the energy of each pixel has no direct dependence on the linkspan  $d$ , because, as the distance increases, less energy arrives at the camera and the number of pixels where the energy is projected decreases. The channel gain  $H_p(0)$ , as derived in [30], is given by:

$$H_p(0) = \frac{A_{px}^2 A_{lens}}{f^2 A_{tx}} R(\theta, \varphi), \quad (1)$$

where  $A_{px}$  and  $A_{tx}$  are the areas of a pixel of the ROI and the transmitter's light source, respectively,  $f$  is the camera lens' focal length, and  $R(\theta, \varphi)$  is the LED's radiation pattern, evaluated at the angles of arrival  $\theta$  and  $\varphi$  in spherical coordinates at the camera, taking the axis of symmetry of the lens as the  $z$ -axis. As it was aforementioned, the contribution of the background noise and the sunlight have been neglected. The extinction due to atmospheric conditions has been further studied in [25], [26], [29]. In outdoor conditions, the scattering induced by particles in the air and the turbulence induced by temperature differences along the transmission path must be considered. It does depend on  $d$ , which can be modeled employing the spatial impulse response of the system, commonly referred to as the point spread function (PSF).

An efficacious statistical tool for both the estimation of the PSF and for the synchronization of packets in the decoding stage of the receiver, and possibly the detection of nodes in the photograms generated by the camera is the Pearson's correlation coefficient, which has also been used in previous works to estimate the signal quality in OCC, as an alternative to other well-known metrics [29], [31]. It essentially quantifies the degree of similarity between two signal, as in [29]:

$$r_{xy} = \frac{\sum_{i=1}^N (x_i - \bar{x})(y_i - \bar{y})}{\sqrt{\sum_{i=1}^N (x_i - \bar{x})^2} \sqrt{\sum_{i=1}^N (y_i - \bar{y})^2}}, \quad (2)$$

where,  $\{x_i, y_i\}_{i=1}^N$  are  $N$  samples of a pair of signals  $x, y$ , and  $\bar{x}, \bar{y}$  are the mean values of them, respectively.

Then, for estimating the values of the PSF, when defined in the domain of the image pixels for  $n, m$  the horizontal and vertical coordinates, respectively, the correlation can be used as follows. Assuming the pixel of highest energy within the projection of the transmitter is known to be at coordinates  $n_0, m_0$ , the neighboring pixels can be evaluated and obtain a correlation matrix  $C_{w \times w}$  for an odd number  $w$  the width (and

height) of the ROI. The PSF can be then estimated as a  $w \times w$  matrix in these conditions as in [25]:

$$PSF \approx C_{w \times w} = \{c_{j,k}\}, j \leq w, k \leq w \quad (3)$$

where each component  $c_{j,k}$  of the matrix  $C$  is given by the correlation between the signal at the pixel  $n_0, m_0$  and the signal at the pixel  $n_0 - \lceil w/2 \rceil + j, m_0 - \lceil w/2 \rceil + k$ , using the definition in Equation (2). With this estimation of the PSF, the reference to pixel  $n_0, m_0$  is placed in the center of the matrix, *i.e.* the component  $c_{\lceil w/2 \rceil, \lceil w/2 \rceil}$  and its value is 1. The PSF has a two-dimensional structure similar to a Gaussian distribution, as shown in Fig. 2, and its spread increases according to various factors, including the camera lens' focus setting, the scattering in the air, among others.

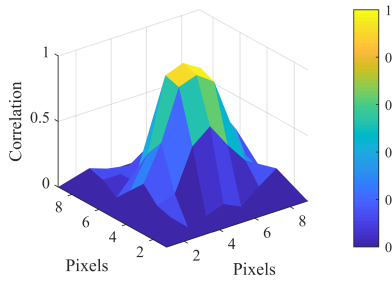


Fig. 2. Example of a point spread function estimated by means of the Pearson's correlation coefficient for a light-emitting diode (LED) transmitter ( $T_x$ ) at 90 m from a camera-based receiver, as reported in previous work [26].

### III. METHODOLOGY

In this section, the design and implementation of the experimental setup for studying WSN using OCC are developed for an emulated farming scenario in a test field. The development considers the most relevant hardware constraints for communication purposes and energy management of the sensing nodes. The scenario's configuration is first simulated to have a tool for estimating the geometrical distribution of the nodes and their optimal orientation to the receiver. The blocks of the sensing and receiving nodes are described.

#### A. Simulation

The geometrical configuration of nodes was simulated in order to estimate their optimal orientation and for further studies. The orientation of the  $T_x$  LED considers the peak power as the z-axis of the transmitter's relative coordinate system; in other words, the radiation pattern peaks at the axis of symmetry of the device. Likewise, the camera-based receiver's z-axis is the normal vector in the center of the primary lens.

The X, Y positions of  $n_{T_x}$  sensing nodes can be set in grid shape or randomly on the field, whereas the orientations are adjusted pointing to a specific coordinate. In Fig. 3, a number of  $n_{T_x} = 75$  nodes were randomly placed in a field of 100 by 100 m, and all  $T_x$  units' orientations were set to coordinates

(-1,-1,1) with respect to the global coordinates of the field, assuming no precise orientation of the transmitters can be guaranteed in a real deployment. The camera-based  $R_x$  is placed in one corner of the field, at coordinates (0,0,3) with orientation (1,1,-0.1) pointing into the field.

By using trigonometrical tools of spherical coordinate systems, the optimal orientations of each node can be calculated, and by including the LED's radiation pattern, the received power from each node can be estimated. Issues like occlusion between nodes can be further estimated by including a model of the camera optics as derived in [32].

#### B. Experimental Setup

The system implemented for the experiments consisted of a transmitting node, comprised by a 5 mm white LED (Vishay VLHW5100) connected to the digital output of a microcontroller, powered by an energy harvesting system based on a 0.3 by 0.4 m photovoltaic (PV) cell (solar panel), a 1200 mAh Li-ion battery, a charging circuit (Microchip MCP73831), and a step-up direct current (DC)-to-DC boost converter that outputs a fixed 5 V DC signal to the microcontroller. A secondary LED sending a fixed square signal was installed to test the synchronization of the microcontroller's clock during processing. The results obtained are shown only for the primary LED. The modulation of the LED is based on an on-off keying (OOK) modulation at 7.5 baud, using a packet structure defined in [25].

An alternative energy harvesting module of a similar cost of accumulator was tested using a 5 F ultracapacitor. As the capacity in Wh is about a hundred times smaller, the PV module was changed to 35 by 50 mm, with 1.5  $W_p$  peak power. The advantages of this alternative setup are the simplicity that it does not require a charging circuit nor a boost converter and the longer lifespan compared to using lithium-ion cells thanks to the solid-state nature of ultracapacitor. Nevertheless, this configuration requires developing sleep mode strategies for the microcontrollers needed to save energy. This requirement is compatible with the low data rates required by the farm monitoring.

The receiving node, in turn, was built using a CMOS camera with RS acquisition (Sony IMX219) controlled by a computer (Raspberry Pi 4) which was connected to mains (grid power) and a Wi-Fi hotspot. The camera allows 30 fps framerate video using full HD (1920 by 1080 px). Different configurations of exposure time ( $t_{exp}$ ) and analog gain [29] were tested, although the examples shown in this paper only consider  $t_{exp}$  of 120  $\mu s$  and default gain. The distance between both nodes was approximately 100 m. The most relevant parameters of the experimental setup are summarized in Table I.

Figure 4 shows the diagram of the experimental setup deployed at the facilities of the Institute for Technological Development and Innovation in Communications (IDeTIC), Spain. The setup consists of the aforementioned LED-based transmitter installed in a field next to IDeTIC's building. The receiver, inside the Institute, connected to the cloud, captures

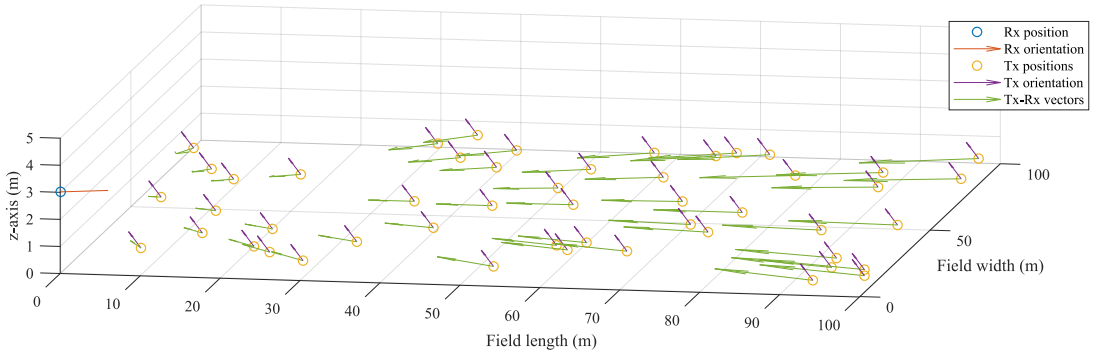


Fig. 3. The scenario of the simulation of WSN in a precision farming field including  $n_{Tx} = 75$  nodes, one receiver.

TABLE I  
KEY EXPERIMENTAL PARAMETERS

Module	Parameter	Value
$T_x$	Light Source	Single 5 mm white LED [33]
	PV cell 1 Peak Power	5.0 W <sub>p</sub>
	PV cell 2 Peak Power	1.5 W <sub>p</sub>
	Microcontroller	Atmel ATmega328p [34]
	Accumulator 1	Li-ion 18650-type cell 1200 mAh
Channel	Accumulator 2	5 F 5.5V ultracapacitor
	Link span ( $d$ )	100 m
$R_x$	Image sensor	Sony IMX219 [35]
	Video resolution	1920 x 1080 px
	Frame rate	30 fps
	Exposure time ( $t_{exp}$ )	120 $\mu$ s

a video of the field every ten minutes and saves the data in a server for offline processing.

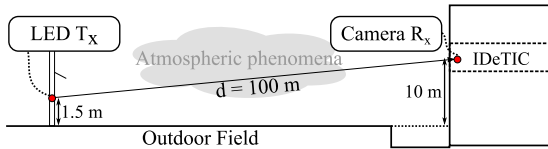


Fig. 4. Diagram of the experimental OCC setup employed in this work.

The block diagram shown in Fig. 5 summarizes the stages of the OCC workflow implemented in the experiments and is described as follows. The sensors' data are read by the microcontroller using separated digital inputs or a shared input implementing a bus structure. The data is prepared in a packet structure that facilitates the detection using correlation-based techniques, as developed in [25], [26]. The packet data is transformed into a voltage signal at a microcontroller's digital output that drives the LED directly. If the LED's current would be higher than the maximum allowed by the microcontroller, a transistor connected to the power source must drive the LED.

The light travels through the field as a wireless signal and is affected by occlusions, degradation of the transmitter's surface, scattering due to particles in the atmosphere, turbulence in

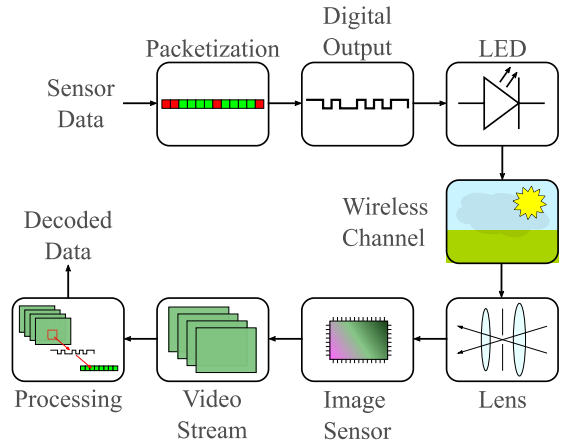


Fig. 5. Flow diagram of the OCC system

the air, and other meteorological phenomena. It arrives at the camera lens, where the image is focused and formed to be digitalized by the image sensor. The effects over the signal by the quantification carried out by CMOS have been studied in [29]. At this stage, the camera gain, exposure time, and framerate are set. A video stream is generated by the camera equipment and saved in video format locally or remotely for processing. In the processing stage (carried out offline in this case), the ROI detection and signal decoding is done using correlation techniques. For these experiments, the ROI has been determined manually.

The final implementation of the  $T_x$  node components in the field is depicted in Fig. 6.

#### IV. RESULTS AND DISCUSSION

The results of the experimentation are summarized and discussed in this section. The frames captured by the camera and the signals obtained from processing are shown to depict the system's performance. The result of using two different energy harvesting systems is discussed.



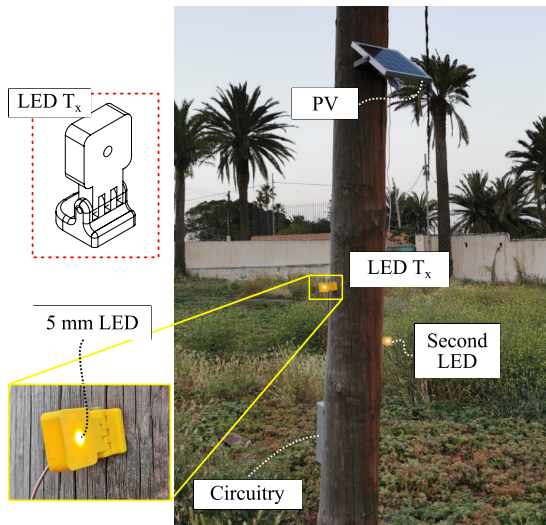


Fig. 6. LED-based  $T_x$  node using a photovoltaic (PV) energy harvesting system deployed in a field.

The video captures performed by the camera every ten minutes are continuously stored in the cloud and processed offline. The video frames are cut into an arbitrary pre-ROI for smaller storage demand. In Fig. 7, the frames obtained from the camera's output video before pre-ROI cut are shown, highlighting the region of pre-ROI with respect to the full-frame from the original video. The final ROI, which was selected arbitrarily during the processing stage, includes only the  $T_x$  in the image. According to the pixel found with the highest signal power in the ROI, the decoding and the estimation of the PSF were carried out using the correlation process, as reported in [25], [26]. The waveforms obtained at different pixels are shown in Fig. 8. The highest value of signal-to-noise ratio (SNR) obtained was 17 db, which due to the OOK modulation employed would represent a bit-error rate below  $10^{-12}$ .

Although high data rates are not pursued in precision farming sensor networks, it is worth mentioning that if data aggregation of all transmitting nodes is possible, and assuming no occlusions by nodes or other features of the field, OCC WSN systems can potentially achieve only about tens of kbps. In the example of the simulated scenario shown before, the case of 75 nodes transmitting continuously would achieve a throughput of about 500 bps, according to the simulations.

## V. CONCLUSIONS

This work showed the technical developments and experimental results of a concrete application of OCC to WSN in precision farming environments. A system comprised of a single 5 mm LED sending light pulses to a CMOS camera was built and deployed in a field outdoors. The camera video output

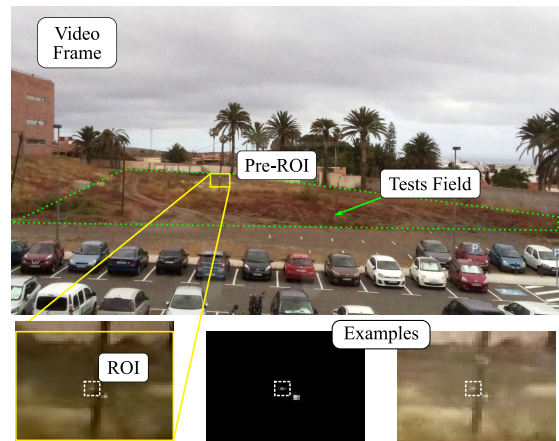


Fig. 7. An example of a video frame obtained by the camera, highlighting the region of interest (ROI) and different examples obtained throughout the experimentation.

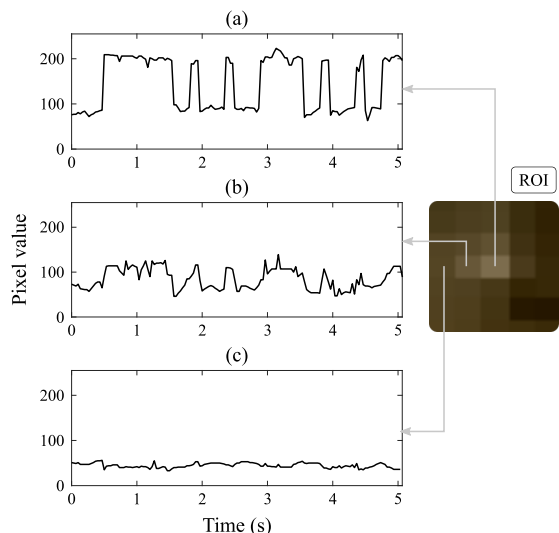


Fig. 8. Example of the waveforms obtained at different pixels in the projection of the transmitter. (a) Shows the highest power pixel's signal. (b) Shows the signal at a pixel in the neighborhood at distance 1 px. (c) Shows the signal at a pixel in the neighborhood at a distance 2 px.

allows monitoring the field while the photographs' processing obtains the transmitter's information at a 100 m distance.

Energy harvesting technologies were considered for powering the sensing nodes, which are set to consume low powers using the sleep mode of their embedded microcontroller. Different configurations of PV panels and Li-ion battery cells as well as ultracapacitors as accumulators were tested. Depending on the nature of the monitored variable, the sleep times can be adjusted. Lithium-ion batteries' solutions are less expensive

than using ultracapacitors, although they are challenged by faster degradation.

Geometrical simulations were carried out to calculate the optimal pointing angles for the transmitters in the sensing nodes. These simulations should be further developed to evaluate critical issues such as occlusions between nodes, pointing error ranges, the effect of different radiation patterns in the LEDs, and the lens configuration of the camera.

Further works should consider the combination of OCC schemes with other existing technologies, such as narrow-band IoT and low-power wide-area network, into a heterogeneous network that could achieve longer link spans. The OCC system would serve to aggregate sensing nodes locally in the short range, and the RF technologies mentioned could serve as a link for longer ranges.

#### REFERENCES

- [1] Z. Ghassemlooy, W. Popoola, and S. Rajbhandari, *Optical wireless communications: system and channel modelling with Matlab*. CRC press, 2019.
- [2] W. A. Cahyadi, Y. H. Chung, Z. Ghassemlooy, and N. B. Hassan, "Optical camera communications: Principles, modulations, potential and challenges," *Electronics*, vol. 9, no. 9, 2020.
- [3] N. Saeed, S. Guo, K.-H. Park, T. Y. Al-Naffouri, and M.-S. Alouini, "Optical camera communications: Survey, use cases, challenges, and future trends," *Physical Communication*, vol. 37, p. 100900, 2019.
- [4] N. T. Le, M. Hossain, and Y. M. Jang, "A survey of design and implementation for optical camera communication," *Signal Processing: Image Communication*, vol. 53, pp. 95–109, 2017.
- [5] P. H. Pathak, X. Feng, P. Hu, and P. Mohapatra, "Visible light communication, networking, and sensing: A survey, potential and challenges," *IEEE communications surveys & tutorials*, vol. 17, no. 4, pp. 2047–2077, 2015.
- [6] Y. Almadani, D. Plets, S. Bastiaens, W. Joseph, M. Ijaz, Z. Ghassemlooy, and S. Rajbhandari, "Visible light communications for industrial applications—challenges and potentials," *MDPI Electronics*, vol. 9, no. 12, 2020.
- [7] Z. Ghassemlooy, L. N. Alves, S. Zvanovec, and M.-A. Khalighi, *Visible light communications: theory and applications*. CRC press, 2017.
- [8] D. Moreno, J. Rufo, V. Guerra, J. Rabadan, and R. Perez-Jimenez, "Optical multispectral camera communications using led spectral emission variations," *IEEE Photonics Technology Letters*, pp. 1–1, 2021.
- [9] D. Moreno, J. Rufo, V. Guerra, J. Rabadan, and R. Perez-Jimenez, "Effect of temperature on channel compensation in optical camera communication," *Electronics*, vol. 10, no. 3, 2021.
- [10] D. Moreno, B. Majlesejn, J. Rufo, V. Guerra, J. Rabadan, and R. Perez-Jimenez, "Thermally-induced spectral variations of led applied to optical multispectral camera communications," in *2020 12th International Symposium on Communication Systems, Networks and Digital Signal Processing (CSNDSP)*, pp. 1–6, 2020.
- [11] V. Guerra, J. R. Ticay-Rivas, V. Alonso-Eugenio, and R. Perez-Jimenez, "Characterization and performance of a thermal camera communication system," *Sensors*, vol. 20, no. 11, 2020.
- [12] IEEE Standard Association, "IEEE standard for local and metropolitan area networks-part 15.7: short-range wireless optical communication using visible light," *IEEE: Piscataway, NJ, USA*, pp. 1–309, 2011.
- [13] C. Jurado-Verdu, V. Guerra, J. Rabadan, R. Perez-Jimenez, and P. Chavez-Burbano, "Rgb synchronous vlc modulation scheme for occ," in *2018 11th International Symposium on Communication Systems, Networks Digital Signal Processing (CSNDSP)*, pp. 1–6, July 2018.
- [14] O. I. Younus, N. Bani Hassan, Z. Ghassemlooy, P. A. Haigh, S. Zvanovec, L. N. Alves, and H. L. Minh, "Data rate enhancement in optical camera communications using an artificial neural network equaliser," *IEEE Access*, vol. 8, pp. 42656–42665, 2020.
- [15] E. Eso, S. Teli, N. B. Hassan, S. Vitek, Z. Ghassemlooy, and S. Zvanovec, "400 m rolling-shutter-based optical camera communications link," *Opt. Lett.*, vol. 45, pp. 1059–1062, Feb 2020.
- [16] P. Chavez-Burbano, V. Guerra, J. Rabadan, D. Rodriguez-Esparragon, and R. Perez-Jimenez, "Experimental characterization of close-emitter interference in an optical camera communication system," *Sensors*, vol. 17, no. 7, p. 1561, 2017.
- [17] M. Karbalayghareh, F. Miramirkhani, H. B. Eldeeb, R. C. Kizilirmak, S. M. Sait, and M. Uysal, "Channel modelling and performance limits of vehicular visible light communication systems," *IEEE Transactions on Vehicular Technology*, vol. 69, no. 7, pp. 6891–6901, 2020.
- [18] M. Elamassie, M. Karbalayghareh, F. Miramirkhani, R. C. Kizilirmak, and M. Uysal, "Effect of fog and rain on the performance of vehicular visible light communications," in *2018 IEEE 87th Vehicular Technology Conference (VTC Spring)*, June 2018.
- [19] N. Chaudhary, O. I. Younus, L. N. Alves, Z. Ghassemlooy, S. Zvanovec, and H. Le-Minh, "An indoor visible light positioning system using tilted leds with high accuracy," *Sensors*, vol. 21, no. 3, 2021.
- [20] E. A. Jarchlo, E. Eso, H. Doroud, A. Zubow, F. Dressler, Z. Ghassemlooy, B. Siessegger, and G. Caire, "Flla: A novel frequency diversity and link aggregation solution for handover in an indoor vehicular vlc network," *IEEE Transactions on Network and Service Management*, pp. 1–1, 2021.
- [21] K. L. Bober, S. Maravanchery Mana, M. Hinrichs, S. Mohammad Kouhni, C. Kotte, D. Schulz, R. Freund, and V. Jungnickel, "Distributed multiuser mimo for lifi in industrial wireless applications," *Journal of Lightwave Technology*, pp. 1–1, 2021.
- [22] J. Yick, B. Mukherjee, and D. Ghosal, "Wireless sensor network survey," *Computer networks*, vol. 52, no. 12, pp. 2292–2330, 2008.
- [23] M. Ayaz, M. Ammad-Uddin, Z. Sharif, A. Mansour, and E. M. Aggoune, "Internet-of-things (iot)-based smart agriculture: Toward making the fields talk," *IEEE Access*, vol. 7, pp. 129551–129583, 2019.
- [24] T. Ojha, S. Misra, and N. S. Raghuvanshi, "Wireless sensor networks for agriculture: The state-of-the-art in practice and future challenges," *Computers and Electronics in Agriculture*, vol. 118, pp. 66–84, 2015.
- [25] V. Matus, V. Guerra, C. Jurado-Verdu, J. Rabadan, and R. Perez-Jimenez, "Demonstration of a sub-pixel outdoor optical camera communication link," *IEEE Latin America Transactions*, vol. 19, pp. 1798–1805, Apr. 2021.
- [26] V. Matus, V. Guerra, C. Jurado-Verdu, S. Zvanovec, and R. Perez-Jimenez, "Wireless sensor networks using sub-pixel optical camera communications: Advances in experimental channel evaluation," *Sensors*, vol. 21, no. 8, 2021.
- [27] N. Qi, Y. Yin, K. Dai, C. Wu, X. Wang, and Z. You, "Comprehensive optimized hybrid energy storage system for long-life solar-powered wireless sensor network nodes," *Applied Energy*, vol. 290, p. 116780, 2021.
- [28] G.-Z. Hong and C.-L. Hsieh, "Application of integrated control strategy and bluetooth for irrigating romaine lettuce in greenhouse," *IFAC-PapersOnLine*, vol. 49, no. 16, pp. 381–386, 2016. 5th IFAC Conference on Sensing, Control and Automation Technologies for Agriculture AGRICONTROL 2016.
- [29] V. Matus, E. Eso, S. R. Teli, R. Perez-Jimenez, and S. Zvanovec, "Experimentally derived feasibility of optical camera communications under turbulence and fog conditions," *Sensors*, vol. 20, p. 757, Jan 2020.
- [30] T. Yamazato, M. Kinoshita, S. Arai, E. Souke, T. Yendo, T. Fujii, K. Kamakura, and H. Okada, "Vehicle motion and pixel illumination modeling for image sensor based visible light communication," *IEEE Journal on Selected Areas in Communications*, vol. 33, no. 9, pp. 1793–1805, 2015.
- [31] V. Matus, V. Guerra, C. Jurado-Verdu, S. Teli, S. Zvanovec, J. Rabadan, and R. Perez-Jimenez, "Experimental evaluation of an analog gain optimization algorithm in optical camera communications," in *2020 12th International Symposium on Communication Systems, Networks Digital Signal Processing (CSNDSP)*, pp. 1–5, 2020.
- [32] V. Matus, V. Guerra, C. Jurado-Verdu, J. Rabadan, and R. Perez-Jimenez, "Simulation of rolling shutter acquisition in optical camera communications," in *2019 15th International Conference on Telecommunications (ConTEL)*, pp. 1–5, 2019.
- [33] Vishay Semiconductors, *Ultrabright White LED, 5 mm Untinted Non-Diffused Package, Datasheet*. Vishay Semiconductors, 2019.
- [34] Atmel Corporation, *ATmega328p, 8-bit AVR Microcontroller with 32K Bytes In-System Programmable Flash, Datasheet*. Atmel Corporation, 2015.
- [35] Sony Corporation, *IMX219PQH5-C, Diagonal 4.60 mm (Type 1/4.0) 8 Mega-Pixel CMOS Image Sensor with Square Pixel for Color Cameras, Datasheet*. Sony Corporation, 2014.

The languages of the scripts developed are *Python* with *Numpy*, *Scipy* and *Matplotlib* libraries, and *MATLAB*®

The repository that contains all the codes developed in this Thesis, as well as the experimental database, is publicly available at: <https://github.com/vmatus-ulpgc/thesis>